8-2019

Modification and Optimization of Conducting Polymer-Modified, Redox-Magnetohydrodynamics (R-MHD) Pumping for Enhanced and Sustained Microfluidics Applications

Md Foysal Zahid Khan
University of Arkansas, Fayetteville

Modification and Optimization of Conducting Polymer-Modified, Redox-Magnetohydrodynamics (R-MHD) Pumping for Enhanced and Sustained Microfluidics Applications

A dissertation submitted in partial fulfillment
of the requirements for the degree of
Doctor of Philosophy in Chemistry

by

Md Foysal Zahid Khan
University of Dhaka
Bachelor of Science in Applied Chemistry and Chemical Engineering, 2011
University of Dhaka
Master of Science in Applied Chemistry and Chemical Engineering, 2013

August 2019
University of Arkansas

This dissertation is approved for recommendation to the Graduate Council.

_____
Ingrid Fritsch, Ph.D.
Dissertation Director

_____
Charles L. Wilkins, Ph.D.
Committee Member

_____
David W. Paul, Ph.D.
Committee Member

_____
Colin D. Heyes, Ph.D.
Committee Member

_____
Steve Tung, Ph.D.
Committee Member

Abstract

In this work, a novel microfluidic pumping approach, redox-magnetohydrodynamics (R-MHD) has improved by materials and device optimization to use in lab-on-a-chip applications. In R-MHD, magnetic flux (B) and ionic current density (j) interacts to generate body force (F_B) in between active electrodes, according to the equation $F_B = j \times B$. This unique fluid pumping approach is scalable, tunable, generates flat flow profile, and does not require any channels or valves. Pumping performance, such as speed scales with the ionic current density (j) and duration depends on the total charge (Q). The ionic current density (j) results from the conversion of electronic current through redox reactions of a conducting polymer like PEDOT (poly-EDOT). The enhancement of j can be obtained by the modification of polymer morphology. Therefore, electropolymerization parameters such as solvent, monomer, electrolyte, and deposition method have been optimized to improve the electrochemical performance of PEDOT. Electrodeposited PEDOT film from propylene carbonate solvent and $TBAPF_6$ electrolyte generated a maximum of 820 μm/s flow velocity and 210 s flow duration. This enhanced system used as an imaging cytometer by coupling with a light sheet confocal microscope. This microfluidic imaging platform was able to differentiate various leukocytes cells with ~ 5000 cell/s theoretical throughput and 0.6 μm image resolution. As, our existing microscope could not analyze the R-MHD velocity profile in height direction, astigmatism particle tracking velocimetry (APTV) was employed to analyze flow profiles in three dimensions. In a microfluidic setup, flow profile is dominated by stream wise component but with no significant contributions in y and z direction. Though we achieved significant improvement in fluidic speed, flow duration was still dependent upon the total charge. Therefore, an automated magnet switching device was built which synchronized the current and magnetic field to push fluid in single direction, for unlimited time.

Acknowledgements

At first, I would like to thank my mentor Dr. Ingrid Fritsch. She has set an example of distinction to me as a scientist, mentor and instructor. Her passion for science and innovation inspired me to be a scientist too. Dr. Ingrid Fritsch has pioneered the R-MHD pumping for microfluidics and I feel very fortunate to have contribution in this innovative project.

I would like to express my appreciation to the PhD committee member Dr. Charles Wilkins, Dr. David Paul, Dr. Colin Heyes, and Dr. Steve Tung. Their thoughtful and scientific discussions and guidance have been very helpful.

I would like to thank our collaborators for their great ideas, support and research help. I am appreciative for the support from Dr. Timothy J. Muldoon, Joshua Hutcheson, and Courtney Hunter for the imaging cytometry project. I also like to show my heartfelt gratitude to Dr. Christian Cierpka and Dr. Jörg König from Technische Universität Ilmenau, Germany for their collaboration in 3D flow profile analysis project. I am also thankful for the support given by David Parette in R-MHD device optimization project.

I am very thankful to my beloved wife Fahmida Afrose. Her endless love and constant support have been an integral part of my success. I want to thank my family, especially my parents Md. Fazlur Rahman Khan (deceased) & Mamtaz Begum and my eldest brother, Md. Fazlarabbi Khan for their relentless support towards my education and upbringing.

I would like to thank my fellow research group members and my friends for supporting me throughout my PhD career.

Research was supported by the National Science Foundation (NSF) (CHE-1808286 and CBET-1336853), Arkansas Biosciences Institute, the major research component of the Arkansas Tobacco Settlement Proceeds Act of 2000, A.L. Chilton Foundation Award, and Provost Collaborative Research Grant, University of Arkansas.

Dedication

In dedication to my beloved parents

Md. Fazlur Rahman Khan (deceased) & Mamtaz Begum,

my lovely wife Jenny, and my brother Dr. Fazlarabbi Khan

Table of Contents

List of Published Papers

1. Khan, F. Z. and Fritsch, I. Chip-Scale Electrodeposition and Analysis of Poly(3,4-ethylenedioxythiophene) (PEDOT) Films for Enhanced and Sustained Microfluidics Using DC-Redox-Magnetohydrodynamics. Journal of the Electrochemical Society 2019. (Chapter 2, in revision)

2. Khan, F. Z.; Hutcheson, J. A.; Hunter, C. J.; Powless, A. J.; Benson, D.; Fritsch, I.; Muldoon, T. J. Redox-Magnetohydrodynamically Controlled Fluid Flow with Poly(3,4-ethylenedioxythiophene) Coupled to an Epitaxial Light Sheet Confocal Microscope for Image Cytometry Applications. Analytical Chemistry 2018, 90 (13), 7862-7870, DOI: 10.1021/acs.analchem.7b05312. (Chapter 4, published)

1. Introduction to Modification and Optimization of Conducting Polymer-Modified, Redox-Magnetohydrodynamics (R-MHD) Pumping

1.1 Introduction

Microfluidics is the science of manipulating small amount of fluid, typically in micro or nano scale. Due to certain advantages, such as short analysis time, small amount of sample requirement, fast analysis, and portability, this technology has made the device size practical for point-of-care applications.[1-2]. Microfluidics has proven very useful in many biomedical research areas, such as drug discovery, enzymatic assay, cell biology, cell sorting, and cytometry. [3-8] One of the most important part of a microfluidic device is the fluid pumping system. Often fluid needs to be transported, controlled, and manipulated through the microfluidic device and they can be performed by various existing approaches, such as pressure, electrostatic, thermo-pneumatic, electroosmotic, and magnetohydrodynamics (MHD) pumps. Regardless of their working principals, these are largely divided into either mechanical or non-mechanical. Mechanical micropumps consist valves, oscillating membranes, and turbines which are costly and difficult to miniaturize. Therefore, many lab-on-a-chip systems often require pumps that will allow flexibility in miniaturization and have better flow controllability.

Redox-Magnetohydrodynamics (R-MHD) is a unique fluid pumping method where the body force, F_B (N/m^3) is generated by the perpendicular interaction of the magnetic flux density, B (T) and ionic current density, j ($C / m^2 s$). R-MHD takes advantages of the magnetic portion of the Lorentz force and the generated body force (F_B) pushes the fluid without needing any channels or valves.[9] Figure 1 shows the basic principle R-MHD pumping, where between two polymer coated electrodes ionic current density (j) works perpendicularly with the magnetic field (B) and the resulted body force (F_B) pushes the fluid by following the right-hand rule. R-MHD

microfluidics uses easily oxidizable- reducible redox species (such as $Fe[(CN)_6]^{-3}$ / $Fe[(CN)_6]^{-4}$) or conducting polymers to generate ionic current density (j) in the electrolyte solution.[10-12] R-MHD consist features that make it useful for microfluidic applications such as channel less or valve less pumping, low operating voltage, flat flow profile, bi-directional flow, stirring and mixing capability, speed and duration tunability, and miniaturizability.

Conducting polymers have recently attracted attentions of the energy and sensor research community due to their fast electron transfer, low ionization potential, electropolymerizability, high conductivity, better charge-discharge capability, and flexibility.[13-15] Poly(3,4-ethylenedioxythiophene) (PEDOT) is a very successful member of the thiophene-based conducting polymer family, which has been successfully used in battery electrode, antistatic coating, photovoltaic cells, and chemical sensor applications.[16-17] PEDOT also exhibited the best performance so far as the source of redox centers in R-MHD pumping. Immobilized PEDOT on the electrode surface not only avoids analyte interference but also allows immediate availability of high current than the solution redox species. Immobilization can be done either by oxidative polymerization or electropolymerization. The later one holds certain advantages over the other, such as 1) uniform and well adhered film 2) small amount of monomer requirement 3) easy polymerization on any electrode geometry 4) tunability in polymer morphology and thickness. [18]

PEDOT electropolymerization and R-MHD pumping experiments were done with microfabricated chips. Each chip (2 in.×1 in.) contains individually addressable gold electrodes which were patterned on silicon wafer substrate by using photolithography.[10] The chip design used for this work has four band electrodes (Figure 2) where each electrode is 1.5 cm long and 650 μm wide. The outermost two electrode pairs and inner two electrode have 0.30 and 0.47 cm gap, respectively.

The R-MHD pumping performance depends on the polymer's electrochemical properties. The flow speed and duration scales with the maximum achievable current and charge density from the polymer film, respectively. These two electrochemical properties also define the capability of ions in the electrolyte solution to permeate through the film and compensate for the charge imbalance. There are different variables which can be optimized to improve these electrochemical properties, such as film morphology and electrolyte strength. Also, polymerizability, film morphology and robustness are function of solvent, monomer, electrolyte, and deposition method used in electrodeposition.

The inspiration of this research work comes from the need to pump fluid at a high speed for indefinite time. Therefore, both materials and device optimization were performed to fulfill the research goal. Chapter 2 discusses the electropolymerization of EDOT by potentiodynamic method at different time scales from organic solvent and various electrolytes. The electrodeposited films were characterized by cyclic voltammetry, chronoamperometry, chronopotentiometry, and impedance spectroscopy in aqueous electrolytes of NaCl, phosphate buffered saline, and glycerol-containing electrolytes. A linear dependency of current density was achieved with the ionic strength of the characterizing solution. A model system was proposed to correlate film thickness with the achievable current response in electrolyte solutions.

Chapter 3 focuses on the polymer electrodeposition by varying monomer, solvent, and deposition techniques. EDOT monomer and propylene carbonate solvent generated optimized film with the best electrochemical properties.

In Chapter 4, we merged the light sheet confocal microscope with our improved R-MHD pumping system to perform continuous high-resolution fluorescence imaging of cellular

suspension in a deep microfluidic chamber (2 mm). This novel imaging cytometry approach resulted in ~ 5000 particles /s theoretical throughput and 0.6 μm lateral image resolution.

Chapter 5 focuses on the fluid flow generation by varying chamber height, pumping solution concentration, and applied current and the resulted flow profiles were analyzed by astigmatism particle tracking velocimetry (APTV). APTV technique has allowed three-dimensional velocity analysis with high resolution.

In chapter 2 and 3, electropolymerization parameters were optimized for maximum current and charge density which translate into flow velocity and duration. Under controlled current condition, flow velocity increases with the applied current but the duration decreases as high current consumes charges on the PEDOT faster. So, high speed fluid flow for elongated time was still a predicament. Therefore, device optimization was performed to sustain the highspeed flow for indefinite time. Chapter 6 addresses a method where two permanent magnets with opposite biases switch under the chip and synchronizes with applied currents to move fluid unidirectionally, and for unlimited time.

The format of this dissertation is compatible for publication in peer reviewed journals. Every chapter has main text and a supporting information section at the end.

1.2 References

(1) Whitesides, G. M. The origins and the future of microfluidics. *Nature* **2006,** *442* (7101), 368-373, DOI: 10.1038/nature05058.

(2) Polson, N. A.; Hayes, M. A. Peer Reviewed: Microfluidics: Controlling Fluids in Small Places. *Analytical Chemistry* **2001,** *73* (11), 312 A-319 A, DOI: 10.1021/ac0124585.

(3) Sackmann, E. K.; Fulton, A. L.; Beebe, D. J. The present and future role of microfluidics in biomedical research. *Nature* **2014,** *507*, 181, DOI: 10.1038/nature13118.

(4) Dittrich, P. S.; Manz, A. Lab-on-a-chip: microfluidics in drug discovery. *Nature Reviews Drug Discovery* **2006,** *5* (3), 210-218, DOI: 10.1038/nrd1985.

(5) Rondelez, Y.; Tresset, G.; Tabata, K. V.; Arata, H.; Fujita, H.; Takeuchi, S.; Noji, H. Microfabricated arrays of femtoliter chambers allow single molecule enzymology. *Nature Biotechnology* **2005,** *23* (3), 361-365, DOI: 10.1038/nbt1072.

(6) Khan, F. Z.; Hutcheson, J. A.; Hunter, C. J.; Powless, A. J.; Benson, D.; Fritsch, I.; Muldoon, T. J. Redox-Magnetohydrodynamically Controlled Fluid Flow with Poly(3,4-ethylenedioxythiophene) Coupled to an Epitaxial Light Sheet Confocal Microscope for Image Cytometry Applications. *Analytical Chemistry* **2018,** *90* (13), 7862-7870, DOI: 10.1021/acs.analchem.7b05312.

(7) Autebert, J.; Coudert, B.; Bidard, F.-C.; Pierga, J.-Y.; Descroix, S.; Malaquin, L.; Viovy, J.-L. Microfluidic: An innovative tool for efficient cell sorting. *Methods* **2012,** *57* (3), 297-307, DOI: https://doi.org/10.1016/j.ymeth.2012.07.002.

(8) Cheung, K. C.; Di Berardino, M.; Schade-Kampmann, G.; Hebeisen, M.; Pierzchalski, A.; Bocsi, J.; Mittag, A.; Tárnok, A. Microfluidic impedance-based flow cytometry. *Cytometry Part A* **2010,** *77A* (7), 648-666, DOI: 10.1002/cyto.a.20910.

(9) Weston, M. C.; Gerner, M. D.; Fritsch, I. Magnetic Fields for Fluid Motion. *Analytical Chemistry* **2010,** *82* (9), 3411-3418, DOI: 10.1021/ac901783n.

(10) Sahore, V.; Fritsch, I. Flat Flow Profiles Achieved with Microfluidics Generated by Redox-Magnetohydrodynamics. *Analytical Chemistry* **2013,** *85* (24), 11809-11816, DOI: 10.1021/ac402476v.

(11) Sahore, V.; Fritsch, I. Redox-Magnetohydrodynamics, Flat Flow Profile-Guided Enzyme Assay Detection: Toward Multiple, Parallel Analyses. *Analytical Chemistry* **2014,** *86* (19), 9405-9411, DOI: 10.1021/ac502014t.

(12) Nash, C. K.; Fritsch, I. Poly(3,4-ethylenedioxythiophene)-Modified Electrodes for Microfluidics Pumping with Redox-Magnetohydrodynamics: Improving Compatibility for Broader Applications by Eliminating Addition of Redox Species to Solution. *Analytical Chemistry* **2016,** *88* (3), 1601-1609, DOI: 10.1021/acs.analchem.5b03182.

(13) Chen, J.; Liu, Y.; Minett, A. I.; Lynam, C.; Wang, J.; Wallace, G. G. Flexible, Aligned Carbon Nanotube/Conducting Polymer Electrodes for a Lithium-Ion Battery. *Chemistry of Materials* **2007,** *19* (15), 3595-3597, DOI: 10.1021/cm070991g.

(14) Naegele, D.; Bittihn, R. Electrically conductive polymers as rechargeable battery electrodes. *Solid State Ionics* **1988,** *28-30*, 983-989, DOI: https://doi.org/10.1016/0167-2738(88)90316-5.

(15) Yoon, H.; Jang, J. Conducting-Polymer Nanomaterials for High-Performance Sensor Applications: Issues and Challenges. *Advanced Functional Materials* **2009,** *19* (10), 1567-1576, DOI: 10.1002/adfm.200801141.

(16) Wang, X.; Sjöberg-Eerola, P.; Eriksson, J.-E.; Bobacka, J.; Bergelin, M. The effect of counter ions and substrate material on the growth and morphology of poly(3,4-ethylenedioxythiophene) films: Towards the application of enzyme electrode construction in biofuel cells. *Synthetic Metals* **2010,** *160* (13), 1373-1381, DOI: https://doi.org/10.1016/j.synthmet.2010.01.033.

(17) Poverenov, E.; Li, M.; Bitler, A.; Bendikov, M. Major Effect of Electropolymerization Solvent on Morphology and Electrochromic Properties of PEDOT Films. *Chemistry of Materials* **2010,** *22* (13), 4019-4025, DOI: 10.1021/cm100561d.

(18) Kumar, S. S.; Mathiyarasu, J.; Phani, K. L. N.; Yegnaraman, V. Simultaneous determination of dopamine and ascorbic acid on poly (3,4-ethylenedioxythiophene) modified glassy carbon electrode. *Journal of Solid State Electrochemistry* **2006,** *10* (11), 905-913, DOI: 10.1007/s10008-005-0041-7.

1.3 Figures

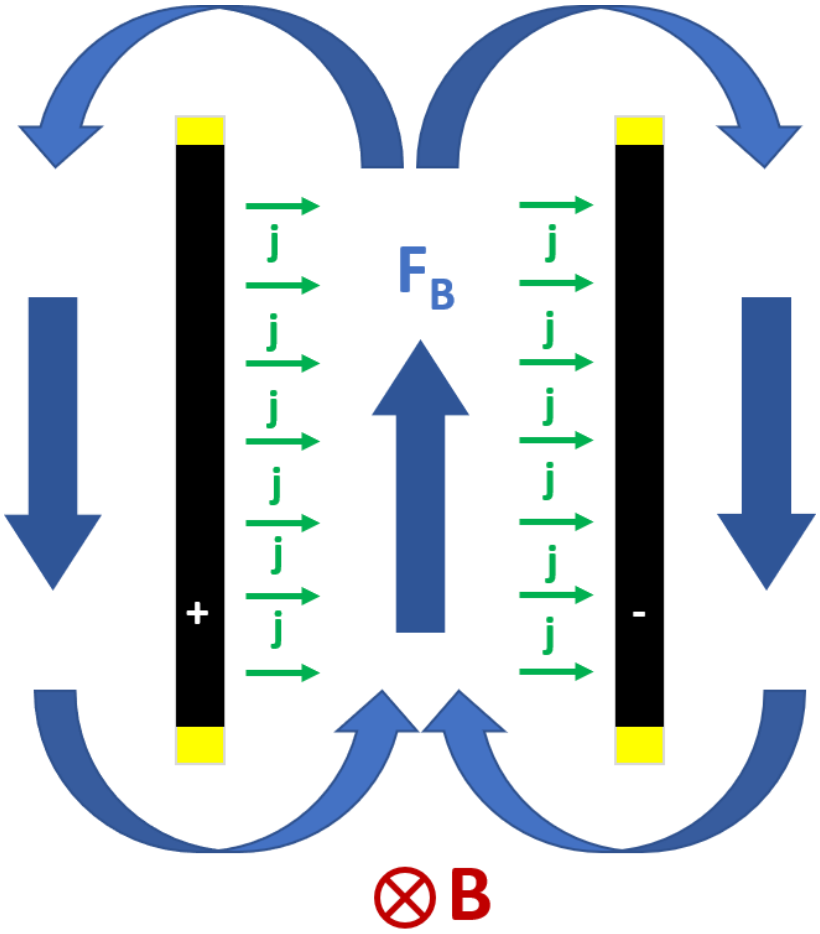

Figure 1: Illustration of MHD flow between two polymer (PEDOT) coated electrodes. Ionic current density (j) occurs in between anode and cathode, whereas magnetic field (B) works in perpendicular with it to result in a body force (F_B) in between the active electrodes.

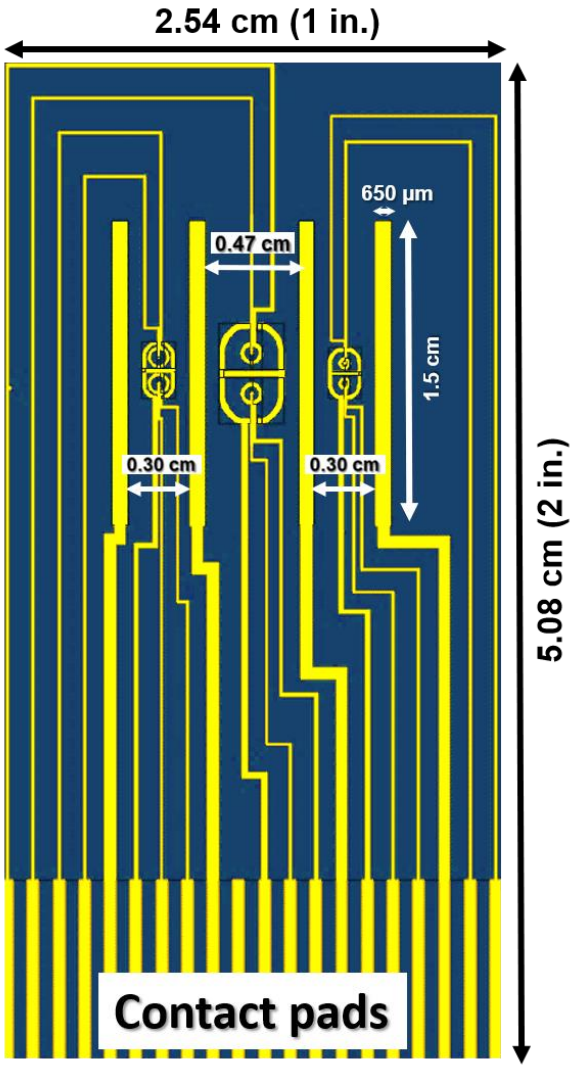

Figure 2: The schematic of the chip consisting four individually addressable band electrodes. The outermost two electrode pairs are 0.30 apart from each other, whereas the inner two electrodes have 0.47 cm gap.

2. Chip-Scale Electrodeposition and Analysis of Poly(3,4-ethylenedioxythiophene) (PEDOT) Films for Enhanced and Sustained Microfluidics Using DC-Redox-Magnetohydrodynamics

2.1 Introduction

Microfluidic devices are of interest in chemical analysis because they use small sample volumes, perform multiple steps, and offer low cost, portability, and short analysis times.[1] They have been used successfully in biological cell analysis with functions like trapping, sorting, and transport. They also have applicability in proteomics and drug discovery.[2-5] Different pumping systems have been used to handle the fluids such as electrokinetic and mechanical approaches.[6-8] Pumping with magnetic fields, specifically with redox-magnetohydrodynamics (R-MHD) and magnetic field gradients, is a more recent approach that can control flow profiles, directions, and paths.[9-10] MHD in particular allows flexibility in device design and size, pumps in a loop, can be configured to avoid electrode corrosion and bubble formation, and offers tunable speed and flow duration. [11-13] In contrast, mechanical pumping (pressure driven) is more complex to miniaturize, produces a parabolic flow profile, and requires a channel to direct the flow. The nonmechanical approach of electroosmosis also provides a flat profile, it is sensitive to physicochemical properties of the channel walls and the fluid, requires high voltages, and can generate heat and bubbles in the pumping solution.[14-15]

MHD microfluidic pumping is governed by the right hand rule, $F_B = j \times B$ (the magnetic part of the Lorentz force), where the body force (F_B) is generated by the perpendicular interaction of a magnetic field (B (T)), produced by a permanent magnet or electromagnet, and an ionic current (j (C/(s m2)), produced between active electrodes.[16] Redox species (either immobilized at the electrode surface or dissolved in solution) convert electronic current into

ionic current by known reactions and therefore avoid bubble formation and electrode corrosion. The addition of solubilized redox species (e,g. $[Fe(CN)_6]^{3-}$/ $[Fe(CN)_6]^{4-}$), however, raises concerns due to reactions with analytes, interference with detection, and additional natural convection.[17] Redox species that are integrated into a material, such as a conducting polymer, which can be electrodeposited onto electrodes, avoid the drawbacks involving redox species in solution.[13] Figure 1 illustrates the main concept.

Poly(3,4-ethylenedioxythiophene) (PEDOT) is a conducting polymer with suitable electrochemical properties and has been investigated for use in a variety of applications. These include capacitors, sensors, antistatic coatings, field effect transistors, acoustic energy harvesters, electrochromic devices, deep brain stimulating microelectrodes, and photovoltaic cells.[18-23]

When a PEDOT-modified electrode undergoes oxidation, it is coupled with migration of electrolyte ions into and out of the film to satisfy charge neutrality.[24-25] A subsequent cathodic current returns the oxidized PEDOT to its original state, reversing the ionic transport. This process generates a net ionic current for a given applied electronic current applied between an anode/cathode pair of PEDOT-modified electrodes, completing the circuit. The ionic current density, j, is further determined by the cross section between the active electrodes.

Electropolymerization provides controlled growth with good adhesion to the substrate and allows transport of dopant ions during monomer oxidation and reduction, affecting film morphology, charge compensation dynamics and charge capacity. [19] PEDOT can be electrodeposited with potentiodynamic (e.g. cyclic voltammetry, CV), potentiostatic (e.g. chronoamperometry, CA), galvanostatic (e.g. chronopotentiometry, CP), and pulse techniques. CV is particularly beneficial because it allows in situ diagnosis of the polymer's evolving

electrochemical properties while it produces electronically- and ionically-conducting films with mass and thickness that are relatively proportional to increasing number of deposition cycles.[26] Organic solutions are usually used because they dissolve the monomer EDOT better than their aqueous counterparts,[27] producing packed and uniform films with higher electronic conductivity.[28] Here, we report the properties of PEDOT films that are electrodeposited by CV from solutions of propylene carbonate (PC) and two different electrolytes (lithium perchlorate ($LiClO_4$) and tetrabutylammonium hexafluorophosphate ($TBAPF_6$). These particular electrolytes and solvent were chosen, because they are most commonly used for electropolymerization of thiophene.[19, 28-29] PEDOT has been deposited by us using CV from $LiClO_4$ in PC with a slow scan rate (5 mV/s for 12 cycles).[30] In the present work, however, we use a series of different scan rates and an additional electrolyte to optimize the PEDOT performance in terms of current and charge densities that are important in MHD pumping and which correspond to fluid speed and pumping duration in a single direction, respectively.

The electropolymerized PEDOT films were then characterized in various aqueous solutions (with electrolytes of different ionic strengths) to determine how pumping solution composition leads to further improvements in maximizing current and charge densities that are vital for optimizing MHD fluid flow. Experiments were performed with PEDOT-modified, microfabricated electrodes on silicon chips with a NdFeB permanent magnet beneath them, and a galvanostat/potentiostat for applying current or potential to the electrodes.

2.2 Experimental Section

2.2.1 Chemicals and Materials

Electrolyte solutions were prepared with deionized water (Ricca Chemical Company , 18 MΩ.cm resistivity, Arlington, TX, and PURELAB Ultra, 18.2 MΩ.cm resistivity, Lowell, MA). Propylene carbonate (anhydrous 99.7%), 3, 4-ethylenedioxythiophene (EDOT), tetrabutylammonium hexafluorophosphate (TBAPF6), and phosphate buffered saline (PBS) tablets were purchased from Sigma-Aldrich (St. Louis, MO). Glycerol (proteomics grade, ≥ 99.00%) was purchased from AMRESCO LLC (Solon, OH). Lithium perchlorate (ACS grade 95%) and polystyrene latex microspheres, 10 μm diameter (2.5 wt % dispersion in water) were purchased from Alfa Aeser (Ward Hill, MA). Potassium ferricyanide and potassium ferrocyanide were obtained from EM Science, Gibbstown, NJ and J.T. Baker, Phillipsburg, NJ, respectively. Potassium chloride (99%) and pre-cleaned micro cover glass (24 mm × 50 mm) were purchased from VWR International, LLC (West Chester, PA). The 0.37 T nickel coated NdFeB permanent magnet (3.5 cm diameter and 1.27 cm height, grade N40) was acquired from Amazing Magnets, Irvine, CA.

Silicon wafers (125 mm diameter, 600−650-μm thickness with 2 μm of thermally grown SiO2 on the surface) were purchased from Silicon Quest International (Santa Clara, CA). A chromium-plated tungsten rod (Kurt J. Lesker Company, Clairton, PA) and gold pieces cut from a coin (Canadian Maple Leaf, 99.99%) placed on a molybdenum boat (Kurt J. Leskar Company, Pittsburgh, PA) were used for thermal metal vapor deposition on the wafer (Edwards E306A coating system). Photo plot masks that defined electrode and insulating layer features were obtained from Fine Line Imaging, Inc. Colorado Springs, CO. Photoresist AZ 4330 was used in

the photolithography process of the electrodes, and tetramethylammonium hydroxide (TMAH) served as the developer. Gold etchant (Transene, GE8148) and chromium etchant (HTA enterprise, CEP200) were used as received. Benzocyclobutene (Cyclotene 4024-40, insulator over the electrode leads) was obtained from Dow Corning Company, Midland, MI.

Edge connectors (solder contact, 20/40 position, and 0.05 in. pitch) were acquired from Sullins Electronics Corp. (San Marcos, CA). For Poly (dimethylsiloxane) (PDMS) fabrication, Sylgard184 silicon elastomer base, Sylgard 184 silicon elastomer curing agent and OS-30 solvent were purchased from Ellsworth Adhesives, Milwaukee, WI.

2.2.2 Electrochemical Instrumentation

A model 760B galvanostat/potentiostat from CH Instruments, Inc. (Austin, TX) was used to perform all investigations involving electrochemistry. CV was used for electrodeposition of PEDOT from PC solutions. CV, CA, CP, and electrochemical impedance spectroscopy (EIS) were used to characterize the PEDOT films in aqueous solutions. CV and EIS were used to characterize the bare electrodes. All the characterization investigations involved a "three-electrode" setup using an Ag/AgCl (saturated KCl) reference electrode and Pt foil counter electrode. In MHD-pumping studies, a constant current was applied using CP and a "two-electrode" arrangement was used. The two-electrode configuration consisted of one PEDOT-modified band on the chip serving as the working electrode and an adjacent coplanar, PEDOT-modified band as a combined counter/quasi-reference electrode.

2.2.3 Electrode Preparation and Modification

A detailed procedure to fabricate chips with patterned gold electrodes on a silicon wafer has been reported by us previously.[11] Each fabricated silicon wafer was diced into 1 in. × 2 in. (2.5 cm x 5.0 cm) chips. Afterwards, each chip was rinsed with deionized water for about a minute to wash away any remaining particulates produced from the sawing process. After drying at room temperature, the chips were plasma cleaned in oxygen plasma (Harrick Plasma Cleaner PDC -32G, Ithaka, NY) for 20 min at 60 mTorr pressure and 6.8 W of power applied to the RF coil for removing organic residue originating from the fabrication process. Figure S-1 shows a chip schematic consisting of four, parallel and coplanar band electrodes (nominally 1.5 cm long, 650 μm wide, and 250 nm thick). The end of one of these electrodes is shown in Figure 2. These electrodes were used for both PEDOT deposition studies and MHD flow generation. Each outermost electrode is separated from the adjacent, inner electrode by 0.30 cm. These electrode pairs were used for MHD pumping investigations. The distance between the two inner electrodes is 0.47 cm.

EDOT was electropolymerized on gold band electrodes by cycling the potential at 5, 50, and 100, mV/s for 12 cycles between -0.455 and either +1.40 V or +1.30 vs Ag/AgCl (saturated KCl). Monomer solutions containing 0.010 M EDOT and 0.100 M $TBAPF_6$ or $LiClO_4$ electrolyte, respectively, in PC were used for electrodeposition. The resulting PEDOT films were dark blue. Before electrodeposition, the chips were plasma cleaned again in an oxygen plasma to remove organic residues from the electrode surfaces with the same parameters as given above. After electrodeposition, the films were cycled at 50 mV/s at least five times in monomer-free electrolyte solution in PC to stabilize them and improve electrochemical performance.[31] After stabilization, the chips were rinsed 2-3 times with propylene carbonate to remove excess

electrolyte, and this was followed by a rinse with DI water (for about a minute). The rinsed chips were stored in 50 mL capped polypropylene centrifuge tubes filled with DI water until further characterization in aqueous electrolyte solution.

The approximate time spent on the deposition of PEDOT for each cycle is reported in Table S-1 in Supporting Information. These values were estimated by dividing twice the difference between onset of oxidation potential and the anodic switching potential with the respective deposition scan rate (V/s). The first cycle is usually different in terms of onset potential than other cycles as it usually occurs at a higher potential. Therefore, the deposition time for each cycle was calculated separately and added together for a total estimated time of deposition for the 12 cycles. In the case of PEDOT deposition at 5 mV/s in PC:$TBAPF_6$, the usual onset potential for oxidation is 0.8 V and switching potential is 1.4 V. Therefore, the time for that cycle is $2\times$ (1.4-0.8 V)/0.005 V s^{-1} = 240 s.

2.2.4 PEDOT Film Thickness Measurements

The chips with electrodeposited PEDOT films were dried in a desiccator for three days before measuring the thickness with a profilometer (Dektak 3030, Veeco Instruments Inc, Plainview, NY). The chip was placed on the measurement stage and positioned for scanning with a video camera. Initially, leveling and zero referencing were done on bare silicon that was outside of the film's edge. Then a single scan with a 2.5 μm radius diamond tip stylus was performed laterally across the film width, for a distance of 1 mm and with a contact force. The scan ended on the bare silicon on the other side of the electrode. Thickness profiling was performed on a single chip for films formed from a given solvent – electrolyte couple, where the PEDOT was electrodeposited on three electrodes, each at one of the three different scan rates.

Each film was measured three times on three different positions across the length of the electrode and the final thickness was reported as an average value of these three measurements. All the measurements included the gold thickness (~250 nm).

2.2.5 Scanning Electron Microscopy

After complete electrochemical characterization in aqueous solution, chips with PEDOT films were rinsed with DI water for about a minute to remove any absorbed species and kept in a desiccator for a week to dry before evaluating surface topography by an Environmental Scanning Electron Microscope (E-SEM, Philips XL30 ESEM). Surface images were taken at 1000× magnification using a secondary electron detector, 10 kV acceleration voltage, and pressure of 0.4 to 1.1 Torr.

2.2.6 Electrochemical Characterization of Bare Electrodes and PEDOT Films

The bare electrodes on the cleaned chips were characterized using CV between 0 V and +0.500 V at 50 mV/s in a solution of aqueous 0.0010 M $K_3Fe(CN)_6$ and 0.100 M KCl, as well as 0.100 M KCl alone (not shown). Before and after film deposition electrodes were characterized in 0.100 M NaCl by CV at 50 mV/s with a potential window of 0 to 0.500 V. PEDOT-modified electrodes were characterized using CA in three different electrolytes of increasing ionic strength, μ: 0.100 M NaCl (μ = 0.100 M), 0.01 M PBS (μ = 0.25 M), and 0.1 M PBS (μ = 2.5 M). The μ values were determine by

$$\mu = \frac{1}{2}\sum_i c_i z_i^2$$

where c_i is the concentration and z_i is the charge of the i^{th} species.

The "0.01 M PBS" solution was prepared by dissolving one PBS tablet in 200 mL of DI water, which results in a buffer containing 0.01 M phosphate, 0.0027 M potassium chloride, and 0.137 M sodium chloride, pH 7.4 at 25 ^{o}C (application procedure according to Sigma-Aldrich).[32] The "0.1 M PBS" solution is made by dissolving one PBS tablet into only 20 mL DI water.

The potential was held first at -0.800 V for 20 s (quiet time) to charge up the polymer, and then stepped to +0.800 V and held for another 20 s. The maximum current was measured at 0.001 s of the CA response and was normalized to the geometric area of the bare electrode to obtain the maximum current density for each deposited film. The available charge in the film was obtained by integrating the CA data. This was also normalized to the geometric electrode area to get the charge density for the 20-s period.

EIS was also performed on bare and PEDOT-modified electrodes. A sinusoidal perturbation around a DC potential of 0.00 V was applied with an amplitude of 0.015 V and frequency range of 0.1-10^5 Hz. Nyquist and Bode plots were extracted from the current responses. Cell resistance, R_{Ω}, charge transfer resistance, R_{ct}, and capacitance, C, values were obtained by the simple analysis of using the x-intercepts of the semicircles in the Nyquist plots, which are R_{Ω} and $R_{ct} + R_{\Omega}$, and the frequency at the maximum real impedance of the semicircle, where $\omega=1/R_{ct}C$.

2.2.7 MHD Pumping Studies

Figure 3 shows the schematic of the experimental setup for MHD. The chip with PEDOT-modified electrodes was inserted into an edge connector to provide an electrical interface between the galvanostat and the electrodes. A PDMS gasket of 781 ± 7 μm thickness with a rectangular opening (3.5 cm × 2 cm) to expose electrodes of interest and define the cell

chamber dimensions was placed on the chip. The chip-gasket-edge connector assembly was carefully positioned flat (without tilt) on a permanent magnet (0.37 T NdFeB, diameter of 3.81 cm (1.5 in.) and height of 1.27 cm (0.5 in.)). The center of the gap between PEDOT-modified anode and cathode was shifted about 5 mm away to the side of the center of the magnet.

The chamber formed by the rectangular cutout of the PDMS gasket could hold 450 μL of the "buffer/glycerol/bead solution" (described below). A glass coverslip was placed on the solution-filled chamber to limit the solution loss from evaporation. Special attention was paid to prevent air bubbles from getting trapped in the MHD chamber during assembly.

The "buffer/glycerol/bead solution" was prepared by mixing 1000 μL of a "buffer/glycerol" solution with 40 μL of the as-received polystyrene latex microspheres. The "buffer/glycerol" consisted of 30:70 v/v of a glycerol solution (1:1 ratio of pure glycerol (>99%) and water) added to 0.01 M PBS (described above). Thus, the pure glycerol content of the final solution was 15% by volume. The glycerol was added to increase the density of the solution to match that of the beads, and thus prolong the buoyancy of the beads

A repeating double-step CP technique was used to apply a constant current for MHD pumping and to monitor the potential response. The current ranged from ±50 μA to ±800 μA, in a "two-electrode" configuration involving two PEDOT-modified electrodes, where one served as the working electrode and the other that served as the combined counter/reference electrode. The current reversed from anodic to cathodic, and vice versa, when the potential reached the preset limits of +1.10 V and -1.00 V, respectively. The sign convention for the electronic current is non-IUPAC—negative current represents oxidation and positive current represents reduction when the working electrode serves as anode and cathode, respectively. The negative limiting

potential was chosen to avoid the non-conductive range of the film and the positive limiting potential was chosen to prevent its over-oxidation.

To visualize the resulting MHD fluid flow, movement of the polystyrene beads was recorded using a Sony Handycam camera that was interfaced with the microscope. Adjustment of the microscope stage determined where fluid flow was measured: the horizontal position over the chip between activated electrodes (using the x-y translation) and the vertical position in the chamber (using the z translation to focus on beads at 320 μm above the chip surface). The flow speed at each applied current was determined by analyzing the videos of bead motion using Tracker® (V 4.87, www.opensourcephysics.com) software. The start frame, step size (n, every n^{th} frame will be used for the analysis purpose) and end frame was selected for each flow video. A focused bead in the video was selected as a point mass, and the velocity of that bead was evaluated from the position-time data using the Finite Difference algorithm. Currents were applied in low to high, high to low and random fashions, generating three videos for each of five current magnitudes, and totaling fifteen videos. Two focused beads were tracked for each video and a total of six individual beads were analyzed for each applied current. Bead speed was measured from the anodic excursion and flow duration was determined from the cathodic excursion for each CP cycle.

2.3 Results and Discussion

2.3.1 Electrodeposition Characteristics

Figure 2 (a) and (b) show representative CV responses for each of the 12 sequential deposition cycles at 5 mV/s for solutions containing EDOT in $TBAPF_6$ and $LiClO_4$ in PC, respectively. CV responses for deposition at 50 mV/s and 100 mV/s scan rates in each of the

two solutions exhibit similar trends, but with a small anodic shift in the oxidation wave, as can be seen in Figure S-2 (a), (b), (d), and (e) in the Supporting Information. The first deposition cycle is distinctly different than the rest of the cycles at all scan rates and in both solutions. The isolated first cycles for depositions at 5 mV/s are shown in Figure S-2 (c) and (f) of the Supporting Information. In the forward sweep of that first cycle, the monomer oxidizes at the bare gold electrode at 1.26 V for PC:$TBAPF_6$ and 1.19 V for PC:$LiClO_4$ in an initial monomer nucleation process, forming initial products (dimers, oligomers, and bipolarons), and with a rapid increase in anodic current. The reverse scan crosses the forward scan as these products are easier to oxidize further and the oxidation potential shifts to lower values for subsequent deposition cycles.[33]

The polymer continues to grow with each cycle. Starting with cycle 2 in the PC:$TBAPF_6$, an anodic peak appears at 1.34 V in the forward sweep (Figure 2(a)) that suggests diffusion controlled oxidative polymerization of EDOT. During deposition in PC:$LiClO_4$ (Figure 2(b)), there is also a peak in cycle 2, but at 1.29 V and is very close to the 1.30 V switching potential, explaining why an oxidation peak is not well resolved. This switching potential is 0.10 V short of that used in the $TBAPF_6$ case, which leads to less polymerization time, and therefore, diminished film properties as described further below. At the faster scan rates of 100 mV/s and 50 mV/s for both electrolyte conditions, however, (see Figure S-2 (a), (b), (d), and (e), in Supporting Information), an anodic maximum is no longer observed within the potential window. This may be explained by a larger voltage drop in solution due to higher currents for a given uncompensated resistance or kinetic limitations where increased overpotentials are needed for oxidation at the shorter time scales.

Measurement of the charging current can be used to follow the polymer deposition. As the potential sweeps back to -0.455 V in the first deposition cycle, the PEDOT films exhibit a cathodic background current that is 21× that of the bare electrode. Upon the forward sweep of the subsequent cycles, the anodic background current is also larger than that in the previous cycle. The insets of Figure 2(a) and (b) provide an expanded view of the current from 0.4 to 0.5 V, illustrating this point. This behavior is much like that of the charging of a capacitor and is consistent with reports of the electrochemistry of PEDOT by other investigators. [21, 30, 34-35] The increasing charging current suggests that an additional layer of PEDOT is deposited with each cycle, and therefore a thicker film is formed. A plot of charging current obtained during deposition as a function of the cycle number (Figure S-3 in Supporting Information) is fairly linear with an R^2 values of 0.981 to 0.990, suggesting that similar amounts of polymer are deposited with each iteration for a given scan rate. The linear equations resulting from the least squares fit of the plots at all scan rates for an electrolyte solution are similar. The reason for the similarity is that less time is spent during the oxidation part of each CV cycle at the faster scan rates, and therefore thinner polymer films are deposited. The lower charge in the film is offset by a faster scan rate that yields a proportionally higher charging current. Another presentation of these data is to divide the charging current by the scan rate to attain the film capacitance and generate the plots in Figure 2(d) and (e). The data show that each deposition cycle produces a new layer where virtually all of the charge from the previous cycle appears to remain accessible. The plots also confirm that deposition of PEDOT at faster scan rates produces thinner films with proportionally lower overall capacitance. For example, for $TBAPF_6$ in Figure 2(d), the R^2 values are 0.9937, 0.9970 and 0.9917 for deposition scan rates of 5 mV/s, 50 mV/s, and 100 mV/s, respectively. The slopes at 5 mV/s and 50 mV/s are a factor of 18.6 and 1.9 compared to that for

100 mV/s, and correlate well to factors of 20 and 2 of the deposition times when compared to the time for 100 mV/s. Similarly, for capacitances of films deposited in PC:$LiClO_4$ (Figure 2(e)) the slopes at 5 mV/s and 50 mV/s are 23.8 and 2.2 times that for 100 mV/s, respectively. Overall however, the films deposited in $TBAPF_6$ have higher capacitances than those from $LiClO_4$, at least partly due to longer oxidation times from the later switching potential that deposit more material. Estimates of times during deposition by CV based on the onset of monomer oxidation and switching potential are provided in Table S-1. Specifically, the ratio of the slopes from Figure 2(d) and (e), which is the change in capacitance per cycle, between the two electrolyte systems at 5 mV/s, 50 mV/s, and 100 mV/s deposition scan rates are quite similar at all three scan rates: at 1.61 ± 0.05, 1.62 ± 0.02, and 1.91 ± 0.05 mF cm^{-2} per cycle, respectively.

Films with different thicknesses can be observed by eye and were measured. After 12 cycles at the slowest scan rate of 5 mV/s for both electrolyte solutions, the PEDOT film has overgrown the electrode edges and formed fingerlike projections as shown in Figure 2(c). At the shorter deposition times manifested by faster scan rates, however, thinner films are produced and have less overgrowth (see Figure S-4 (c) and (f) and Figure S-5 (c) and (f) in Supporting Information), as expected. Measurements of the total film thickness after 12 cycles are provided in Table S-1 and plotted in Figure S-6 in the Supporting Information as a function of the inverse of the scan rate (i.e. approximately proportional to the duration of oxidation) and are also linear, with R^2 values of 0.999. Because of these linear dependences of thickness and capacitance on inverse scan rate and of capacitance on number of cycles, control of these parameters allows the electrodeposition of PEDOT to be quantitative and highly predictable.

The charge passed during the oxidative deposition of the PEDOT was also obtained to determine whether the polymer properties are more closely related to the quantity of monomer

deposited rather than the nature of the electrolyte composition of the monomer solution. The deposition charge was obtained by integrating the anodic faradaic current in the electropolymerization portion of the CV response in both the forward and reverse sweeps for each cycle, for a given deposition scan rate, and for each electrolyte. For example, the anodic faradaic current in the forward sweep for films formed in PC:TBAPF$_6$ was obtained by subtracting the background current measured at 0.8 V from the total current across the electrodeposition region of that sweep (from 0.8 V to 1.4 V). The anodic faradaic current in the reverse sweep was determined in a similar fashion, where the background current at 0.8 V in the reverse sweep was subtracted from the total current of that sweep across the range from 1.4 V to 0.8 V. After integrating the faradaic current in each sweep and dividing by the scan rate, the absolute values of the resulting forward and reverse charge were combined. The results are shown in Figure S-7 in the Supporting Information. This approach to estimate the amount of monomer incorporated into the polymer is only qualitative because it is challenging to accurately subtract the charging current that dynamically adds while the polymer forms. The overall trend is the same for films deposited from both electrolytes and at all scan rates: the deposition charge increases rapidly over the first three cycles, and then starts to roll over with subsequent cycles. The charge deposited in each cycle never becomes constant, however, as would be expected if each additional polymer layer were identical to the previous one. This could be due to a polymer film that continues to spread outward, increasing its geometric and surface areas, and therefore accessing more monomer to deposit on the next cycle. This effect is less dramatic at the faster deposition scan rates because the growth and therefore the change in geometric area with each cycle are also smaller. Nonetheless, the integrated oxidative current for a given cycle is inversely proportional to the scan rate for each of the electrolyte compositions, just as the capacitance of

the films depends on the inverse of the deposition scan rate, which suggests that the amount of PEDOT formed is indeed due to the time of oxidation, which decreases with increasing scan rate.

There are also consistencies between the two electrolyte systems at each of the different scan rates when considering the *total* oxidative charge accumulated over the 12 deposition cycles, which is related to the total amount of monomer polymerized into a film, and the final film capacitances. This further supports the notion that the quantity of monomer that polymerizes remains accessible and contributes proportionally toward the film's capacitance. For example, the accumulated oxidative charge is 144 ± 14 mC in PC:$TBAPF_6$, which is 1.4 times that of 100. 6 ± 1.2 mC in PC:$LiClO_4$. The final capacitances are 128.5± 10.5 mF/cm^2 and 80.6 ± 1.6 mF/cm^2, respectively (Figure 2(d) and (e)), yielding a ratio of 1.6, which is similar to the ratio of the accumulated charge. For deposition scan rates of 50 mV/s and 100 mV/s, the accumulated charge is 16.7 ± 0.7 mC and 7.7 ± 0.7 mC in PC:$TBAPF_6$ and 8.80 ± 0.9 and 3.95 ± 0.2 mC in PC:$LiClO_4$, respectively, yielding a corresponding ratio of 1.9 between the two electrolyte systems at both deposition scan rates. The final capacitances of the films formed at the two deposition scan rates are 12.8 ± 1.2 and 6.8 ± 0.7 mF/cm^2 in PC:$TBAPF_6$ and 7.7 ± 0.5 and 3.4 ± 0.1 mF/cm^2 in PC:$LiClO_4$, yielding ratios of 1.7 and 2 for the two electrolytes, respectively. These capacitance ratios are consistent with the relative amounts of polymerized monomer.

The ratio of the final film thicknesses for the two electrolyte conditions, however, is 2.3 (obtained from the ratio of the slopes in Figure S-6), somewhat higher than the ratio of deposition charge and total capacitance, especially for the longest deposition times at 5 mV/s. This appears to be a consequence of the different morphologies of the films that result from deposition in the different electrolytes and is described in more detail below.

2.3.2 Scanning Electron Microscopy (SEM) Analysis of PEDOT Films

SEM images at the center of PEDOT films deposited for 12 cycles under the six different conditions are given in Figure 4. They suggest that the type of electrolyte in the deposition solution has a significant effect on film morphology. For both PC:$TBAPF_6$ and PC:$LiClO_4$ solutions, the PEDOT films become rougher with decreasing scan rates (increasing deposition time). However, the films formed in PC:$TBAPF_6$ (Figure 4 (a), (b), (c)) exhibit even rougher structures than those formed in PC: $LiClO_4$ (Figure 4 (d), (e) and (f)).

Further comparisons of morphologies are provided in Figures S-4 and S-5 in Supporting Information. There, SEM images at the center of PEDOT-modified electrodes are compared to those at the electrode edges and with the optical images for depositions from PC:$TBAPF_6$ and PC:$LiClO_4$. Figure S-4 (h) and (i) show the extended finger-like projections for PC:$TBAPF_6$ film beyond the electrode boundary, while PC:$LiClO_4$ shows smaller projections (Figure S-5 (h) and (i)).

These trends in roughness for the two electrolyte systems and across the three scan rates are consistent with the film thickness measurements in Table S-1 in Supporting Information. For a given electrolyte system, the increasing deposition time that occurs with decreasing scan rate clearly explains the increasing film thicknesses and yields a linear relationship in Figure S-6 of Supporting Information. However, for a given scan rate, the different times spent during monomer oxidation cannot alone explain the varied film roughness and thicknesses for the two different electrolytes. For example, PC: $LiClO_4$ films are deposited for shorter times at a given scan rate than for PC: $TBAPF_6$ films owing to an anodic switching potential that is 0.100 V less. Table S-1 in the Supporting Information lists those estimated deposition times. However, the

thickness and roughness of films deposited for a more similar time, for example about half for PC :$TBAPF_6$ (at 100 mV/s, for 115 s) in comparison to that from PC:$LiClO_4$ (at 50 mV/s for 216 s), still exhibit greater roughness (Figure 4(a) vs 3(e)) and thickness (1.77 ± 0.05 μm vs 1.55 ± 0.01 μm).

The rougher structure of the film formed in PC: $TBAPF_6$ must be due to differences in ion inclusion and trapping in the film, compared to PC: $LiClO_4$. The potentiodynamic method of deposition allows cycling of oxidation and reduction and therefore cycling of the transport of electrolytes and solvent through the freshly deposited film.[36] Thus, it is expected that variation of ion size and shape in the electrolyte solution will affect the morphology of the polymer.[18] For example, the slightly larger PF_6^- with an ionic radius of 0.254 nm might help form a more expanded structure than the smaller ClO_4^- with an ionic radius of 0.237 nm.[37] The much larger and hydrophobic cation TBA^+, compared to Li^+, may also contribute to a more expanded film, especially if it becomes trapped within the PEDOT.

In the next section, the available charge of these PEDOT films in aqueous electrolytes is compared. These correlate more closely with the time of deposition than with the thickness of the films. This further supports the idea that film morphology is linked to the type of electrolyte used during deposition, and that both structures are sufficiently open for ions to access most of the film during its oxidation and reduction.

2.3.3 Electrochemical Characterization of PEDOT Films in Aqueous Electrolyte to Predict R-MHD Performance: Maximum Current and Charge Density

Performance of PEDOT-modified electrodes for redox-MHD pumping may be characterized by the maximum achievable current and the total charge, which are proportional to

the maximum attainable fluid speed and pumping duration in a single direction, respectively. These two features also describe the facility of ions to permeate and compensate for oxidation and reduction and the quantity of charge that is accessible in the film. Such electrochemical responses of the PEDOT films are compared here in three aqueous electrolytes that are compatible with many biological analytes in microfluidic systems (0.100 M NaCl, 0.01 M PBS, and 0.1 M PBS).

Figure S-8 in Supporting Information shows diagnostic CV responses in aqueous 0.100 M NaCl at a single scan rate of 50 mV/s for PEDOT films that were formed from monomer in both electrolyte solutions at the three deposition scan rates. The shapes of the CV responses look like those for capacitors and are consistent with the capacitor-like behavior observed during film deposition described above and in Figures 2(a), 2(b), and S-2. The charging currents from CV in the aqueous solutions of the PEDOT films deposited from both electrolytes at 5, 50, and 100 mV/s are nearly 1400, 125, and 70 times more than at a bare electrode, respectively, confirming the advantage of PEDOT-modified electrodes over unmodified ones for R-MHD pumping. Also, this charging current is approximately inversely proportional to the scan rate that was used for the film deposition. This can be explained by a greater available charge when PEDOT is deposited at longer times (slower deposition scan rates) and is consistent with the analysis of individual deposition cycles with scan rate in Figures 2(d), 2(e), and S-3. Therefore, the facility to access the charge in a solution of a given ionic strength is independent of film thicknesses. This and the total available charge are further quantified with CA.

Figure 5 shows examples of CA responses in aqueous 0.100 M NaCl over a 20 s step at +0.800 V vs. Ag/AgCl (saturated KCl) (after charging for 20 s at -0.800 V) and their integration for PEDOT films formed from the two deposition electrolytes in PC at the three scan rates. The

area-normalized maximum current at 0.001 s and total charge over 20 s for 0.100 M NaCl, 0.01 M PBS and 0.1 M PBS are tabulated in Tables S-2 and S-3 in Supporting Information.

Initially, the CA current changes rapidly with time, and the dependence is expected to be exponential for RC circuits. However, the expanded view of the CA response for the thickest film (deposited at 5 mV/s), shows three distinctively different current regions: an initial drop in the absolute anodic current, then a noticeable increase, which is followed by a second drop. We attribute this behavior to at least three stages of expansion as the film receives more anions upon oxidation. These stages may also be present in the thinner films, but could be too short-lived for the temporal resolution used here to be clearly observed by CA. The EIS data suggest that those thinner films do experience similar behavior, but at shorter time scales. See an illustration of the proposed model for the thickest films in Figure 6. One stage involves a reduced and compressed structure that receives an initial rush of counter anions within the first 0.01 s due to migration to charge the polymer/solution interface. As the polymer begins to expand upon receiving additional anions, from 0.01 s to 0.03 s for films formed in PC: $LiClO_4$ and to 0.08 s for films formed in PC:$TBAPF_6$, it exposes an increasing area of the polymer/electrolyte interface, leading to an increase in the anodic current. We have observed physical expansion and contraction of other thick PEDOT films by optical microscopy during electrochemistry. Once the polymer achieves its most expanded form at about 0.03 s or 0.08 s, respectively, the current becomes limited by the mass transport of the ions into the film's deeper and more compact regions. Electrostatic repulsions may also play a role. As positive charges redistribute themselves throughout the polymer network, counter anions that are already associated with the film could be drawn even further into it. As discussed below, EIS data further confirm these stages: >100 Hz (determined from 1/0.01 s), between 13 (1/0.08 s) or 33 Hz (1/0.03 s) and 100 Hz, and

between 0.1 Hz and 13 or 33 Hz. These stages would be expected to shift to higher frequencies for thinner films deposited at 50 and 100 mV/s.

The maximum current density for a given PEDOT film exhibits a linear relationship with increasing ionic strength of the surrounding aqueous electrolytes (0.100 M NaCl (μ = 0.10 M) < 0.01 M PBS (μ = 0.25 M) < 0.1 M PBS (μ = 2.5 M)) as depicted in Figure S-9 in Supporting Information. For example, films that were deposited from PC:$TBAPF_6$ and PC:$LiClO_4$ at 5 mV/s exhibit a maximum current density, y, that depends on the ionic strength, x, of the surrounding solution as follows: $y = (308.70 \pm 7.80 \text{ mA cm}^{-2} \text{ mol}^{-1} \text{ L}) x + 165.54 \text{ mA cm}^{-2}$, $R^2 = 0.9994$, and $y = (290.55 \pm 5.18 \text{ mA cm}^{-2} \text{ mol}^{-1} \text{ L}) x + 160.08 \text{ mA cm}^{-2}$, $R^2 = 0.9997$, respectively. Therefore, the maximum R-MHD pumping speed can be enhanced in a predictable manner by increasing the ionic strength of the fluid. This is expected for a highly reversible charge-discharge processes, when the internal resistance of the film diminishes with an increase of the conductance of the permeating electrolyte.[38] (The conductance of an electrolyte depends on the ion concentration and mobility.) Also, at the initial potential step, the number of charging centers must be sufficiently higher than the number of compensating available ions in solution.

Interestingly however, the maximum current densities of PEDOT in a given aqueous electrolyte are statistically the same (at the 95% confidence) for all films formed from a given deposition electrolyte in PC, regardless of the deposition scan rate, as shown in Figure 7. This result further supports conclusions from the CV data that the maximum R-MHD pumping speed will be similar for all film thicknesses.

Unlike the maximum current density, the total charge density, which was also obtained by characterization with CA in aqueous electrolyte, is proportional to how much PEDOT had

been electrodeposited. Thus, charge density of a film increases linearly with its deposition time or with the inverse of the deposition scan rate (100 mV/s < 50 mV/s < 5 mV/s) (Figure 8 (a) and (b)). Also in contrast to the maximum current density, the magnitude of the charge density is essentially the same in two of the three aqueous electrolytes in which the measurement was performed, increasing only by 1.3% from 0.100 M NaCl (μ = 0.10 M) to 0.010 M PBS (μ = 0.25 M) based on the slopes of the least squares fit to the data in Figure 8. Therefore, these two electrolytes must be accessing a given PEDOT film to the same extent, despite the fact that one of them (0.010 M PBS) does this 2.5 times faster (higher current density) than the other (0.100 M NaCl). A comparison of one type of electrolyte at two different ionic strengths, however, when 0.100 M PBS is at ten times the ionic strength of 0.010 M PBS, an additional 36% of the film's charge is accessible, which can translate to increasing the MHD pumping time by 36%. This effect is consistent with the expanding charging model of PEDOT that is used to explain the CA behavior above for the thickest film. While the initial current depends on charging at the polymer/electrolyte interface and therefore on the ionic strength of the surrounding electrolyte, the type of electrolyte becomes more important at later times when ions must permeate more deeply through the polymer to compensate for additional PEDOT oxidation. Therefore, more charge can be extracted from a film when a given electrolyte is more concentrated, and thereby extend the time that MHD can pump fluid in a single direction. [39]

2.3.4 Electrochemical Impedance Spectroscopy Investigations on the Different PEDOT Films.

Bode magnitude plots are shown in Figure 9 and the Bode phase and Nyquist (complex-plane impedance) plots from EIS measurements are provided in Figure S-10 in Supporting Information. These were obtained in 0.100 M NaCl for bare and PEDOT-modified electrodes,

where the films had been deposited from the two electrolytes in PC and at the three scan rates. The potential was set at 0.0 V vs. Ag/AgCl (saturated KCl) which is in a region where the current response during CV is relatively flat and featureless (see Figure S-8 in Supporting Information). A typical equivalent circuit model to explain EIS of PEDOT films is that of a transmission line of capacitance and faradaic resistance connected with pore resistance elements with constant phase and faradaic leakage pathways.[40] This has been further modified as a hybrid with an intercalation model and a morphological explanation for domination of the ohmic range by solution electrolyte ions in the porous paths of the film.[41] The EIS results show that all PEDOT films dynamically change during electrochemical response to a sinusoidal perturbation potential of ±15 mV, and are consistent with the three stage model described in Figure 6. The truncated Nyquist plots in Figure S-10 (a) and (b) show two regimes at the higher frequencies (>300 Hz), one with a semicircle and the start of a mass transfer branch. Note that this time scale for the thinnest films (>1000 Hz) is faster than the temporal resolution of the CA data described above and explains why the dynamics were not fully observable by CA. Values of R_{Ω}, R_{ct}, and C are listed in Table S-4 in Supporting Information for the PEDOT films. They are all within an order of magnitude of each other and are consistent with films in the first stage of the model. The high frequency intersection of the Nyquist plot at the real Z axis, yields values of R_{Ω} 4.0-5.4 Ω for all films and the bare electrode, providing information about solution and cell resistance, and is consistent with a cell that was set up reproducibly. The R_{ct} is just slightly lower for PEDOT deposited at 100 mV/s (75.1 Ω for both electrolytes) compared to films deposited more slowly at 50 mV/s (80.4 and 81.0 Ω, from $TBAPF_6$ and $LiClO_4$, respectively). These results suggest that there is only a slightly higher resistance for ions to compensate for polymer oxidation with the thicker films (deeper paths where the polymer interfaces with the solution). Larger semicircles

for the thicker films usually demonstrate higher interfacial resistance with poorer charge propagation.[42] However, the thickest films prepared at 5 mV/s in both types of PC electrolytes, have slightly smaller R_{ct} values of 62.0 and 69.3 Ω, respectively. The charge transfer resistance may be facilitated with the rougher polymer morphology, as observed by SEM and optical microscopy, that gives ions access to larger areas.

The capacitance values determined from the frequency at the apex of the semicircle in the Nyquist plots usually corresponds to double layer capacitance, are also relatively similar among all of the polymer films deposited from both PC electrolytes at all three scan rates. They range from 3.2 x 10^{-4} mF (3.3 x 10^{-3} mF/cm^2) to 7.0 x 10^{-4} mF (7.2 x 10^{-3} mF/cm^2), and are generally higher (1.2 to 1.8 times) for the films deposited from $TBAPF_6$ at a given scan rate as compared to deposition from $LiClO_4$ and for the thickest films compared to the thinnest films. A higher surface area of polymer can explain these variations. These areal capacitances are about a factor of ten lower than that for a bare electrode in similar electrolytes (~5 x 10^{-2} mF/cm^2 in 0.100 M NaCl). At these time scales, therefore, the PEDOT appears to behave like a partially blocked or contaminated electrode and would not be advantageous over a flat, bare electrode for providing the charge needed to sustain MHD pumping.

The beginning of the mass transfer branch at lower frequencies are where faradaic processes and charge compensation by ions permeating the films start to become important. The features in Figure S-10 (a) and (b) for the two thinner films (formed at 50 and 100 mV/s) in a given deposition electrolyte are rather typical, with the thinnest of the two exhibiting a shorter mass transport arm, because the thinner polymer film is more limiting to the faradaic process. The more vertical portion beyond the mass transfer region suggests better charge propagation behavior with ideal super capacitive performance. The branch for the thickest films is unusual. It

is longer than that for the thinnest films deposited at 100 mV/s and shorter than those deposited at 50 mV/s. Beyond this region toward even lower frequencies, the response reverses and is consistent with an expanding film morphology (stage 2) that further diminishes R_{ct} and increases C. Nyquist plots and the inserts in Figure S-10 (c) and (d) show that this behavior is observed with the two thinner films, as well, but at higher frequencies. The thinner films cannot expand as far because there is less material and because of the shorter distance to the gold electrodes to which they are tethered. The Nyquist plots for the two thinner films begin to exhibit behavior like that of the bare electrode at the lowest frequencies as the films can no longer expand and ions experience more resistance in entering the polymer (stage 3). This latter stage is not clearly observed for the thickest films in under these EIS conditions, but it the shape of the Nyquist plot suggests that at even lower frequencies, even the thickest film is expected to similar behavior as those thin films.

A look at the Bode magnitude plots of the EIS data in Figure 9, further clarify the polymer behavior. The trends of total impedance with frequency are similar for all films for the majority of the frequencies studied. At high frequencies, the electrochemical behavior of a bare electrode, where double layer charging dominates and the cell is typically represented by an R_uC equivalent circuit, is essentially indistinguishable from that of the films from10^5 to 4000 Hz and from 10^5 to 6000 Hz for PEDOT deposited from PC:$TBAPF_6$ and PC:$LiClO_4$, respectively. The unique electrochemistry of PEDOT films becomes evident when the total impedance becomes constant at a value of about 100 Ω (mostly due to faradaic processes) across the range of 4000 to ~25 Hz for PC:$TBAPF_6$ and of 6000 Hz to ~60 Hz for PC:$LiClO_4$. This region coincides with a phase angle (Figure S-10 (e) and (f)) that has returned to zero, confirming the dominance of faradaic processes. This ohmic region is consistent with what Rubinson and co-workers describe

as being shortened or extended based on the thickness of the porous layer.[43] Thus, the thinner PEDOT films begin to exhibit increasing total impedance with a further decrease in frequency, where the thinnest films (formed at 100 mV/s) deviate before the thicker ones (formed at 50 mV/s), representing the relative time scales when consumption of faradaic sites takes place. The Bode phase plots show a corresponding transition toward -90° in these regions. Finally, at 0.6 Hz for PC:$TBAPF_6$ and 1 Hz for PC:$LiClO_4$, the total impedance of the thickest PEDOT films (formed at 5 mV/s), which have the largest quantity of redox sites, increases as the phase angle returns to -90°. This transition could be attributed to stage 2 in Figure 5. At even lower frequencies, the phase angle remains at -90 °C and the total impedance continues to rise for all films and can represent stage 3, where the capacitive behavior dominates the impedance magnitude

In conclusion, our model is only partly consistent with morphological effects in a porous layer and compact layer as described by Rubinson and co-workers.[41] However, because of the greater thicknesses of our films there are additional features that appear in the EIS and CA responses that we explain by a film that dynamically changes its morphology. Our model in Figure 6 attempts to combine these concepts and considers the association of the counter ions. Because of the complexity of the dynamic morphology of our model, further extraction of a more specific equivalent circuit representation that includes these changes has not been developed here.

2.3.5 Magnetohydrodynamic (MHD) Fluid Flow with PEDOT-Modified Electrodes under Controlled Current Conditions.

Because MHD pumping produces a fluid speed that scales proportionally with ionic current density in the presence of a constant magnetic flux density, it can be more easily tuned by directly controlling the electronic current between electrodes than indirectly by applying a potential.[11, 13, 44] We used chronopotentiometry (CP) with a galvanostat to achieve current control because it simultaneously monitors the potential and can be programmed to automatically reverse the current when the potential reaches set limits that avoid overoxidation of the polymer and conversion into its undoped form. Shown in Figure S-11 in the Supporting Information are examples of the double step function of current (from open circuit to -50 and then to +50 μA, and from open circuit to -200 and then to +200 μA) applied between a pair of PEDOT-modified electrodes and the corresponding triangular-like CP response in "buffer / glycerol / bead " solution for a PEDOT film that was deposited from PC:$TBAPF_6$ at 5 mV/s.

The fluid speed in the x-y plane, v, produced by MHD in the middle of the gap was monitored by tracking beads in the solution using a setup like that in Figure 3. Detail of the setup in Figure S-12 of the Supporting Information shows that the flow profile at a height of 320 μm in the chamber is uniform between and parallel to the active electrodes. The MHD flow was generated by performing CP at five different currents in "buffer / glycerol / bead "solution and the corresponding potential responses are shown in Figure S-13 of the Supporting Information. The speed was quantified during the first step of each CP run and is plotted as a function of the applied current, |i|, in Figure 10 (b). The speeds ranged from 49.4 ± 6.0 μm/s and 53.0 ± 6.1 μm/s at 50 μA to 823.1 ± 28.0 μm/s and 845.1 ± 104.7 μm/s at 800 μA or films formed at 5 mV/s in PC:$TBAPF_6$ and PC:$LiClO_4$, respectively. A least-squares analysis achieved highly

linear equations for PEDOT films formed in both organic solutions. These are v(PC:$TBAPF_6$) = (1.035 ± 0.007 μm s^{-1} μA^{-1}) |i| - (3.1 ± 2.9 μm s^{-1}), R^2 = 0.9998, and v (PC:$LiClO_4$) = (1.072 ± 0.030 μm s^{-1} μA^{-1}) |i| - (4 ± 13 μm s^{-1}), R^2 = 0.9968. The y-intercepts are within error of the origin. Thus, when there is no current, there is no MHD flow. The slopes are within error of each other, because the governing parameters for the different kinds of PEDOT films in this experiment are the same. Namely, the fluid velocity produced from the MHD force, only depends on **j** and **B**, and is dampened by viscous forces, which depend on the viscosity and density of the solution and the location and geometries of the features in the microfluidic chamber. Consequently, as long as the electrode modification does not significantly alter the fluid path or its confinement, the calibration of speed with current is independent of the materials that generate and support the ionic current.

Because the initial charged state of PEDOT will vary from one experiment to another, the duration of the first step of the CP will also vary. However, the second step has well-defined starting (+1.10 V) and ending (-1.00 V) cutoff potentials, and thus, a measurement of the time it takes to switch between these values at the applied current equals the duration of MHD pumping in a single direction. See Figure S-11 in the Supporting Information. The pumping durations for an applied current of 50 μA were 212 ± 8 s and 146 ± 1 s, for PEDOT films that were formed in PC:$TBAPF_6$ and PC:$LiClO_4$, respectively. At 800 μA, when the charge is being consumed 16 times faster, the pumping durations were only 9.1 ± 0.1 s and 6.6 ± 0.2 s, respectively. An inverse relationship of flow duration with applied current for a given PEDOT film was established previously where the electrochemical behavior was modeled as an RC circuit,[30]

$$t = \left(-\frac{1}{i_2} \right) \left(C_T \left(E(t) - E(0) \right) \right) - \left(2RC_T \right) \quad (1)$$

and where i_2 is the current in the second step (using the non-IUPAC sign convention), E(0) is the starting potential, and E(t) is the final potential in the second step of the CP. Figure 10(a) shows the corresponding plots of data for each type of PEDOT film. Least squares analyses yield the following equations: $|t|(PC:TBAPF_6) = (10816 \pm 68)$ s μA) $|1/i|$ - (5.30 ± 0.070 s), $R^2 = 0.9998$, and $|t|(PC:LiClO_4) = (7450. \pm 13)$ s μA) $|1/i|$ - (2.85 ± 0.17 s), $R^2 = 1.0000$. The capacitance, C, for one of the two PEDOT-modified electrodes (where $C_T = C/2$) and the total resistance (from the electrode, film, solution and connector), R, can be obtained from the slopes and y-intercepts, and electrode area is determined from nominal dimensions (bare electrode). These C and R parameters are not necessarily the same as the C and R obtained above for short time frames from EIS (>100 Hz), but rather are the apparent C and R for the films that result over the entire pumping time for the potential difference between the pairs of PEDOT-modified electrodes to go from -1.000 V to 1.100 V. They are $C(PC:TBAPF_6) = 105.7 \pm 0.7$ mF/cm^2 and $R(PC:TBAPF_6) = 515 \pm 3$ Ω and $C(PC: LiClO_4) = 72.8 \pm 0.1$ mF/cm^2 and $R(PC: LiClO_4) = 402 \pm 24$ Ω. Because the PEDOT films formed from $PC:TBAPF_6$ are thicker and contain more charge than those formed from $PC:LiClO_4$, they possess a higher total capacitance, C_T, and will contribute toward a longer pumping time in the first term of eqn. 1. The resistance, R, is important in the second term of eqn. 1 and coupled with C_T, where RC_T is like a time constant that contributes toward diminishing pumping time and it gets larger. The value of RC_T is 1.05 s—the same for both types of films. Thus, it is simply the capacitance that can be used to screen PEDOT films to identify which ones will pump for the longest time.

For comparison, the capacitance calculated from the total charge obtained by integrating the CA in 0.1 M PBS and dividing by the potential difference of 1.6 V (stepping from -0.8 V to +0.8 V), are 175 ± 28 and 123 ± 14 mF/cm^2 for the two types of films, respectively. The

capacitance values obtained by eqn. 1 are lower than those the CA studies here because of the 0.7-fold dilution and increased viscosity introduced by adding glycerol to 0.1 M PBS for the MHD studies. However, the ratio of the capacitance values for the two types of films of 1.4 is the same for those obtained by integrating the CA in 0.1 M PBS and by eqn. 1 in the PBS/glycerol solution. Thus, the concept that electrochemical characterization can predict MHD behavior is further confirmed; in this case it takes the form of obtaining capacitance of PEDOT films in a given pumping solution to determine pumping duration.

An alternative approach to obtain C and R with the same data set involves inspection of each CP response directly. There is loss in potential across the resistance of the cell that manifests itself as a vertical drop in potential, ΔV, equal to i_2R, immediately upon application of current in the second step of the CP. The magnitude of the potential drop increases with increasing current as labeled in Figure S-11 and measured for the series of CP responses in Figure S-13 in the Supporting Information. By knowing the applied current and measuring this change in voltage, the resistance was calculated. The capacitance was then determined by calculating the total charge generated during that step from i_2 t and dividing by the adjusted potential, which is the difference in cutoff potentials minus ΔV, $E(t) – E(0) - \Delta V$. When this corrected total capacitance is plotted as a function of the applied current, a line with a zero slope is obtained. Therefore, the resistance remains unchanged for all currents investigated. Plots of the total capacitances that are uncorrected (using E(t)-E(0)) and corrected (using $E(t) – E(0) - \Delta V$) for the i_2R drop as a function of applied current are shown in Figure S-14 in the Supporting Information. The average, area-normalized total capacitances (C_T/A) obtained in this way for PEDOT films formed in PC:$TBAPF_6$ and PC:$LiClO_4$, are 51.1 ±0.1 and 36.3 ± 0.4 $mFcm^2$, respectively, and doubling these to get C/A yields 102.2 ±0.2 and 72.6 ± 0.8 mF/cm^2. These

values are the same as those obtained with eqn. 1, the ratio of the values is again 1.4-1.5. The resistances obtained with this alternative approach are $763 \pm 6\ \Omega$ and $748 \pm 6\ \Omega$, respectively, which are a factor of 1.5 and 1.86 times those determined by eqn. 1.

2.4 Conclusions

Investigations were performed toward maximizing the current and charge densities of PEDOT modified electrodes through controlled electropolymerization of EDOT using 12 cycles of oxidizing CV at three different scan rates from solutions of PC solvent with the two different electrolytes $TBAPF_6$ and $LiClO_4$. The resulting PEDOT films were subsequently evaluated in three different aqueous solutions by CV, CA, and EIS to develop a deeper fundamental understanding of how ionic current, j, which is essential in generating R-MHD microfluidics in the presence of a perpendicular magnetic field, is associated with the electrochemical behavior of the polymer. Although the work described here is directly relevant to improving R-MHD microfluidics in terms of fluid speed and duration, the ability to control the properties of PEDOT can extend to other applications where large quantities of quickly accessible charge is important.

The PEDOT films that performed best in aqueous solutions were produced by electrodeposition at the slowest scan rate of 5 mV/s in PC: $TBAPF_6$. These conditions generated the thickest PEDOT films with the highest accessible charge. This feature allows R-MHD to pump fluid in a single direction for the longest duration. The duration was also shown to be linearly dependent on the inverse of the applied pumping current. Because all PEDOT films that were investigated demonstrated the same maximum current density regardless of electrodeposition conditions, all would be expected to offer the same highest pumping speed for a given aqueous pumping fluid. Thus, it is the *quantity* of electropolymerized EDOT that is the

most desirable characteristic for R-MHD microfluidics that was studied herein. The accessible charge within the PEDOT film can be further enhanced by ionic strength and composition of the pumping electrolyte. The results on electrodes modified with the thick PEDOT films offer a unique contribution to the existing body of knowledge of this material.

It is anticipated that there is a maximum amount of PEDOT that no longer benefits R-MHD microfluidics, although that limit was not reached in these studies. For example, the film could come off of the electrode if forces resulting from expansion and contraction of thicker films exceed forces adhearing the PEDOT to the electrode surface. In addition, the branching of PEDOT beyond the electrode edges could cause shorting to neighboring electrodes if the gap between them is less than the length of the dendrites. It is also possible that excessively bulky PEDOT could perturb the fluid flow.

Characterization by EIS and CA in the aqueous electrolytes support a model for electrochemical behavior of these films in aqueous solutions that involve a changing morphology. The results are consistent with a combination of both porous and more compact features that are accessed at shorter and longer time scales, respectively. However, there is an initial surface charging period observed here at the shortest times scales, after which the films expand to provide greater access for ion compensation, presumably through increasing pore sizes and an increasing polymer/electrolyte interface. Further work is needed to extract an equivalent circuit that addresses these dynamics.

We are engaged in ongoing studies that will be reported elsewhere that compare electrodeposition by CV to that by CA and CP, where quantities of polymer are more controllable and where the background current can be deconvoluted from the faradaic current.

These other investigations also consider different solvents and derivatives of EDOT-like monomers.

Extending the duration of R-MHD pumping with electrodes modified with larger quantities of PEDOT than previously described[13] has several possible advantages. One is for slower repetitive reversal of microfluidics flow–forward (discharging of PEDOT) and backward (recharging of PEDOT)–to image white blood cells by coupling R-MHD with epitaxial light sheet confocal microscopy.[30,45] Another is to lower alternating frequencies that diminish inductive heating when synchronizing a sinusoidally varying magnetic field of an electromagnet with a sinusoidally varying current at the PEDOT-modified electrodes to pump indefinitely in a single direction.[46]

2.5 Supporting Information

Supporting information includes tables of current and charge densities in aqueous electrolytes, film thicknesses of PEDOT films that were formed under different conditions, and data extracted from EIS; details of electrode chip design; CV responses during deposition of PEDOT films; plots of charging current measurements during CV deposition as a function of cycle number; CV characterization of PEDOT films in aqueous electrolytes compared to bare electrodes; plots of PEDOT thickness as a function of the scan rate used for deposition; scanning electron and optical micrographs of PEDOT films; current function and CP responses showing switching time dependency for films; detail of R-MHD setup and horizontal velocity flow profile; CP responses of PEDOT-modified electrodes during R-MHD; PEDOT capacitances obtained from CP data as a function of applied current in aqueous solution; Nyquist and Bode plots for PEDOT films in aqueous solution; oxidative charge as a function of cycle during CV

deposition of EDOT; dependence of maximum current densities of PEDOT films in aqueous electrolytes of different ionic strengths.

2.6 Acknowledgments

We are grateful for financial support from the National Science Foundation (CBET-1336853 and CMI-1808286), the Women's Giving Circle, and the Arkansas Bioscience Institute, the major research component of the Arkansas Tobacco Settlement Proceeds Act of 2000. We recognize Mr. Mathew Gerner for the initial chip design and Mr. Benjamin J. Jones for the design modification. We thank J. Faye Rubinson for helpful discussions.

2.7 References

(1) Whitesides, G. M. The origins and the future of microfluidics. *Nature* **2006,** *442,* 368, DOI: 10.1038/nature05058.

(2) Andersson, H.; van den Berg, A. Microfluidic devices for cellomics: a review. *Sensors and Actuators B: Chemical* **2003,** *92* (3), 315-325, DOI: 10.1016/s0925-4005(03)00266-1.

(3) Mark, D.; Haeberle, S.; Roth, G.; von Stetten, F.; Zengerle, R. Microfluidic lab-on-a-chip platforms: requirements, characteristics and applications. *Chemical Society Reviews* **2010,** *39* (3), 1153-1182, DOI: 10.1039/b820557b.

(4) Wang, X.; Yi, L.; Mukhitov, N.; Schrell, A. M.; Dhumpa, R.; Roper, M. G. Microfluidics-to-Mass Spectrometry: A review of coupling methods and applications. *Journal of chromatography. A* **2015,** *0*, 98-116, DOI: 10.1016/j.chroma.2014.10.039.

(5) Sackmann, E. K.; Fulton, A. L.; Beebe, D. J. The present and future role of microfluidics in biomedical research. *Nature* **2014,** *507* (7491), 181-189, DOI: 10.1038/nature13118.

(6) Lazar, I. M.; Karger, B. L. Multiple Open-Channel Electroosmotic Pumping System for Microfluidic Sample Handling. *Analytical Chemistry* **2002,** *74* (24), 6259-6268, DOI: 10.1021/ac0203950.

(7) Liu, Y.; Rauch, C. B.; Stevens, R. L.; Lenigk, R.; Yang, J.; Rhine, D. B.; Grodzinski, P. DNA Amplification and Hybridization Assays in Integrated Plastic Monolithic Devices. *Analytical Chemistry* **2002,** *74* (13), 3063-3070, DOI: 10.1021/ac020094q.

(8) Sanders, J. C.; Breadmore, M. C.; Mitchell, P. S.; Landers, J. P. A simple PDMS-based electro-fluidic interface for microchip electrophoretic separations. *Analyst* **2002,** *127* (12), 1558-1563, DOI: 10.1039/b206808g.

(9) Weston, M. C.; Gerner, M. D.; Fritsch, I. Magnetic Fields for Fluid Motion. *Anal. Chem.* **2010,** *82,* 3411-3418.

(10) Haehnel, V.; Khan, F. Z.; Mutschke, G.; Cierpka, C.; Uhlemann, M.; Fritsch, I. Combining magnetic forces for contactless manipulation of fluids in microelectrode-microfluidic systems. *Scientific Reports* **2019,** *9,* 5103.

(11) Sahore, V.; Fritsch, I. Flat Flow Profiles Achieved with Microfluidics Generated by Redox-Magnetohydrodynamics. *Analytical Chemistry* **2013,** *85* (24), 11809-11816, DOI: 10.1021/ac402476v.

(12) Sahore, V.; Fritsch, I. Microfluidic rotational flow generated by redox-magnetohydrodynamics (MHD) under laminar conditions using concentric disk and ring microelectrodes. *Microfluidics and Nanofluidics* **2015,** *18* (2), 159-166, DOI: 10.1007/s10404-014-1427-6.

(13) Nash, C. K.; Fritsch, I. Poly(3,4-ethylenedioxythiophene)-Modified Electrodes for Microfluidics Pumping with Redox-Magnetohydrodynamics: Improving Compatibility for Broader Applications by Eliminating Addition of Redox Species to Solution. *Analytical Chemistry* **2016,** *88* (3), 1601-1609, DOI: 10.1021/acs.analchem.5b03182.

(14) Bazant, M. Z.; Ben, Y. Theoretical prediction of fast 3D AC electro-osmotic pumps. *Lab on a Chip* **2006,** *6* (11), 1455-1461, DOI: 10.1039/b608092h.

(15) Jacobson, S. C.; Hergenroder, R.; Koutny, L. B.; Ramsey, J. M. High-Speed Separations on a Microchip. *Analytical Chemistry* **1994,** *66* (7), 1114-1118, DOI: 10.1021/ac00079a029.

(16) Weston, M. C.; Nash, C. K.; Fritsch, I. Redox-Magnetohydrodynamic Microfluidics Without Channels and Compatible with Electrochemical Detection Under Immunoassay Conditions. *Analytical Chemistry* **2010,** *82* (17), 7068-7072, DOI: 10.1021/ac101377a.

(17) Sahore, V.; Kreidermacher, A.; Khan, F. Z.; Fritsch, I. Visualization and Measurement of Natural Convection from Electrochemically-Generated Density Gradients at Concentric Microdisk and Ring Electrodes in a Microfluidic System. *J. Electrochem. Soc.* **2016,** *163* (4), H3135-H3144.

(18) Wang, X.; Sjöberg-Eerola, P.; Eriksson, J.-E.; Bobacka, J.; Bergelin, M. The effect of counter ions and substrate material on the growth and morphology of poly(3,4-ethylenedioxythiophene) films: Towards the application of enzyme electrode construction in biofuel cells. *Synthetic Metals* **2010,** *160* (13-14), 1373-1381, DOI: 10.1016/j.synthmet.2010.01.033.

(19) Poverenov, E.; Li, M.; Bitler, A.; Bendikov, M. Major Effect of Electropolymerization Solvent on Morphology and Electrochromic Properties of PEDOT Films. *Chemistry of Materials* **2010,** *22* (13), 4019-4025, DOI: 10.1021/cm100561d.

(20) Bobacka, J.; Lewenstam, A.; Ivaska, A. *Electrochemical impedance spectroscopy of oxidized poly(3,4-ethylenedioxythiophene) film electrodes in aqueous solutions*, 2000; Vol. 489, p 17-27.

(21) Österholm, A. M.; Shen, D. E.; Dyer, A. L.; Reynolds, J. R. Optimization of PEDOT Films in Ionic Liquid Supercapacitors: Demonstration As a Power Source for Polymer Electrochromic Devices. *ACS Applied Materials & Interfaces* **2013,** *5* (24), 13432-13440, DOI: 10.1021/am4043454.

(22) Kim, Y.; Na, J.; Park, C.; Shin, H.; Kim, E. PEDOT as a Flexible Organic Electrode for a Thin Film AcousticEnergy Harvester. *ACS Appl. Mater. Interfaces* **2015,** *7*, 16279−16286.

(23) Bodart, C.; Rossetti, N.; Hagler, J.; Chevreau, P.; Chhin, D.; Soavi, F.; Schougaard, S. B.; Amzica, F.; Cicoira, F. Electropolymerized Poly(3,4-ethylenedioxythiophene) (PEDOT)Coatings for Implantable Deep-Brain-Stimulating Microelectrodes. *ACS Appl. Mater. Interfaces* **2019** ASAP, DOI: 10.1021/acsami.9b03088.

(24) Kayinamura, Y. P.; Ovadia, M.; Zavitz, D.; Rubinson, J. F. Investigation of Near Ohmic Behavior for Poly(3,4-ethylenedioxythiophene): A Model Consistent with Systematic Variations in Polymerization Conditions. *ACS Applied Materials & Interfaces* **2010,** *2* (9), 2653-2662, DOI: 10.1021/am100480s.

(25) Vedrine, C.; Fabiano, S.; Tran-Minh, C. *Amperometric tyrosinase based biosensor using an electrogenerated polythiophene film as an entrapment support*, 2003; Vol. 59, p 535-44.

(26) Vorotyntsev, M. A.; Zinovyeva, V. A.; Konev, D. V. Mechanisms of Electropolymerization and Redox Activity: Fundamental Aspects. In *Electropolymerization*; Wiley-VCH Verlag GmbH & Co. KGaA: 2010; pp 27-50.

(27) Sakmeche, N.; Aeiyach, S.; Aaron, J.-J.; Jouini, M.; Lacroix, J. C.; Lacaze, P.-C. Improvement of the Electrosynthesis and Physicochemical Properties of Poly(3,4-ethylenedioxythiophene) Using a Sodium Dodecyl Sulfate Micellar Aqueous Medium. *Langmuir* **1999,** *15* (7), 2566-2574, DOI: 10.1021/la980909j.

(28) Huang, J.-H.; Kekuda, D.; Chu, C.-W.; Ho, K.-C. Electrochemical characterization of the solvent-enhanced conductivity of poly(3,4-ethylenedioxythiophene) and its application in polymer solar cells. *Journal of Materials Chemistry* **2009,** *19* (22), 3704, DOI: 10.1039/b822729b.

(29) Groenendaal, L.; Zotti, G.; Aubert, P. H.; Waybright, S. M.; Reynolds, J. R. Electrochemistry of Poly(3,4-alkylenedioxythiophene) Derivatives. *Advanced Materials* **2003,** *15* (11), 855-879, DOI: 10.1002/adma.200300376.

(30) Khan, F. Z.; Hutcheson, J. A.; Hunter, C. J.; Powless, A. J.; Benson, D.; Fritsch, I.; Muldoon, T. J. Redox-Magnetohydrodynamically Controlled Fluid Flow with Poly(3,4-ethylenedioxythiophene) Coupled to an Epitaxial Light Sheet Confocal Microscope for Image Cytometry Applications. *Analytical Chemistry* **2018,** *90* (13), 7862-7870, DOI: 10.1021/acs.analchem.7b05312.

(31) Hillman, A. R.; Daisley, S. J.; Bruckenstein, S. Solvent effects on the electrochemical p-doping of PEDOT. *Physical Chemistry Chemical Physics* **2007,** *9* (19), 2379-2388, DOI: 10.1039/B618786B.

(32) 79382 Sigma, Phosphate bufferedsaline tablet, acess year2019, https://www.sigmaaldrich.com/catalog/product/sigma/79382?lang=en&region=US

(33) Diaz, A. F.; Crowley, J.; Bargon, J.; Gardini, G. P.; Torrance, J. B. Electrooxidation of aromatic oligomers and conducting polymers. *Journal of Electroanalytical Chemistry and Interfacial Electrochemistry* **1981,** *121*, 355-361, DOI: https://doi.org/10.1016/S0022-0728(81)80592-X.

(34) Pandey, G. P.; Rastogi, A. C. Synthesis and characterization of pulsed polymerized poly(3,4-ethylenedioxythiophene) electrodes for high-performance electrochemical capacitors. *Electrochimica Acta* **2013,** *87*, 158-168, DOI: https://doi.org/10.1016/j.electacta.2012.08.125.

(35) Snook, G. A.; Kao, P.; Best, A. S. Conducting-polymer-based supercapacitor devices and electrodes. *Journal of Power Sources* **2011,** *196* (1), 1-12, DOI: 10.1016/j.jpowsour.2010.06.084.

(36) Otero, T. F.; Boyano, I. Comparative Study of Conducting Polymers by the ESCR Model. *The Journal of Physical Chemistry B* **2003,** *107* (28), 6730-6738, DOI: 10.1021/jp027748j.

(37) Jow, T. R.; Xu, D.; Deng, S. P. *Nonaqueous Electrolyte Development for ElectrochemicalCapacitors*; DOE/ID/13451; U.S.Department of Energy: Washington, DC, 1999; p 17.

(38) Conway, B. E. *Electrochemical Supercapacitors:Scientific Fundamentals and Technological Applications*, Springer US: 1999.

(39) SHE, P.-P.; Wang, Z.-H. Studies on Charging Processes and Capacitances of Oxidized PEDOT Films. *Chinese Journal of Chemistry* **2005,** *23*, 806-810.

(40) Conway, B. E. *Electrochemical Supercapacitors,* Kluwer Academic/Plenum Publishers: New York, 1999.

(41) Kayinamura, Y. P.; Ovadia, M.; Zavitz, D.; Rubinson, J. F. Investigation of Near Ohmic Behavior for Poly(3,4-ethylenedioxythiophene): A Model Consistent with Systematic Variations in Polymerization Conditions. *ACS Appl. Mater. Interfaces* **2010,** *2* (9), 2653–2662.

(42) Si, P.; Ding, S.; Lou, X.-W.; Kim, D.-H. An electrochemically formed three-dimensional structure of polypyrrole/graphene nanoplatelets for high-performance supercapacitors. *RSC Advances* **2011,** *1* (7), 1271-1278, DOI: 10.1039/c1ra00519g.

(43) Kayinamura, Y. P.; Roberts, J. H.; Rubinson, J. F. Near-Ohmic Behavior for Conducting Polymers: Extension BeyondPEDOT on Gold-Plated Platinum to Other Polymer-Counterion/Substrate Combinations. *ACS Appl. Mater. Interfaces* **2012,** *4*, 1601−1607, DOI: dx.doi.org/10.1021/am2017706.

(44) Weston, M. C.; Fritsch, I. Manipulating fluid flow on a chip through controlled-current redox magnetohydrodynamics. *Sensors and Actuators B: Chemical* **2012,** *173* (Supplement C), 935-944, DOI: https://doi.org/10.1016/j.snb.2012.07.006.

(45) Hutcheson, J. A.; Khan, F. Z.; Powless, A. J.; Benson, D.; Hunter, C.; Fritsch, I.; Muldoon, T. J. A light sheet confocal microscope for image cytometry with a variable linear slit detector, *Proc. SPIE.* **2016**, 9720, 97200U, DOI: https://doi.org/10.1117/12.2211164.

(46) Nash, C. K. Advanced Microfluidic Pumping at Poly(3,4-ethylenedioxythiophene)-Modified Electrodes via AC-Magnetohydrodynamics. *ECS Interface* **2014,** *Winter*, 83-84.

2.8 Figures

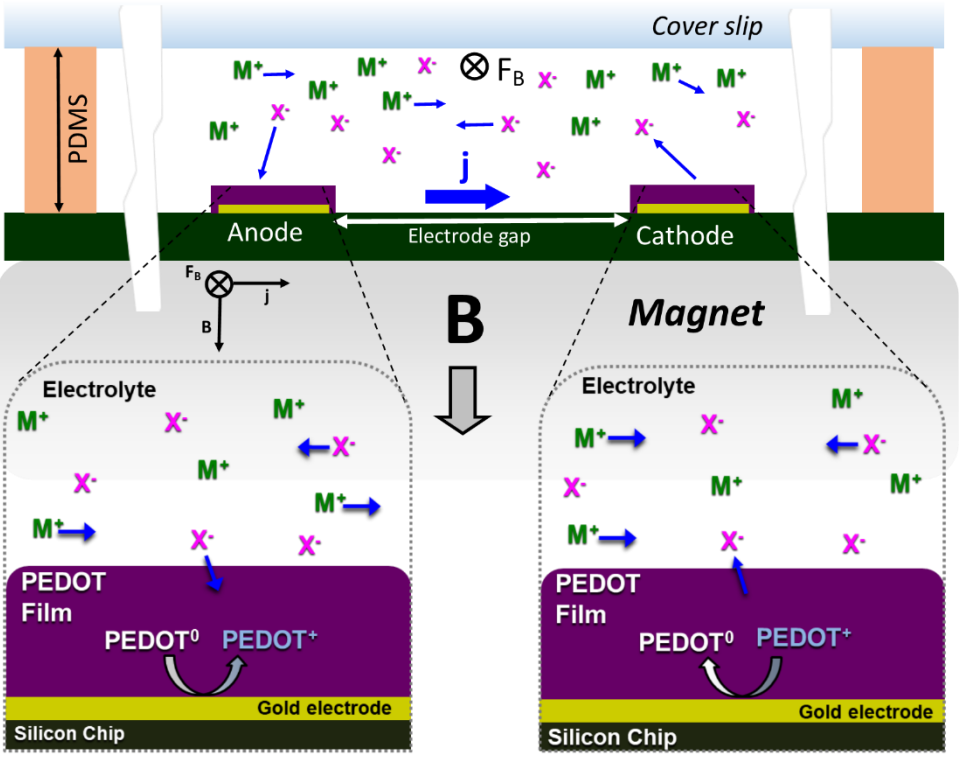

Figure 1: Illustration of how MHD fluid flow is generated using PEDOT-modified electrodes, which produce **j** between anode and cathode upon application of an electronic current, and in a chamber containing electrolyte of M^+ and X^- ions, over a permanent magnet, which provides **B.** The M^+ and X^- are generic representations of cations and anions, respectively, where in this work M^+ is Na^+ or K^+ and X^- is Cl^-, $H_2PO_4^-$, HPO_4^{2-}, or HPO_4^{3-}.

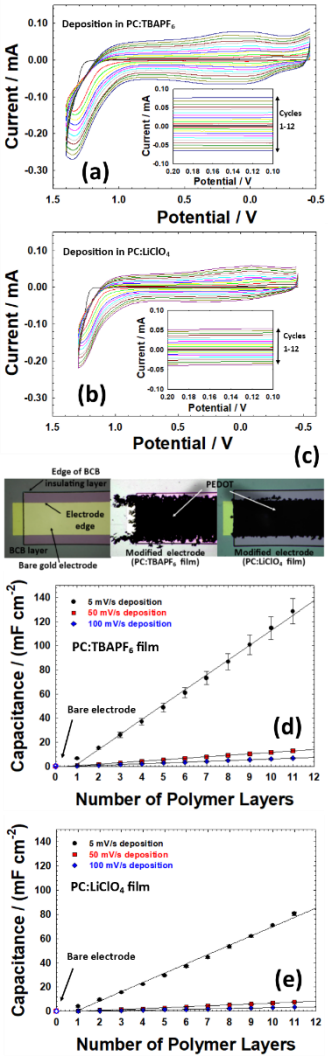

Figure 2: (a) and (b) show CV responses during electropolymerization of PEDOT at 5 mV/s for 12 consecutive cycles in monomer solutions containing 0.010 M EDOT in PC with electrolyte of (a) 0.100 M $TBAPF_6$ and (b) 0.1000 M $LiClO_4$. The oxidation of monomer occurs at a potential > 1.00 V vs Ag/AgCl (saturated KCl). The insets show the current increment as more cycles build up. Microscope images in (c) shows dark PEDOT films are formed on a bare electrode (left) after 12 cycles of successive deposition in both PC:$TBAPF_6$ (middle) and PC:$LiClO_4$ (right). (d) and (e) show the linear dependency of area normalized capacitance at 100, 50 and 5 mV/s deposition scan rates with number of deposition cycles obtained during electrodeposition in PC:$TBAPF_6$ and PC:$LiClO_4$, respectively.

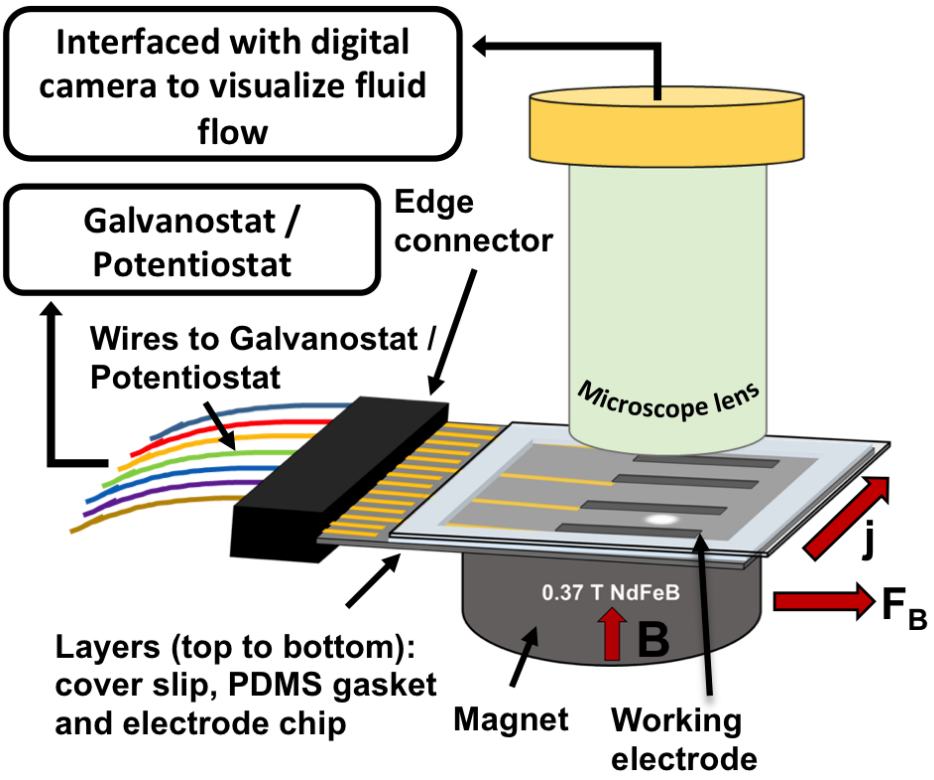

Figure 3: Schematic of simplified MHD setup where electrodes on chip are modified with PEDOT films. The PDMS gasket on the chip holds the electrolyte solution and a glass coverslip functions as a lid. The chip, inserted into an edge connector, is placed upon a permanent magnet, and the whole MHD assembly is then placed under microscope to observe fluid movement by monitoring microbeads that have been added to the solution.

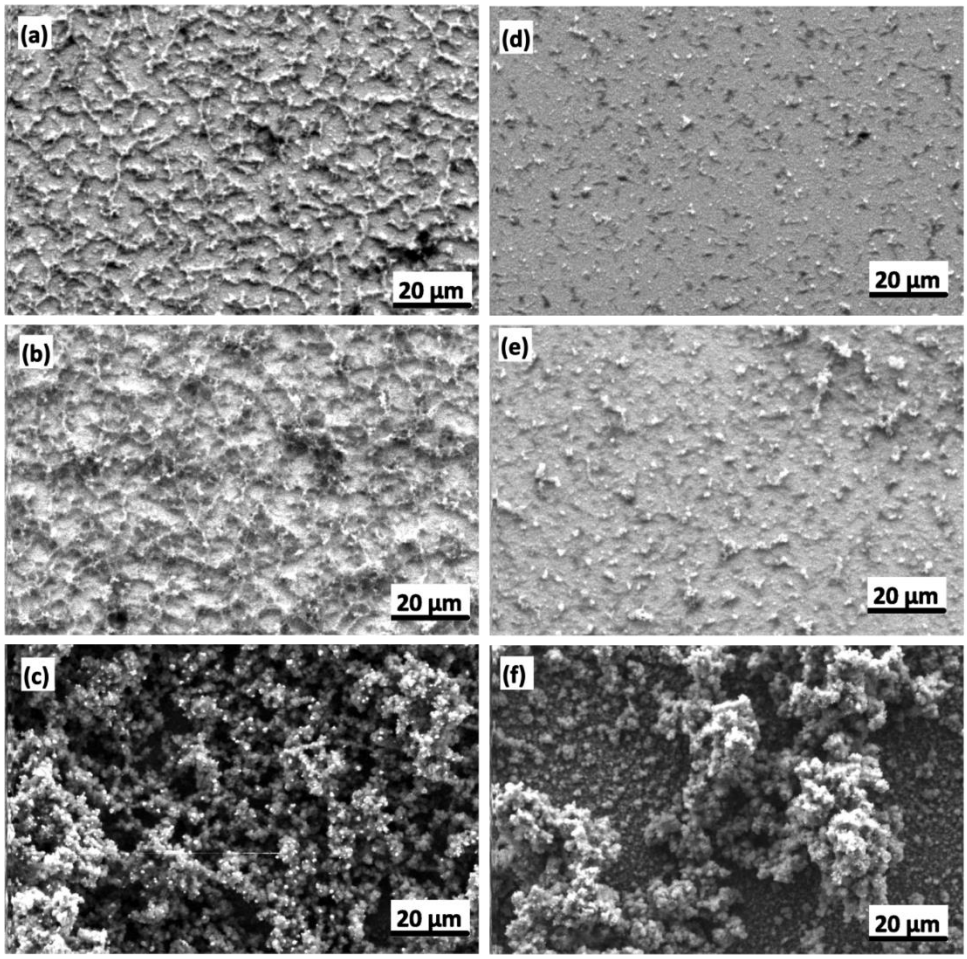

Figure 4. SEM images were taken at 1000X magnification. (a) – (c) show SEM images of films deposited from a monomer solution containing PC:$TBAPF_6$ at 100 mV/s, 50 mV/s, and 5 mV/s scan rate for 12 cycles, respectively. (d) – (f) show images with same deposition parameters but with PC:$LiClO_4$ electrolyte. Table S-1 in Supporting Information provides estimates of total deposition times for each.

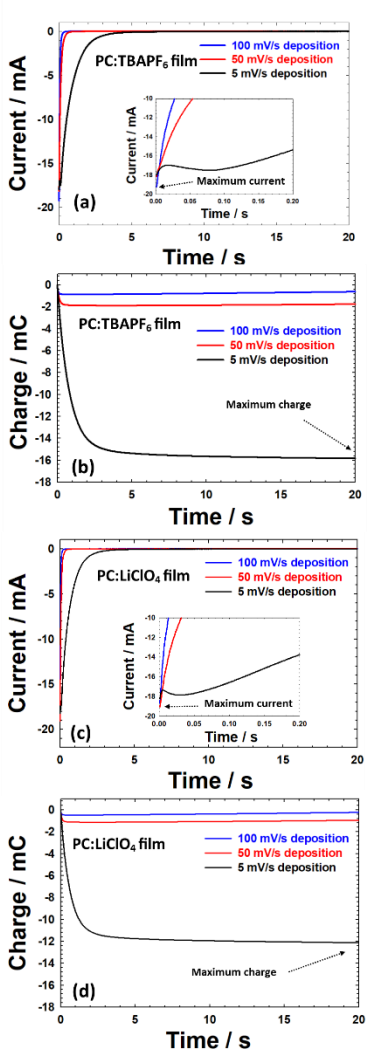

Figure 5: Current responses for CA in 0.100 M NaCl solution for films of PEDOT deposited at 5, 10, 100 mV/s for 12 cycles from EDOT monomer solutions in (a) PC:$TBAPF_6$ and (c) PC:$LiClO_4$. A three-electrode system was used with an Ag/AgCl (saturated KCl) reference electrode and Pt counter electrode in a 20 mL glass beaker. The maximum current response was obtained at 0.001 s after stepping the potential from -0.800 to 0.800 V. The potential was held at -0.800 V for a quiet time of 20 s prior to the step, and the potential was held at 0.800 V for 20 s after the step. By integrating the current in (a) and (c), the charge responses were obtained and are shown in (b) and (d), respectively. The total charge was measured at the end of 20 s.

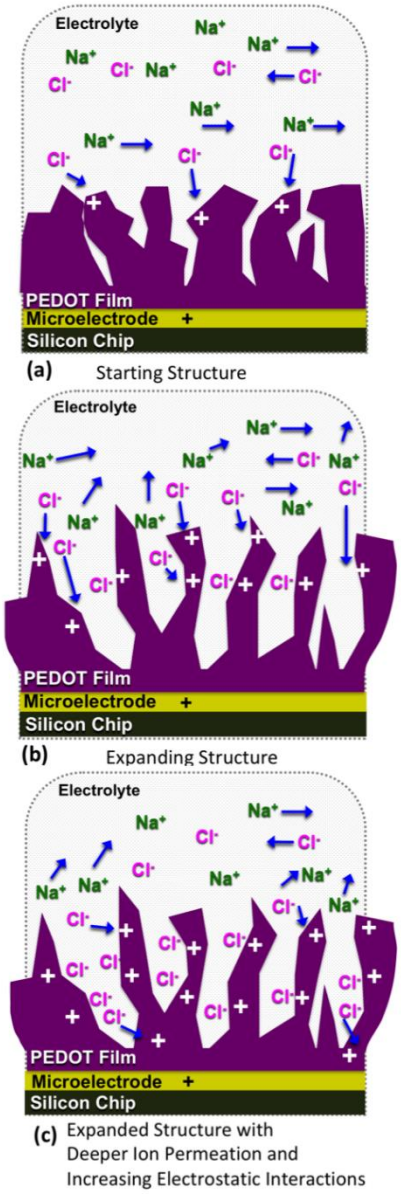

Figure 6: Model depicting three stages of PEDOT transformation during oxidation. (a) Initial charging at the solution/polymer interface. (b) Expansion with further oxidation, exposing additional polymer surface area to the solution, and thereby increasing the current. (c) Permeation of ions more deeply into the polymer, when the nature of the ions (e.g. size and chemical properties) becomes important. This latter stage could also be viewed as transport through regions that are relatively more compact, and areas increasingly affected by electrostatic repulsions.

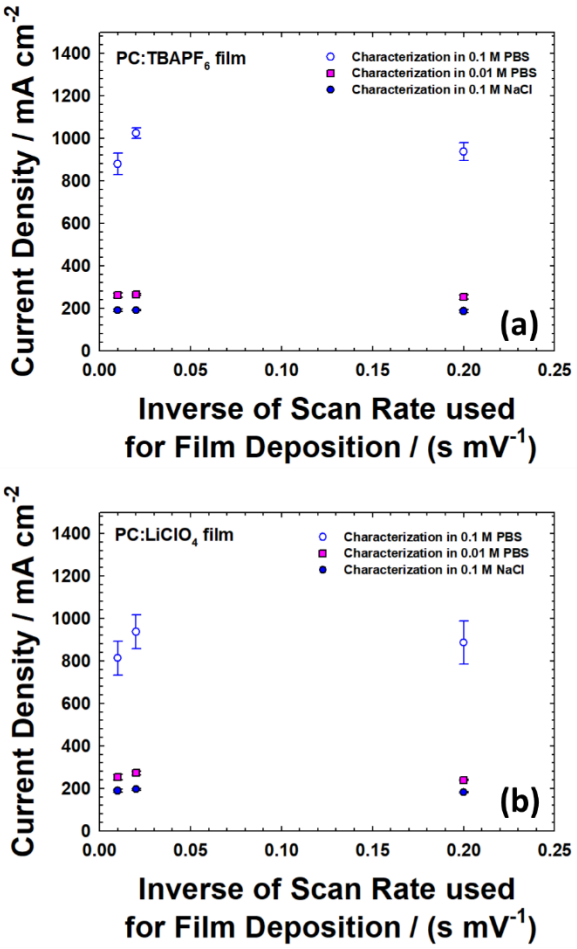

Figure 7: Maximum current densities of PEDOT films obtained for different ionic strengths of aqueous electrolyte and as a function of different thicknesses as expressed as 1/ scan rate used for deposition. Where: 0.100 M NaCl (μ = 0.10 M) < 0.01 M PBS (μ = 0.25 M) < 0.1 M PBS (μ = 2.5 M). The least squares fit and corresponding R^2 values of maximum current density as a function of ionic strength for films formed in PC:$TBAPF_6$ at 5, 50, and 100 mV/s are: y = (309 ± 8 mA cm^{-2} mol^{-1} L) x + (166 ± 11 mA cm^{-2}) , R^2 = 0.9994; y = (343 ± 8 mA cm^{-2} mol^{-1} L) x + (166 ± 12 mA cm^{-2}) , R^2 = 0.9994; and y = (282 ± 10. mA cm^{-2} mol^{-1} L) x + (176 ± 15 mA cm^{-2}), R^2 = 0.9987. Those for films formed in PC:$LiClO_4$ are: y = (291 ± 5 mA cm^{-2} mol^{-1} L) x + (160 ± 8 mA cm^{-2}) , R^2 = 0.9997; y = (303 ± 12 mA cm^{-2} mol^{-1} L) x + (181 ± 17 mA cm^{-2}) , R^2 = 0.9986; and y = (256± 10, mA cm^{-2} mol^{-1} L) x + (176 ± 14 mA cm^{-2}) , R^2 = 0.9985

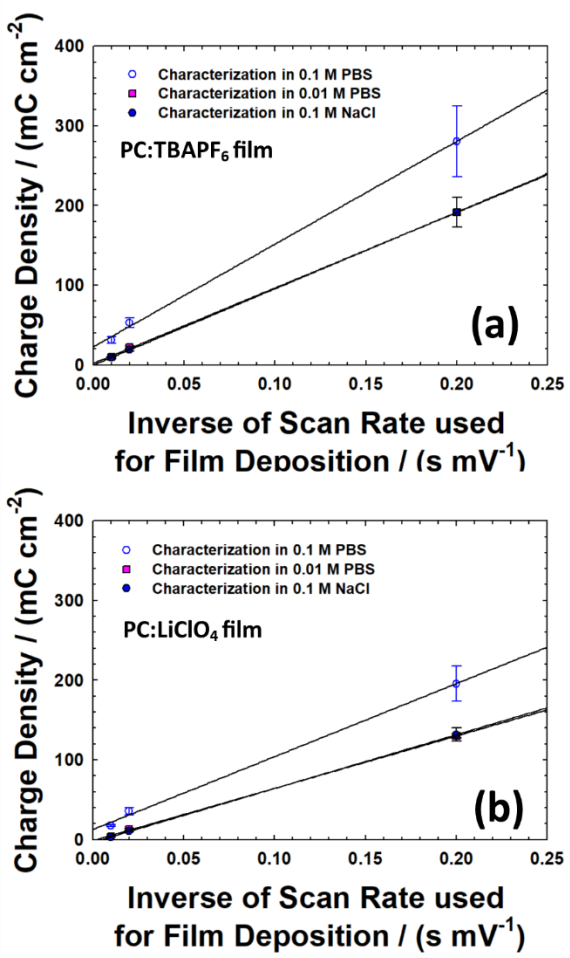

Figure 8: Total charge densities of PEDOT films obtained for different ionic strengths of aqueous electrolyte and as a function of different thicknesses as expressed as 1/scan rate. Where: 0.100 M NaCl (μ = 0.10 M) < 0.01 M PBS (μ = 0.25 M) < 0.1 M PBS (μ = 2.5 M). The least squares fit and corresponding R^2 values of maximum charge density of PC:$TBAPF_6$ film in 0.10 M NaCl, 0.01 M PBS, and 0.10 M PBS are: y = (961.00 ± 4.17 mC cm^{-2} mV s^{-1}) x - (0.48 ± 0.48 mC cm^{-2}), R^2 = 0.9994; y = (948.41 ± 12.24 mC cm^{-2} mV s^{-1}) x + (1.69 ± 1.42 mC cm^{-2}), R^2 = 0.9998; and y = (1291.43 ± 42.06 mC cm^{-2} mV s^{-1}) x + (22.36 ± 4.89 mC cm^{-2}), R^2 = 0.9989 respectively. Those for films formed in PC:$LiClO_4$ are y = (675.16 ± 6.31 mC cm^{-2} mV s^{-1}) x - (3.40 ± 0.73 mC cm^{-2}), R^2 = 0.9999; y = (657.04 ± 11.84 mC cm^{-2} mV s^{-1}) x - (1.44 ± 1.37 mC cm^{-2}), R^2 = 0.9997; and y = (916.03 ± 42.32 mC cm^{-2} mV s^{-1}) x + (12.54 ± 4.92 mC cm^{-2}), R^2 = 0.9979 respectively.

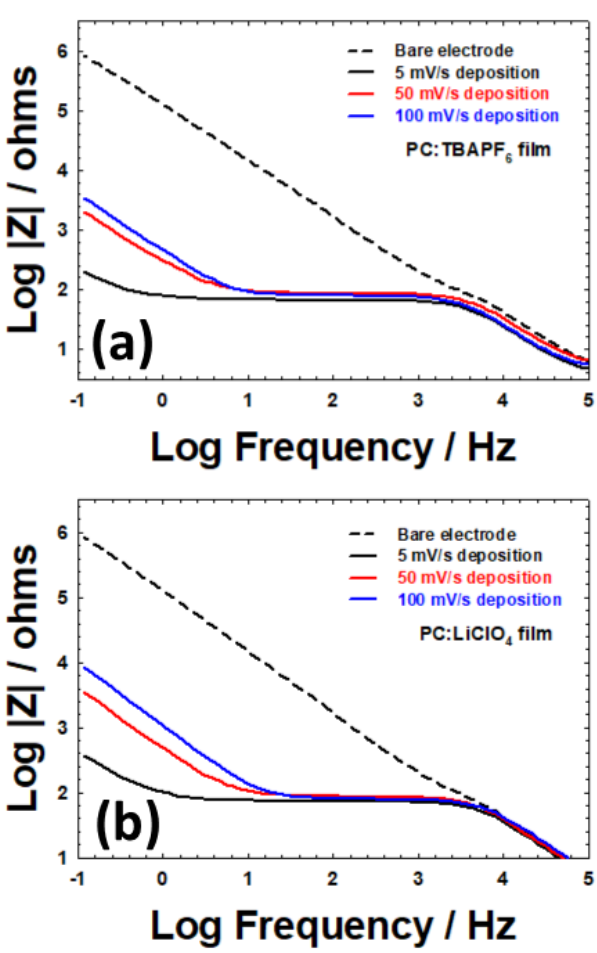

Figure 9: Bode phase plots from EIS of PEDOT-modified electrodes characterized in 0.100 M NaCl, using a three-electrode setup with a Ag/AgCl (saturated KCl) reference electrode. The films were deposited at 5, 50, and 100 mV/s from PC:$TBAPF_6$ (a) and from PC:$LiClO_4$ (b). The chip was placed vertically in a 20 mL solution of 0.10 M NaCl containing Ag/AgCl (saturated KCl) reference and Pt flag counter electrodes. EIS parameters: DC potential of 0 V, AC amplitude of 0.015 V, and frequency range of 0.1-10^5 Hz.

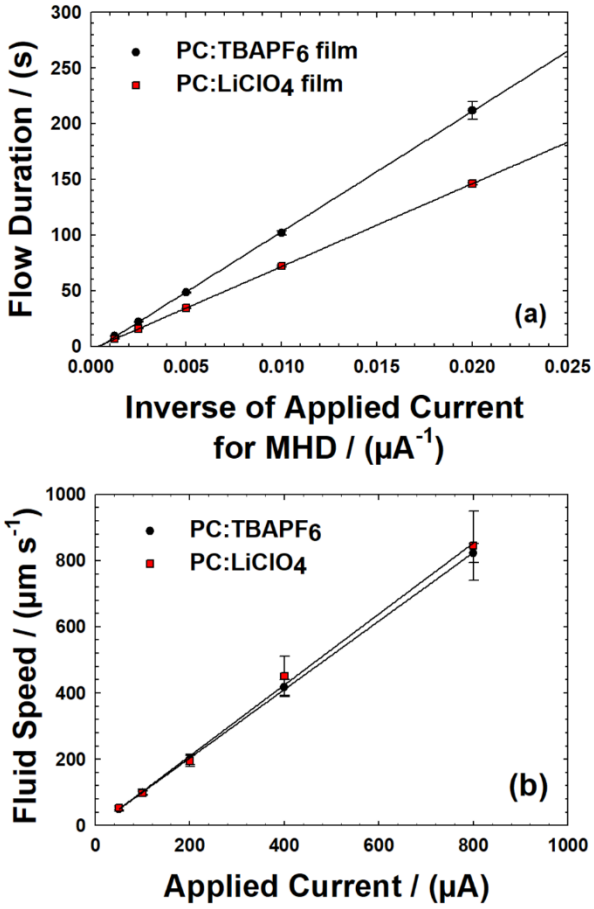

Figure 10: The influence of applied current on fluid speed and duration of MHD pumping of an "buffer / glycerol / bead "solution in a chamber of 781 ± 7 μm height. Performance is shown for using PEDOT films that were deposited in PC: $TBAPF_6$ and PC: $LiClO_4$ at 5 mV/s **(a)** Pumping duration has a linear dependence on the inverse of the applied current. Long pumping times were 211.7 ± 8.0 s and 148.3 ± 4.8 s for PC:$TBAPF_6$ and PC:$LiClO_4$ films for 50 μA. Short pumping durations of 9.1 ± 0.1 s, and 6.6 ± 0.2 were obtained for the higher current 800 μA. Least squares analysis yield the following equations: for a film deposited in PC:$TBAPF_6$, |t|(PC:$TBAPF_6$) = (10816 ± 68) s μA) |1/i| - (5.30 ± 0.070 s), R^2 = 0.9998, and for a film deposited in PC:$LiClO_4$, |t|(PC:$LiClO_4$) = (7450. ± 13) s μA) |1/i| - (2.85 ± 0.17 s), R^2 = 1.0000. **(b)** Bead speed (320 μm above the chip surface) is directly dependent on applied current, with values of 823 ± 28 μm s^{-1} and 845 ± 104 μm s^{-1} for 800 μA for both PC:$TBAPF_6$ and PC:$LiClO_4$ films, respectively. Measurements of microbead motion was at 320 μm above the chip surface.

2.S Supporting Information: Chip-Scale Electrodeposition and Analysis of Poly(3,4-ethylenedioxythiophene) (PEDOT) Films for Enhanced and Sustained Microfluidics Using DC-Redox-Magnetohydrodynamics

Supporting information includes tables of current and charge densities in aqueous electrolytes, film thicknesses of PEDOT films that were formed under different conditions, and data extracted from EIS; details of electrode chip design; CV responses during deposition of PEDOT films; plots of charging current measurements during CV deposition as a function of cycle number; CV characterization of PEDOT films in aqueous electrolytes compared to bare electrodes; plots of PEDOT thickness as a function of the scan rate used for deposition; scanning electron and optical micrographs of PEDOT films; current function and CP responses showing switching time dependency for films; detail of R-MHD setup and horizontal velocity flow profile; CP responses of PEDOT-modified electrodes during R-MHD; PEDOT capacitances obtained from CP data as a function of applied current in aqueous solution; Nyquist and Bode phase plots for PEDOT films in aqueous solution; oxidative charge as a function of cycle during CV deposition of EDOT; dependence of maximum current densities of PEDOT films in aqueous electrolytes of different ionic strengths.

2.S1 Supporting Information Tables

Table S 1: PEDOT film thicknesses resulting from deposition for 12 cycles at different scan rates and in solutions containing 0.010 M EDOT in different electrolytes.

Scan rates of deposition (mV/s)	Film thickness (µm)	Total oxidation time (s)	Solvent – electrolyte combination
100	1.77 ± 0.05	140 ± 3	Propylene carbonate – 0.100 M $TBAPF_6$
50	3.90 ± 0.18	276	
5	28.40 ± 3.16	2766 ± 16	
100	0.64 ± 0.05	112 ± 2	Propylene carbonate – 0.100 M $LiClO_4$
50	1.55 ± 0.01	224	
5	12.06 ± 1.30	2800	

Table S 2 Maximum current and charge density of PEDOT films deposited from 0.010 M EDOT in an electrolyte solution of 0.100 $TBAPF_6$ in propylene carbonate and characterized in 0.100 M NaCl, 0.01 M PBS and 0.1 M PBS.

Scan rates of deposition (mV/s)	Max. current density in 0.1 M NaCl (mA/cm^2)	Max. charge density in 0.1 M NaCl (mC/cm^2)	Max. current density in 0.01 M PBS (mA/cm^2)	Max. charge density in 0.01 M PBS (mC/cm^2)	Max. current density in 0.1 M PBS (mA/cm^2)	Max. charge density in 0.1 M PBS (mC/cm^2)
5	186 ± 6	192 ± 19	254 ± 10.	191 ± 19	937 ± 42	280 ± 45
50	190. ± 3	19 ± 2	264 ± 4	22 ± 2	1024 ± 25	53 ± 6
100	191 ± 6	9 ± 2	261 ± 10.	10. ± 1	879 ± 51	31 ± 4

Table S 3: Maximum current and charge density of PEDOT films deposited from 0.010 M EDOT in an electrolyte solution of 0.100 M $LiClO_4$ in propylene carbonate and characterized in 0.100 M NaCl, 0.01 M PBS and 0.1 M PBS.

Scan rates of deposition (mV/s)	Max. current density in 0.1 M NaCl (mA/cm^2)	Max. charge density in 0.1 M NaCl (mC/cm^2)	Max. current density in 0.01 M PBS (mA/cm^2)	Max. charge density in 0.01 M PBS (mC/cm^2)	Max. current density in 0.1 M PBS (mA/cm^2)	Max. charge density in 0.1 M PBS (mC/cm^2)
5	182 ± 4	132 ± 8	240. ± 4	130. ± 3	886 ± 100.	196 ± 22
50	196 ± 4	11 ± 1	272 ± 8	13 ± 1	937 ± 80.	36 ± 5
100	188 ± 7	2.7 ± 0.4	253 ± 14	3.9 ± 0.3	814 ± 80.	17.3 ± 0.9

Table S 4: Data extracted from Nyquist plots for PEDOT-modified electrodes in 0.100 M NaCl in a three-electrode setup. A sinusoidal amplitude of 0.015 V was applied around 0.000 V for frequencies of 0.1 to 10^5 Hz.

Deposition parameters for PEDOT films		Data from Nyquist plots obtained for PEDOT films in aqueous 0.100 M NaCl		
Deposition Electrolyte for PEDOT film formed in PC with 0.010 M EDOT	Scan rates of deposition (mV/s)	R_Ω (ohms)	R_{ct} (ohms)	C (mF)
0.100 M $TBAPF_6$	5	4	62	7.0×10^{-4}
	50	5.4	80.4	4.3×10^{-4}
	100	4.9	75.1	5.7×10^{-4}
0.100 M $LiClO_4$	5	4.0	69.3	4.2×10^{-4}
	50	5.4	81.0	3.6×10^{-4}
	100	4.9	75.1	3.2×10^{-4}

2.S2 Supporting Information Figures

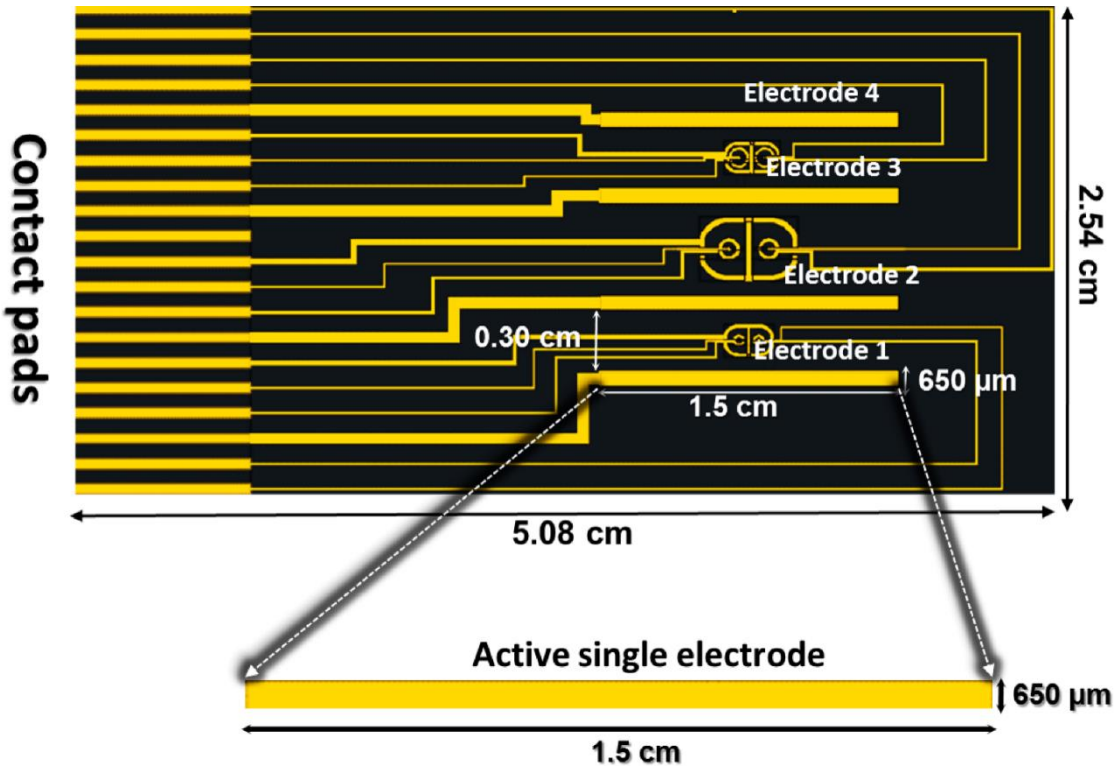

Figure S-1: The 1 in. × 2 in. (2.54 cm × 5.08 cm) microfabricated chip contains four band electrodes where each electrode measures nominally 1.5 cm in length, 650 µm in width and 250 nm in thickness. The outermost electrodes are spaced apart by 0.30 cm from their adjacent electrodes, and the distance between middle two electrodes is 0.46 cm. Contact pads on the chip electrically connect the electrodes to the potentiostat/galvanostat to individually address each electrode.

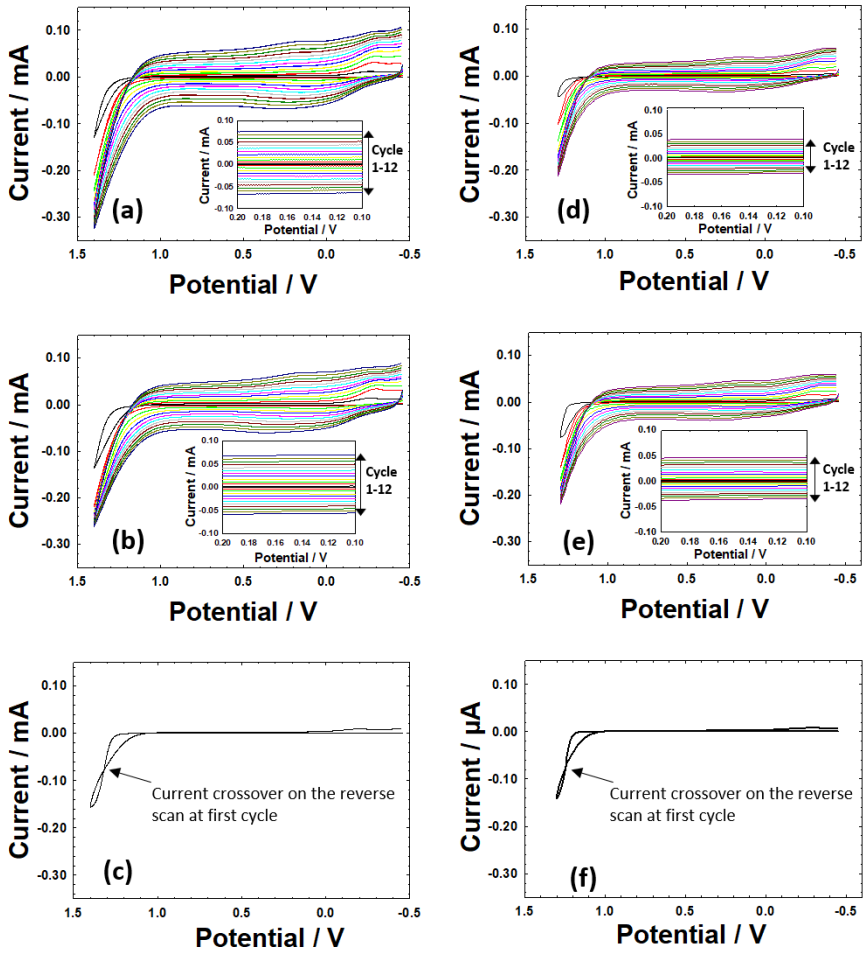

Figure S-2: CV responses during electropolymerization in propylene carbonate solutions containing 0.010 M EDOT in (a-c) 0.100 M $TBAPF_6$ in a potential window of -0.455 to 1.40 V and in (d-f) 0.100 M $LiClO_4$ in a potential window of -0.455 to 1.3 V. Twelve continuous cycles are shown for scan rates of (a and d) 100 mV/s and (b and e) 50 mV/s. The insets of (a), (b), (d), (e) show that charging current increases incrementally with each cycle. (c) and (f) show CV responses for the first cycle at 5 mV/s where current crossover on the reverse scan is evident. A three-electrode cell was used with a Ag/AgCl (saturated KCl) reference and Pt flag counter electrodes.

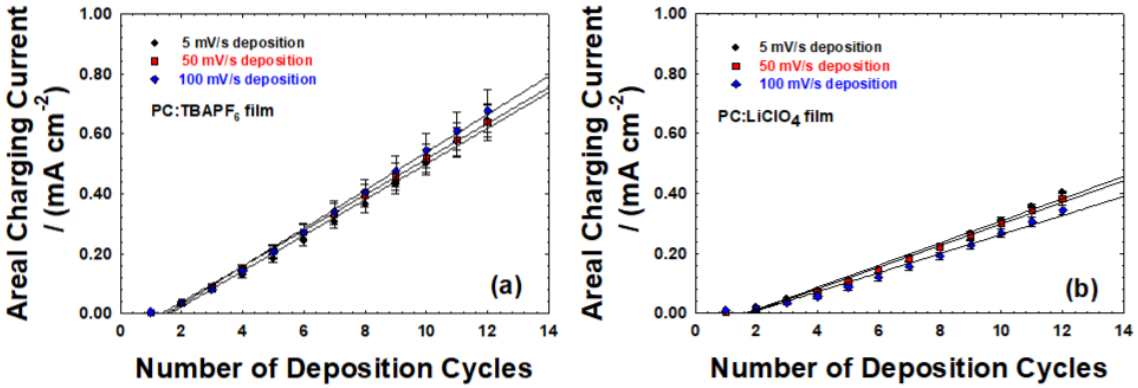

Figure S-3: Linear dependency of area normalized charging current with number of deposition cycles while films are being formed in solutions of EDOT in PC:$TBAPF_6$ and PC:$LiClO_4$. Least squares analysis of the data obtained at 5, 50 and 100 mV/s deposition scan rates yielded the following equations. For (a) in PC:$TBAPF_6$: y = 0.060 (±0.002)x -0.096 (±0.012), R^2= 0.9922, y = 0.060 (±0.001) x -0.080 (± 0.006), R^2= 0.9981, and y = 0.063 (±0.001) x -0.096 (± 0.01), R^2= 0.9952, respectively. For (b) in PC: $LiClO_4$: y = 0.037 (±0.001)x -0.061 (± 0.009), R^2= 0.9901; y = 0.036 (±0.001) x -0.062 (± 0.008) , R^2= 0.9901; and y = 0.032 (±0.001)x -0.055 (±0.01), R^2= 0.9829, respectively. The slopes have units of mA cm^{-2} / deposition cycle and the y-intercepts have units of mA cm^{-2}.

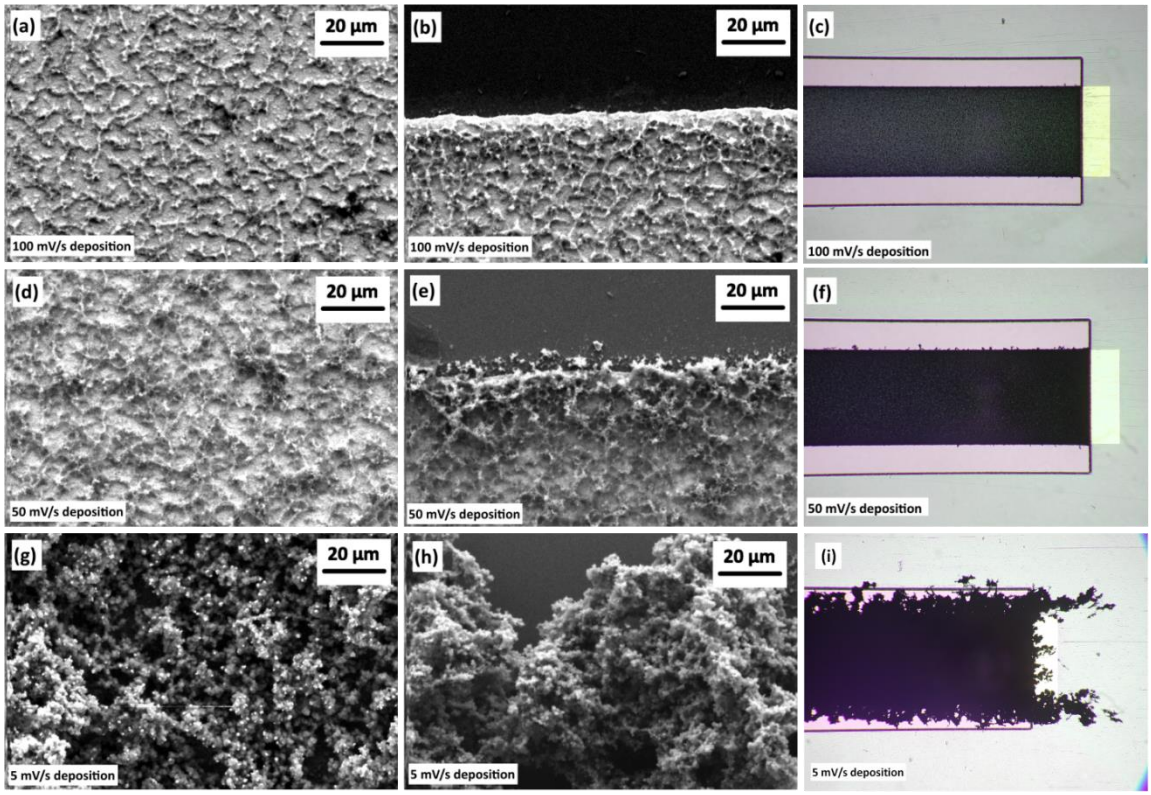

Figure S-4: Images of PEDOT films that were electrodeposited from a solution of EDOT in PC:TBAPF$_6$ for 12 cycles at 100 mV/s (a-c), 50 mV/s (d-f), and 5 mV/s (g-i) scan rates. The SEM images were obtained at the middle (left column, a, d, and g) and at the edge (center column, b, e, and h) of the electrodes. The optical microscopy images (right column, c, f, and i) were obtained at the end of the electrodes. In (i), the extended finger-like projections around the electrode are evident. All SEM images were acquired with 1000× magnification. The optical microscopy images were acquired with 5× magnification.

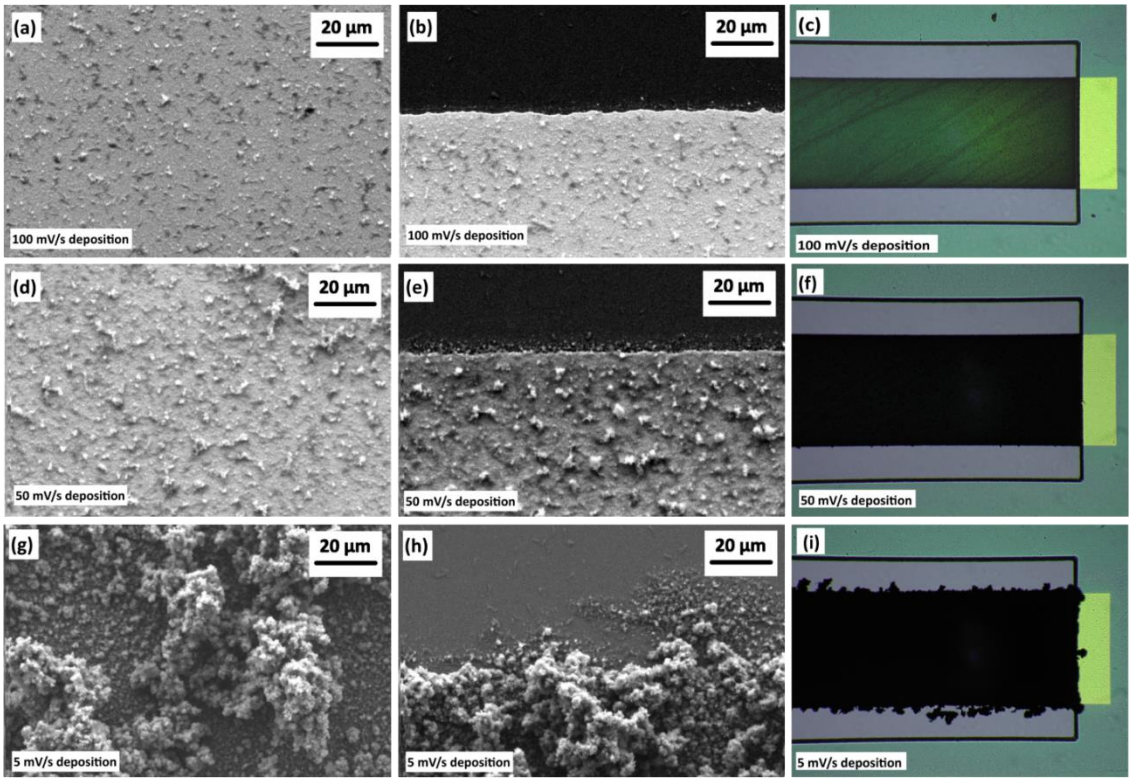

Figure S-5: Images of PEDOT films that were electrodeposited from a solution of EDOT in PC:$LiClO_4$ for 12 cycles at 100 mV/s (a-c), 50 mV/s (d-f), and 5 mV/s (g-i) scan rates. The SEM images were obtained at the middle (left column, a, d, and g) and at the edge (center column, b, e, and h) of the electrodes. The optical microscopy images (right column, c, f, and i) were obtained at the end of the electrodes. In (i) the extended finger-like projections around the electrode are evident. All SEM images were acquired with 1000× magnification. The optical microscopy images were acquired with 5× magnification

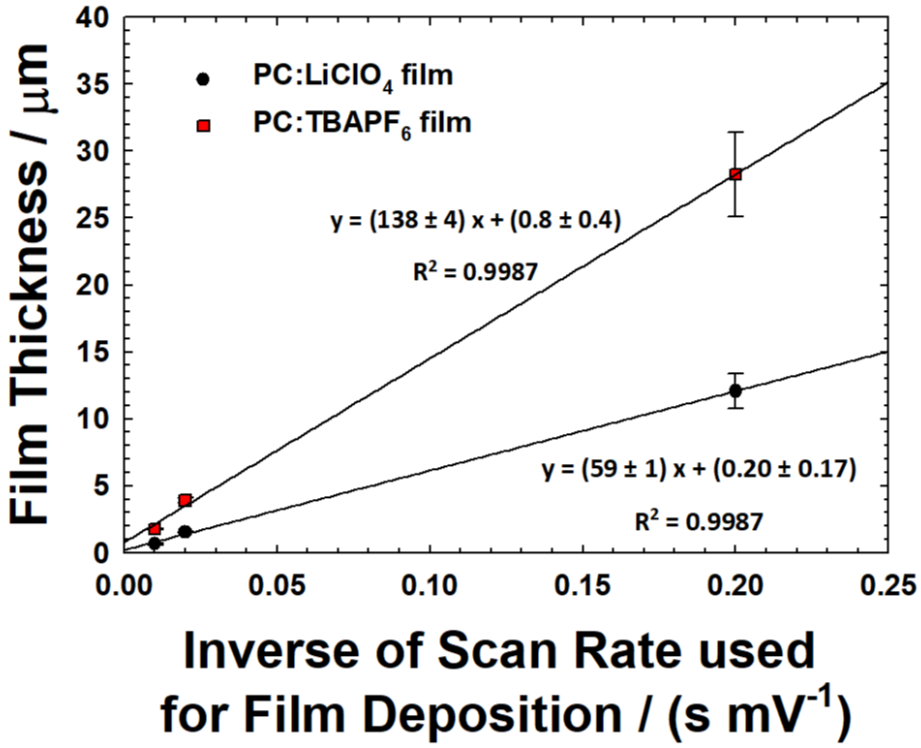

Figure S-6: Film thickness trends with the inverse of the scan rate by which PEDOT films were deposited from propylene carbonate solutions containing 0.01 M EDOT and either 0.100 $TBAPF_6$ or 0.100 M $LiClO_4$ electrolyte. PEDOT films were electropolymerized by CV at 100 mV/s, 50 mV/s, and 5 mV/s scan rates for 12 cycles using a three-electrode configuration with Ag/AgCl (saturated KCl) reference and Pt flag counter electrodes in 20 mLof solution. Electrodeposited films on the chip were dried in a desiccator for 72 h before measuring the thickness with a Dektak stylus profilometer. Three measurements were done on a PEDOT film (for each electrolyte and scan rate combination) at different regions across the length of the electrode. The thickness of the gold electrode is nominally 250 nm. Least squares analysis of the data obtained by PC:$TBAPF_6$ and PC:$LiClO_4$ films yielded y = 138 (± 4)x + 0.8 (± 0.4), R^2 = 0.9987 and y = 59 (± 1)x + 0.20 (± 0.17), R^2 = 0.9987 equations respectively. The slopes and y-intercepts have units of µm mV s^{-1} and µm, respectively.

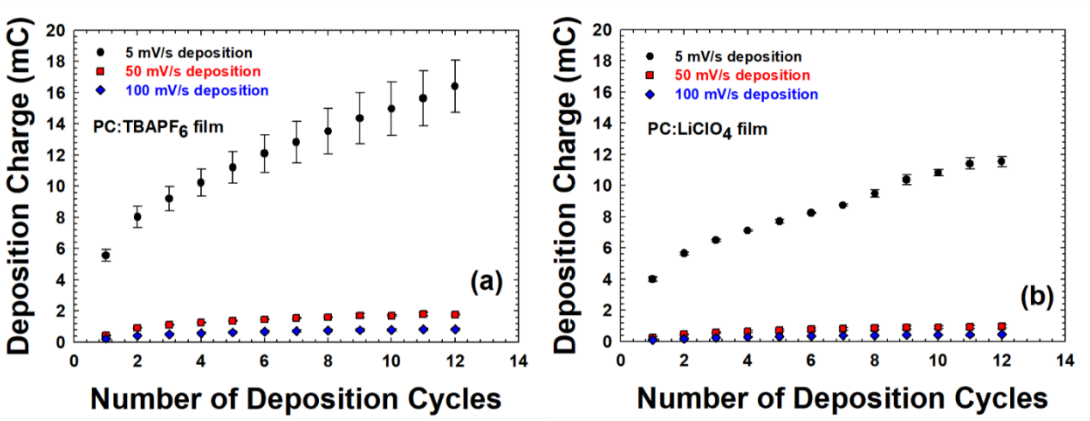

Figure S-7: Amount of charge in the polymer deposition region, obtained by integrating the CV response in PC:$TBAPF_6$ and PC:$LiClO_4$ as a function of deposition cycle. Electrodepositions were performed in a three-electrode setup with Ag/AgCl (saturated KCl) reference and Pt flag counter electrodes in 20 ml monomer solution. The monomer solution contained 0.01 M EDOT and either (a) 0.10 M $TBAPF_6$ or (b) 0.10 M $LiClO_4$ in propylene carbonate. The potential windows for electrodeposition in the PC:$TBAPF_6$ and PC:$LiClO_4$ systems were -0.455 to 1.40 V and 0.455 to 1.30 V, respectively. The deposition charge for each cycle was calculated by integrating currents under the oxidation peak, generally over the 0.8 to 1.4 V for PC:$TBAPF_6$ and 0.7 to 1.3 V for PC:$LiClO_4$ systems. Error bars represent ± one standard deviation for measurements made from three (N=3) electrodes with PEDOT films deposited from each solvent / electrolyte system and scan rate.

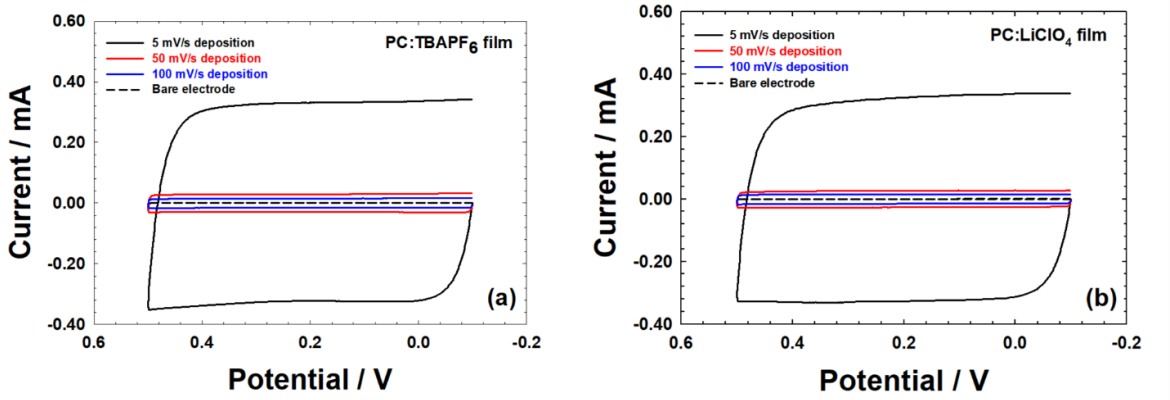

Figure S-8: CV characterization at 50 mV/s in 0.100 M NaCl aqueous solution of bare and PEDOT modified electrodes. PEDOT films were deposited for 12 cycles at 5, 50, and 100 mV/s from (a) PC:$TBAPF_6$ and from (b) PC:$LiClO_4$. A three-electrode system was used with Ag/AgCl (saturated KCl) reference and a Pt flag counter electrode in 20 mL of 0.10 M NaCl of solution in a 20 mL glass beaker. Each electrode underwent five continuous CV cycles. The CV responses shown here are the 5^{th} cycle among the five consecutive CV responses. Charging current was measured at +0.25 V for all five of the CV responses and averaged. The charging current for the bare electrode is 0.23 ± 0.001 µA. The charging currents at +0.25 V for PEDOT films deposited from PC:$TBAPF_6$ are 325.00 ± 2.45, 28.72 ± 0.18, and 15.80 ± 1.13 µA and for those deposited from PC:$LiClO_4$ are 325.43 ± 2.16, 26.86 ± 0.45, and 15.46 ± 0.16 µA for films deposited at 5, 50, and 100 mV/s, respectively. . Charging current for PEDOT films are nearly 1400, 125, and 70 times those at the bare electrode, respectively.

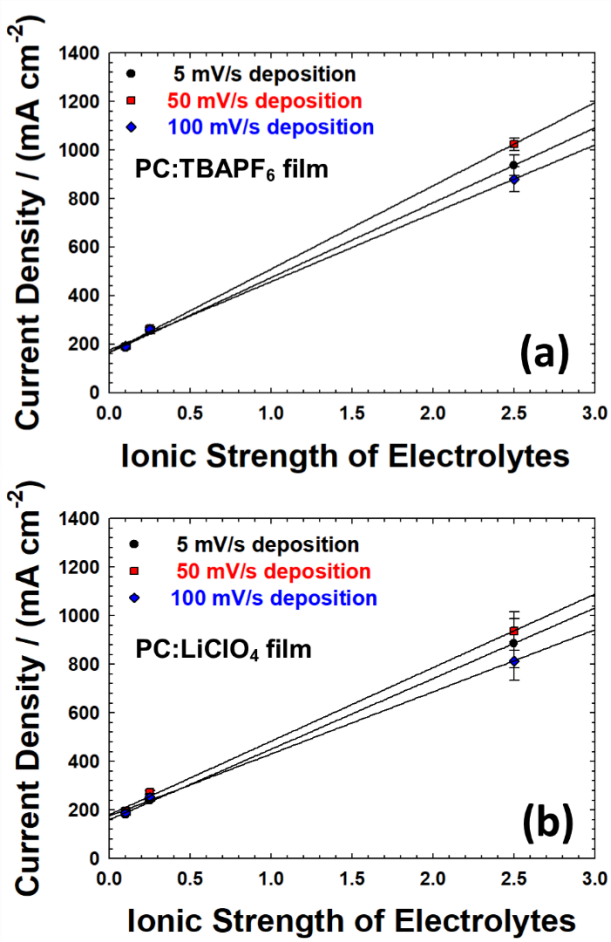

Figure S-9: Maximum current densities of PEDOT films with different thicknesses (designated as 1/scan rate) as a function of different ionic strengths of aqueous electrolyte, where: 0.100 M NaCl (μ = 0.10 M) < 0.01 M PBS (μ = 0.25 M) < 0.1 M PBS (μ = 2.5 M). The least squares fit and corresponding R^2 values of maximum current density as a function of ionic strength for films formed in PC:$TBAPF_6$ at 5, 50, and 100 mV/s are: y = (308.70 ± 7.80 mA cm^{-2} mol^{-1} L) x + (165.54 ± 11.30 mA cm^{-2}) , R^2 = 0.9994; y = (343.20 ± 8.35 mA cm^{-2} mol^{-1} L) x + (166.43 ± 12.12 mA cm^{-2}) , R^2 = 0.9994; and y = (281.61 ± 10.34 mA cm^{-2} mol^{-1} L) x + (176.27 ± 15.01 mA cm^{-2}) , R^2 = 0.9987. Those for films formed in PC:$LiClO_4$ are: y = (290.55 ± 5.18 mA cm^{-2} mol^{-1} L) x + (160.08 ± 7.53 mA cm^{-2}) , R^2 = 0.9997; y = (302.86 ± 11.50 mA cm^{-2} mol^{-1} L) x + (180.65 ± 16.70 mA cm^{-2}) , R^2 = 0.9986; and y = (255.61 ± 9.93 mA cm^{-2} mol^{-1} L) x + (175.54 ± 14.41 mA cm^{-2}) , R^2 = 0.9985.

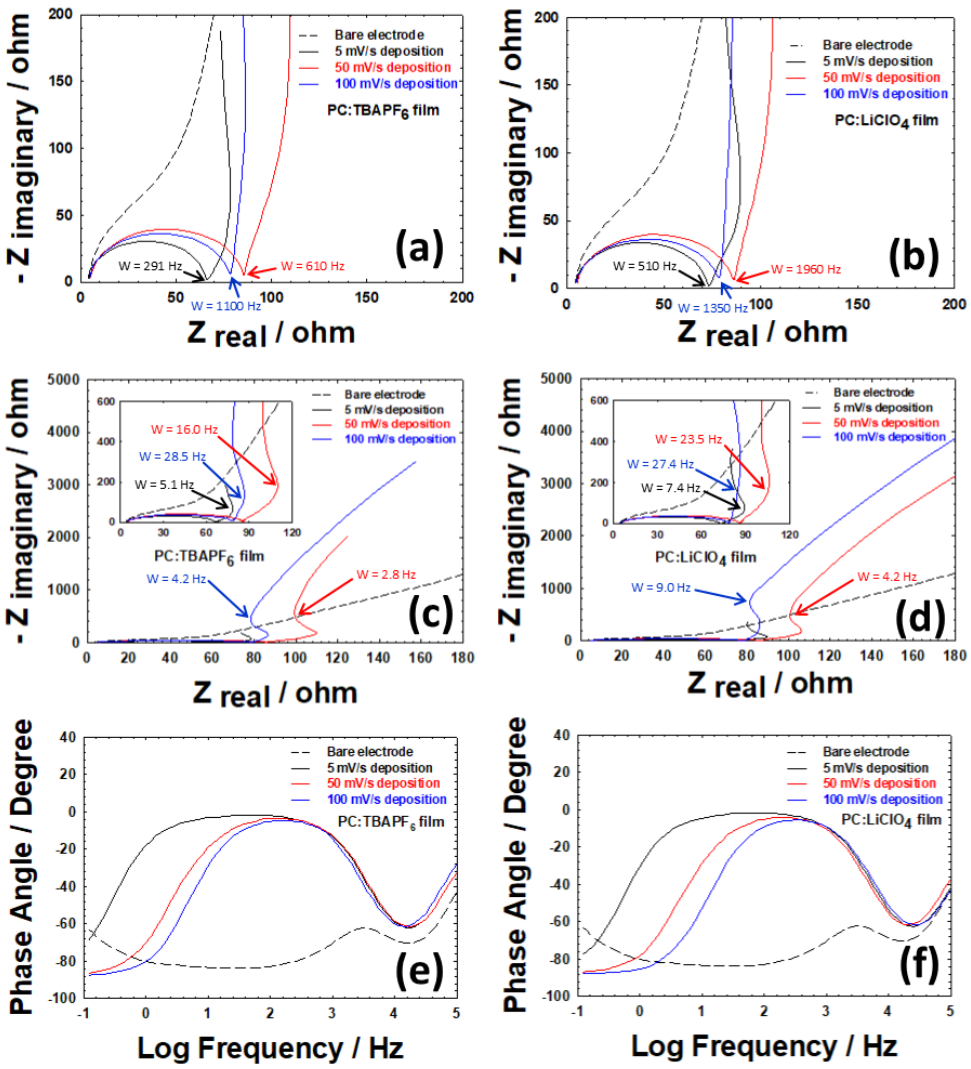

Figure S-10: Characterization of PEDOT-modified electrodes in 0.100 M NaCl by EIS, using a three-electrode setup with an Ag/AgCl (saturated KCl) reference electrode. Nyquist (a-d) and Bode phase (e) and (f) plots are shown for electrodes modified with films deposited at 5, 50, and 100 mV/s from PC:$TBAPF_6$ ((a), (c), and (e)) and from PC:$LiClO_4$ ((b), (d), (f)). The three Nyquist plots for each deposition condition are for different frequency ranges, each starting from the high end of 10^5 Hz. The Bode plots are for the entire frequency range. The chip was placed vertically in a 20 mL solution of 0.10 M NaCl containing Ag/AgCl (saturated KCl) reference and Pt flag counter electrodes. EIS parameters: DC potential of 0 V, AC amplitude of 0.015 V, and frequency range of 0.1-10^5 Hz. The frequency at the maximum of the Nyquist semicircles are (a) 3700, 4600, 3700 Hz and in (b) 5500, 5500, and 6600 Hz for PEDOT films deposited at 5, 50, and 100 mV/s, respectively.

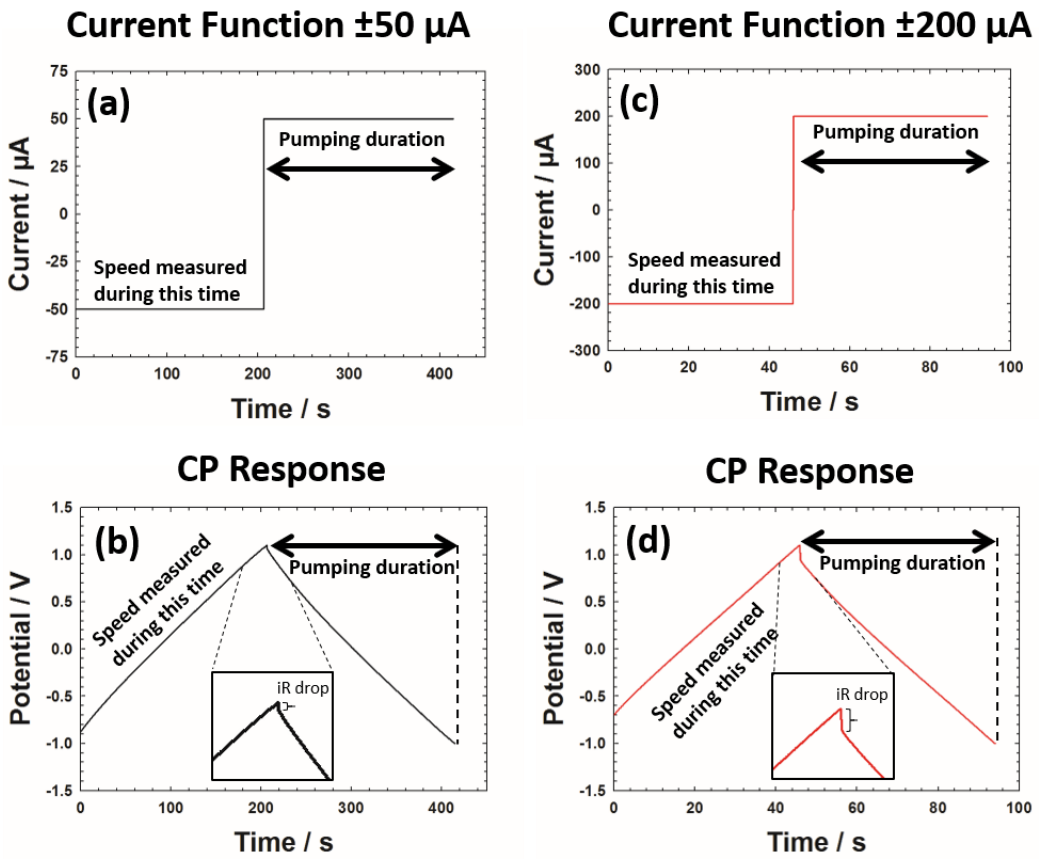

Figure S-11: Examples of chronopotentiometry current functions for steps of (a) ±50 µA and (c) ±200 µA and the corresponding responses (b) and (d), respectively, involved in characterizing R-MHD fluid flow in the microfluidics device containing the 450 µL of "buffer/glycerol/bead solution". Two adjacent PEDOT-modified electrodes were activated with the galvanostat, where one served as the "working" electrode and the other as the combined "quasi reference/counter" electrode. Fluid speeds were obtained during the first half of the current function and pumping duration was determined during the second half. Cutoff voltages of +1.100 V and -1.000 V were used to avoid overoxidation and the undoped form of the PEDOT, and they defined the voltage range for the duration studies.

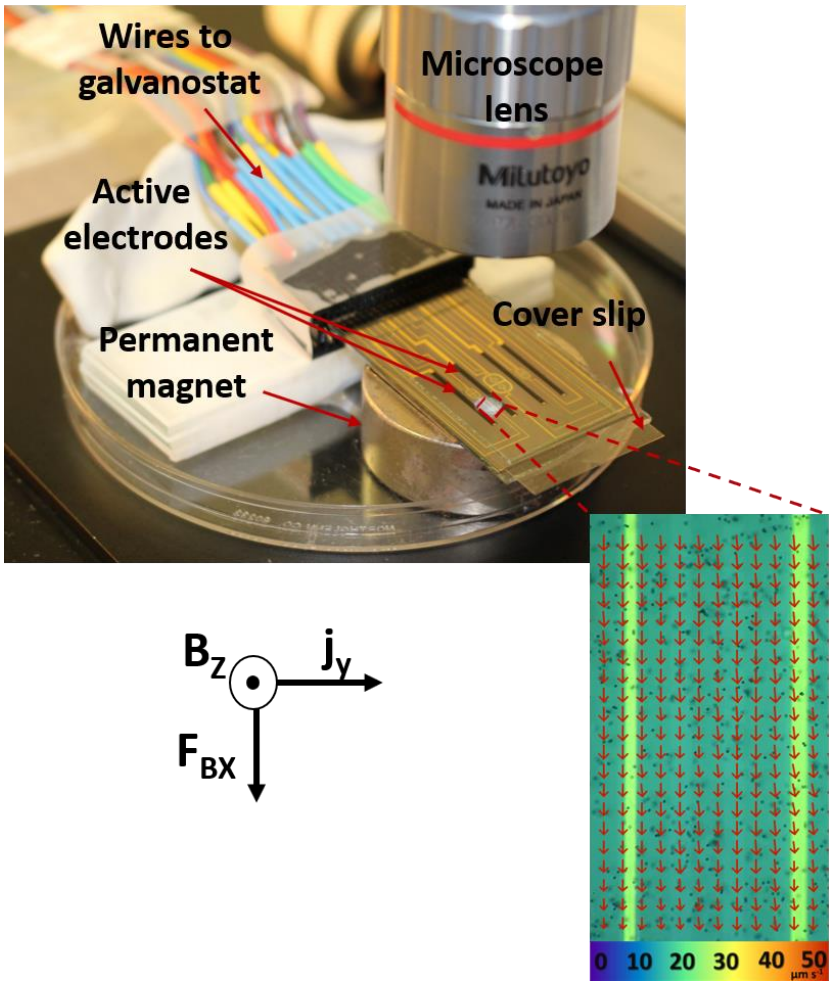

Figure S-12: Photograph of the complete MHD setup on the microscope stage, consisting a glass cover slip that is placed on top of the PDMS gasket to contain the pumping solution. The inset shows velocity vectors (red arrows) produced from particle image velocimetry (PIV) analysis of microbead movement during the MHD experiment. These fluidic velocity data were obtained between activated PEDOT-modified electrodes in the area outlined by the dashed red rectangle on the photograph of the chip, at a height of 320 µm above the chip surface, and with 50 µA applied current in 450 µL of "buffer/glycerol/bead solution" . The highly parallel and uniform fluid flow as indicated by the vectors supports the existence of a horizontal flat flow profile between the active electrodes. The PEDOT films in this example had been deposited from PC:$TBAPF_6$ at 5 mV/s for 12 cycles. (The yellow lines in the expanded view are insulated gold leads to other features of the chip and do not play a role in MHD pumping.)

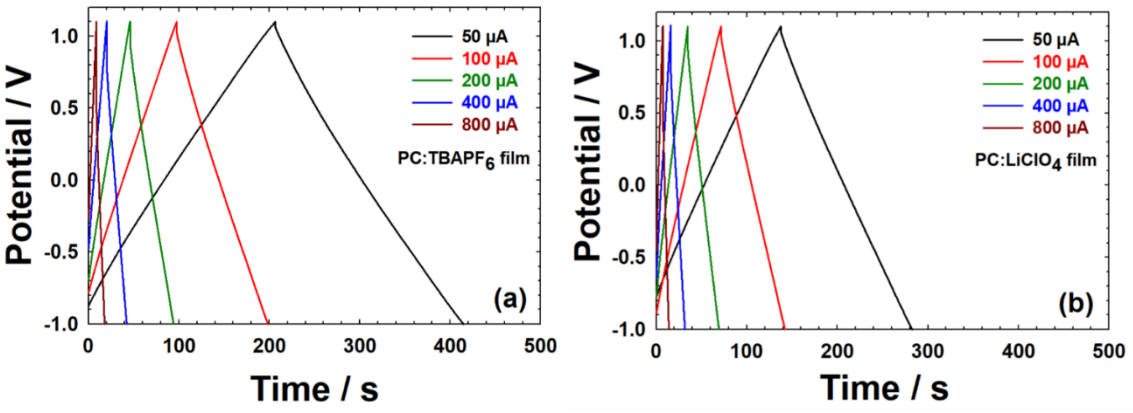

Figure S-13: Chronopotentiometry (CP) responses in the "buffer/glycerol/bead solution" during MHD experiments of PEDOT films that had been deposited from (a) PC:$TBAPF_6$ and (b) PC:$LiClO_4$. A galvanostat applied ± 50, ± 100, ± 200, ± 400, and ± 800 µA current with -1.000 to 1.100 V potential cut-offs. During the anodic process, the potential changes from -1.000 to +1.100 V with time and fluid flows in one direction by following $F_B = j \times B$. During the cathodic excursion (1.100 to -1.000 V), the fluid flows in the opposite direction. The anodic-cathodic duration decreases with increasing applied current, and therefore, so does the MHD flow duration.

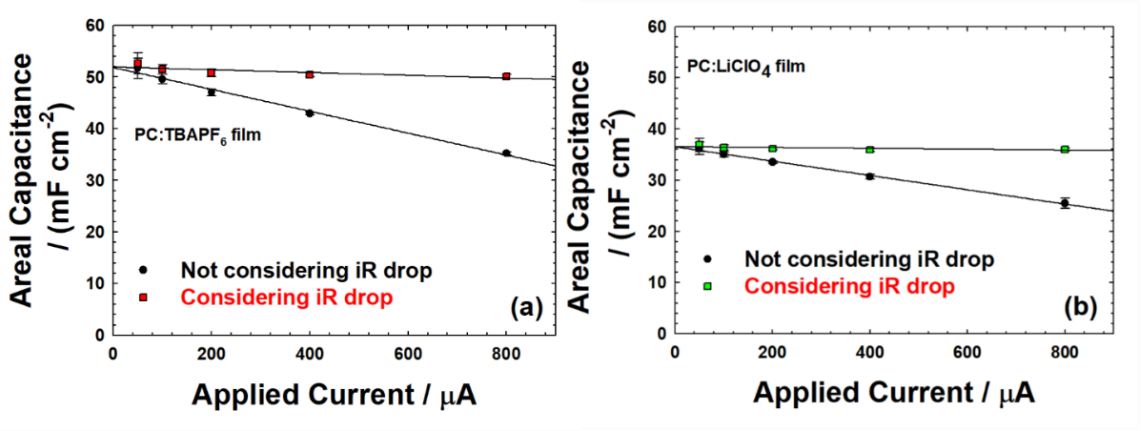

Figure S-14: The total areal capacitance (C_T/nominal electrode geometry) dependency on the applied current during MHD experiments in the "buffer/glycerol/bead solution" with and without accounting for the iR drop for PEDOT films that had been deposited from (a) PC:$TBAPF_6$ and from (b) PC:$LiClO_4$ at 5 mV/s. A least squares fit shows a linear decrease in capacitance with increasing applied current (not considering iR drop) with equations of $|C_{uncorrected}| = -0.020\ (\pm 0.001)\ |i_2| + 52.0\ (\pm 0.5)$, $R^2 = 0.991$ and $|C_{uncorrected}| = -0.0140\ (\pm 0.0005)\ x + 36.5\ (\pm 0.2)$, $R^2 = 0.996$. When the iR drop is accounted for, the areal capacitance is constant with applied current and within error of the measurements. The slopes and y-intercepts have units of mC $cm^{-2}\mu A^{-1}$and mC cm^{-2}, respectively. Two adjacent PEDOT-modified electrodes were used. One served as the "working" and the other as the combined "quasi reference/counter" electrode. Cutoff voltages of +1.100 V and -1.000 V were used to avoid overoxidation of the PEDOT film.

3. Electrochemical Performance of PEDOT and PproDOT Conducting Polymers, Electrodeposited Using Different Routes and Solvents, and the Resulting Impact on Applications in R-MHD Microfluidics

3.1 Introduction

Magnetohydrodynamics (MHD) is a valve-less, channel less pumping approach, which makes use of magnetic field (B) and ionic current density (j) of the fluid element to create a body force (F_B) on it. [1-3] This unique pumping approach takes advantage of the magnetic portion of the Lorentz force, F_B (N/m^3). The ionic current density, j ($c/ (s\ m^2)$) in the fluid element converts from electronic current and the magnetic flux, B (T) interacts with j, to create a body force (F_B).[4] MHD pumping has proved its applicability in different microfluidic applications due to allowing downsizing capability, flat flow profiles, three-dimensional fluid flow tunability, bi-directional and rotational flow, aqueous and non-aqueous solution compatibility, low voltages, no moving parts, and larger pumping chamber height. [4-10] Easily oxidizable and reducible chemical species added in the fluid element coined the word "redox-MHD" (R-MHD) which prevents the bubble generation from water electrolysis and electrode corrosion due to operating electrochemistry at less extreme voltage. [4-5] Later, the advancement in "redox-MHD" came with introducing the electropolymerizable poly (3,4 ethylenedioxythiophene) (PEDOT), a conducting polymer (CP), as an alternative to solution redox species. This electrode confined conducting polymer has solved the interference concerns with the analytes for detection applications, achieved a wider sustainable voltage range, and higher currents. [11] Conducting polymers, PEDOT is a promising material in different applications, such as biotechnology, electrochromic device, electronics, and nanotechnology. [12-15] This versatile application is due to having a high conductivity, charge storage capability, fast doping - dedoping process, biocompatibility, and thermal and electrical

stability. [16-18] Charge storage capabilities and fast doping-dedoping process of CP made it as a perfect candidate for R-MHD applications. Higher ionic current density due to faster doping-dedoping of counter ions from the electrolyte solution and higher charge density from polymer film defines the maximum achievable fluid speed and flow duration in R-MHD pumping. Electrochemical deposition (by controlling potential or current) of CP offers film uniformity, controlled film thickness, dopant insertions and good spatial resolution. [19-21] The deposition parameters, such as monomer type, concentration, purity, solvent, background electrolyte, deposition techniques and parameters, presence of the extra components, such as electron donor / acceptor, electrode material, temperature, and hydrodynamic conditions play important roles in film properties. [20-22] The morphological property dependency with deposition parameter affects the ionic migration through the films, therefore achievable current and charge density. So, there was enough rational behind the study for optimizing deposition parameters to achieve maximum fluidic speed and pumping duration. A prior work has studied the performance of organic solvent (propylene carbonate) for PEDOT deposition and varied ionic strengths of pumping electrolyte to maximize current and charge responses in R-MHD.[23]

The present work can be divided into two steps. 1) Deposition technique optimization, where PEDOT electropolymerized by cyclic voltammetry (CV), chronoamperometry (CA), and chronopotentiometry (CP) on gold electrodes in propylene carbonate (PC) solvent and tetrabutyl ammonium hexafluoro phosphate ($TBAPF_6$) electrolyte. In 2) Solvent and monomer optimization, by using improved deposition approach from step 1, PEDOT and 3,4 propylenedioxythiophene (PProDOT) electrodeposited in two different organic solvents (PC and acetonitrile (MeCN)). The performance (total charge and current response) of polymer films electrodeposited in different solvents, monomer, and deposition methods was evaluated by CV,

CA, and impedance spectroscopy techniques. Scanning electron microscopy (SEM) was performed to study morphological properties of different films. Though, different deposition techniques resulted with a similar charge and current response from the polymer film, PC and EDOT proved to be the better combination for improved electroactivity, film robustness, and stability.

3.2 Experimental Section

3.2.1 Chemicals and Materials

Propylene carbonate (anhydrous 99.7%), acetonitrile (anhydrous 99.8%), 3, 4-ethylenedioxythiophene (EDOT), 3, 4-propylenedioxythiophene (ProDOT), and tetrabutylammonium hexafluorophosphate ($TBAPF_6$) were purchased from Sigma-Aldrich (St. Louis, MO). Lithium perchlorate (ACS grade 95%) and Polystyrene latex microspheres, 10 μm diameter (2.5 wt % dispersion in water) were acquired from Alfa Aeser (Ward Hill, MA). Potassium chloride and pre-cleaned micro cover glass (24 × 50 mm) were purchased from VWR International, LLC (West Chester, PA). Glycerol (proteomics grade, ≥ 99.00%) was purchased from AMRESCO LLC (Solon, OH). The 0.37 T nickel coated NdFeB (3.5 cm diameter and 1.27 cm height, grade N40) permanent magnet was bought from Amazing Magnets, Irvine, CA. Edge connectors (solder contact, 20/40 position, and 0.05 in. pitch) were acquired from Sullins Electronics Corp. (San Marcos, CA). Sylgard184 silicon elastomer base, Sylgard 184 silicon elastomer curing agent and OS-30 solvent were purchased from Ellsworth Adhesives, Milwaukee, WI. Silicon wafers (2 μm of thermally grown SiO_2, 125 mm diameter, and 600-650 μm thickness) were purchased from Silicon Quest International (Santa Clara, CA).

3.2.2 Microelectrode Preparation

The design and fabrication procedure for microelectrode preparation was reported previously.[7] The patterned 5 in. wafer was cut into 1 × 2 in. (25.4 × 50.8 mm) chips, where each of them has four gold band electrodes (1.5 cm × 650 µm × 250 nm). The outermost electrodes and inner two electrodes have 0.32 cm and 0.47 cm gaps. Optical microscopy was used to measure electrode dimensions. Figure S-1 (a) and (b) show optical images of the fabricated chips, where four long band electrodes were used for electrodeposition, characterization, and MHD experiments. All four individually addressable electrodes were connected electronically through contact pads. Figure S-1 (a) shows chips with a bare electrode and (b) shows PEDOT coated electrodes.

3.2.3 Modification of Electrodes with PEDOT Conducting Polymers by Using Different Deposition Methods

Any organics from gold electrode surfaces were removed with an oxygen plasma (Harrick Plasma Cleaner PDC -32G, Ithaka, NY) for 20 min at 60 mTorr pressure and 6.8W power applied to RF coil. Each chip has four individually addressable parallel co-planner gold electrodes (650 µm × 1.5 cm × 250 nm).

0.01 M 3,4 ethylenedioxy thiophene (EDOT) monomer were well mixed with 0.10 M $TBAPF_6$ electrolyte in 20 ml propylene carbonate solution. Electrodepositions were performed in a 3-electrode cell set-up, where Ag/AgCl (saturated KCl) and platinum foil used as a reference and counter electrode. Three electrodeposition techniques were used to coat the electrode surface with PEDOT film; a) cyclic voltammetry (CV) b) chronopotentiometry (CP) and c) chronoamperometry (CA). Figure S-2 (a), (b), and (c) illustrates electrochemical responses

during PEDOT deposition. In CV method, the potential was cycled for 12 times from -0.455 to 1.4 V, at 50 mV/s scan rate for the total of 16.80 ± 0.7 mC charge. An anodic current of 50 µA applied for 336 sec in CP method to accumulate a total charge of 16.50 ± 0.01 mC. In CA method, the potential was held at 1.4 V for 146 sec to deposit 16.72 ± 0.09 mC charge. For every deposition technique, three electrodes out of four in a chip were electro-deposited individually. After deposition, chips were rinsed with propylene carbonate solution and then followed by DI water to remove excess and unattached electrolytes. Chips were then kept in DI water filled 50-ml centrifuge tubes for further characterization. Figure S-2 (d), (e), and (f) show optical microscope images of film deposited by CV, CP, and CA methods, respectively.

3.2.4 Electrodeposition of Different Monomers in Different Organic Solvents

EDOT and ProDOT (3,4-propylenedioxythiophene), both monomers were electropolymerized by CA method from acetonitrile (MeCN) and propylene carbonate (PC) solvents with $TBAPF_6$ electrolyte. 0.01 M EDOT and ProDOT were dissolved with 0.10 M $TBAPF_6$ electrolyte into 20 ml of propylene carbonate and acetonitrile solvents. These monomer solutions were used in a 3-electrode deposition set-up, where Ag/AgCl (saturated KCl) and platinum foil used as a reference and counter electrode, respectively. PEDOT/ PC, PEDOT / MeCN, PProDOT/PC, and PProDOT/MeCN films were deposited for 16.72 ± 0.09, 16.26 ± 1.13, 17.23 ± 0.65, and 16.64 ± 1.15 mC charge, respectively by holding the potential at 1.4 V. Though the potential was same, the time required for a similar charge deposition were varied. Figure S-3 (a), (b), (c), and (d) show the electrochemical responses during deposition and corresponding optical images of PEDOT/ PC, PEDOT / MeCN, PProDOT/PC, and PProDOT/MeCN films, that electro-deposited for 145.75 ± 0.50, 33.75 ± 0.90, 360, 76.25 ± 6.5

sec, respectively. Solvent rinsed polymer coated chips were kept in DI water for further characterizations.

3.2.5 Electrochemical Techniques for Electrode Characterization

A potentiostat (760B, CH Instruments, Austin, TX) was used to characterize electrodes before and after electropolymerization. Cyclic voltammetry (CV), chronoamperometry (CA), chronopotentiometry (CP), and impedance spectroscopy (EIS) were performed for electrode characterization in the electrolyte solution. Bare electrode characterization was performed both in 0.10 M NaCl and 0.10 M $K_3Fe(CN)_6$ in 0.10 M KCl solutions, with a 3-electrode cell setup and Figure S-4 shows of these overlaid electrochemical responses. After polymerization with different organic solvents and monomers at 3 deposition techniques, polymer films were characterized by CV, CA, CP, and EIS. In post- polymerization CV, films were cycled at the same potential range as bare electrode (0 to 0.5 V) in 0.10 M NaCl (Figure S-5). Maximum current (at peak oxidation potential) and the greatest charge were achieved by CA characterization in 0.10 M NaCl and 0.010 M phosphate buffer saline (PBS) solution. The potential was held at -0.800 V for a quiet time of 20 s before the step and then held at +0.800 V for 20 s after the step. Figure S-6 shows, a representative CA and integrated CA (CC) at -0.800 to +0.800 voltage window with 20 sec time scale. CP (applied current) experiments on films deposited from different deposition methods, were performed for 500 cycles at -0.5 to 0.7 V potential window. These were performed to calculate the percent capacitance loss after 500 cycles (Figure 4). Electrochemical impedance spectroscopy (EIS) experiments were performed on films deposited from different techniques, monomer, and solvents in 0.10 M NaCl solution in a three-electrode setup. A platinum flag was the counter and Ag/AgCl (in sat'd KCl) was the

reference electrode. The frequency range for EIS was 0.10–10^5 Hz, at zero (0) initial voltage, and 15 mV amplitude.

3.2.6 Experimental Setup for R-MHD Studies and Video Microscopy

Figure 3 illustrates the experimental R-MHD setup for pumping. The chip was first connected with an edge connector. A PDMS gasket of 781.0 ± 7.3 µm thickness was settled over the chip by exposing pumping electrodes with a 3.5 × 2 cm rectangular opening. Then, 500 µl solution, consisting 60:40 mixture of 0.01 M PBS and glycerol (50% v/v) was pipetted into the chamber surrounded by the PDMS gasket. 25 µl polystyrene bead (10 µm) solution was added to the PBS: glycerol mixture to track beads in the flowing solution. Glycerol helped to keep buoyancy of beads in the solution. A glass coverslip placed on top of the gasket to limit the vertical fluid movement and make a sealed chamber. The whole chip-gasket-edge connector assembly was placed over a permanent magnet (0.37 T NdFeB) and set under the microscope. Precautions were taken to avoid any gas bubble formation inside the solution chamber. R-MHD experiments were performed in a "two-electrode" setup where one polymer modified electrode acted as working and other as counter / reference electrode. ±50 µA to ±800 µA currents were applied to generate fluid flow in between the active electrodes with a voltage range of -0.10 to 1.1 V. Figure S-7 shows CP responses of different applied currents during an R-MHD experiment. Right after an anodic bias, a cathodic bias of same magnitude of current applied to reduce (recharge) the oxidized film (discharge). The fluid flow movement was recorded by interfacing a Sony Handycam camera with the microscope. The horizontal and vertical position of the recording window was selected by adjusting the "y" translation of the microscope stage. The chip position relative to the microscope lens in "z" direction was adjusted to determine the

focused beads position in the chamber. The videos were recorded at 320 µm above the chip surface for this work. For each ± applied current, three videos were generated with two focused beads for each video and analyzed with Tracker® (V 4.87 www. opensourcephysics.com) software. This individual bead tracking helped to determine fluid speed with better time resolution than standard PIV system.

3.3 Results and Discussion

3.3.1 Comparison of PEDOT Films Deposited from Different Electrodeposition Methods

PEDOT from PC and $TBAPF_6$ was electro-deposited by CV, CP, and CA methods for 16.80 ± 0.70, 16.72 ± 0.09, and 16.85 ± 0.01 mC charge respectively (statistically insignificant at 95% confidence interval). The time required for PEDOT deposition by CV, CP, and CA methods are 890, 336 and 146 sec, respectively. So, CA method deposits film 6X faster than CV and 2.3X faster than CP method, for a similar charge. Characterization of these films by an applied potential (CA) method was implemented in 0.10 M NaCl and 0.01 M PBS electrolyte solution for maximum current and charge density (Table 1 in the supporting information). CA was performed each electrode by holding the potential at -0.80 V for 20 sec (quiet time) and then run for another 20 sec at +0.80 V. Holding the potential at -0.80 V was to regenerate the film before applying any oxidizing voltage. Maximum current was achieved from the beginning of the experiment (at 0.100 sec) and then the current response was integrated to determine the total achievable charge. The area normalized current and charge (coulomb) provides maximum current and charge density. The usual CA response in the electrolyte solution from polymer coated film can be divided into three regions a) double layer charging region b) semi-infinite diffusion region and c) exhausted finite diffusion region. [24] The maximum current densities

obtained across CV, CP and CA deposited films in both 0.10 M NaCl and 0.01 M PBS electrolyte were statistically same (in 95% CI), but in 0.010 M PBS, films show nearly 33% higher current density than 0.10 M NaCl. This is due to having 2.5 X ionic strength than 0.10 M NaCl. The 33% increase in the maximum current density is primarily due to an increase in the double layer charging current (Figure S-8) in higher ionic strength electrolyte. Figure S-8 shows comparative CA responses up to 4.0 sec time scale in both electrolyte solutions for PEDOT film deposited by CV method. Both the CA responses reaches the exhausted finite diffusion region around the same time (0.50 sec). Charge densities of PEDOT films across different deposition methods are statistically same (95 % CI) in 0.10 M NaCl, but slightly different in 0.01 M PBS solution (CP > CA > CV). Charge density increases across electrolytes about 12% for CV deposited PEDOT, and around 17 % for CP and CA deposited PEDOT film, due to increased ionic strength of 0.01 M PBS. Figure S-2 (a), (b), (c) and (d), (e), (f) show electrochemical responses and optical images of PEDOT electrodeposition by CV, CP, and CA techniques, respectively. In CV deposition, current was increased around at 1.2 V due to monomer oxidation and formed PEDOT on the electrode surface. Successive 12 CV cycles formed PEDOT in layer by layer, by depositing a single layer in each cycle. While, CV electrodeposition provides discontinuous oxidation of monomer, CA and CP deposition generates polymer in a continuous fashion. [25] In CA deposition, the initial spike in the current is due to double layer charging, and then a mass transport limited slow increase in current for the next 10 sec corresponds to the formation of PEDOT nuclei, followed by a polymer growth region where current do not change with time.[26] During CP deposition, potential of the electrode was measured at a constant current. The PEDOT film was deposited at about 1.26 V with 50 µA anodic current. Figure-1 shows SEM micrograph of PEDOT films deposited by three deposition technique from PC solvent and

$TBAPF_6$ electrolyte. (a)–(c) shows the morphology of films at the middle of the electrode and (e)–(f) depicts the edges. In both the middle and edge of the electrode ((c) and (d)), CP deposited film shows globular, short–polymer chain morphology, unlike CV and CA deposited films. This globular shape morphology has already observed before with similar lower applied current density (0.50 mA cm^{-2}) deposition approach.[25] Both CV and CA generates films with longer interconnected polymer chain (Fig 1 (a), (b) and (e), (f)). Between CV and CA, CV generates polymer film with disordered structure. The reason might be the continuous change between the insulating and conductive state, which accompanies with solvent and electrolyte exchange and provokes the disorderly change in the polymer matrix. An interesting finding was the nature of polymer spreading around the edge of the gold electrode. We achieved largest polymer spreading from electrode edge by CA deposition and least for CP deposition. The spreading for CA, CV and CP films (Figure-1 (f), (b) and (d)) are ranged from 22 to 40 μm, 6-27 μm, and 1-9 μm, respectively. Thicknesses for CV, CP, and CA deposited films (performed by stylus profilometer) were 3.90 ± 0.18, 4.67 ± 0.57, and 4.54 ± 0.35 μm, respectively. Across these films, thickness differences were insignificant at 95% CI. The larger polymer spreading is especially disadvantageous for chips with closely spaced electrodes because the conductive PEDOT spreading will short adjacent electrodes (if the electrodes gap ≤ 40 μm for this case). So, having individually addressable electrodes would not be possible. Also, PEDOT deposition for a longer time (more deposition charge) will produce even larger polymer spreading. So, for a small microfabricated device where electrodes are closely spaced, CP deposition would be a better choice than CA.

3.3.2 Comparison of PEDOT and PProDOT Films Formed in Different Solvents

In this section, the electrochemical performance of two different monomers (EDOT and ProDOT) deposited from two solvents, PC and acetonitrile (MeCN) will be discussed. PC is more polar than the MeCN (6.1 relative polarity compared to 5.8) and used widely for polymer electrodeposition. The gaps between outermost and middle two electrodes (Figure S-1) on the chip were 0.32 and 0.47 cm, respectively. So, electrode gaps were well beyond for the CA deposited PEDOT spreading region, that discussed in the previous section. Owing to have shorter deposition time and nearly same electrochemical response compared to others, CA was selected as the deposition approach for this part of the study. The deposition charge difference for all four films were statistically insignificant (95% CI).

3.3.3 PC Solvent

Table-2 in supporting information provides the maximum current and charge densities in both 0.10 M NaCl and 0.01 M PBS electrolyte solution. PEDOT generates around 67% and 50% higher current densities in 0.10 M NaCl and 0.010 M PBS, respectively than PProDOT. Although, they have similar charge densities in both characterizing solutions. Figure -2 (a) and (c) show SEM micrograph of PEDOT and PProDOT films deposited from PC solvent. PProDOT shows smoother with globular morphology while PEDOT has rough interconnected structure. In another study, PProDOT film proved as more hydrophobic than PEDOT (3× higher contact angle on ITO substrate) but with reduced roughness.[27] Besides, PProDOT shows little or no electrode edge polymer spreading compared to CA deposited PEDOT film (Figure S-9 (a) and (b)). ProDOT is one or two magnitudes lower in conductivity than EDOT.[28] The reduced current density for PProDOT film can be explained by the difficulty of electrolyte ion moving through

the film and can be explained by the comparative cyclic voltammetry responses (Figure-5). In PProDOT CV response, electro activity shuts off around -0.32 V, while PEDOT film is active until -0.72 V. This extra |0.40| V electroactive region for PEDOT allows more ionic migration, hence higher current response in unit time. PProDOT shows a peak in oxidative wave (~0.25 V) unlike the PEDOT film.

3.3.4 MeCN Solvent

PC has a greater dielectric constant (65) than MeCN (37), and EDOT monomer solubility is 3 times higher in PC than MeCN. In PC, during electrodeposition large number of short oligomers go into solution and so, long polymer chain in films is expected. In MeCN, short oligomers were deposited on the electrode surface. This leads to high nucleation centers and ended with short oligomers chain compared to PC solvent.[20] Though polythiophene electrodeposition is thermodynamically and kinetically favored in MeCN, the resulted films have a more compact structure. Besides, PC generate films with finer morphology and better mechanical properties.[29] Solvents with high polarity (PC, 6.1) generates polymer surface with structure and various shapes while less polar solvent (MeCN, 5.8) produce smoother film.[30] This confirms the smoother morphology of PEDOT and PProDOT films deposited from MeCN. Figure 2 (b) and (d) are magnified SEM images (1000X) for PEDOT / MeCN and PProDOT / MeCN, respectively, where patches of micro-sized holed PEDOT or PProDOT sparsely distributed on a smoother surface. These islands of PEDOT / PProDOT patches can be seen in 100X magnified SEM images in Figure S-10. Also, MeCN deposited films showed little or no electrode edge polymer spreading (Figure S-9 (c) and (d)). Similar to PC solvent, MeCN deposited PEDOT shows higher current density than PProDOT film (57% and 61% higher in 0.10 M NaCl and 0.01 M PBS, respectively). But PProDOT / MeCN film showed less charge

density than PProDOT / PC (29 % and 35.5 % lesser in 0.10 M NaCl and 0.01 M PBS, respectively).

Despite having similar electrochemical performances (except PProDOT/ MeCN film) MeCN deposited films were not practical for R-MHD pumping use, because of poor mechanical adhesion on the gold electrode surface. During electropolymerization and film characterization in electrolytes only, polymer films delaminated multiple times. Better mechanical stability of conducting polymers electrodeposited from PC compared to MeCN solvents have been reported before.[29, 31]

3.3.5 Electrochemical Impedance Spectroscopy (EIS) Characterization of PEDOT and PProDOT Films

Figure 6 (a) and (b) show Nyquist plots of PEDOT film deposited by CV, CA and CP techniques and film deposited from different monomers and solvents, respectively. Solution resistance (Rs) is ~ 5 Ω for all the films. CA deposited PEDOT film shows lower (~70 Ω) charge transfer resistance (Rct) than CV and CP deposited film (~75 Ω). This lower Rct value can be explained by the increased in surface roughness of CA deposited film compared to others. [32] According to Figure 6 (b), regardless of the deposition solvent, PEDOT have lower Rct values than PProDOT. PEDOT / PC and PEDOT / MeCN has a similar charge transfer resistance (~75 Ω), while PProDOT / PC and PProDOT / MeCN has around 75 Ω and 85 Ω, respectively. Similar ion diffusion characteristics were found in each film for having similar semi-infinite Warburg region.

3.3.6 R-MHD Pumping with Optimized Films under Controlled Current Condition

Applied potential (CA) technique requires the shortest time compared to CP and CV to modify electrodes with similar electrochemical properties relevant (current and charge density) to R-MHD pumping. EDOT could generate around 50% higher maximum current density than ProDOT in characterizing electrolyte solution. Because of having higher dielectric potential, monomer dissolves more easily in PC than MeCN. Another practical advantage of using PC than MeCN is, its 3× higher boiling point. The high boiling point of PC helps to sustain the original electrolyte and monomer concentration throughout deposition period, in a 3-electrode deposition setup. The evaporation of MeCN solvent during polymerization may have detrimentally influenced the film's mechanical stability. We used 0.01 M PBS over 0.10 M NaCl as MHD pumping solution, due to having 27 % - 42% increased ionic current density. Although, the 40% glycerol added with PBS (to match the bead density) decreased the solution concentration and increased solution viscosity.

PEDOT / PC film was electrodeposited for R-MHD experiment by CA method for 110 mC charge. The fluid flow in R-MHD can be precisely controlled by applying current, so a range of currents (± 50 to ± 800 μA) applied in between the PDOT coated electrodes. It has been confirmed in earlier work that fluid speed changes linearly with the applied current. [10-11] For each current, both the anodic and negative bias sequentially applied for multiple cycles to recharge/ discharge the film after initial discharging / charging. The presence of sequential opposite bias ionic current densities (j) and a constant magnetic field (B) makes the fluid to flow back and forth with same duration and speed to satisfy the right-hand rule ($F_B = j \times B$). To be consistent, all fluidic speed and duration were measured during the forward flow only. Figure 7 (a) and (b) shows a linear dependency of fluid speed and duration with current and inverse of the current,

respectively. The maximum fluidic speed (793 ± 4 µm/s) achieved at 800 µA, but with shortest duration (6.7 ± 0.5 s) owing to use up all the accessible charge faster with a high current. The maximum duration (170 ± 8 s) achieved with 50 µA, but with a minimum of 48.2 ± 0.7 µm/s fluid speed. This tunable pumping approach has generated 2× and 2.44 × faster fluidic speed compared to previous achievements by Nash and Sahore et al. with comparable gasket thickness, chip design, applied current, and height above the chip surface.[7, 11] Nash et al. used CV deposited PEDOT (finite amount of charging centers) from an aqueous medium and could pump only 34 s, at 50 µA which is 5× shorter than this study.

3.4 Conclusions

If electrode shorting is not a concern, CA can be used for faster polymer deposition. Otherwise, CP is a better candidate for slow and controlled film growth. EDOT provides larger potential range for electrochemical activity compared to ProDOT monomer. PC solvent produces robust films and allow easier electrodeposition by sustaining the monomer and electrolyte concentration over a longer period. But, the monomer, solvent, and deposition techniques optimization can only improve the robustness of films, fluidic speed, and duration for a limited time. The next challenge is to pump fluid in a single direction for an unlimited time under R-MHD condition. It is necessary for applications like circular on-chip separation, and long duration imaging cytometry. We need the device optimization along with the material study to make R-MHD an ubiquitous hand-held pumping method for a wide range of on-site bioanalytical applications.

3.5 Supporting Information

Supporting information includes, tables of current and charge densities of polymer films obtained from different deposition methods, monomers, and solvents. It also includes electrode design, electrochemical response during polymerization, chronoamperometric and chronocoulometric responses of polymer-modified electrodes, chronopoteniometry (CP) responses for pumping experiments, SEM micrographs of PEDOT and PProDOT films that deposited from PC and MeCN solvents.

3.6 Acknowledgements

We are grateful for financial support from the National Science Foundation (CBET-1336853), the Women's Giving Circle, and the Arkansas Bioscience Institute, the major research component of the Arkansas Tobacco Settlement Proceeds Act of 2000.

3.7 References:

(1) Grant, K. M.; Hemmert, J. W.; White, H. S. Magnetic Field-Controlled Microfluidic Transport. *Journal of the American Chemical Society* **2002,** *124* (3), 462-467, DOI: 10.1021/ja016544y.

(2) Leventis, N.; Gao, X. Magnetohydrodynamic Electrochemistry in the Field of Nd−Fe−B Magnets. Theory, Experiment, and Application in Self-Powered Flow Delivery Systems. *Analytical Chemistry* **2001,** *73* (16), 3981-3992, DOI: 10.1021/ac010172u.

(3) Qian, S.; Bau, H. H. Magneto-Hydrodynamics Based Microfluidics. *Mechanics research communications* **2009,** *36* (1), 10-21, DOI: 10.1016/j.mechrescom.2008.06.013.

(4) Weston, M. C.; Nash, C. K.; Fritsch, I. Redox-Magnetohydrodynamic Microfluidics Without Channels and Compatible with Electrochemical Detection Under Immunoassay Conditions. *Analytical chemistry* **2010,** *82* (17), 7068-7072, DOI: 10.1021/ac101377a.

(5) Anderson, E. C.; Weston, M. C.; Fritsch, I. Investigations of Redox Magnetohydrodynamic Fluid Flow At Microelectrode Arrays Using Microbeads. *Analytical Chemistry* **2010,** *82* (7), 2643-2651, DOI: 10.1021/ac9020177.

(6) Pamme, N. Magnetism and microfluidics. *Lab on a Chip* **2006,** *6* (1), 24-38, DOI: 10.1039/B513005K.

(7) Sahore, V.; Fritsch, I. Flat Flow Profiles Achieved with Microfluidics Generated by Redox-Magnetohydrodynamics. *Analytical Chemistry* **2013,** *85* (24), 11809-11816, DOI: 10.1021/ac402476v.

(8) Sahore, V.; Fritsch, I. Microfluidic rotational flow generated by redox-magnetohydrodynamics (MHD) under laminar conditions using concentric disk and ring microelectrodes. *Microfluidics and Nanofluidics* **2015,** *18* (2), 159-166, DOI: http://dx.doi.org/10.1007/s10404-014-1427-6.

(9) Sahore, V.; Fritsch, I. Redox-Magnetohydrodynamics, Flat Flow Profile-Guided Enzyme Assay Detection: Toward Multiple, Parallel Analyses. *Analytical Chemistry* **2014,** *86* (19), 9405-9411, DOI: 10.1021/ac502014t.

(10) Khan, F. Z.; Hutcheson, J. A.; Hunter, C. J.; Powless, A. J.; Benson, D.; Fritsch, I.; Muldoon, T. J. Redox-Magnetohydrodynamically Controlled Fluid Flow with Poly(3,4-

ethylenedioxythiophene) Coupled to an Epitaxial Light Sheet Confocal Microscope for Image Cytometry Applications. *Analytical Chemistry* **2018,** *90* (13), 7862-7870, DOI: 10.1021/acs.analchem.7b05312.

(11) Nash, C. K.; Fritsch, I. Poly(3,4-ethylenedioxythiophene)-Modified Electrodes for Microfluidics Pumping with Redox-Magnetohydrodynamics: Improving Compatibility for Broader Applications by Eliminating Addition of Redox Species to Solution. *Analytical Chemistry* **2016,** *88* (3), 1601-1609, DOI: 10.1021/acs.analchem.5b03182.

(12) Meng, H.; Zheng, J.; Lovinger, A. J.; Wang, B.-C.; Van Patten, P. G.; Bao, Z. Oligofluorene−Thiophene Derivatives as High-Performance Semiconductors for Organic Thin Film Transistors. *Chemistry of Materials* **2003,** *15* (9), 1778-1787, DOI: 10.1021/cm020866z.

(13) Donavan, K. C.; Arter, J. A.; Pilolli, R.; Cioffi, N.; Weiss, G. A.; Penner, R. M. Virus−Poly(3,4-ethylenedioxythiophene) Composite Films for Impedance-Based Biosensing. *Analytical Chemistry* **2011,** *83* (7), 2420-2424, DOI: 10.1021/ac2000835.

(14) Lin, P.; Yan, F. Organic Thin-Film Transistors for Chemical and Biological Sensing. *Advanced Materials* **2011,** *24* (1), 34-51, DOI: 10.1002/adma.201103334.

(15) DeLongchamp, D.; Hammond, P. T. Layer-by-Layer Assembly of PEDOT/Polyaniline Electrochromic Devices. *Advanced Materials* **2001,** *13* (19), 1455-1459, DOI: 10.1002/1521-4095(200110)13:19<1455::AID-ADMA1455>3.0.CO;2-7.

(16) Ryu, K. S.; Lee, Y.-G.; Hong, Y.-S.; Park, Y. J.; Wu, X.; Kim, K. M.; Kang, M. G.; Park, N.-G.; Chang, S. H. Poly(ethylenedioxythiophene) (PEDOT) as polymer electrode in redox supercapacitor. *Electrochimica Acta* **2004,** *50* (2), 843-847, DOI: https://doi.org/10.1016/j.electacta.2004.02.055.

(17) Snook, G. A.; Kao, P.; Best, A. S. Conducting-polymer-based supercapacitor devices and electrodes. *Journal of Power Sources* **2011,** *196* (1), 1-12, DOI: https://doi.org/10.1016/j.jpowsour.2010.06.084.

(18) Asplund, M.; Thaning, E.; Lundberg, J.; Sandberg-Nordqvist, A. C.; Kostyszyn, B.; Inganäs, O.; Holst, H. v. Toxicity evaluation of PEDOT/biomolecular composites intended for neural communication electrodes. *Biomedical Materials* **2009,** *4* (4), 045009.

(19) Wang, X.; Sjöberg-Eerola, P.; Eriksson, J.-E.; Bobacka, J.; Bergelin, M. The effect of counter ions and substrate material on the growth and morphology of poly(3,4-ethylenedioxythiophene) films: Towards the application of enzyme electrode construction in

biofuel cells. *Synthetic Metals* **2010,** *160* (13), 1373-1381, DOI: https://doi.org/10.1016/j.synthmet.2010.01.033.

(20) Poverenov, E.; Li, M.; Bitler, A.; Bendikov, M. Major Effect of Electropolymerization Solvent on Morphology and Electrochromic Properties of PEDOT Films. *Chemistry of Materials* **2010,** *22* (13), 4019-4025, DOI: 10.1021/cm100561d.

(21) Groenendaal, L.; Jonas, F.; Freitag, D.; Pielartzik, H.; Reynolds, J. R. Poly(3,4-ethylenedioxythiophene) and Its Derivatives: Past, Present, and Future. *Advanced Materials* **2000,** *12* (7), 481-494, DOI: 10.1002/(SICI)1521-4095(200004)12:7<481::AID-ADMA481>3.0.CO;2-C.

(22) Vorotyntsev, M. A.; Zinovyeva, V. A.; Konev, D. V. Mechanisms of Electropolymerization and Redox Activity: Fundamental Aspects. In *Electropolymerization*; Wiley-VCH Verlag GmbH & Co. KGaA: 2010; pp 27-50.

(23) Khan, F. Z.; Fritsch, I. Chip-Scale Electrodeposition and Analysis of Poly(3,4-ethylenedioxythiophene) (PEDOT) Films for Enhanced and Sustained Microfluidics Using DC-Redox-Magnetohydrodynamics. *Journal of The Electrochemical Society* **2019,** *(in revision)*.

(24) Ping-Ping, S.; Zheng-Hao, W. Studies on Charging Processes and Capacitances of Oxidized Polyethylenedioxythiophene Films. *Chinese Journal of Chemistry* **2005,** *23* (7), 806-810, DOI: 10.1002/cjoc.200590806.

(25) Patra, S.; Barai, K.; Munichandraiah, N. Scanning electron microscopy studies of PEDOT prepared by various electrochemical routes. *Synthetic Metals* **2008,** *158* (10), 430-435, DOI: https://doi.org/10.1016/j.synthmet.2008.03.002.

(26) Schottland, P.; Zong, K.; Gaupp, C. L.; Thompson, B. C.; Thomas, C. A.; Giurgiu, I.; Hickman, R.; Abboud, K. A.; Reynolds, J. R. Poly(3,4-alkylenedioxypyrrole)s: Highly Stable Electronically Conducting and Electrochromic Polymers. *Macromolecules* **2000,** *33* (19), 7051-7061, DOI: 10.1021/ma000490f.

(27) Sulaiman, Y.; Kataky, R. Effect of Monomer Modifications on the Physical Properties of Electropolymerised PEDOT Films. *Journal of The Electrochemical Society* **2011,** *159* (2), F1-F9.

(28) Elschner, A.; Kirchmeyer, S.; Lovenich, W.; Merker, U.; Reuter, K. PEDOT: Principles and Applications of an Intrinsically Conductive Polymer. **2010**.

(29) Zhang, W.; Plieth, W.; Koβmehl, G. Kinetic study of the bithienyl electropolymerization. *Electrochimica Acta* **1997,** *42* (11), 1653-1661, DOI: https://doi.org/10.1016/S0013-4686(96)00301-5.

(30) Wolfs, M.; Darmanin, T.; Guittard, F. Versatile Superhydrophobic Surfaces from a Bioinspired Approach. *Macromolecules* **2011,** *44* (23), 9286-9294, DOI: 10.1021/ma200430n.

(31) Sun, B.; Jones, J. J.; Burford, R. P.; Skyllas-Kazacos, M. Stability and mechanical properties of electrochemically prepared conducting polypyrrole films. *Journal of Materials Science* **1989,** *24* (11), 4024-4029, DOI: 10.1007/BF01168967.

(32) Castagnola, V.; Bayon, C.; Descamps, E.; Bergaud, C. Morphology and conductivity of PEDOT layers produced by different electrochemical routes. *Synthetic Metals* **2014,** *189*, 7-16, DOI: https://doi.org/10.1016/j.synthmet.2013.12.013.

3.8 Figures

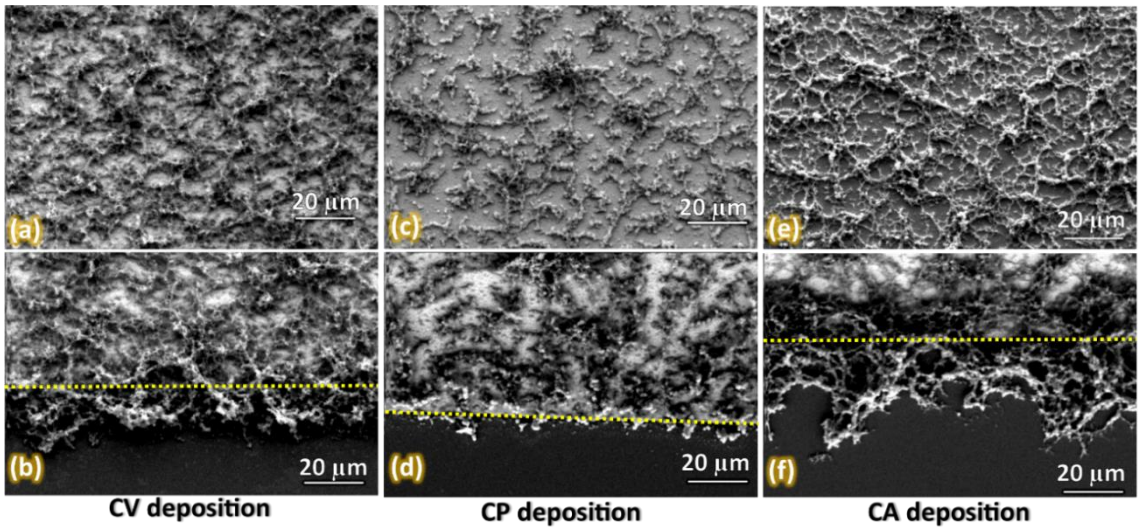

Figure 1: (a), (c), (e) and (b), (d), (e) are SEM micrographs at the middle and edge of the electrode, respectively for CV, CP, and CA deposition. The yellow dotted lines in (b), (d), and (e) are showing the electrode edge. All SEM images were taken at 1000x magnification (20 µm scale bar).

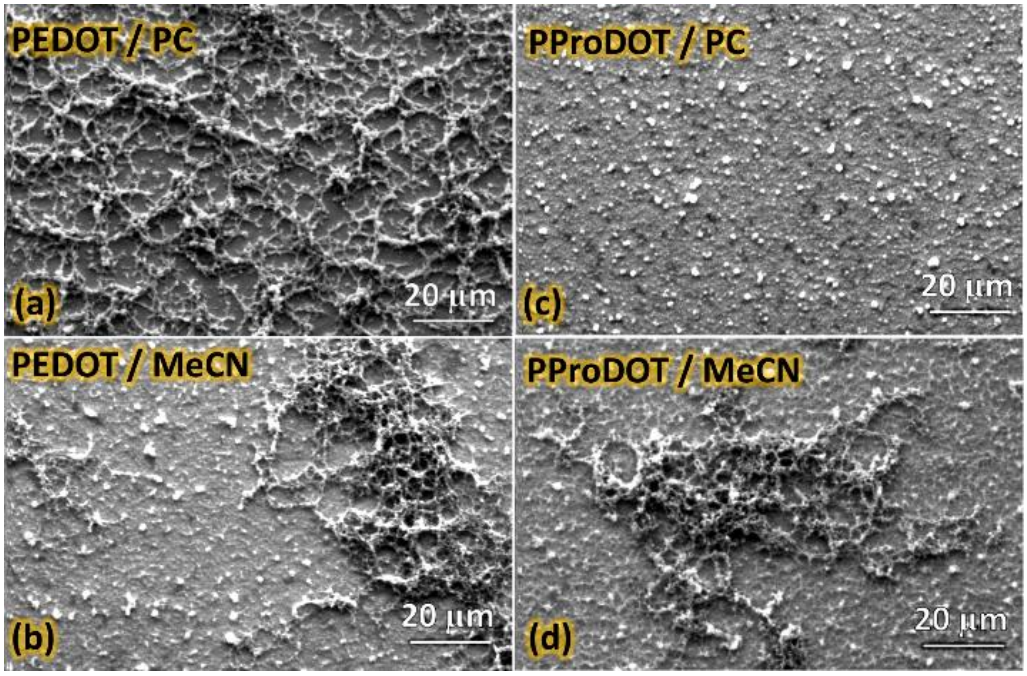

Figure 2: (a) to (d) are SEM micrographs at the middle of the electrode for PEDOT / PC, PEDOT / MeCN, PProDOT / PC, and PProDOT / MeCN films. All SEM images were taken at 1000x magnification (20 µm scale bar).

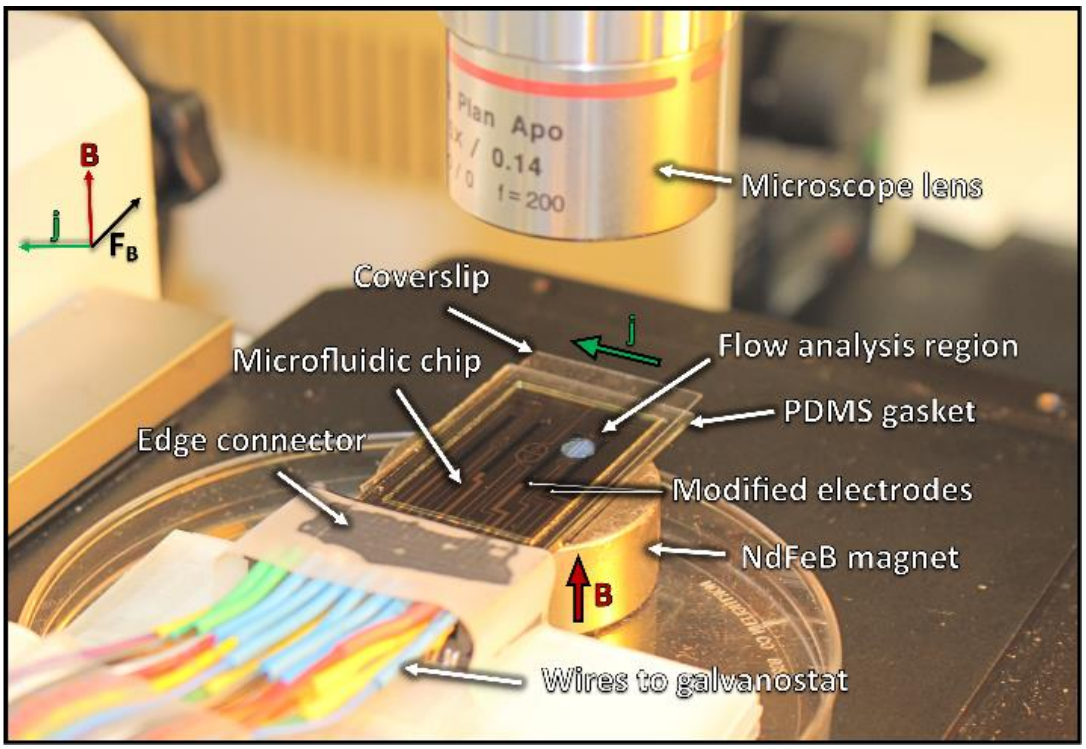

Figure 3: Experimental setup for the R-MHD experiment where the chip-gasket-coverslip assembly placed under the microscope lens. Under the chip a 0.37 T NdFeB permanent magnet used for R-MHD. The first two electrodes of the chip (on the right side) used as working–counter / reference electrode. A PDMS gasket holds the MHD solution (PBS: Glycerol) on the chip and a coverslip over the gasket to seal the system. The chip was connected to the galvanostat through an edge connector. Flow analysis region was in between active electrodes (circular white spot) and the fluid flow was recorded by coupling a Sony Handycam with the microscope (not in the figure).

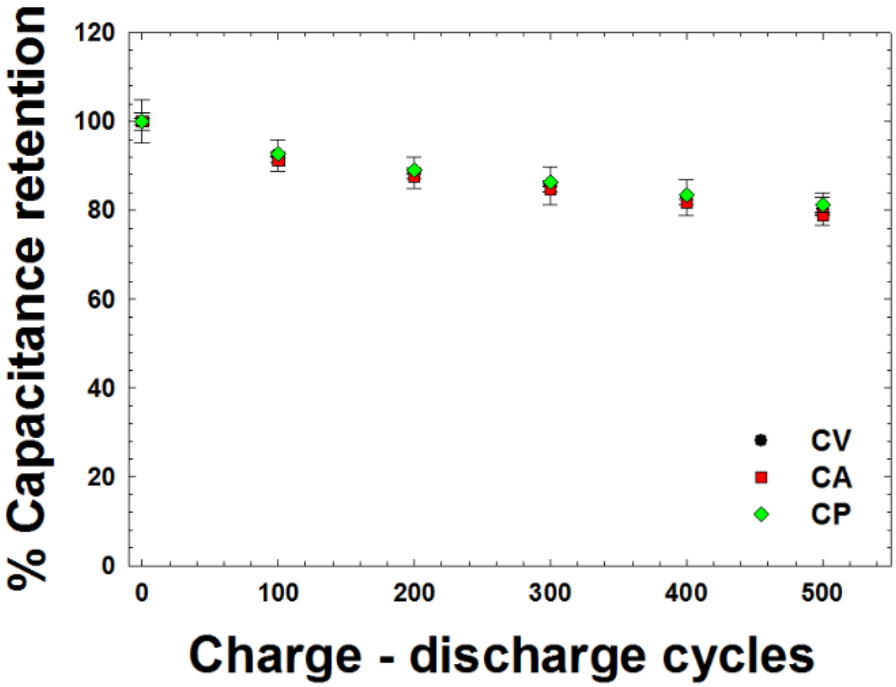

Figure 4: Capacitance retention relationship with charge-discharge cycles. 500 cycles of chronopotentiometry (CP) experiments were done with ± 150 µA applied current in 0.10 M NaCl solution. A three-electrode system was used with an Ag/AgCl (saturated KCl) reference electrode and Pt counter electrode in a 20 ml glass beaker. Cutoff voltages of -0.50 to 0.70 V would have to avoid over-oxidation of PEDOT film.

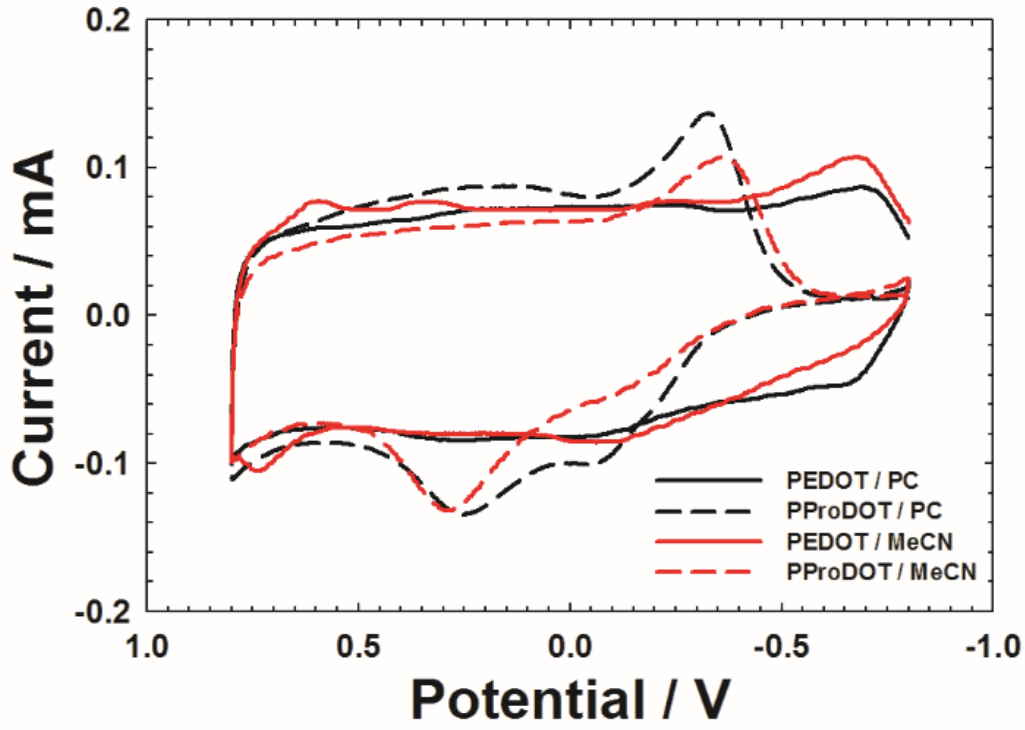

Figure 5: Comparative cyclic voltammetry responses of PEDOT and PProDOT films deposited from PC and MeCN solvents. A three-electrode system was used with an Ag/AgCl (saturated KCl) reference electrode and a Pt flag counter electrode in a 20 ml glass beaker. CV was performed in 0.10 M NaCl at 50 mV/s scan rate with -0.800 to +0.800 V voltage window. The solid black and red represents CV responses for PEDOT films deposited from PC and MeCN solvents, respectively. Dotted black and red represents PProDOT films electrodeposited from PC and MeCN solvents, respectively.

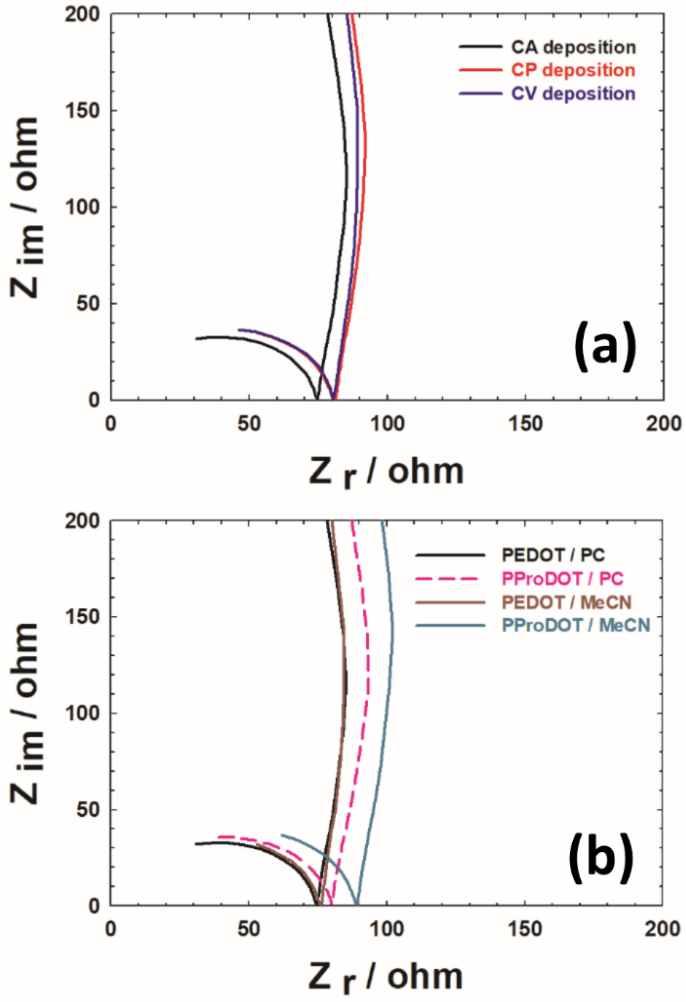

Figure 6: (a) Nyquist plots of PEDOT film deposited from CA, CP, CV techniques (b) Nyquist plots for PEDOT and PProDOT film deposited from PC and MeCN solvents by CA method. EIS spectra were obtained by applying 15 mV sinusoidal AC voltage at 0 V DC potential and in the 0.10–10^5 Hz frequency range.

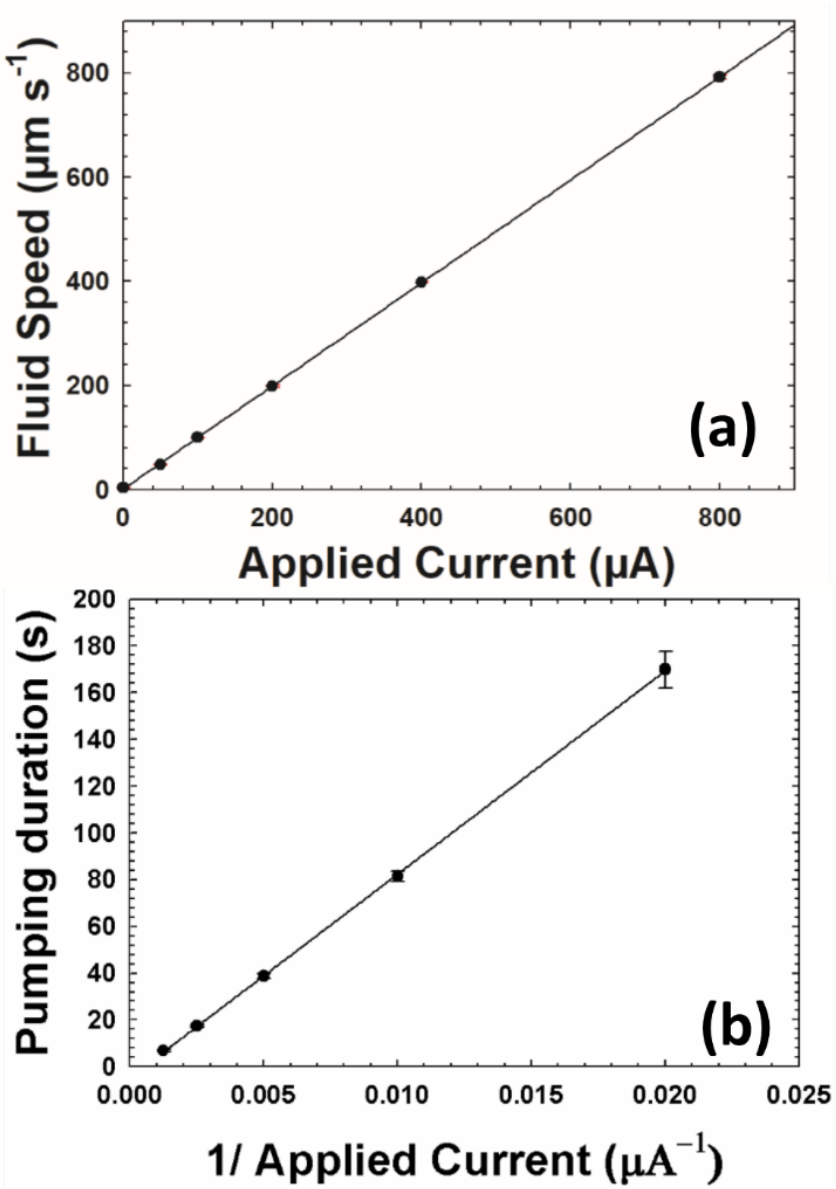

Figure 7: (a) Calibration curve of fluidic speed based upon bead motion in the MHD solution, as the function of applied current. Least square analysis yields |Vx| = (0.9896 ± 0.0024 μms^{-1} μA^{-1}) |i| + (0.9899 ± 0.9000 μm s^{-1}) with R^2 = 1.000 for 320μm above the chip surface. (b) Fluid pumping duration as a function of inverse of applied current. Least square analysis yields flow duration = (8698.53 ± 48.60 μA s) | i^{-1}| − (4.64 ± 0.50 s) with R^2 = 0.9999.

3.S Supporting Information: Electrochemical Performance of PEDOT and PproDOT Conducting Polymers, Electrodeposited Using Different Routes and Solvents, and The Resulting Impact on Applications in R-MHD Microfluidics

Supporting information includes tables consisting current and charge densities of films obtained from different deposition methods, monomers, and solvents. Supporting information also includes electrode design, electrochemical response during polymerization, chronoamperometric and chronocoulometric responses of PEDOT film-modified electrodes, chronopoteniometry (CP) responses for pumping experiments, SEM micrographs of PEDOT and PProDOT films deposited from PC and MeCN solvents.

3.S1 Supporting Information Tables

Table S 1. Current densities, charge densities and capacitance obtained from CV, CP, and CA deposited films in 0.10 M NaCl and 0.01 PBS

PEDOT deposited by	Current density in 0.10 M NaCl ($mA.cm^{-2}$)	Charge density in 0.10 M NaCl ($mC.cm^{-2}$)	Current density in 0.01 M PBS ($mA.cm^{-2}$)	Charge density in 0.01 M PBS ($mC.cm^{-2}$)	% Capacitance retention in 0.1 M NaCl
CV	198.52 ± 4.93	21.14 ± 0.37	258.55 ± 9.06	23.66 ± 0.83	80.22 ± 3.64
CP	193.08 ± 4.82	23.96 ± 1.45	270.28 ± 13.02	28.04 ± 1.30	81.22 ± 1.80
CA	191.82 ± 3.80	22.30 ± 1.26	245.85 ± 14.82	26.20 ± 0.81	78.98 ± 0.10

Table S 2. Current and charge densities obtained from PC and MeCN deposited PEDOT and PProDOT films in 0.10 M NaCl and 0.01 PBS

Film composition	Current density in 0.10 M NaCl ($mA.cm^{-2}$)	Charge density in 0.10 M NaCl ($mC.cm^{-2}$)	Current density in 0.01 M PBS ($mA.cm^{-2}$)	Charge density in 0.01 M PBS ($mC.cm^{-2}$)
PC: PEDOT (W22C3, n=3)	191.82 ± 3.80	22.30 ± 1.26	245.85 ± 14.82	26.20 ± 0.81
MeCN: PEDOT (W20C5, n=4)	200.30 ± 3.15	22.05 ± 1.70	260.02 ± 5.07	24.35 ± 0.68
PC:PProDOT (W20C6, n=3)	114.82 ± 2.43	21.88 ± 0.40	164.30 ± 3.75	23.81 ± 0.20
MeCN:PProDOT (W20C4, n=4)	127.66 ± 1.43	17.14 ± 2.29	161.45 ± 3.06	17.97 ± 2.14

3.S2 Supporting Information Figures

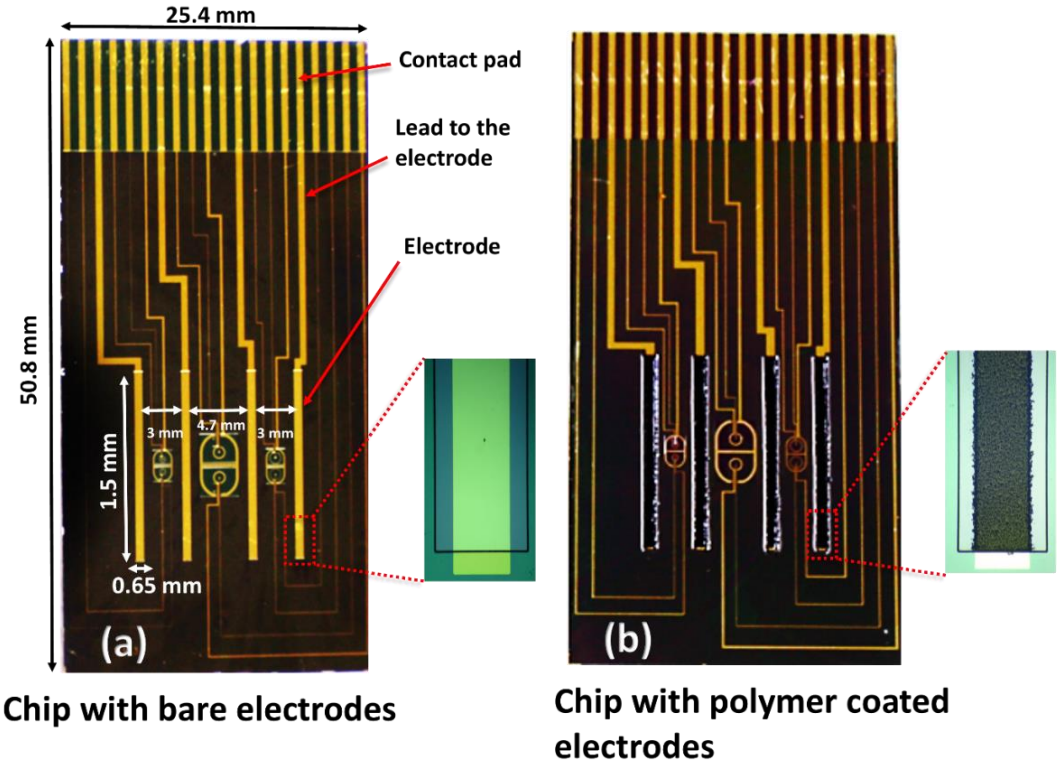

Figure S-1: (a) Electrode design for the microfabricated chip (50.8 mm × 25.4 mm). The chip contains four band electrodes, each with 1.5 mm in length, 0.65 mm in width, and ~ 250 nm thick. The outer and inner two electrodes were separated by 3 mm and 4.7 mm gaps. The contact pad at one end of the chip connect electrodes with potentiostat with an edge connector. The inset shows an optical image of the gold electrode with an insulating layer, BCB around it. (b) Polymer coated chip, where each electrode was deposited with PEDOT by CA method. The white outlining around the electrode is due to the reflected light from the water-soaked polymer, while the picture was taken.

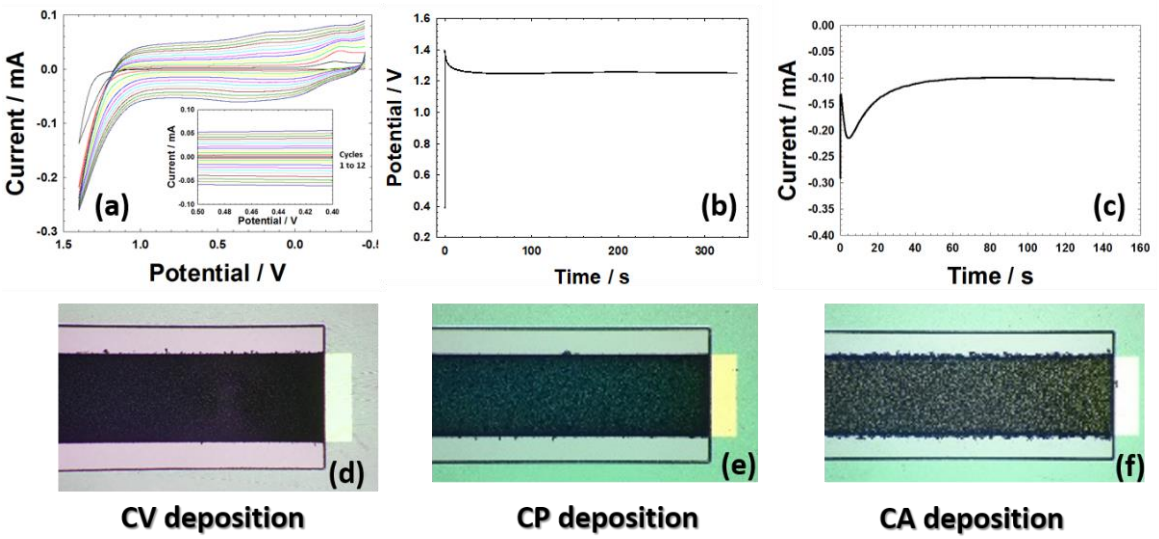

Figure S-2: (a), (b), and (c) are electrochemical responses of PEDOT deposition by CV, CP, and CA routes. During CV electrodeposition, potential was cycled from -0.455 to 1.4 V for 12 times at 0.05 V/s. 50 µA anodic current applied for 336 seconds in CP deposition. In CA approach, potential was held at 1.4 V for 146 seconds. All electrodepositions were done in 3-electrode system where Pt flag used as counter and Ag/AgCl (saturated KCl) as reference electrode. Monomer solution prepared with 0.010 M EDOT and 0.100 M $TBAPF_6$ in propylene carbonate. (d), (e), and (f) are optical images of electrodeposited films from CV, CP, and CA routes

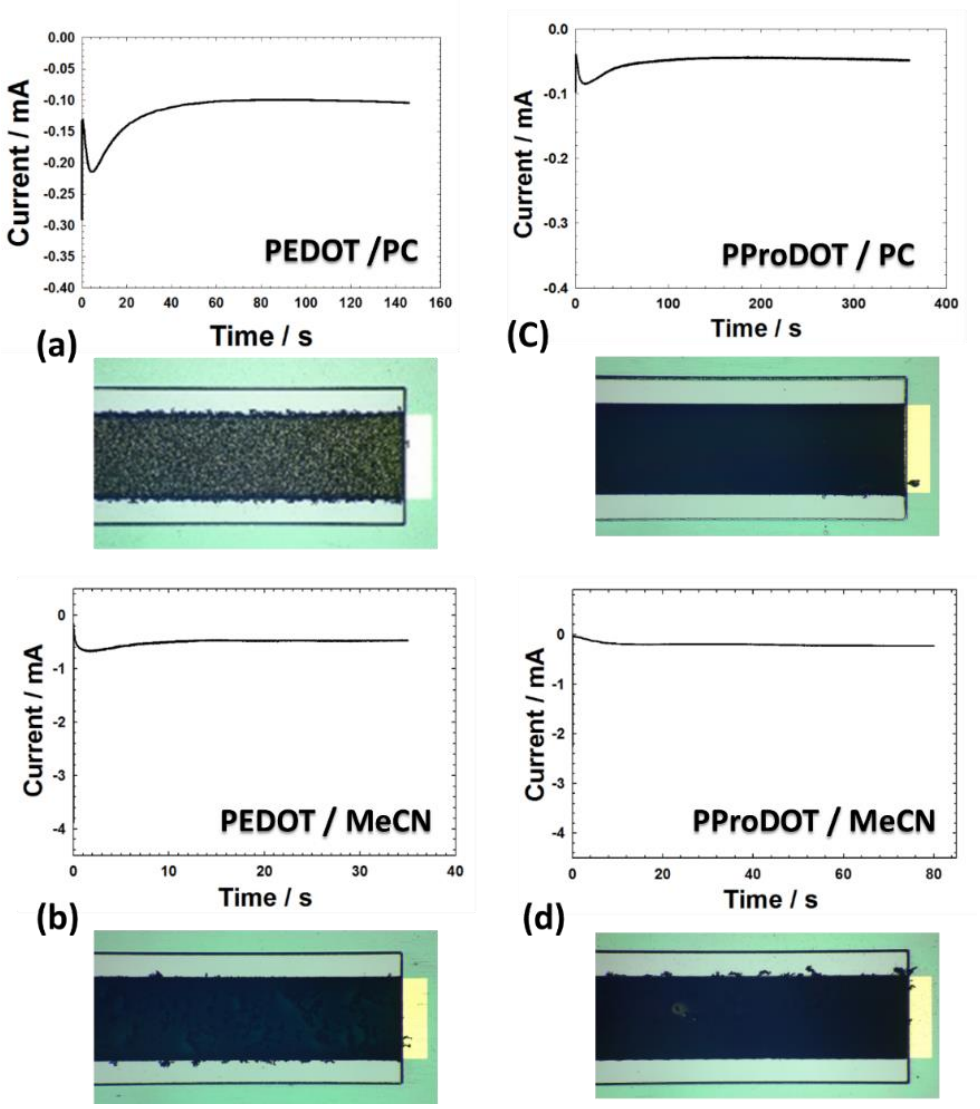

Figure S-3: (a), (b), (c), and (d) are electrochemical responses during CA electrodeposition and associated optical images of PEDOT / PC, PEDOT / MeCN, PProDOT / PC, and PProDOT / MeCN films. All electrodepositions were done in 3-electrode system where Pt flag used as counter electrode and Ag/AgCl (saturated KCl) as reference electrode. Monomer solution prepared with 0.010 M monomer along with 0.100 M $TBAPF_6$ electrolyte in propylene carbonate (PC) and acetonitrile (MeCN) solvents.

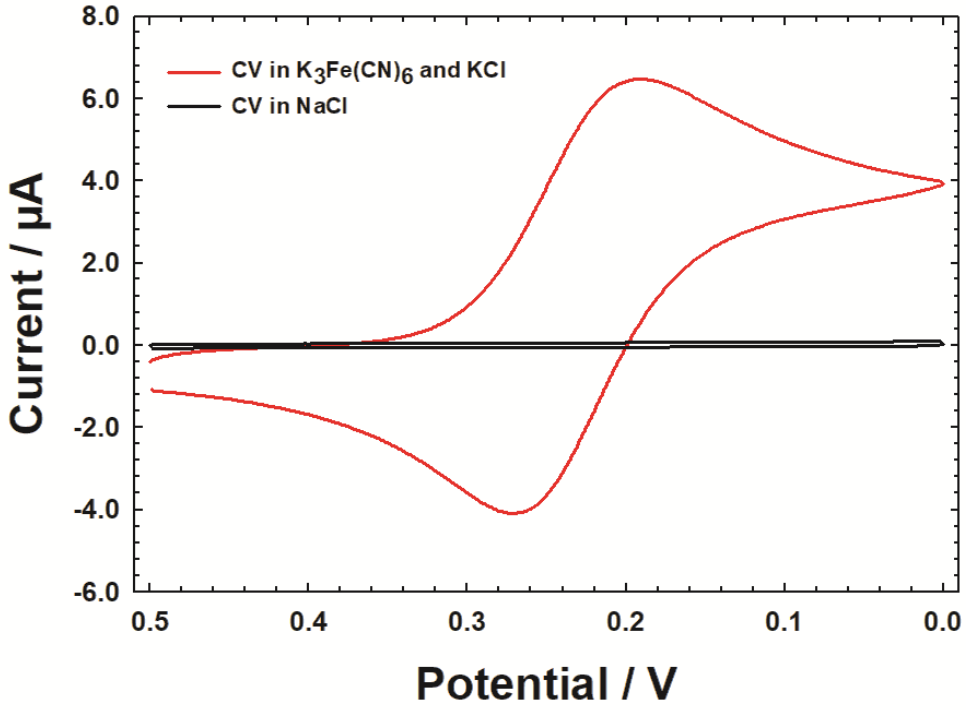

Figure S- 4: Comparative cyclic voltammetry responses of bare electrode (without any polymer coating) in 0.10 M NaCl solution (black) and 0.10 $K_3Fe(CN)_6$ in 0.10 M KCl solution (red). CV was done in a 3-electrode system where Pt flag used as counter electrode and Ag/AgCl (saturated KCl) as reference electrode.

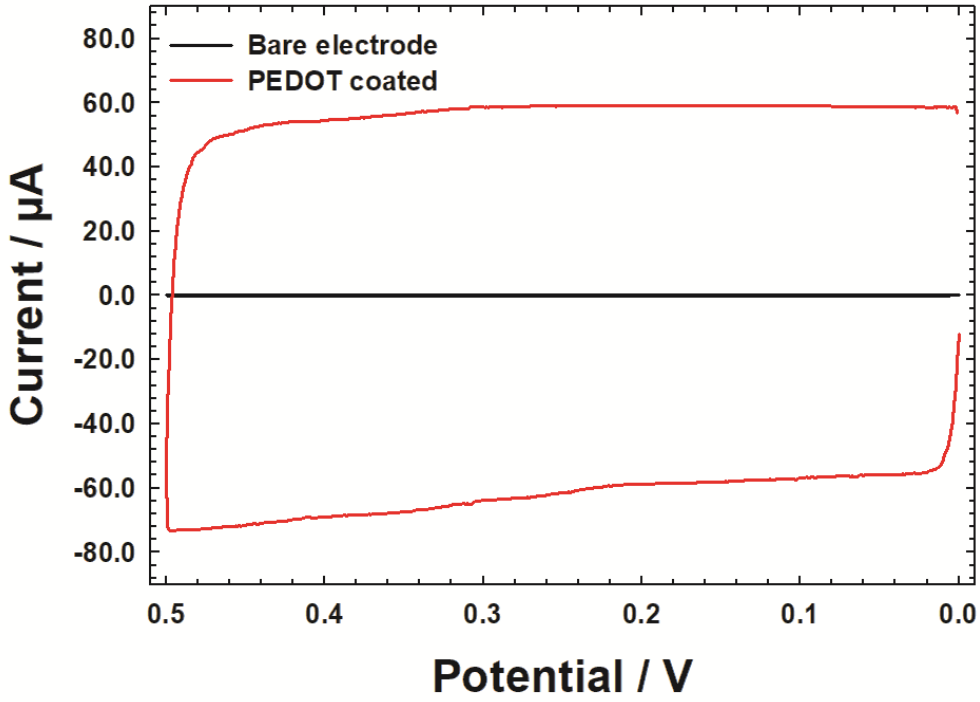

Figure S-5: Overlay of cyclic voltammetry responses (0.050 V/s) of PEDOT coated electrode (red) and bare electrode (black) in 0.10 M NaCl solution. This post-polymerization CV is from CA deposited PEDOT / MeCN film and performed in a 3-electrode system where Pt flag used as counter electrode and Ag/AgCl (saturated KCl) as reference electrode.

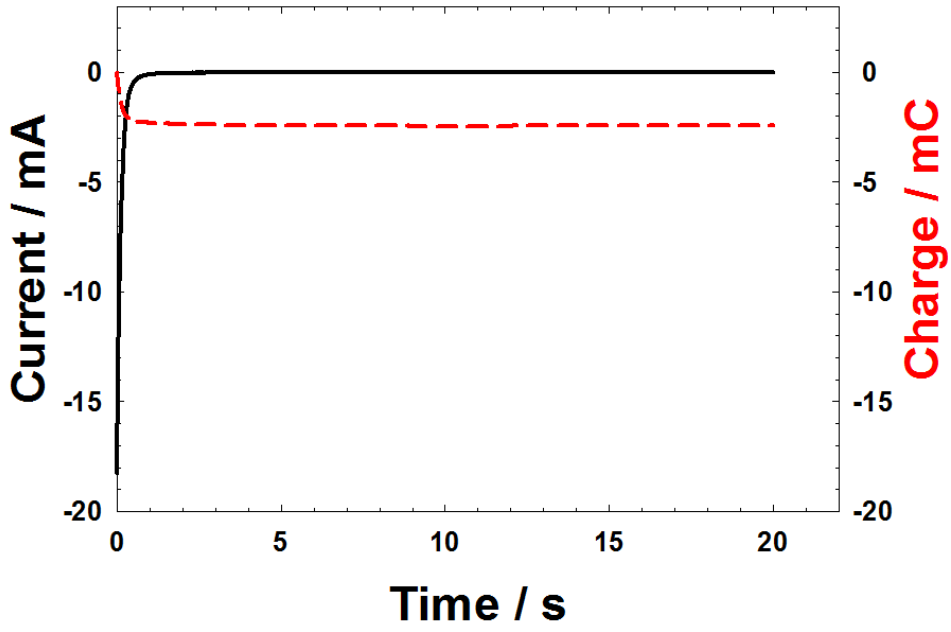

Figure S- 6: Current (solid black curve) and charge (dashed red curve) response in 0.10 M NaCl solution of one PEDOT coated electrode. PEDOT was electrodeposited from MeCN solvent by CA deposition route. A three-electrode system was used with an Ag/AgCl (saturated KCl) reference electrode and Pt counter electrode in 20 ml 0.10 M NaCl. The potential was held at -0.800 V for a quiet time of 20 s prior to the step, and then held at 0.800 V for 20 s after the step. Maximum current and total charge over the period of 20 sec (red dashed line) were achieved by CA data.

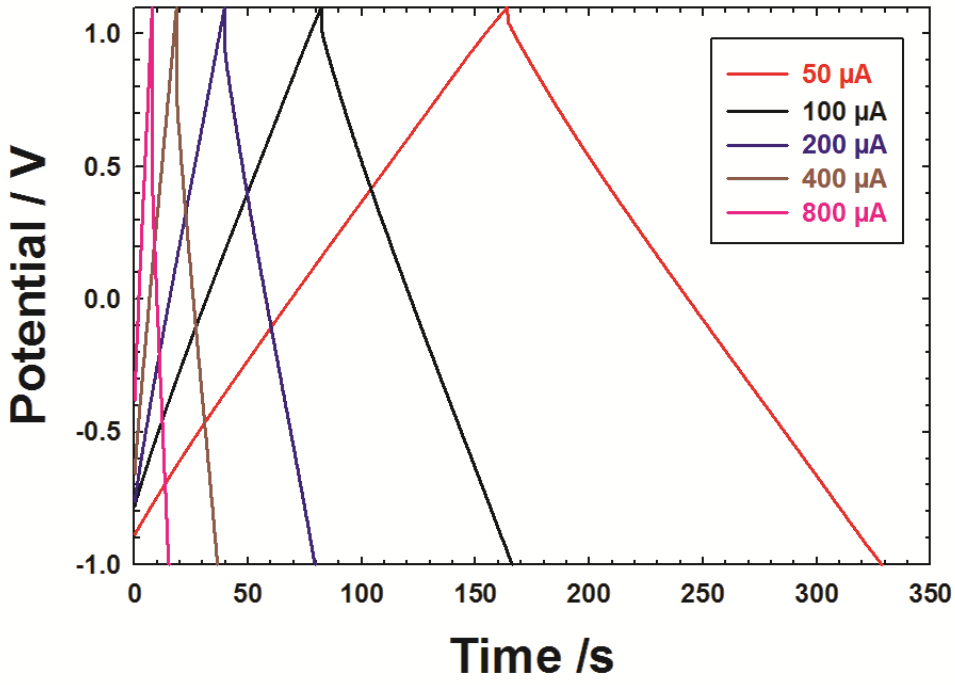

Figure S-7: On-chip chronopotentiometry (CP) responses of PEDOT / PC films during MHD experiment. Two adjacent PEDOT / PC coated electrodes were activated by supplying current from a galvanostat, while one used as "working" and other as "quasi counter-reference" electrode. Currents of ± 50, ± 100, ± 200, ± 400, and ± 800 µA were applied to generate fluid flow between the active electrodes in MHD chamber.

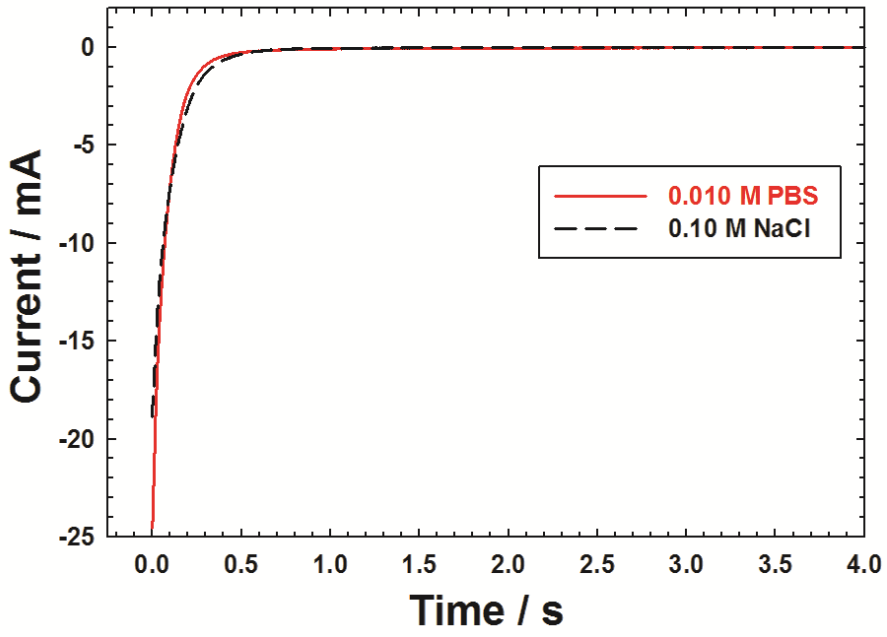

Figure S-8: Comparison of CA responses of PC/PEDOT film (deposited by CV method) in 0.10 M NaCl 9dashed black curve) and 0.01 M PBS (solid red curve). The potential was initially held -0.800 V to charge the polymer over a quiet time of 20 s, and then stepped and held at 0.800 V for 20 s while the current was recorded. A three-electrode setup in 20 mL was used, where an Ag/AgCl (saturated KCl) served as reference electrode and a Pt flag served as counter electrode.

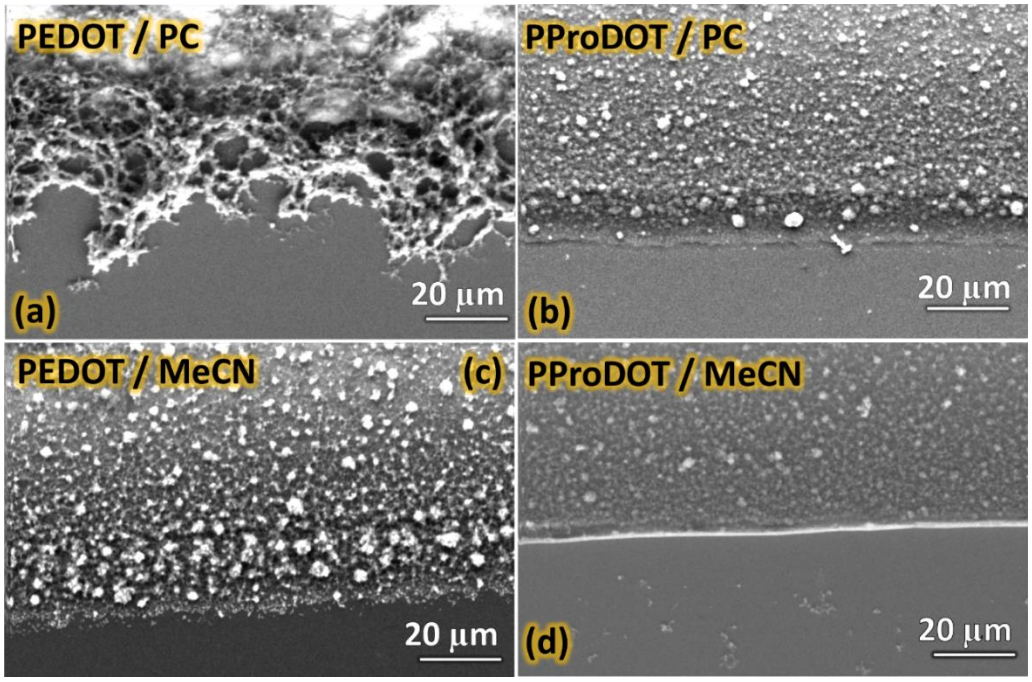

Figure S-9: (a), (b), (c) and (d) are SEM micrograph obtained at the edge of electrode from PEDOT / PC, PProDOT / PC, PEDOT / MeCN, and PProDOT / MeCN. All films were electrodeposited by CA techniques. All SEM images were taken at 1000x magnification (20 µm scale bar)

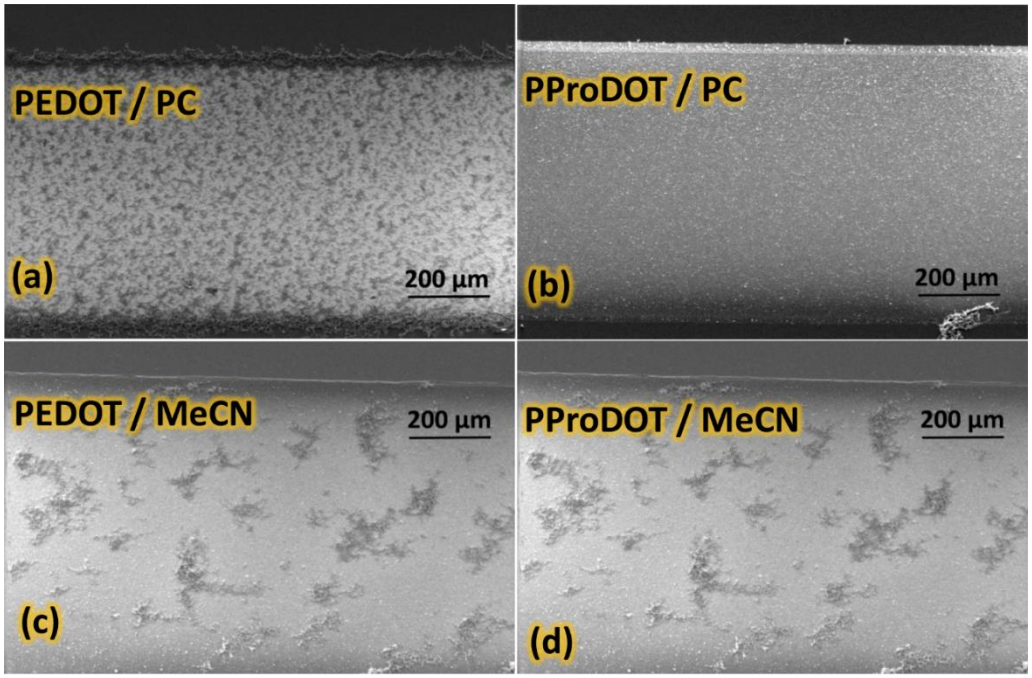

Figure S-10: (a), (b), (c), and (d) are SEM micrographs obtained at the middle of electrode from PEDOT /PC, PProDOT / PC, PEDOT / MeCN, and PProDOT / MeCN. All films were electrodeposited by CA techniques. All SEM images were taken at 100x magnification (200 µm scale bar)

4. Redox-Magnetohydrodynamically Controlled Fluid Flow with Poly(3,4-Ethylenedioxythiophene) (PEDOT) Coupled to an Epitaxial Light Sheet Confocal Microscope for Image Cytometry Applications

4.1 Introduction

Conventional flow cytometry enables the study and characterization of large numbers of individual cells, which can be used for classification and diagnostic applications via quantification of expression levels of certain cellular proteins and receptors. Throughput for flow cytometry is typically >10,000 cells per second.[1-3] However, flow cytometry is typically limited to only a few data points per cell, representing the relative intensity of the fluorescent reporters or via forward or side-scattered light, which can be used to differentiate cells based on certain morphological features, such as nuclear to cytoplasmic ratio (and resultant refractive error mismatch between these two cellular compartments). While highly useful and widely used clinically, conventional flow cytometry methods are relatively insensitive to subcellular morphology, which can have diagnostic significance. Image-based cytometry approaches to classify populations of cells based on morphologic assessment of these subcellular structures have been developed, but typically feature substantially slower sampling speeds relative to flow cytometry.[4-5]

Image cytometry methods may allow for improved classification scheme of cell populations regardless of having lower throughput than conventional cytometry methods. Recently described applications include cell-cycle characterization, oral dysplasia screening, pharmaceutical testing, and live-cell shape dynamics.[6-9] These innovations have focused on the development of automated algorithms and novel imaging techniques to enable analysis of these large and complex data sets. In order to effectively translate these largely laboratory-based methods to clinical applications, low-cost and portable systems for transporting small volumes of biofluids (such as saliva or blood) will be required.

Other methods for high-resolution cytometry (featuring a spatial resolution better than approximately 4 μm, enough to directly resolve subcellular features) to distinguish between cell populations based on different localizations of fluorescent molecules in microfluidic structures have been reported previously. They all use one or more syringe pumps that add bulk and additional power requirements, and in some cases the optical components are not easily translated to hand-held devices. Simmonet et al.[10] demonstrated a poly(dimethylsiloxane) (PDMS) device with a maximum throughput of 20 yeast cells/s (~5-μm diameter and concentration of ~10^9 cells /mL) at a 0.5 μm lateral resolution in a 750 × 110 μm channel at ~0.6 mm/s. To achieve this high resolution, a submicrometer, hydrodynamically-focused flow path of 0.5 μm thickness was necessary to view a single layer of particles at a time and the microscope stage had to be precisely translated in the opposite direction of the fluid flow for a particle to remain static long enough for the requisite exposure time (e.g. 100 ms). Wang et al.[11] used total internal reflection fluorescence to detect fluorescent protein present at the periphery of the cell surface in order to improve the throughput, yet still differentiate between cell populations. They analyzed chicken DT40 B cells in a microfluidic device with a throughput of 100-150 cells/s

(10.8 μm diameter and concentration of 10^7 cells/mL) in a 200 μm × 18 μm channel at 200 μL/h, and single cell detection required a hydrodynamically-focused flow path of 20 μm for the cells (sample stream of ~770 mm/s when two side flows of 400 μL/h are introduced) and an oil immersion microscope objective. Zhu et al.[12] established a simpler fluorescence cytometer using a cell phone and demonstrated imaging of 4- to 1-μm fluorescent beads that were static with a spatial resolution of only 2 μm (concentration of 1.14×10^8 particles / mL). However, imaging was not demonstrated under flowing or static conditions for white blood cells. Only their density was reported (with a concentration of about 7×10^5 cells/mL, at a flow rate of 60 μL/h, (0.13 mm/s) and in a channel of 3 mm × 44 μm dimensions). To achieve high throughput and portability, there remains a need to combine continuous high spatial imaging with microfluidics.

Typical imaging requirements for cytometric applications involving fluid flow include high frame rates to minimize motion blur, as in widefield imaging geometries, where a full-frame field of view is captured[13-14] and, for three-dimensional suspensions of cells in fluids, some type of optical sectioning ability (typically using point scanning approaches similar to laser scanning confocal microscopy).[13, 15-16] Wide-field microscopy uses a two-dimensional imaging camera and may enable faster frame rates, but faces significant limitations when objects are present above or below the focal plane of interest, as in three-dimensional fluid flow. Point scanning imaging can reduce the out-of-focus blurriness, but its frame rate might be ineffective for moving fluid transport. Line scanning confocal microscopy, which both illuminates and collects light across a one-dimensional path simultaneously, offers combined advantages of the other two approaches:[17-18] a greater speed than point-scanning and suitability for compact instrumentation for clinical applications.[19-20] An important requirement, however, is that all points of the sample passing beneath the imaging line must exhibit a uniform linear speed perpendicular to the linear

image sensor. Continuous imaging using a linear sensor (also known as a "push broom" geometry) has been previously demonstrated for image cytometry.[10] The approach presented in this paper is aligning a light sheet to a linear image sensor in an epitaxial configuration. The optical sectioning contributed by the camera sensor allows to reject the out-of-plane emission light.

A linear imaging system can continuously image cells when they are fixed on a microscope slide, but that requires a motorized stage and additional sample preparation. Microfluidics offers simplified ways to translate cell suspensions. Traditional approaches,[21-22] which include syringe pumping, do not offer a uniform flow profile across several millimeters. An on-chip dual membrane pump has been used previously to assist in cell sorting, but only to redirect flow, where the main stream is still pumped with a syringe.[23] There are various on-chip membrane pumps that can move fluid through a channel, although have not been demonstrated for cytometry.[24-25] Such pumps produce non-uniform flow profiles with either slow (nL/min) flow rates [23-24] or relatively slow speeds (0.072 mm/s),[25] and generally involve complex fabrication procedures. Besides, the need for external actuators, pumps, and check valves causes complex fabrication steps. Recent advances in microfluidics pumped by redox-magnetohydrodynamics (R-MHD) have not only demonstrated a requisite flat horizontal flow profile,[26-27] but also expanded compatibility with biological samples by using immobilized redox films at the electrode and improved linear fluid velocity.[28] On-chip R-MHD pumping is also relatively simpler to fabricate and more easily programs fluid flow than membrane-based pumps.

MHD produce a body force, $\mathbf{F_B}$ (N / m^3), when magnetic field **B** (T) interacts with ionic current density **j** (C/ s m^2) and follows the right hand rule $\mathbf{F_B = j \times B}$.[29-31] Adding redox species to an electrolyte solution facilitates conversion of electronic to ionic current without bubble

generation and electrode corrosion.[26, 32] This generates sufficient ionic current with low voltage for microfluidic propulsion in the presence of low |**B**| from a permanent magnet, but suffers from interference issues.[33-34] We have immobilized the conducting polymer poly(3,4-ethylenedioxythiophene (PEDOT) onto electrode surfaces to replace solution redox species and therefore avoid chemical interferences, achieve higher currents (and velocities), and afford easier use.[28] However, its finite charge capacity can limit operation time, and its electrodeposition from aqueous solutions onto the R-MHD electrodes is time consuming and requires a solubilizer.

Here, we provide an in-depth analysis of combining an epitaxial-light sheet confocal microscope (e-LSCM) with R-MHD transport as a unique approach to image cytometry (Figure 1). A preliminary work based on this concept was demonstrated by us previously.[35] A deep-well, MHD microfluidics chamber minimizes the risk of clogging with biological specimens. Also, electrodeposition of PEDOT from a non-aqueous solution facilitates monomer dissolution (without added solubilizer) and produces films with greatly improved MHD pumping duration than previously reported. Besides, this application benefits by the repeated change in pumping direction, which allows the PEDOT polymer to be charged and discharged repeatedly during the analysis. Therefore, this combined system offers continuous, confocal imaging without moving parts (i.e. galvanometers or acousto-optical modulators) and shows promise for a point-of-care diagnostic technology.

4.2 Experimental Section

4.2.1 Chemicals and Materials

All chemicals were reagent grade unless otherwise specified and used as received. The sources and grade of all chemicals and materials used for experiments are discussed in the Supporting Information.

4.2.2 Optical Instrumentation Assembly

Some aspects of the basic setup were reported previously.[35] The light sheet confocal fluorescence microscope uses a 445 ± 5 nm laser light source for excitation (FTEC2 440-20, Blue Sky Research, Milipitas, CA) coupled to a single mode fiber to produce a Gaussian output beam, providing up to 20 mW of optical power. To generate a light sheet, this beam has extended to fill the back aperture of the objective and subsequently passes through a cylindrical lens (200 mm focal length, Thorlabs, Newton, NJ). This extended beam is reflected by a dichroic mirror (Chroma Technologies, Bellows Falls VT) and subsequently transmitted through an objective lens (20X, 0.5 NA or 10X, 0.3 NA, Nikon where NA is the numerical aperture). After passing through the dichroic mirror, the emitted light is focused onto a linear image sensor (ELiiXA+ 8k/4k, e2v, Chelmsford, UK) by an achromatic doublet lens (150 mm, Thorlabs, Newton, NJ). The sensor at the image plane, was co-aligned with the light sheet, and featured electronically controlled binning modes to control the aperture. This has allowed the device to optically section without requiring any mechanical slit. A mechanical stage, placed below the objective, is controlled in three dimensions using motorized linear actuators (Thorlabs, Newton, NJ). A graphical user interface (GUI) in MATLAB (Mathworks, MA) used to control the imaging platform.

4.2.3 Quantitative Axial Resolution of Optical Setup

After removing the emission filter, a mirror was placed at the focal plane to measure the axial resolution of the system. The mirror was then translated ±30 μm from the focal plane in 0.5 μm increments using the z-axis linear actuator. An image was taken at each interval and the mean pixel intensity was calculated from each image, normalized to the maximum signal obtained at the 20 μm binning mode (when the mirror is directly at the focal plane), and plotted to demonstrate changing remitted signal as a function of distance from the focal plane. Laser power was adjusted and maintained constant throughout the experiment to ensure none of the images exhibited saturated pixels when the mirror was at the focal plane. Two different magnifications of 10x and 20x and three binning modes (5, 10, and 20 μm) were used to demonstrate variable axial resolution.

4.2.4 Bead Phantom

Experimental details of three-dimensional bead phantom imaging as a qualitative assessment of axial resolution are provided in the Supporting Information.

4.2.5 Electrode Chip Design

A 2 in. × 1 in. silicon-based chip consisting of coplanar, parallel gold band electrodes, 649.9 ± 0.8 μm wide and 1.50 cm long, modified by PEDOT and separated by 0.32 cm (see Figure S-1 in Supporting Information) were used for MHD experiments. Further details of electrode dimensions and the fabrication process are provided in the Supporting Information.

4.2.6 PEDOT Deposition and Characterization

PEDOT was electrodeposited using 12 successions of cyclic voltammetry (CV) at band electrodes of the chip from a solution containing 0.01 M EDOT (3,4-ethylenedioxythiophene (EDOT)) and 0.10 M $LiClO_4$ electrolyte in propylenecarbonate (PC), and subsequently characterized by CV in aqueous 0.10 M KCl. See the Supporting Information, Figure S-1, and Figure S-2 for details.

4.2.7 Solution Preparation with Beads for Studies Involving R-MHD

Each PBS tablet was dissolved in 200 mL of deionized water resulting in a "buffer" of 0.01 M phosphate (from sodium and potassium phosphates), 0.003 M potassium chloride, and 0.14 M sodium chloride of pH 7.4 at 25 ^{o}C. The solution used for diluting both microspheres and biological cells for MHD studies is called "buffer/glycerol" here and was prepared with a 60:40 v/v ratio of "buffer" and a glycerol solution (1:1 ratio of pure glycerol (>99%) and water). The resulting solution was 20% glycerol by volume. The glycerol enabled neutral buoyancy of the particles in the deep R-MHD microfluidics chamber. A solution of 500 µL of beads was spun down with a centrifuge (Model: VWR, Galaxy 7, 2000 rpm for 6 min) and the supernatant drawn off with a pipette, leaving the beads at the bottom of the centrifuge tube. A 1000 µL aliquot of "buffer/glycerol" solution was added, and the beads resuspended. This final solution used for MHD studies is referred to as the "buffer/glycerol/bead" solution.

4.2.8 Assembly of the R-MHD Microfluidics Chamber

Figure S-3 in the Supporting Information and Figure 1 here show the components of the R-MHD microfluidics chamber and the assembly on the platform of the e-LSCM and the stage of an optical microscope, respectively. The latter setup was used for fluid speed studies and calibration. To create the R-MHD microfluidics chamber, the PEDOT-modified electrode chip was inserted into the edge connector, ensuring alignment with contact pads. A free-standing PDMS gasket of 2.14 mm height with a cutout of 3.0 cm x 1.8 cm was placed on the electrode chip and defined the microfluidic chamber dimensions (Figure S-3(a) in Supporting Information). The gasket was made using a procedure similar to that reported previously, but with a different spin-coater speed.[36] This combination was positioned onto the permanent magnet so that the active band electrodes (used for pumping) were near the magnet's center. An aliquot of 1000 µL solution containing beads or leukocytes, respectively, was dispensed into the well and a coverslip was placed on top to serve as the lid. Leads from the potentiostat/galvanostat were clipped to the wires from the edge connector, to activate the selected pair of electrodes for pumping.

4.2.9 Calibration of Linear Fluid Velocity with Applied Current.

Velocities of the fluid in a horizontal plane driven by R-MHD in the enclosed microfluidics chamber were obtained by monitoring movement of beads in the buffer/glycerol/bead solution by optical microscopy. Chronopotentiometry (CP) was used in the manner illustrated in Figure S-4 in the Supporting Information to apply a constant pumping current, starting with cathodic current and stepping to anodic current, of ±150, 270, 390, 510, 630, or 750 µA between two adjacent PEDOT-modified band electrodes, where one served as

"working" and the other as the combined counter/quasi-reference electrode. The current direction switched when the cutoff voltage -1.000 V was reached and finished at +1.100 V vs. the other PEDOT-modified electrode, respectively. (These values were chosen to avoid overoxidation of PEDOT.) Bead movement was recorded with a Sony Handycam (HDR-XR 500 V, Sony electronics, Tokyo, Japan), which was interfaced to the microscope (Leica DM 2500 M, Leica Microsystems, Wetzlar, Germany). The focusing position above the chip surface was adjusted to either 1440 μm or 480 μm by lowering and raising the microscope stage. Speeds were quantified at each of these vertical positions above the chip surface by measuring the displacement of two individual beads for each experiment with particle tracking software (World-in-Motion, Physics ToolKit, Physics Curriculum and Instruction) over a given amount of time for a given current. Three series of experiments were performed: one where current was applied in order from low to high, one in order from high to low, and one with random order, for a total of six beads at each current. The average speed was plotted (plus/minus one standard deviation for N=6) as a function of the applied current to produce calibration curves at the two vertical positions.

4.2.10 Synchronization of Pumping Current and Line Period to Maintain an Image Aspect Ratio of 1:1

The camera's acquisition parameters were set to a 300 μs line period and an integration time of 12.5 μs to eliminate image saturation. To demonstrate the influence of pumping current on image quality, we started at 350 μA with increasing intervals of 50 μA. Image aspect ratio was quantified in post-processing with ImageJ (Broad Institute, USA). The ratio should be 1:1 if the bead is circular, which ensures that the line period is matched to the linear translation speed.

4.2.11 Sample Preparation and Imaging of Leukocytes

Leukocytes were obtained from whole blood as described in the Supporting Information. They were then suspended in the isotonic PBS/BSA solution and subsequently stained with acridine orange dye at a concentration of 20 μg mL^{-1}. Following a 5 min incubation period at 25° C, the stained leukocytes were washed twice in isotonic PBS prior to resuspension in 1000 μL of the buffer/glycerol solution. This leukocyte solution was then added to the well inside the PDMS cutout and covered with a coverslip to form the R-MHD microfluidics chamber. Images were acquired at 350 μs line period, 125 μs exposure time, and 0 dB of gain. A 20x objective was used with a 5 μm x 5 μm binning mode for the linear sensor, while translating the specimens with R-MHD by applying 500 μA.

4.3 Results and Discussion

4.3.1 Electrochemical Behavior and Flow Performance of R-MHD

To achieve longer pumping times for the image cytometry application and simplify the modification of the pumping electrodes than previously reported by our laboratory,[28] we electropolymerized PEDOT from a solution of 0.01 M EDOT in 0.10 M $LiClO_4$/PC instead of in 0.01 M SDS/0.10 M KCl/water. The exceptional solubility of EDOT in PC eliminates the 1 h sonication period and provides highly reproducible deposition of a thick layer of PEDOT. More PEDOT makes more charge available and therefore a volume element can be pumped farther before recharging the polymer. The CV response of a PEDOT-modified electrode in 0.10 M KCl (Figure S-2 in the Supporting Information) is similar to that for the charging of a double layer, as shown previously for this conducting polymer.[28] The "charging current" is 823 times that for a

bare electrode, which reflects the anticipated improvement of the maximum pumping speed by the PEDOT.

Characterization of the PEDOT films in the buffer/glycerol solution by CA further predicts performance of R-MHD microfluidics. A CA response obtained by holding the potential at -0.800 V vs. Ag/AgCl (saturated KCl) for 20 s followed by stepping to +0.800 V and holding for another 20 s is shown in Figure S-5 in the Supporting Information. It yields a maximum electronic current density of 84.07 ± 0.08 mA/cm^2 and establishes the upper limit of applied current values for subsequent pumping studies. Integrating the current over 20 s gives a total charge of 88.6 ± 1.4 mC/cm^2, which corresponds to a capacitive density of 55.4 ± 0.9 mF/cm^2 (for a 1.6 V excursion). These are about 1.5 and 4 times the area-normalized electronic current and capacitance values, respectively, than films reported by us previously.[28] Therefore, the maximum fluid speed and distance pumped should be improved proportionally for similar chamber dimensions.

To interface R-MHD pumping with the line sheet acquisition, it was necessary to evaluate the uniformity of the horizontal flow profile and the predictable nature of the velocity under the same conditions as those used for the image cytometry. The setup shown in Figure S-3 in the Supporting Information used the buffer/glycerol/bead solution in the deep microfluidics chamber at two currents applied between the pair of parallel PEDOT-modified band electrodes. Examples of chronopoteniometric responses during forward and reverse current steps are provided in Figure S-4 in the Supporting Information. PIV analysis reveals a uniform fluid velocity (0.16% to 2.9% RSD, depending on speed and vertical position) across a horizontal region sufficiently wide (924 μm) for imaging by e-LSCM. (See Figure 1(g), Figure S-6, and data analysis in the Supporting Information). Calibration curves in Figure 2(a) show a linear

dependence of MHD fluid speed at two vertical positions on the applied electronic current. The linear behavior is consistent with previous measurements of speed with current for other cell geometries, electrolytes, and electrode and gap dimensions.[18] Slopes of 1.84 ± 0.05 μm s^{-1} μA^{-1} and 2.44 ± 0.07 μm s^{-1} μA^{-1} were obtained at 480 μm and 1440 μm above the electrode chip, respectively. Speeds as fast as 1395 ± 32 μm/s and 1818 ± 55 μm/s, respectively, could be sustained with an applied current of 750 μA (7.70 mA/cm^2, only 9% of the maximum current density) and are a factor of 2.4 and 3 times the transient maximum speeds previously reported.[28] While the flow field is relatively flat (constant) between active electrodes for a given horizontal plane, its profile in the z-axis (i.e. when viewed from the side) can exhibit a parabolic-like shape, as was also observed in previous studies.[24,25] We attribute this largely to higher viscous forces at the walls of the chamber. Therefore, the fluid speed at 1440 μm, the more central vertical position between the floor and lid of the chamber, was faster than at 480 μm for the same current. Consequently, as long as the vertical position of the viewing region is known, the corresponding calibration curve predicts the fluid speed for a given applied electronic current. A different speed for a different height can be compensated for by adjustment of the image sensor frame rate to maintain image aspect ratio and reduce distortion.

An increased applied current consumes charge in the PEDOT film faster, and hence, a fluid element flows for a shorter duration but across the same distance. For example, the duration is 62 ±1 s at 150 μA and 10.4 ± 0.3 s at 750 μA. This behavior would translate to a *net* throughput for image cytometry that is the same for a given pumping direction, regardless of the throughput *rate*. Figure 2(b) shows a highly linear correlation (R^2 = 1.000) between the duration for MHD flow (between -1.000 V and +1.100 V vs. the other pumping PEDOT-electrode) and the inverse of the applied current.

This behavior can be modeled with a simple RC equivalent circuit as depicted in Figure S-7 with a derivation and further discussion in the Supporting Information. The resulting equation is

$$t = \left(-\frac{1}{i_2} \right) \left(C_T \left(E(t) - E(0) \right) \right) - \left(2RC_T \right)$$

where t is the pumping duration for a single direction (i.e. without recharging the PEDOT film), i_2 is the applied current between the electrodes whose potential difference changes from E(0) (at t = 0) to E(t) (i.e. the voltage range), and C_T is the total capacitance of the two PEDOT-modified electrodes in series.

Using this equation, a capacitance value, C, for each electrode (where $C_T = C/2$) of 51.14 ± 0.09 mF/cm^2 (area = 0.0974 cm^2) and a total resistance, R, of 1552 ± 14 ohms (which includes electrode, film, solution, and connector resistances and leads to diminished pumping duration) were obtained from the slope and the negative y-intercept, respectively, of the plot in Figure 2(b). The resistance is constant for all applied currents and suggests that the same amount of charge is accessible, regardless of the demands on ion motion to compensate the film's redox chemistry. Improvements to pumping duration are possible by using larger pumping electrodes and thicker PEDOT films, which increase capacitance and therefore the amount of charge for a given voltage range. We are planning a future paper to report performance of PEDOT films in different electrolytes that are deposited under a diverse set of conditions and have various thicknesses. For the image cytometry application herein, however, PEDOT was deposited on all electrodes under one set of conditions that produce robust films and pumping consistency.

4.3.2 Performance of e-LSCM

A key feature of the image cytometry approach presented here is the ability to image particles epitaxially and at a particular height (Figure 1(d)), while excluding those above and below this plane. Thus, requirements of the sample and the chamber can be fairly flexible in terms of depth (accommodating a large range of particle sizes and concentrations) and transparency (one side can be opaque). Optical sectioning within the flow field is enabled when the fluorescence image (produced upon illuminating the sample with a light sheet of excitation light) falls across the linear camera's sensor (Figure 1(b)). Figure S-8 in the Supporting Information shows how fluorescence imaging with the sensor's 5 μm pixels for the three different binning modes allows axial resolution to change without affecting the lateral resolution. We validate the axial resolution performance (the vertical thickness of this section) of our system both quantitatively and qualitatively under different magnification and sensor binning modes in Figure S-9 and Table S1 of the Supporting Information.

Data processing can be used to provide additional tuning of axial resolution by setting a cutoff threshold for intensity. Figure 3(a) illustrates how changing the threshold from 50% (i.e. FWHM) to 20% of the maximum intensity of axial sectioning ability of the 20X objective and 5 x 5 μm binning mode will change the axial resolution from 4.5 μm to 9.0 μm, respectively. Figure S-10 visualizes the increased number of detectable particles in a bead phantom for four intensity thresholds. The intensity threshold has more practical meaning when transformed into a signal-to-background ratio (S/B)–the mean pixel intensity at the threshold divided by the background intensity measured at 30 μm from the focal plane. Assuming a concentration of uniformly fluorescing objects, one can estimate the impact of S/B on throughput of detectable particles. Quantitative results are shown in Figure 3(b) for both 10X and 20X objectives and

show that throughput can be changed by at least four times using this approach. However, if the particles do not display similar fluorescence intensity or fluorescence distribution, then this approach can cause bias in the particles counted or image contrast.

We selected the conditions giving the best axial sectioning ability (20X objective and 5 x 5 μm binning mode of sensor) and optimal results with the bead phantom for integrating e-LSCM with R-MHD. Experimental parameters for successful implementation were confirmed with fluorescent beads before imaging leukocytes. The R-MHD device was placed in the sample position as shown in Figure 1(c), filled with the buffer/glycerol/bead mixture, and activated as described above to induce flow as illustrated in Figure 1(e)-(g).

The image aspect ratio was quantified as a function of applied current that drives the R-MHD microfluidics. We have previously demonstrated the importance of synchronization of a push broom scanning source with data acquisition of the linear sensor to ensure image quality.[10] Figure 4(a) shows the convergence of aspect ratio to an R-MHD current of 850 μA when a line exposure period was set to 300 μs. Figure 4(b) shows resulting images of fluorescent microspheres with high lateral resolution. The diffraction limited lateral resolution for the 10X and 20X objectives, given by the formula $0.61\lambda_{em}/NA$ (where λ_{em} is the emission wavelength), is 1.0 μm and 0.6 μm, respectively.

Figure S-11 in the Supporting Information and Figure 3(c) and (d) show the impact of varying the threshold intensity to further define the extent that beads above and below the focal plane are imaged for the combined e-LSCM/R-MHD instrument. The results are similar to those obtained for the bead phantom. Using intensity-based thresholding alone is effective for samples of uniform fluorescence emission intensity (as with polystyrene fluorescent microspheres), but

this approach may be more challenging to apply to fluorescently stained, intact cells, due to the cell-to-cell variations in dye uptake. Optical sectioning, as applied using our e-LSCM approach, is more broadly applicable to these biological specimens. The theoretical throughputs of particles for our conditions of a 20x objective (472 μm lateral field of view), a concentration of 455 particles/μL, and a fluid speed of 1.24 mm/s, are 1.20 to 9.60 particles/s for axial resolutions from 4.5 μm to 36 μm, respectively.

Because of the rapid acquisition capability of the instrumentation, the theoretical maximum throughput is 4860 particles/s and only limited by the speed at which a hexagonal arrangement of touching particles can pass through the lateral field of view (see Supporting Information). There is a particle concentration above which the imaging rate no longer improves, and which depends on (1) chamber depth of the focal plane and (2) the size of the particles. This is because particles in a focal plane deeper in the chamber are more likely to be blocked by ones in higher positions and fewer particles occupy the same space when they are larger, respectively. This limiting concentration, for example, is 7.36×10^6 particles/mL for 15-μm particles at 1440 μm from the chip surface (700 μm down from the observation window). The maximum possible throughput decreases with decreasing fluid speed and axial resolution and with increasing particle diameter and chamber depth of the focal plane. Values for our highest-measured R-MHD speeds of 2.0 mm/s for 15-μm diameter particles at different focal plane positions and axial resolutions in the chamber are provided in the Supporting Information and illustrated in Figure S-12. For example, the maximum possible throughputs are 13 and 31 particles/s at 700 μm down from the observation window and for axial resolutions of 4.5 and 36 μm, respectively.

4.3.3 Imaging Leuokocytes with Combined e-LSCM and R-MHD

Figure 5 demonstrates the integrated microfluidic system's ability to image biological samples. Three examples of the major subpopulations of leukocytes (lymphocytes, monocytes, and granulocytes) from a blood sample are shown. These cells were stained using acridine orange and imaged by driving them past the e-LSCM in the microfluidics chamber with R-MHD. Each type of leukocyte can be easily identified, as shown when comparing the images to those of similar cells visualized with conventional Giemsa staining. Faint horizontal lines can be seen in the images that indicate some "pixilation" due to individual line scans. The subcellular structure of the leukocytes is at the resolution limit of the experimental microscopy platform as configured, but still demonstrate clear subjective differences between cell types.

4.4 Conclusions

Merging R-MHD and e-LSCM for image cytometry was evaluated in terms of performance using fluorescent microspheres and demonstrated successfully for the differentiation of leuokocytes. This approach offers several advantages over other high spatial resolution microfluidic systems reported previously. The bulk of a mechanical syringe pump and controller are replaced with programmable electronics that can be powered by batteries. Device design and construction are simplified because the R-MHD microfluidics do not require sidewalls to be built into the device and the confocal feature eliminates the need for shallow channels and sample focusing, tolerating three-dimensional cell suspensions. Throughput is enhanced because lateral imaging over large areas is possible from the wide parallel flow path and tunable fluid speeds faster than 0.60 mm/s are possible (1.24 mm/s used here). For example, we estimate a maximum throughput of 73 times that of Simmonet et al.[10] (for one-third of the

particle concentration), and 1.5 times the throughput at a depth of 700 μm and for only 1/140th of the concentration. In addition, our system works with larger particle sizes. Also, the fluid speed is eight times that of Zhu et al.[12] while maintaining a spatial lateral resolution of one-third and with optical components that can be adapted for handheld instrumentation.

The continuous image cytometry approach that we have demonstrated here is well-suited to miniaturization without compromising performance. There has been significant advancement in recent years in developing precision, miniaturized optics and optical assemblies for various microscopic, endoscopic, and point of care applications which suggest a path toward this end [37]. Tkaczyk et al. have recently described an all-plastic millimeter-scale precision endoscopic imaging objective capable of nonlinear microscopy which could be adapted to greatly reduce the size, weight, and cost of a point-of-care imaging system based on technology described in this manuscript.[38] Because shaping a Gaussian beam from a fiber-coupled laser only requires a single cylindrical lens, further miniaturization using similar lens manufacturing approaches would be trivial. Large numerical aperture objectives at relatively low magnification can be constructed using high refractive index materials, which would further improve volumetric imaging speed without sacrificing spatial resolution or miniaturization potential. Other point-of-care platforms have merged low-cost optical elements with existing, consumer-grade imaging systems and processing elements, such as smartphones. Such systems offer extremely low-cost access to not only image acquisition capabilities, but also to on-board image and spectroscopy classification tools, which could be used to provide leukocyte sub-population analysis.[39-40] Miniaturization of optical systems for point-of-care applications presents unique challenges as design trade-offs must be made, which may lead to the emergence of new spherical or chromatic aberrations. However, ongoing work to objectively classify image data in these miniaturized imaging systems

using known training data sets and machine learning algorithms has proven highly successful in accurately predicting–without human intervention–the presence of epithelial dysplasia in both oral epithelium and in Barrett's esophagus.[41-42] Applying these advancements to the novel platform described in this manuscript could lead to the development of highly impactful point-of-care devices for clinical decision-making across a broad array of biomedical applications.

4.5 Supporting Information

Supporting information includes experimental details of chemicals and materials, electrode chip design, PEDOT (poly 3,4-ethylenedioxythiophene) electrodeposition and characterization by cyclic voltammetry (CV), leukocyte preparation, device setup for performing magnetohydrodynamics (MHD), chronoamperometric and chronocoulometric responses of PEDOT film-modified electrodes, chronopotentiometry (CP) responses for pumping experiments, derivation of pumping time as a function of applied current, calculation of maximum particle concentration and throughput, fluid flow tracked by particle image velocimetry analysis, bead phantom imaging, binning patterns of the linear sensor, axial resolution measurements as a function of magnification, sensor pixel width, and intensity cutoff for phantom and R-MHD setups, a table comparing theoretical and measured axial resolutions. This material is available free of charge via the Internet at http://pubs.acs.org.

4.6 Acknowledgments

We are grateful for financial support from the National Science Foundation (CBET-1336853), the Women's Giving Circle, and the Arkansas Bioscience Institute, the major research component of the Arkansas Tobacco Settlement Proceeds Act of 2000.

4.7 References

(1) Porichis, F.; Hart, M. G.; Griesbeck, M.; Everett, H. L.; Hassan, M.; Baxter, A. E.; Lindqvist, M.; Miller, S. M.; Soghoian, D. Z.; Kavanagh, D. G. High-throughput detection of miRNAs and gene-specific mRNA at the single-cell level by flow cytometry. *Nat. Commun.* **2014,** *5*.

(2) Edwards, B. S.; Oprea, T.; Prossnitz, E. R.; Sklar, L. A. Flow cytometry for high-throughput, high-content screening. *Curr. Opin. Chem. Biol.* **2004,** *8* (4), 392-398.

(3) Basiji, D. A.; Ortyn, W. E.; Liang, L.; Venkatachalam, V.; Morrissey, P. Cellular image analysis and imaging by flow cytometry. *Clin. Lab Med.* **2007,** *27* (3), 653-670.

(4) Schonbrun, E.; Gorthi, S. S.; Schaak, D. Microfabricated multiple field of view imaging flow cytometry. *Lab Chip* **2012,** *12* (2), 268-273.

(5) Mohan, K.; Mondal, P. P. Light sheet based imaging flow cytometry on a microfluidic platform. *Microsc. Res. Tech.* **2013,** *76* (11), 1101-1107.

(6) Gordonov, S.; Hwang, M. K.; Wells, A.; Gertler, F. B.; Lauffenburger, D. A.; Bathe, M. Time series modeling of live-cell shape dynamics for image-based phenotypic profiling. *Integr. Biol.* **2016,** *8* (1), 73-90.

(7) Blasi, T.; Hennig, H.; Summers, H. D.; Theis, F. J.; Cerveira, J.; Patterson, J. O.; Davies, D.; Filby, A.; Carpenter, A. E.; Rees, P. Label-free cell cycle analysis for high-throughput imaging flow cytometry. *Nat. Commun.* **2016,** *7*.

(8) MacAulay, C.; Poh, C. F.; Guillaud, M.; Williams, P. M.; Laronde, D. M.; Zhang, L.; Rosin, M. P. High throughput image cytometry for detection of suspicious lesions in the oral cavity. *J. Biomed. Opt.* **2012,** *17* (8), 0860041-08600411.

(9) Cerignoli, F.; Charlot, D.; Whittaker, R.; Ingermanson, R.; Gehalot, P.; Savchenko, A.; Gallacher, D. J.; Towart, R.; Price, J. H.; McDonough, P. M. High throughput measurement of Ca 2+ dynamics for drug risk assessment in human stem cell-derived cardiomyocytes by kinetic image cytometry. *J. Pharmacol. Toxicol. Methods* **2012,** *66* (3), 246-256.

(10) Simonnet, C.; Groisman, A. High-Throughput and High-Resolution Flow Cytometry in Molded Microfluidic Devices. *Anal. Chem.* **2006,** *78*, 5653-5663.

(11) Wang, J.; Bao, N.; Paris, L. L.; Geahlen, R. L.; Lu, C. *Anal. Chem.* **2008,** *80*, 9840-9844.

(12) Zhu, H.; Mavandadi, S.; Coskun, A. F.; Yaglidere, O.; Ozcan, A. Optofluidic Fluorescent Imaging Cytometry on a Cell Phone. *Anal. Chem.* **2011,** *83*, 6641-6647.

(13) Pichaandi, J.; Boyer, J.-C.; Delaney, K. R.; van Veggel, F. C. Two-photon upconversion laser (scanning and wide-field) microscopy using Ln3+-doped NaYF4 upconverting nanocrystals: a critical evaluation of their performance and potential in bioimaging. *J. Phys. Chem. C* **2011,** *115* (39), 19054-19064.

(14) Grebenik, E. A.; Nadort, A.; Generalova, A. N.; Nechaev, A. V.; Sreenivasan, V. K.; Khaydukov, E. V.; Semchishen, V. A.; Popov, A. P.; Sokolov, V. I.; Akhmanov, A. S. Feasibility study of the optical imaging of a breast cancer lesion labeled with upconversion nanoparticle biocomplexes. *J. Biomed. Opt.* **2013,** *18* (7), 076004-076004.

(15) Gainer, C. F.; Utzinger, U.; Romanowski, M. Scanning two-photon microscopy with upconverting lanthanide nanoparticles via Richardson-Lucy deconvolution. *J. Biomed. Opt.* **2012,** *17* (7), 0760031-0760037.

(16) Yu, M.; Li, F.; Chen, Z.; Hu, H.; Zhan, C.; Yang, H.; Huang, C. Laser scanning up-conversion luminescence microscopy for imaging cells labeled with rare-earth nanophosphors. *Anal. Chem.* **2009,** *81* (3), 930-935.

(17) Higgins, L. M.; Zevon, M.; Ganapathy, V.; Sheng, Y.; Tan, M. C.; Riman, R. E.; Roth, C. M.; Moghe, P. V.; Pierce, M. C. Line-scanning confocal microscopy for high-resolution imaging of upconverting rare-earth-based contrast agents. *J. Biomed. Opt.* **2015,** *20* (11), 110506-110506.

(18) Wolleschensky, R.; Zimmermann, B.; Kempe, M. High-speed confocal fluorescence imaging with a novel line scanning microscope. *J. Biomed. Opt.* **2006,** *11* (6), 064011-064011-14.

(19) Sabharwal, Y. S.; Rouse, A. R.; Donaldson, L.; Hopkins, M. F.; Gmitro, A. F. Slit-scanning confocal microendoscope for high-resolution in vivo imaging. *Appl. Opt.* **1999,** *38* (34), 7133-7144.

(20) Larson, B.; Abeytunge, S.; Rajadhyaksha, M. Performance of full-pupil line-scanning reflectance confocal microscopy in human skin and oral mucosa in vivo. *Biomed. Opt. Express* **2011,** *2* (7), 2055-2067.

(21) Cheng, Y.; Ye, X.; Ma, Z.; Xie, S.; Wang, W. High-throughput and clogging-free microfluidic filtration platform for on-chip cell separation from undiluted whole blood. *Biomicrofluidics* **2016,** *10* (1), 014118.

(22) Chung, A. J.; Hur, S. C. *High-Speed Microfluidic Manipulation of Cells*, Wiley-VCH Verlag GmbH & Co. KGaA, Weinheim, Germany: 2015.

(23) Sakuma, S.; Kasai, Y.; Hayakawa, T.; Arai, F. On-chip cell sorting by high-speed local-flow control using dual membrane pumps. *Lab Chip* **2017,** *17*, 2760-2767.

(24) Eddings, M. A.; Gale, B. K. A PDMS-based gas permeation pump for on-chip fluid handling in microfluidic devices. *J. Micromech. Microeng.* **2006,** *16*, 2396-2402.

(25) Kim, J. H.; Lau, K. T.; Shepherd, R.; YanzheWu; GordonWallace; Diamond, D. Performance characteristics of a polypyrrole modified polydimethylsiloxane (PDMS) membrane based microfluidic pump. *Sens. Actuat. A* **2008,** *148*, 239-244.

(26) Anderson, E. C.; Weston, M. C.; Fritsch, I. Investigations of redox magnetohydrodynamic fluid flow at microelectrode arrays using microbeads. *Anal. Chem.* **2010,** *82* (7), 2643-2651.

(27) Sahore, V.; Fritsch, I. Flat Flow Profiles Achieved with Microfluidics Generated by Redox-Magnetohydrodynamics. *Anal. Chem.* **2013,** *85* (24), 11809-11816.

(28) Nash, C. K.; Fritsch, I. Poly (3, 4-ethylenedioxythiophene)-Modified Electrodes for Microfluidics Pumping with Redox-Magnetohydrodynamics: Improving Compatibility for Broader Applications by Eliminating Addition of Redox Species to Solution. *Anal. Chem.* **2016,** *88* (3), 1601-1609.

(29) Davidson, P. A. *An introduction to magnetohydrodynamics*, Cambridge university press: 2001.

(30) Grant, K. M.; Hemmert, J. W.; White, H. S. Magnetic field-controlled microfluidic transport. *J. Am. Chem. Soc.* **2002,** *124* (3), 462-467.

(31) Leventis, N.; Gao, X. Magnetohydrodynamic electrochemistry in the field of Nd-Fe-B magnets. Theory, experiment, and application in self-powered flow delivery systems. *Anal. Chem.* **2001,** *73* (16), 3981-3992.

(32) Aguilar, Z. P.; Arumugam, P. U.; Fritsch, I. Study of magnetohydrodynamic driven flow through LTCC channel with self-contained electrodes. *J. Electroanal. Chem.* **2006,** *591*, 200-209.

(33) Weston, M. C.; Nash, C. K.; Fritsch, I. Redox-magnetohydrodynamic microfluidics without channels and compatible with electrochemical detection under immunoassay conditions. *Anal. Chem.* **2010,** *82* (17), 7068-7072.

(34) Cheah, L. T.; Fritsch, I.; Haswell, S. J.; Greenman, J. Evaluation of heart tissue viability under redox-magnetohydrodynamics conditions: Toward fine-tuning flow in biological microfluidics applications. *Biotechnol. Bioeng.* **2012,** *109* (7), 1827-1834.

(35) Hutcheson, J. A.; Khan, F. Z.; Powless, A. J.; Benson, D.; Hunter, C.; Fritsch, I.; Muldoon, T. J. A light sheet confocal microscope for image cytometry with a variable linear slit detector, *Proc. SPIE*. **2016**, 9720, 97200U, DOI: https://doi.org/10.1117/12.2211164

(36) Lewis, P. M.; Sheridan, L. B.; Gawley, R. E.; Fritsch, I. Signal Amplification in a Microchannel from Redox Cycling with Varied Electroactive Configurations of an Individually-Addressable Microband Electrode Array. *Anal. Chem.* **2010,** *82* (5), 1659-1668.

(37) Kester, R. T.; Christenson, T.; Kortum, R. R.; Tkaczyk, T. S. Low cost, high performance, self-aligning miniature optical systems. *Appl. Opt.* **2009,** *48* (18), 3375-3384, DOI: 10.1364/ao.48.003375.

(38) Kyrish, M.; Utzinger, U.; Descour, M. R.; Baggett, B. K.; Tkaczyk, T. S. Ultra-slim plastic endomicroscope objective for non-linear microscopy. *Opt. Express* **2011,** *19* (8), 7603-7615, DOI: 10.1364/oe.19.007603.

(39) Zhu, H.; Isikman, S. O.; Mudanyali, O.; Greenbaum, A.; Ozcan, A. Optical imaging techniques for point-of-care diagnostics. *Lab Chip* **2013,** *13* (1), 51-67.

(40) D'Ambrosio, M. V.; Bakalar, M.; Bennuru, S.; Reber, C.; Skandarajah, A.; Nilsson, L.; Switz, N.; Kamgno, J.; Pion, S.; Boussinesq, M.; Nutman, T. B.; Fletcher, D. A. Point-of-care quantification of blood-borne filarial parasites with a mobile phone microscope. *Sci. Transl. Med.* **2015,** *7* (286), 286re4-286re4, DOI: 10.1126/scitranslmed.aaa3480.

(41) Muldoon, T. J.; Thekkek, N.; Roblyer, D.; Maru, D.; Harpaz, N.; Potack, J.; Anandasabapathy, S.; Richards-Kortum, R. Evaluation of quantitative image analysis criteria for the high-resolution microendoscopic detection of neoplasia in Barrett's esophagus. *J. Biomed. Opt.* **2010,** *15* (2), 026027-7, DOI: 10.1117/1.3406386.

(42) Muldoon, T. J.; Roblyer, D.; Williams, M. D.; Stepanek, V. M.; Richards-Kortum, R.; Gillenwater, A. M. Noninvasive imaging of oral neoplasia with a high-resolution fiber-optic microendoscope. *Head Neck* **2012,** *34* (3), 305-12, DOI: 10.1002/hed.21735.

4.8 Figures

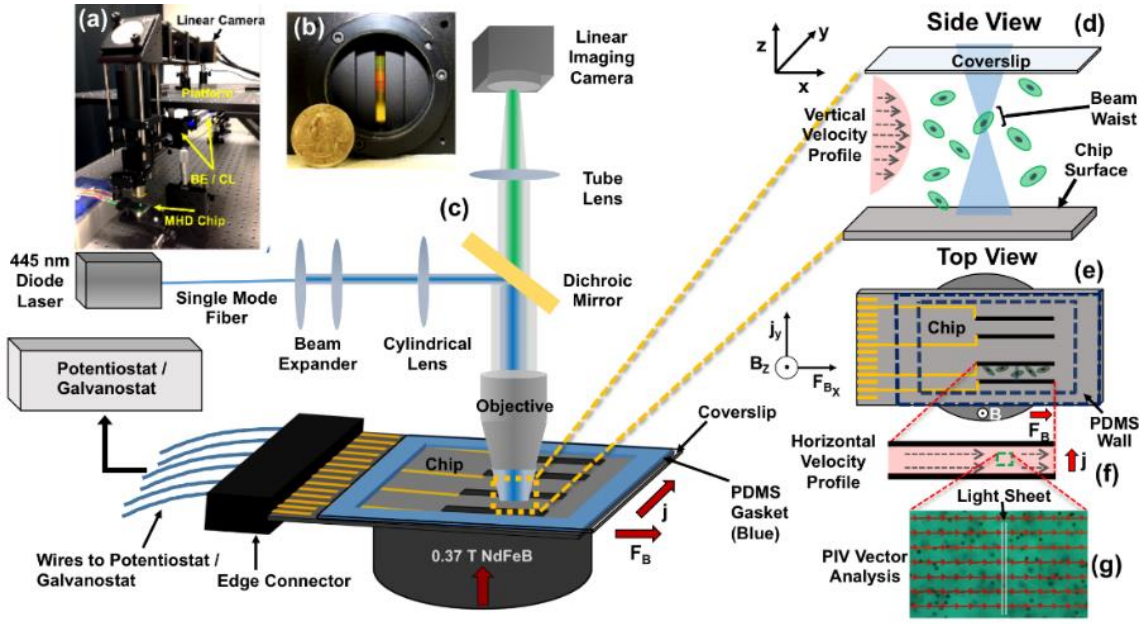

Figure 1: The two interfaced technologies. Photographs of (a) the complete e-LSCM/MHD platform and (b) the linear sensor. (c) Simplified schematic of the e-LSCM light path in epitaxial configuration and the R-MHD setup placed at the sample plane. (d) Expanded side view with the coordinate system of a vertical cross section of fluid between the electrode chip and glass lid (a coverslip), showing a biological cell at the beam waist at a specific height from the chip's surface and the expected non-uniform vertical flow profile. (e) Top-down schematic of the R-MHD chip on the magnet with electrodes 1 and 2 activated for pumping and placement of PDMS gasket. The coordinate system applies to (e) through (g). (f) Expanded top-down schematic illustrating the expected flat horizontal flow profile from $\mathbf{F_B}$ between activated electrodes that results from the cross product of **j** and **B**. (g) Vectors showing horizontal fluid velocities experimentally obtained from monitoring bead movement (experimental details in Figure S-5 of Supporting Information). Line sheet is to-scale and superimposed over image to illustrate illumination over the region having a flat fluid profile.

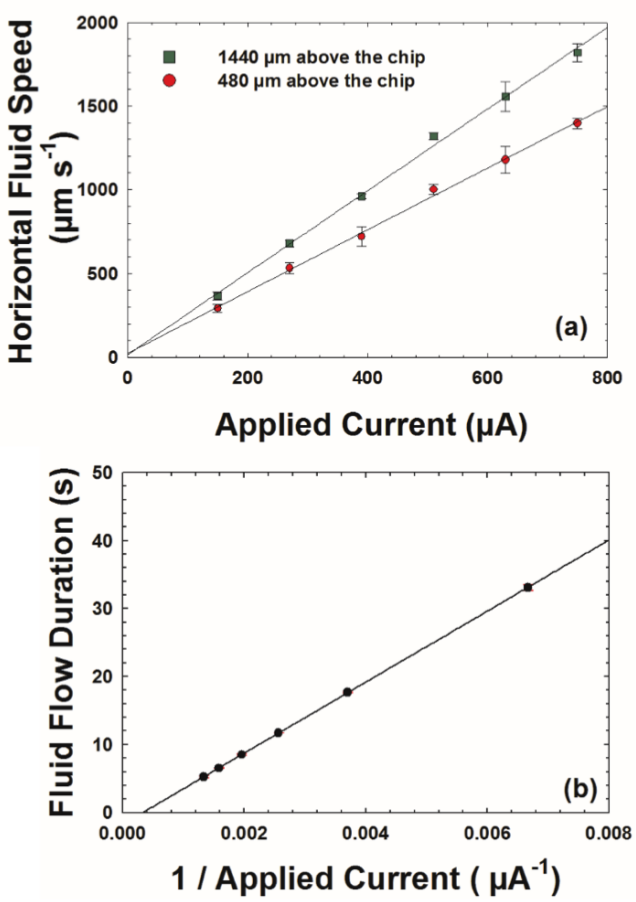

Figure 2: (a) Calibration curves of fluid speed based on bead motion as a function of applied current between pumping electrodes at two different vertical positions above the electrode chip (480 μm and 1440 μm). Least squared analysis yields: $|v_x| = (2.44 \pm 0.07\ \mu m\ s^{-1}\ \mu A^{-1})\ |i| + (16.35 \pm 32.58\ \mu m\ s^{-1})$ with $R^2 = 0.9971$ for 1440 μm above the chip surface and $|v_x| = (1.84 \pm 0.05\ \mu m\ s^{-1}\ \mu A^{-1})\ |i| + (23.42 \pm 23.14\ \mu m\ s^{-1})$ with $R^2 = 0.9974$ for 480 μm above the chip surface. **(b)** The maximum pumping time (fluid flow duration in a single direction) decreases with increasing applied current between pumping electrodes, because a higher current (i.e. faster speed) consumes charge faster than a lower current (i.e. slower speed). Least squared analysis yields: fluid flow duration $= (5230.0 \pm 9.6\ \mu A\ s)|i^{-1}| - (7.73 \pm 0.03\ s)$ and $R^2 = 1.000$.

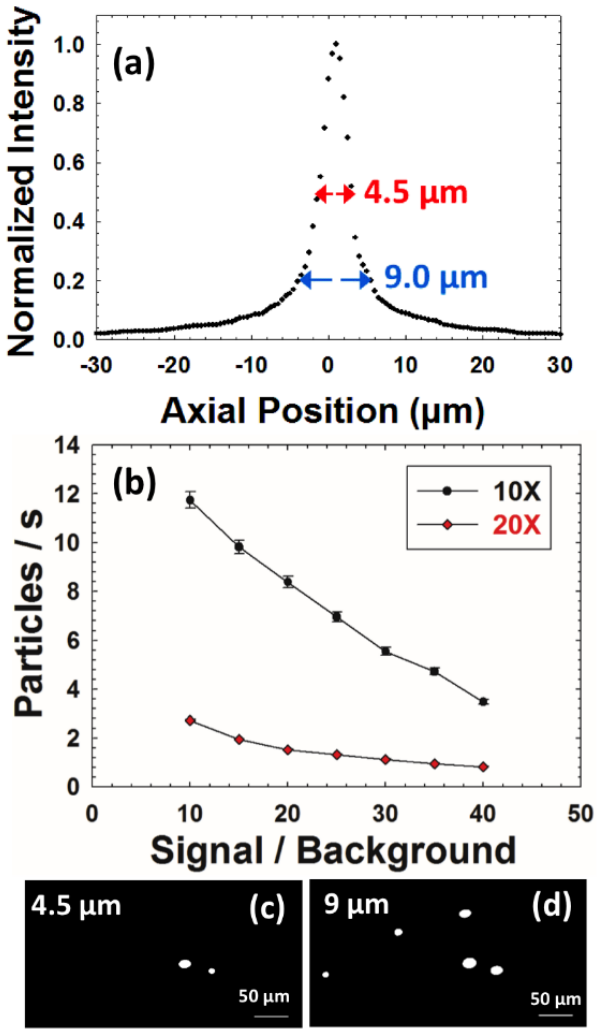

Figure 3: Performance characteristics of the e-LSCM system. A quantitative example of optical sectioning is shown in (a) for 20x magnification and 5 µm × 5 µm binning and is in the form of light intensity (with emission filter removed) as a function of the displacement of a mirror above and below the focal plane (±30 µm). Plots in (b) are derived from measurements depicted in (a) for 20× and at 10× magnification (not shown here). The theoretical particle throughput is plotted for different threshold intensities that are expressed in the form of signal/background (S/B) values. Examples of bead images obtained with R-MHD (1.24 mm/s), for 454.54 particles/µL, and at 20× magnification and 5 µm x 5 µm binning size illustrate the impact of intensity thresholding conditions for an axial resolution of (c) 4.5 µm and in (d) 9.0 µm.

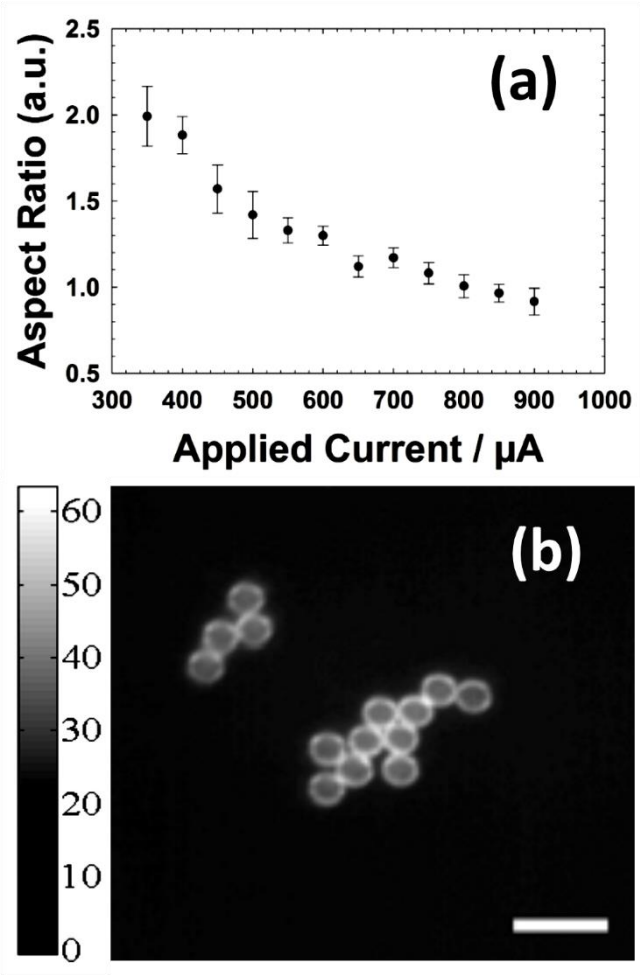

Figure 4: (a) The relationship of aspect ratio to applied current when the line period is 300 µs. (b) The image with an aspect ratio of 1:1 for microspheres was obtained with the e-LSCM/R-MHD platform by using the parameters in the plot. Scale bar is 30 µm. (Fig. 4(b) reprinted with permission from Hutcheson, J. A.; Khan, F. Z.; Powless, A. J.; Benson, D.; Hunter, C.; Fritsch, I.; Muldoon, T. J., "A light sheet confocal microscope for image cytometry with a variable linear slit detector" in High-Speed Biomedical Imaging and Spectroscopy: Toward Big Data Instrumentation and Management, SPIE, vol 9720, 2016. Copyright 2016 SPIE.)

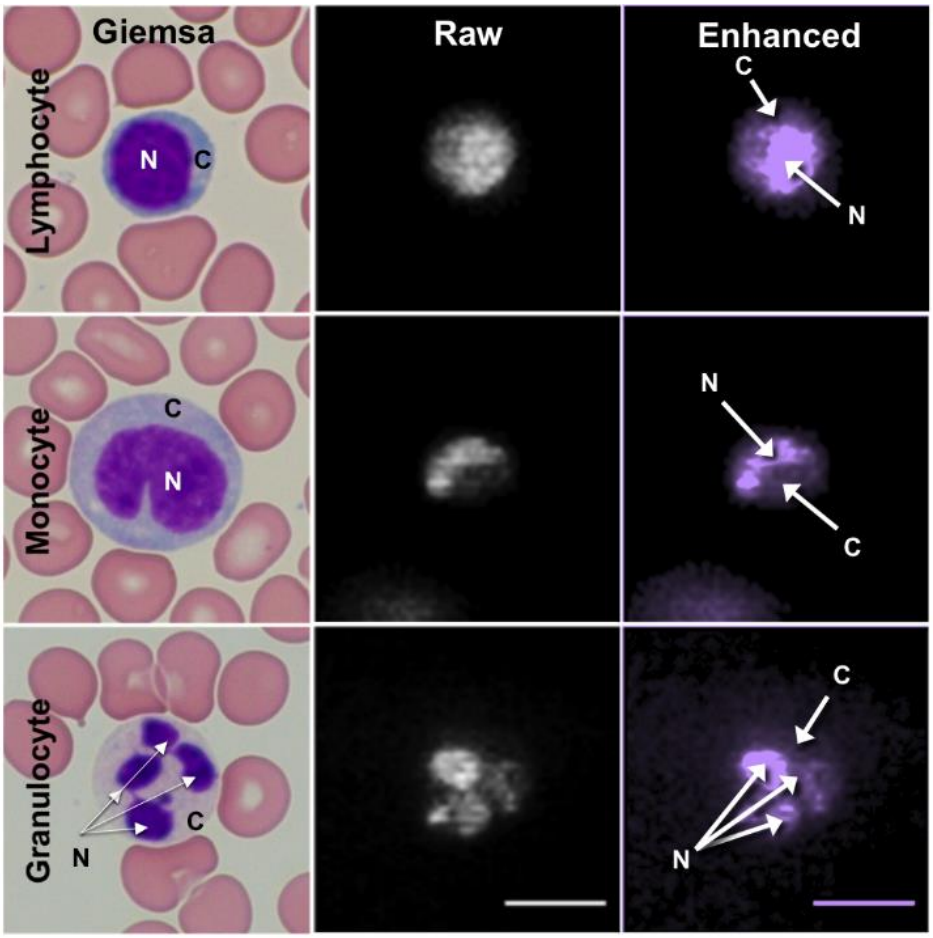

Figure 5: Images of three types of leukocytes. Left column: Giemsa-stained cells. Middle column: Images of acridine orange-stained leukocytes obtained in the R-MHD microfluidics chamber with e-LSCM to demonstrate high-resolution imaging of biological samples. Right column: Contrast-enhanced and colorized images to show detail. Morphologic features are annotated (N = nucleus, C = cytoplasm). Note the presence of multilobar nucleai in granulocytes. Scale bar is 10 µm.

4.9 Appendix: Biosafety Approval Letter

UNIVERSITY OF ARKANSAS

Office of Research Compliance

March 26, 2018

MEMORANDUM

TO:	Dr. Timothy Muldoon
FROM:	Bob Beitle, Acting Biosafety Committee Chair
RE:	Protocol Modification
PROTOCOL #:	14008
PROTOCOL TITLE:	Imaging of morphologic and colorimetric features in oral epithelial cells, blood, and urine
APPROVED PROJECT PERIOD:	**Start Date** August 8, 2013 **Expiration Date** August 7, 2019

The Institutional Biosafety Committee (IBC) has approved your request, dated February 14, 2018, to modify Protocol # 14008, “Imaging of morphologic and colorimetric features in oral epithelial cells, blood, and urine”.

The IBC appreciates your assistance and cooperation in complying with University and Federal guidelines for research involving hazardous biological materials.

1424 W. Martin Luther King, Jr. • Fayetteville, AR 72701
Voice (479) 575-4572 • Fax (479) 575-6527

4.10 Appendix: Supporting Letter

College of Engineering
Department of Biomedical Engineering

July 15, 2019

To Whom It May Concern:

This letter is to confirm Md Foysal Zahid Khan was not involved in handling the biological part of the work described within chapter 4, Redox-Magnetohydrodynamically Controlled Fluid Flow with Poly (3,4Ethylenedioxythiophene) (PEDOT) Coupled to an Epitaxial Light Sheet Confocal Microscope for Image Cytometry Applications.

Sincerely,

Timothy J. Muldoon, M.D., Ph.D.
Associate Professor
Department of Biomedical Engineering
University of Arkansas
tmuldoon@uark.edu

4.S Supporting Information: Redox-Magnetohydrodynamically Controlled Fluid Flow with Poly(3,4-Ethylenedioxythiophene) (PEDOT) Coupled to an Epitaxial Light Sheet Confocal Microscope for Image Cytometry Applications

Supporting information includes experimental details of chemicals and materials, electrode chip design, PEDOT (poly 3,4-ethylenedioxythiophene) electrodeposition and characterization by cyclic voltammetry (CV), leukocyte preparation, device setup for performing magnetohydrodynamics (MHD), chronoamperometric and chronocoulometric responses of PEDOT film-modified electrodes, chronopotentiometry (CP) responses for pumping experiments, derivation of pumping time as a function of applied current, calculation of maximum particle concentration and throughput, fluid flow tracked by particle image velocimetry analysis, bead phantom imaging, binning patterns of the linear sensor, axial resolution measurements as a function of magnification, sensor pixel width, and intensity cutoff for phantom and R-MHD setups, a table comparing theoretical and measured axial resolutions. This material is available free of charge via the Internet at http://pubs.acs.org.

4.S1 Chemicals and Materials

Propylene carbonate (PC, anhydrous 99.7%), the monomer 3,4-ethylenedioxythiophene (EDOT), lyophilized powder ≥ 96%, acridine orange hemi (zinc chloride) salt (~ 80% dye content), phosphate buffered saline (PBS) tablets, glycerol (for the bead phantom studies, (ACS grade ≥ 99.5%) and isotonic PBS/0.1% (w/v) bovine serum albumen (BSA) for suspending leukocytes were obtained from Sigma-Aldrich (St. Louis, MO). Glycerol for MHD studies (Proteomics grade, ≥ 99.0%) were purchased from AMRESCO LLC (Solon, OH). Lithium perchlorate (ACS min 95 %) was obtained from Alfa Aeser (Ward Hill, MA). Ammonium chloride solution (for red blood cell lysing) containing 0.8% NH_4CL and 0.1 mM EDTA in $KHCO_3$ buffered water at a pH of 7.4 was purchased from STEMCELL Technologies (Product #07800, Canada). Deionized water (18 MΩ, ACS reagent grade) used for almost all aqueous solutions was obtained from Ricca Chemical Company (Arlington, TX). Water for R-MHD experiments with biological cells and bead phantom was acquired from a Direct-Q® 8 UV Water Purification System (Darmstadt, Germany). Potassium ferricyanide and potassium ferrocyanide were obtained from EM Science, Gibbstown, NJ and J.T. Baker, Phillipsburg, NJ, respectively. Fluorescent polystyrene microspheres (15-μm diameter, green fluorescent, 1×10^6 beads/mL) were purchased from Life Technologies, Grand Island, New York. The cylindrical 0.37 T NdFeB (3.5 cm diameter, 1.27 cm high) permanent magnet was acquired from Amazing Magnets, Irvine, CA. Agarose, electrophoresis grade, was purchased from Acros Organics (New Jersey, USA). The edge connector (Category S28626, solder contact, 20/40 position, and 0.05 in. pitch) used to connect the chip with the potentiostat/galvanostat was acquired from Sullins Connector Solutions, San Marcos, CA. Sylgard 184 silicon elastomer base and Sylgard 184 silicon elastomer curing agent used for fabricating polydimethylsiloxane (PDMS) gasket were acquired

from Dow Corning corporation (Midland, MI). Precleaned micro cover glasses No. 1.5 (24 mm × 50 mm × 0.16 mm thickness), called "coverslips" herein were obtained from VWR (Radnor, PA).

4.S2 Electrode Chip Design

The 5.08 cm × 2.54 cm (2 in. × 1 in.) chip has multiple design features (see Figure S-1) that include four coplanar gold band electrodes of the same size, and six sets of gold concentric microdisk and ring electrodes of different sizes. All electrodes are individually addressable. Each band electrode is ~100 nm thick, 649.9 ± 0.8 μm wide, and 1.50 cm long. The gap between electrode pair 1 and 2 and that between electrode pair 3 and 4 is 0.32 cm. The separation between electrodes 2 and 3 is 0.47 cm. All electrode dimensions were measured using optical microscopy. The gold layer thickness was estimated with an uncalibrated piezoelectric monitor attachment during thermal evaporation (Edwards Auto 6 Evaporator). A detailed fabrication procedure for the electrode chips was described previously.[1] After modification with PEDOT, electrode pairs 1 and 2 or 3 and 4 were selected as the pumping electrodes.

4.S3 PEDOT Deposition and Characterization

A CHI 760B bipotentiostat/galvanostat (CH Instrument, Austin, TX) was used for PEDOT deposition and electrode characterization. The instrument was not used as a "bipotentiostat". Only one of the two working leads was used in experiments herein. Before deposition of PEDOT films, the chip was cleaned in an oxygen plasma (Harrick Plasma Cleaner PDC -32G, Ithaca, NY) for 15 min at 60 mTorr pressure with 6.8W of power applied to RF coil to remove organic residues. EDOT was electropolymerized potentiodynamically to form PEDOT on band electrodes from a solution containing 0.01 M EDOT and 0.10 M $LiClO_4$ in

propylenecarbonate (PC). The potential of the electrodes was cycled 12 times without stopping at 0.005 $V \cdot s^{-1}$ from -0.455 V to 1.300 V vs. Ag/AgCl (saturated KCl) and using a platinum flag as the counter electrode with a three-electrode arrangement in a beaker. Figure S-1(b) shows representative CV responses during the electropolymerization onto a band electrode of the chip (Figure S-1(a)). It exhibits an increase in charge with each of the 12 successive CV cycles and forms a dark film. As observed previously by us when PEDOT was electrodeposited from an aqueous solution, the first cycle has a greater overpotential (at ~+0.800 V) and steep oxidative current, with subsequent waves appearing at less positive potentials.

After deposition, films were cycled five times in monomer-free solution to stabilize and improve the reproducibility of electrochemical responses.[2] PEDOT- modified chips were usually stored in a 50 mL centrifuge tube filled with DI water. Before characterizing in electrolyte (e.g. 0.10 M KCl) the chips were soaked in that solution for 20 min. However, prior to R-MHD experiments the chips were not first soaked in the relevant fluid. Characterization by CV in 0.10 M KCl of an electrode before and after modification with PEDOT is shown in Figure S-4.

4.S4 Leukocyte Preparation

Whole blood was drawn via venipuncture in accordance with IRB protocol (# 13-06-759) at the University of Arkansas. Red blood cells were then removed using an isotonic, fixative-free ammonium chloride lysing solution, following. To remove red blood cells, the protocol provided by STEMCELL Technologies for product #07800 was used. In brief, 9 mL of an isotonic, fixative-free ammonium chloride lysing solution was added to 1 mL of the freshly collected peripheral whole blood, followed by incubating on ice for 10 min, and washing twice (via centrifugation at 200x*g* for 2 min and followed by resuspension in isotonic PBS).

4.S5 Three-Dimensional Bead Phantom Imaging as a Qualitative Assessment of Axial Resolution

A 90 µL volume of a solution of 2% (w/v) agarose in water at 80° C was mixed with 30 µl of the beads,and suspended over a glass slide. When cooled to room temperature, the solid bead suspension was approximately 3 mm in height, used soon thereafter to avoid drying, and estimated to have a concentration of 250 particles/µL (assuming no volume change upon gel-formation). A coverslip was placed over the top of the optical phantom. This assembly was positioned under the e-LSCM and used to qualitatively assess optical sectioning. Images were acquired with magnifications of 20x and 10x, and camera parameters were set to 0 dB and 1.20 mm s^{-1} translation speed at a consistent depth in the phantom. The integration time was 300 µs for the 20x and 550 µs for the 10x magnification to preserve a 1:1 bead aspect ratio (defined as the ratio of the bead's length to width) while the field of view expanded due to the decrease in magnification.[3]

4.S6 Derivation of Equation for Duration of Pumping Time for a Single Flow Direction as a Function of the Inverse Applied Current

The dependence of R-MHD pumping duration on inverse applied current is derived here for an R-MHD system of equally sized, parallel, PEDOT-modified band electrodes. We define "pumping duration" as the maximum time the R-MHD device can pump in a single direction without recharging the PEDOT-modified electrodes. This is equivalent to the time it takes for the potential difference between the pair of electrodes to change from a starting value to a final value when a constant current is applied. Thus, selecting a larger potential range will produce a longer pumping time. However, the actual potentials should be selected to avoid damage to the

polymer (i.e. from overoxidation at very positive potentials) or shutting down its charging capacity (i.e. at very negative potentials). The model assumes that each PEDOT film exhibits behavior like that of a capacitor, C, in series with a resistor, R, (e.g. from solution conductivity, edge connector impedance, thin conducting metal on the chip, and ion transport through the film that directly restricts the ability of the film to charge). This assumption is consistent with the shapes of the CV and CP responses (Figures S-4 and S-2) and discussion in the literature.[3-7]

Figure S-7 depicts the model as an RC equivalent circuit. The current function is shown in Figure S-7 (a). An initial constant cathodic current of i_1 was applied (at the electrode assigned as the "working electrode" in the experiment) until the potential difference between the electrodes of $E(0)$ = -1.000 V was reached. This step is analogous to charging the PEDOT to a specific state. The current was then stepped to a constant anodic current of i_2, which is of the same magnitude, but opposite sign of i_1 ($i_2 = -i_1$) and held for a time, t, until the final potential difference of +1.100 V was reached. This function was applied between two PEDOT-modified electrodes as shown in Figure S-4(b). The duration of the R-MHD pumping was determined as the time, t, for the system to charge up from $E(0)$, when time is defined to be zero ($t = 0$), to the potential at the final time $t = t_f$, when $E(t_f) = +1.100$ V.

In Figure S-4(c) it is assumed that the total capacitance is due to the combination of the individual capacitances, C, of each electrode in series. Thus, the total capacitance, C_T, is equal to $C/2$. The resistance, R, is intended to represent all resistances in the system in series with the capacitors. The excellent fit of the experimental data to this model suggests that any resistance in parallel with the capacitors is much greater than the impedance of the capacitors during the experiment so that no significant current circumvents them.

The non-IUPAC sign convention was used in the experiments and therefore is used here for the derivation, where the sign of the anodic current is negative and that of the cathodic current is positive. The potential drop across the resistance $E_R(t)$ at time, t, is then

$$E_R(t) = - i(t)R \quad , \tag{1}$$

where $i(t)$ is the current at time, t, and the potential drop across a given capacitor $E_C(t)$ at time, t, is

$$E_C(t) = \frac{- Q_c(t)}{C}. \tag{2}$$

where $Q_C(t)$ is the charge on one capacitor at time, t.

Thus, the total potential drop across the circuit at a given t (after the circuit is charged up) is

$$E(t) = \left(E_{C_T}(t) + E_R(t)\right) \tag{3}$$

where $E_{CT}(t)$ is the total drop across the two capacitors in series ($2\ E_C(t) = E_{CT}(t)$) and the potential drop across the circuit when it is initially charged up (when $t = 0$) is expressed by eq. (4),

$$E(0) = \left(E_{C_T}(0) + E_R(0)\right) \tag{4}$$

The duration is determined for the time needed to charge the circuit from a total system potential of $E(0)$ to $E(t_f)$, or $E(t_f) - E(0)$. At t, this quantity is expressed by eq. (5),

$$E(t) - E(0) = \left(E_{C_T}(t) + E_R(t)\right) - \left(E_{C_T}(0) + E_R(0)\right) \tag{5}$$

Grouping terms separately for the potentials across the capacitors and resistor, one obtains eq. (6),

$$E(t) - E(0) = \left(E_{C_T}(t) - E_{C_T}(0)\right) - \left(E_R(0) - E_R(t)\right). \tag{6}$$

When we substitute $-Q_{CT}(t)/C_T(t)$ for $E_{CT}(t)$ and the potential drop across the resistor as the product of the current, $i(t)$, at that time and the resistance, $-i(t)R$ for $E_R(t)$, and combine like terms, eq. (6) becomes eq. (7),

$$E(t) - E(0) = \left(\frac{1}{C_T}\left(-Q_c(t) + Q_c(0)\right)\right) + \left(R\left(i(0) - i(t)\right)\right). \tag{7}$$

However, the total charge passed during the experiment is the integration of the applied current with time. At time, t, then, the charge that has passed equals the charge at that time minus the charge at the beginning of the experiment, or $Q_{CT}(t) - Q_{CT}(0)$. Eq. (7) then becomes eq. (8),

$$E(t) - E(0) = \left(\frac{1}{C_T}\left(-\int_0^t i(t)\,dt\right)\right) + \left(R\left(i(0) - i(t)\right)\right) \tag{8}$$

In our experiments, the current is constant and the following boundary conditions apply:

$$\left.\begin{array}{l} \text{When } t \le 0,\ i(t) = i_1. \\ \text{When } t > 0,\ i(t) = i_2. \\ \text{Also, } -i_2 = i_1. \end{array}\right\} \tag{9}$$

Substituting these conditions into eq. (8), we obtain eq. (10),

$$E(t) - E(0) = -\left(\frac{i_2 t}{C_T}\right) - \left(2Ri_2\right) \tag{10}$$

Rearranging eq. (10), and solving for time, we obtain an equation relating time during the experiment to the inverse applied current and to the potential across the circuit at that time,

$$t = \left(-\frac{1}{i_2}\right)\left(C_T\left(E(t) - E(0)\right)\right) - \left(2RC_T\right) \tag{11}$$

Therefore, a linear plot of time as a function of the inverse current, yields a slope from which we can obtain the capacitance of a PEDOT-modified electrode,

$$C_T = \frac{\left(slope\right)}{E(t) - E(0)}, \text{ and } C = \frac{2\left(slope\right)}{\left(E(t) - E(0)\right)} \tag{12}$$

and we can obtain the resistance from the y-intercept,

$$R = \frac{-(y\,\text{int})}{2C_T} = \frac{-(y\,\text{int})}{C} \tag{13}$$

4.S7 Analysis of Experimental Data Using the RC Equivalent Circuit Model for Duration of Pumping Time as a Function of the Inverse Applied Current

A capacitance value for each electrode of 51.14 ± 0.09 mF/cm^2 (area = 0.0974 cm^2) can be obtained from the slope of the plot in Figure 2(b) of the Main Document and eq. (12) here. This value is slightly lower than (by 8%) and outside one standard deviation of the capacitance obtained by CA but can be explained by an older film of PEDOT. Repeated use typically decreases the film's charge. The negative y-intercept of Figure 2(b) of the Main Document is the RC time constant (from eq. (13) here) and yields an R value of 1552 ± 14 ohms. This value is

eight times the resistance (193 ± 3 ohms) obtained from the RC time constant (1.04 s at 37% of maximum current) of the CA response. The lower R value under CA conditions is due to a three-electrode setup in the unrestricted volume of a beaker.

4.S8 Calculation of Maximum Particle Concentration and Throughput

Imagine a projection of all the particles in the volume element that is imaged per unit time. Our approach cannot image more particles than a projection of those particles into a plane that has a hexagonal pattern with the particle edges touching. Only the particle closest to the observation window at a given horizontal position can be imaged from a top-down perspective. A particle vertically beneath that particle is blocked and therefore cannot be viewed. Only 91% of an area can be filled with circles (projection of spherical particles into a plane) for a layer of particles of closest spacing in a hexagonal arrangement. From this area, we can calculate the maximum concentration that can be imaged at a given height in the chamber. Figure S-12(a) is a top-down view illustrating how nine different horizontal layers of particles could project a closest hexagonal arrangement into a single horizontal plane. Figure S-12(b) represents a side view of each layer. The axial resolution will determine how many of those layers will be in focus at one time. For example, an axial resolution of 4.5 μm will not show more than the equivalent of one layer of 15-μm particles in focus at one time. An axial resolution of 36 μm could show the equivalent of a few more particles than in two layers in focus at a time. The greatest depth in which the focal plane can be set so that the particles will not be blocked by particles above them is layer 9 in this illustration.

Assume that all the particles are evenly distributed in a way that the projection of the volume to a depth of the imaging position appears as a hexagonally arranged set of touching

circles. The maximum space filled by circles (cross sections of a sphere) and arranged in a plane is 91%. The imaging area is determined by the speed of the fluid (v) for a given time (t) and the width of the lateral field of view (w). Thus, the maximum number of particles, $N_{p,max}$, that can be imaged per unit time is,

$$\frac{N_{p,\max}}{t} = 0.91\frac{vl}{\rho r^2} \tag{14}$$

where πr^2 is the projected area of a spherical particle having a radius, r. For a focal plane at a vertical position of h, relative to the observation window, the maximum concentration that can be imaged is,

$$C_{p,\max} = \frac{0.91}{\rho r^2 h} \tag{15}$$

Concentrations higher than this value will start to block particles at the focal plane position and prevent imaging. An axial resolution narrower than the vertical depth of the focal plane from the observation window will further diminish the number of particles that can be imaged per unit time. This is because only those particles within the axial resolution will be in focus. For evenly distributed particles throughout the volume of depth h, an axial resolution of Δh_{axial} will only be able to image the fraction of molecules filling this space, and is proportional to $\Delta h_{axial}/h$. Thus, the maximum throughput for a given axial resolution is

$$\frac{N_{p,axial}}{t} = 0.91\left(\frac{vl}{\rho r^2}\right)\left(\frac{\Delta h_{axial}}{h}\right) \tag{16}$$

Using Eqn. (14), we can calculate the maximum concentration that should be used to image spherical particles with a projected hexagonal, closest arrangement of 15 μm diameter

spherical particles. For a depth of 15 μm, just enough to fit a monolayer of particles, the maximum concentration is 3.43 x 10^8 particles/mL. It is only 7.36 x 10^6 particles/mL when imaged at 700 μm below the observation window (1440 μm above the chip), and 3.10 x 10^6 particles/mL when imaged at 1660 μm below the observation window (480 μm above the chip).

Maximum throughputs for imaging 15-μm particles calculated from Eqn. (14), given our highest measured R-MHD speed of 2.0 mm/s and lateral imaging fields for the 20x (472 μm) and 10x (944 μm) objectives, are 4860 and 9720 particles/s, respectively. This maximum depends on the speed of the flow and the lateral imaging length. It does not depend on the concentration or the axial resolution, because we cannot image more than a projection of particles into a plane that have a close hexagonal arrangement. However, using Eqn. (16) for when a cross section of particles is imaged with a 20x objective and axial resolution of 4.5 μm at a depth of 700 μm and 1660 μm below the observation window, the maximum theoretical imaging throughput is 31 and 13 particles/s, respectively. For the same conditions, but with an axial resolution of 36 μm, these are 250 and 105 particles/s, respectively.

4.S9 Performance of e-LSCM

In order to quantify performance of the e-LSCM imaging system, we first calculated the theoretical diffraction-limited axial resolution. This was calculated to be 10.3 and 3.5 μm for the 10x (0.3 NA) and 20x (0.5 NA) objectives, respectively from eq. (17), [8]

$$\text{Resolution}_{axial} = \frac{0.98n\bar{I}}{\left(n - \sqrt{n^2 - (NA)^2}\right)} \quad (17)$$

where n is the refractive index (1.0) and $\bar{\lambda}$ is the mean of the excitation and emission wavelengths ((445 + 520)/2 = 483 nm).

Table S1 compares the theoretical values with the experimentally determined axial resolutions for the two objective lenses and shows additional, electronically controlled "tuning" of resolution by using three binning modes (5 x 5 µm, 5 x 10 µm, and 5 x 20 µm) of the linear sensor. The experimental resolutions equal the full widths at half maximum (FWHM) of the light intensity measured as a function of the position of a mirror at the sample location translated in and out of the focal plane (with emission filter removed). The intensity data are shown in Figure S-9 (g) and (h). The experimental axial resolutions (using the 10X objective at 5 x 10 µm binning mode) are larger by ~37% than the theoretical ones. The decreased actual performance, when compared to theoretical performance, is likely due to slight misalignment of the objective and tube lenses in our experimental setup. The significantly smaller axial resolutions for the 20X objective than for the 10X are due to the higher numerical aperture of the 20X objective. The improved axial resolutions by ~1.5 µm at the smaller binning modes correlate to increased rejection of out-of-plane light, at the cost of decreased image intensity.

Figure S-9 (a-f) shows visual representations from a bead phantom that validate the affects of these six conditions on axial resolution. Microspheres at positions farther outside the focal plane (examples are designated by arrows in the figure) become detectable for larger effective pixel sizes that can receive more fluorescence and are therefore more sensitive. This effect is more pronounced in the higher numerical aperture 20X objective.

4.S10 References

(1) Sahore, V.; Fritsch, I. Flat Flow Profiles Achieved with Microfluidics Generated by Redox-Magnetohydrodynamics. *Analytical Chemistry* **2013,** *85* (24), 11809-11816, DOI: 10.1021/ac402476v.

(2) Robert Hillman, A.; Daisley, S. J.; Bruckenstein, S. Solvent effects on the electrochemical p-doping of PEDOT. *Physical Chemistry Chemical Physics* **2007,** *9* (19), 2379-2388, DOI: 10.1039/B618786B.

(3) Hutcheson, J. A.; Majid, A. A.; Powless, A. J.; Muldoon, T. J. A widefield fluorescence microscope with a linear image sensor for image cytometry of biospecimens: Considerations for image quality optimization. *Review of Scientific Instruments* **2015,** *86* (9), 093709, DOI: 10.1063/1.4931681.

(4) Lota, K.; Khomenko, V.; Frackowiak, E. Capacitance properties of poly(3,4-ethylenedioxythiophene)/carbon nanotubes composites. *Journal of Physics and Chemistry of Solids* **2004,** *65* (2), 295-301, DOI: https://doi.org/10.1016/j.jpcs.2003.10.051.

(5) Shen, P. K.; Wang, C.-Y.; Jiang, S. P.; Zhang, J.; Sun, X. *Electrochemical energy: advanced materials and technologies*, CRC Press: 2016.

(6) Rudge, A.; Raistrick, I.; Gottesfeld, S.; Ferraris, J. P. A study of the electrochemical properties of conducting polymers for application in electrochemical capacitors. *Electrochimica Acta* **1994,** *39* (2), 273-287, DOI: https://doi.org/10.1016/0013-4686(94)80063-4.

(7) Arbizzani, C.; Mastragostino, M.; Soavi, F. New trends in electrochemical supercapacitors. *Journal of Power Sources* **2001,** *100* (1), 164-170, DOI: https://doi.org/10.1016/S0378-7753(01)00892-8.

4.S11 Supporting Information Tables

Table S1: Comparison of theoretical (using eq. 17) and measured axial resolutions of the optical system (from FWHM of light intensity).

	Magnification and Numerical Aperture of Objective Lens			
	10x, 0.3 NA		20x, 0.5 NA	
Binning Size of Linear Sensor[a]	Theoretical	Experimental	Theoretical	Experimental
5 µm x 5 µm	10.3 µm	13.5 µm	3.5 µm	4.5 µm
5 µm x 10 µm		14.0 µm		4.9 µm
5 µm x 20 µm		14.8 µm		6.3 µm

a- The length of the lateral field of view depends on the magnification: 0.5 mm for 20x and 1.0 mm for 10x.

4.S12 Supporting Information Figures

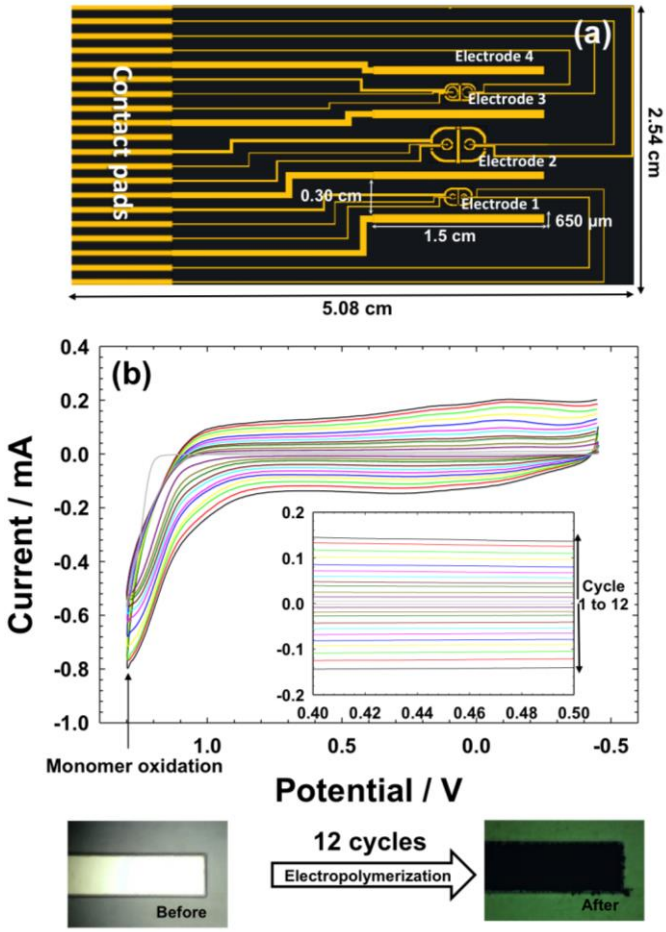

Figure S-1: (a) Electrode design of microfabricated chip (5.08 cm × 2.54 cm; 2 in. × 1 in.) that contains four band electrodes, each measuring 1.5 cm long, 649.9 ± 0.8 µm wide, and ~100 nm in thickness. (b) (Top) CV responses (at 0.005 V/s) during electropolymerization of PEDOT for 12 deposition cycles in monomer solution containing 0.010 M EDOT and 0.100 M $LiClO_4$ in propylene carbonate. Figure shows oxidation of the monomer at potentials >1.0 V vs. Ag/AgCl (saturated KCl) reference electrode. Growth of the polymer film with each deposition cycle is evident in the range of -0.500 V and +1.000 V by an increasing charging current. (b) (Top inset) Expanded view of increasing charging current from +0.500 V to +0.400 V. (b) (Bottom) After 12 successive deposition cycles, a gold bare electrode has been covered by a dark layer of PEDOT.

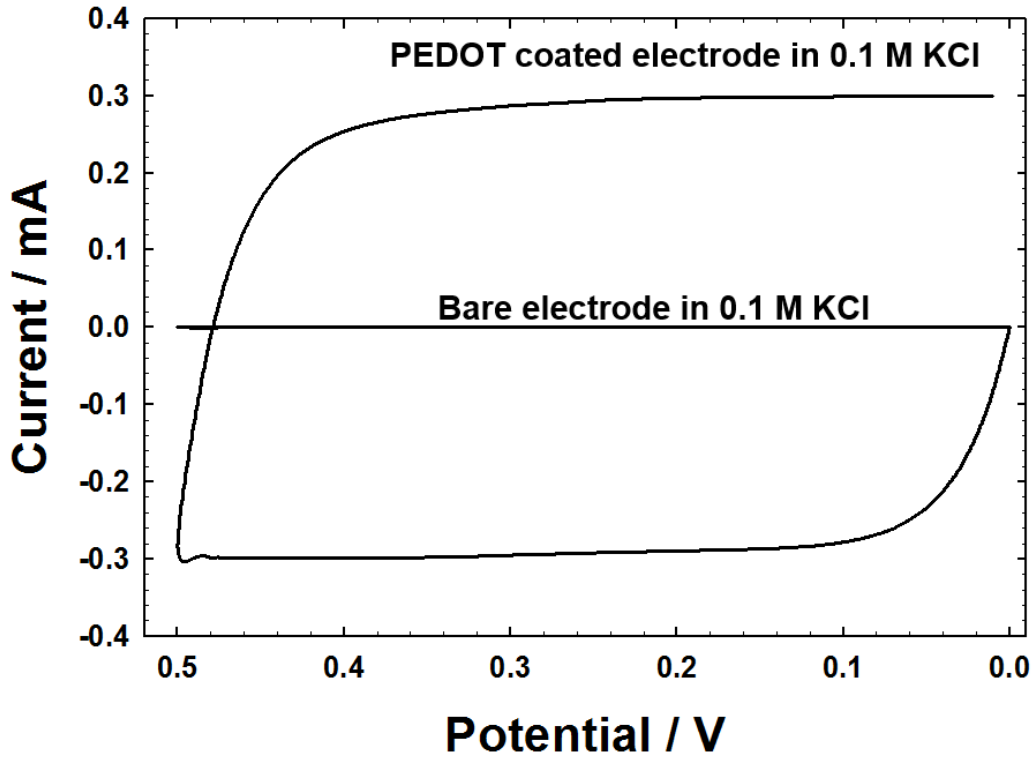

Figure S-2: Overlay of the CV current responses (0.050 V/s) in a solution of 0.1 M KCl for a single bare electrode and a PEDOT-modified electrode (prepared with 12 cycles of deposition). A three-electrode system was used with a Ag/AgCl (saturated KCl) reference electrode and a Pt flag counter electrode in a 20 mL glass beaker. At +0.200 V, the charging current for the bare electrode is 0.36 µA and that for the PEDOT-modified electrode is 0.30 mA (823 times higher). The increased current is expected to allow MHD fluid flow to be faster and to be sustained for longer times at a fixed speed.

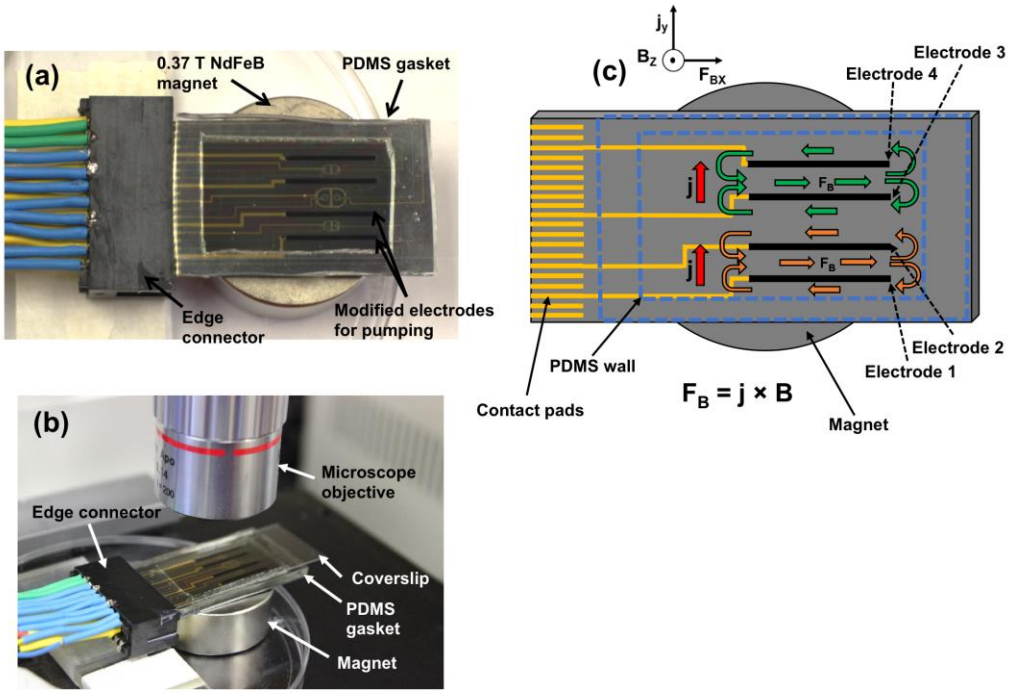

Figure S-3: (a) Electrode chip connected via contact pads with edge connector and wires to the bipotentiostat. (b) Complete MHD setup on the microscope stage, showing a coverslip that is placed on top of the PDMS to contain the solution. (c) Schematic of chip over the magnet showing the direction of fluid flow (orange and green arrows) in between and around the activated electrodes. The right-hand rule and the resulting coordinate system are shown, involving the net fluid motion induced by the MHD force, $\mathbf{F_B}$, from the cross product of the ionic current density, **j,** and magnetic flux, **B**. There are four band electrodes for this chip design, which served as two sets of paired working and counter/reference electrodes. Either electrodes 1 and 2 or 3 and 4 were activated at a time for a given MHD experiment. Blue dotted outline shows the location of the PDMS gasket.

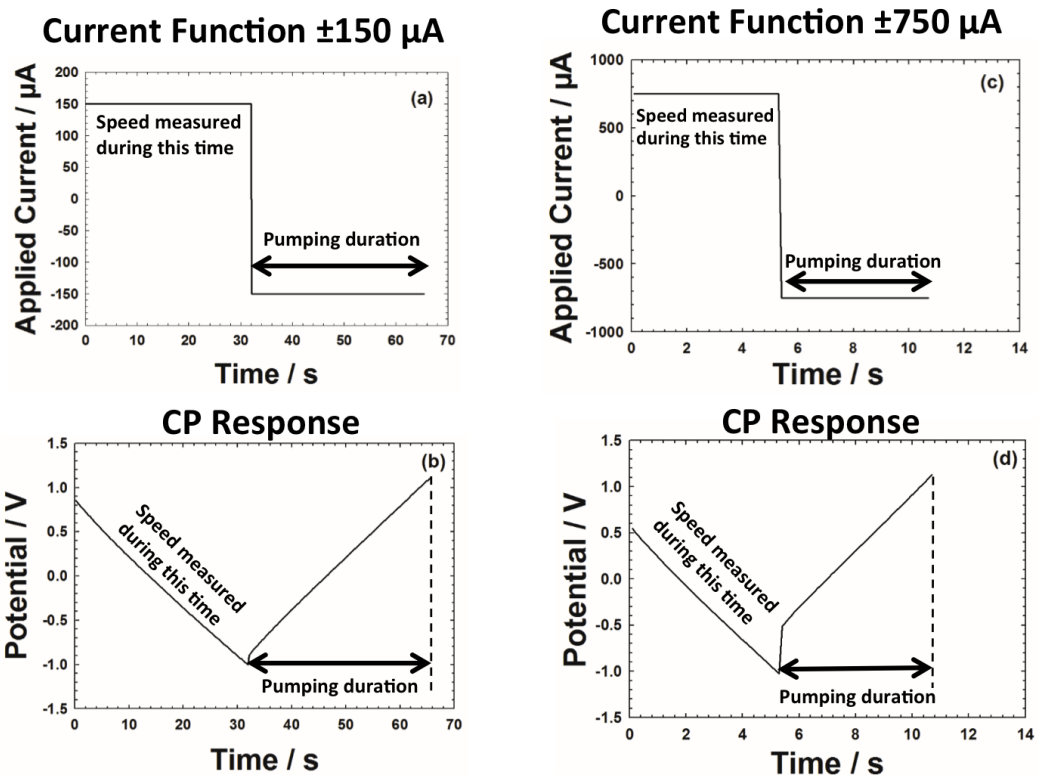

Figure S-4: Examples of chronopotentiometry current functions for steps of (a) ±150 µA and (c) ±750 µA and the corresponding experimental responses (b) and (d), respectively, involved in characterizing R-MHD fluid flow in the microfluidics device containing the buffer/glycerol/bead solution. Two adjacent PEDOT-modified electrodes were activated with the galvanostat, where one served as the "working" electrode and the other as the combined "quasi reference/counter" electrode. Fluid speeds were obtained during the first half of the current function and pumping duration was determined during the second half. Cutoff voltages of -1.000 V and +1.100 V were used to avoid the non-conductive regime and overoxidation of the PEDOT, respectively, and defined the voltage range for the duration studies.

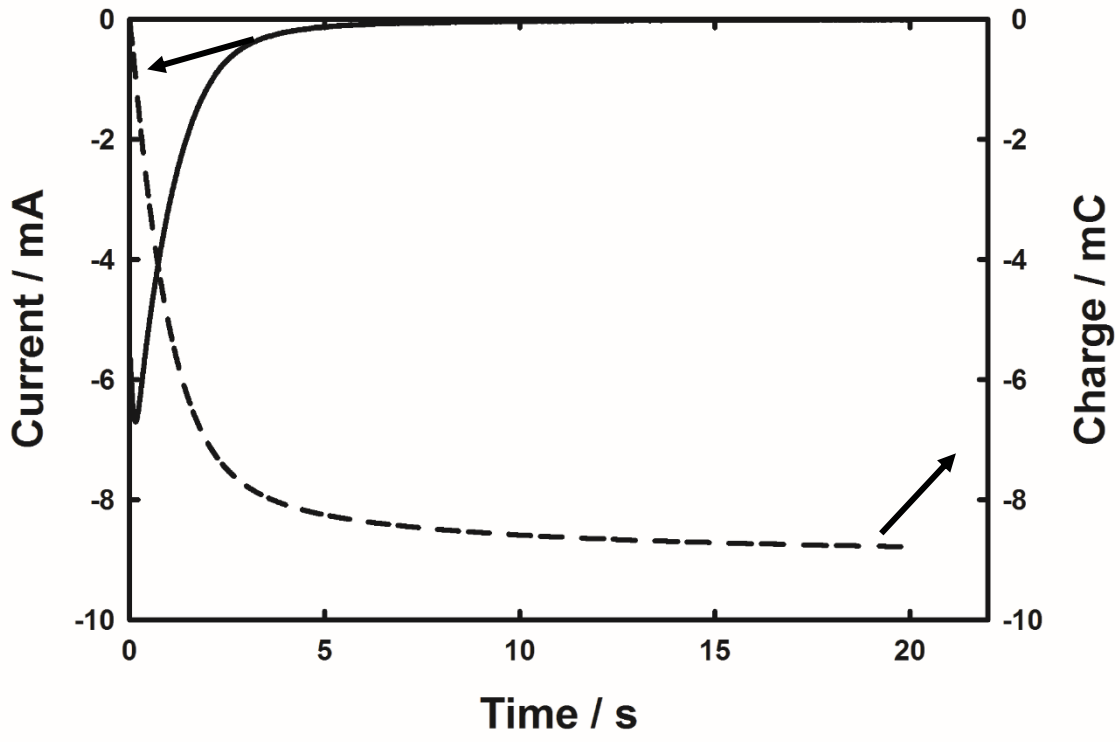

Figure S-5: Current (solid curve) and charge (dashed curve) response in the buffer/glycerol solution of one PEDOT modified electrode after 12 cycles of deposition. A three-electrode system was used with a Ag/AgCl (saturated KCl) reference electrode and Pt counter electrode in a 20 mL glass beaker. A 20 mL solution of the buffer/glycerol was used. The maximum current response was obtained near the beginning of a chronoamperometry (CA) experiment after stepping from -0.800 to 0.800 V. The potential was held at -0.800 V for a quiet time of 20 s prior to the step, and the potential was held at 0.800 V for 20 s after the step. The charge in the film was obtained by integrating the CA data.

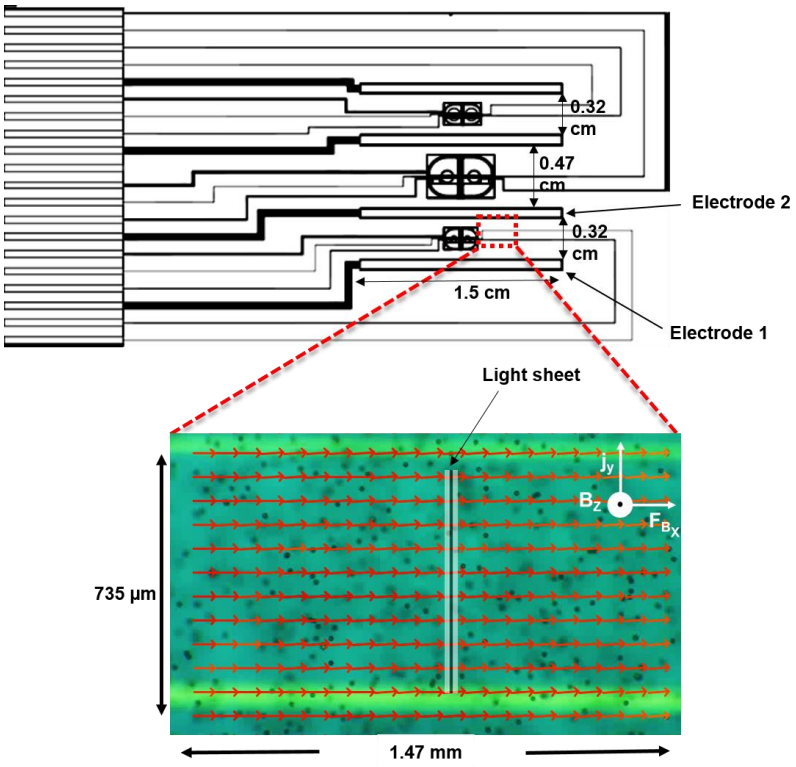

Figure S-6: Particle image velocimetry (PIV) analysis of microbead movement, which tracks fluid flow, produces velocity vectors (red arrows). These data were obtained between the active electrodes in the area outlined by the dashed red rectangle on the Autocad schematic of the chip, at a height of 480 µm above the chip surface, and during an applied current (150 µA, with cutoff voltages of -1.000 and +1.100 V vs counter/reference) MHD experiment. The working anode (electrode 1) and counter/reference cathode (electrode 2) in a two-electrode configuration were activated in the presence of a 0.37 T NdFeB magnet beneath the chip. A line is superimposed on the PIV image to illustrate that the location of the illuminated region used for the epitaxial light sheet confocal microscope (e-LSCM). The average bead speed determined at this particular height and applied current was 287 ± 23 µm/s (N = 6 beads).

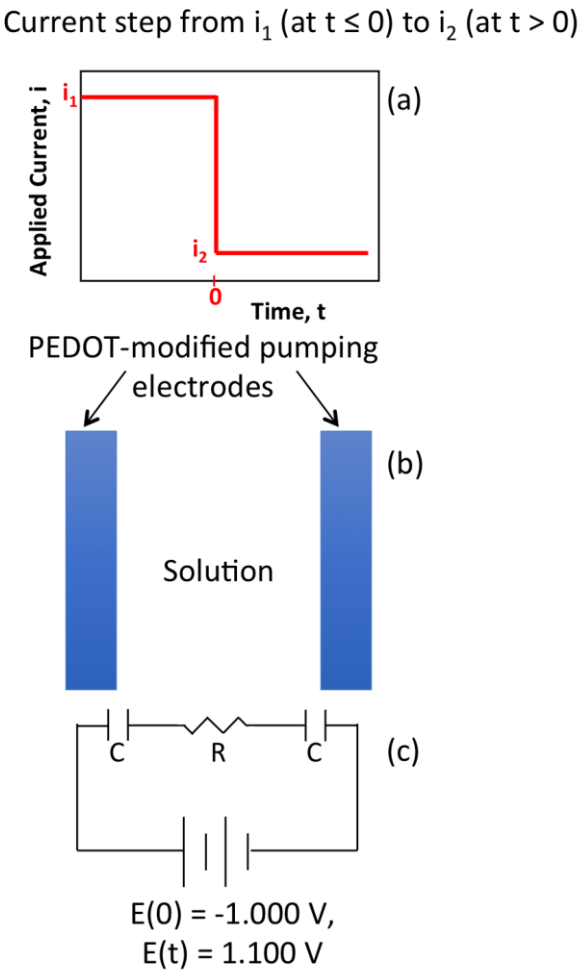

Figure S-7: Schematic diagrams illustrating "RC" equivalent circuit model used for the derivation of pumping duration as a function of applied current. In (a), the applied current function is shown that was used in the experiments that determined duration. In (b) is a diagram showing the two PEDOT-modified electrodes and solution between them. In (c), the equivalent circuit shows that the capacitance, C, is due to the charging of each PEDOT-modified electrode, so that the total capacitance, C_T, is equal to C/2. The resistance, R, in the diagram represents all resistances in series with the capacitors, which would include not only the solution resistance, which is implied by the schematic, but also the resistances in the thin conducting films of the electrodes and the connectors.

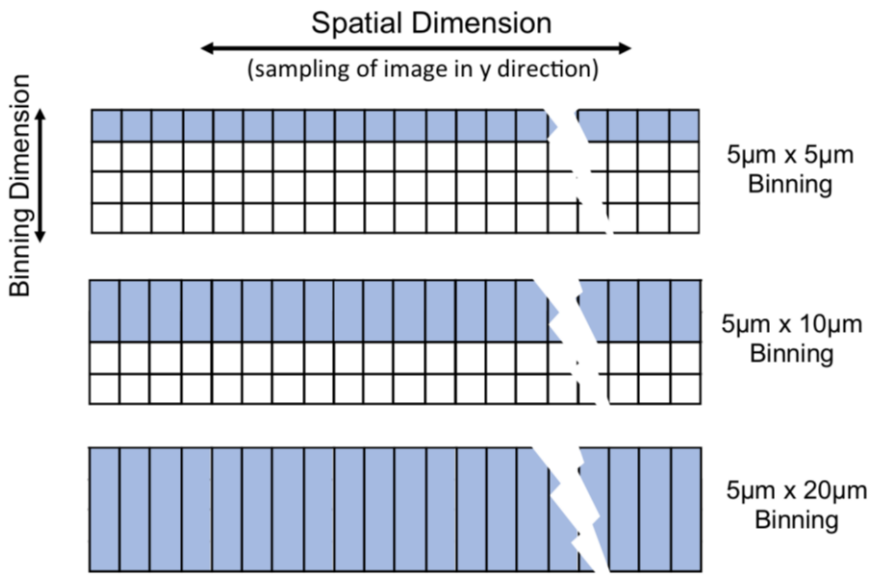

Figure S-8: Illustration of the three programmable binning patterns of the linear image sensor used in this manuscript. The fluorescence resulting from the excitation light sheet is imaged across the pixel array from left to right in this diagram (spatial dimension). The native size of pixels in the image array are 5 µm square. In the 5 µm by 5 µm binning mode (1 pixel by 1 pixel), the image plane is sampled every 5 µm by a single pixel, and the binning dimension (corresponding to the confocal aperture, which controls depth of focus and axial resolution) is also sampled every 5 µm. When the 5 µm by 10 µm or 5 µm by 20 µm binning modes are used, the spatial dimension (and therefore spatial resolution in the y-direction) remains 5 µm, but the binning dimension increases, corresponding to an increase in confocal aperture and degraded axial resolution. This is seen experimentally in Figure S-9. (Note that the x, y, z-coordinate system is defined in Figure 1 of the main document.)

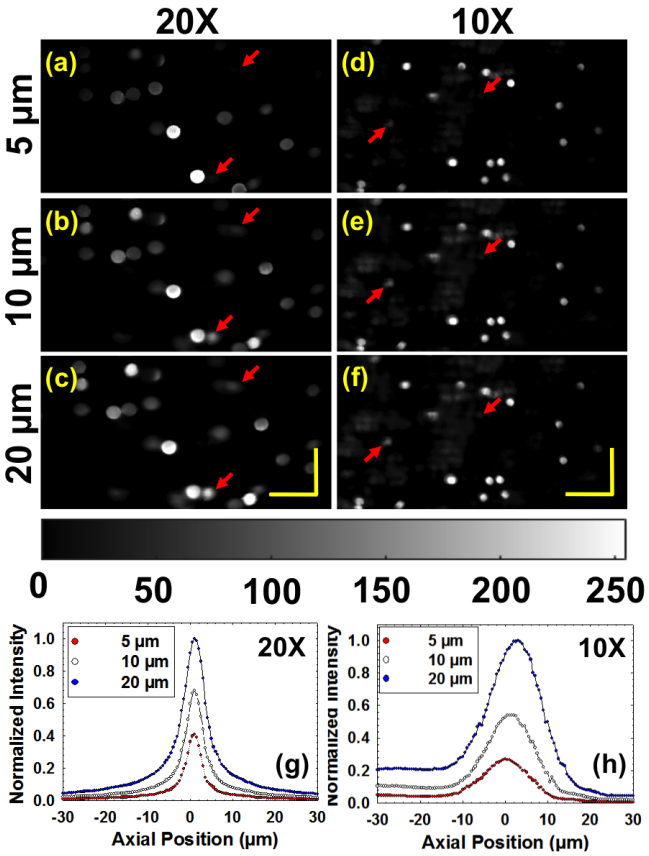

Figure S-9: Qualitative and quantitative measurements of axial resolution of the e-LSCM under different magnification and sensor binning modes. Images (a)-(f) show optical sectioning in a three-dimensional suspension of microspheres in an agarose phantom for magnifications of 10× and 20×. Red arrows point to beads that are more excluded under some conditions than others because of changes in axial resolution. The shade gradient displays pixel value. Scale bar is 30 µm for (a)-(c) and 60 µm for (d)-(f). Plots in (g) and (h) show axial sectioning ability via light intensity (with emission filter removed) as a function of the displacement of a mirror ±30 µm around the focal plane for the same six conditions as in the microsphere images. Preparation of the bead phantom and experimental parameters are described in *Additional Experimental Details* above.

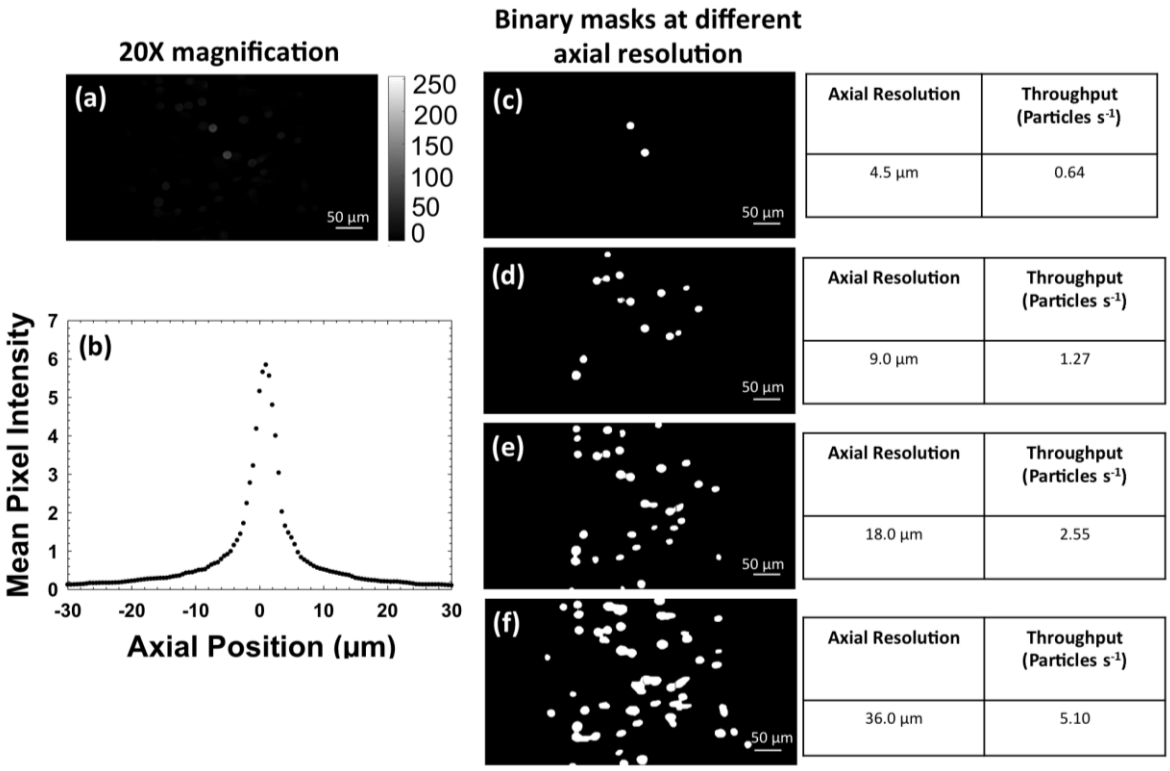

Figure S-10: Data process "tuning" of axial resolution by setting an intensity cut-off and its impact on particle throughput using a bead phantom with 20x magnification and sensor binning of 5 µm x 5 µm. (a) An example of a bead phantom image for a concentration of 250 particles/µL. (b) Axial sectioning ability of the e–LSCM using a mirror placed in the focal plane of the optical setup. (Same as in Figure S-9). Experimental details are provided in the main manuscript. (c)-(f) Bead phantom binary masks- used to delineate the location of detectable beads–derived from pixel threshold values defined by axial resolution intensity cutoff ranging 4.5 µm – 36 µm using plot shown in (b). Preparation of the bead phantom and imaging parameters are described in *Additional Experimental Details* above.

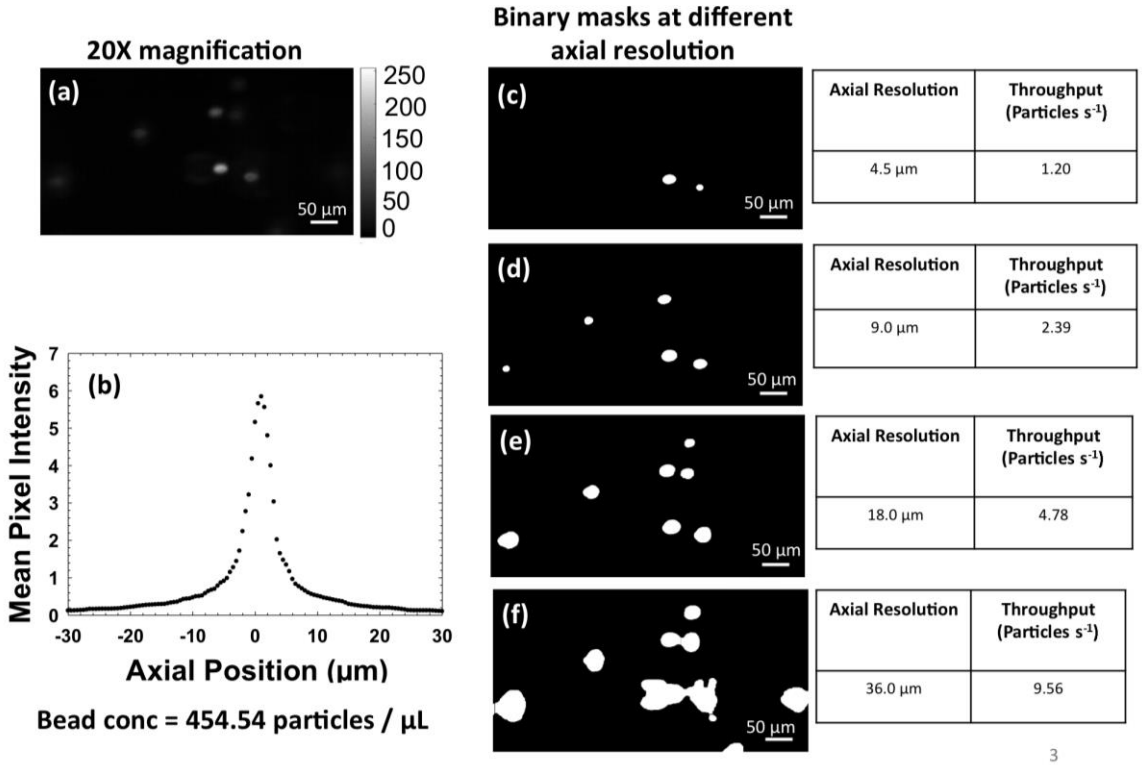

Figure S-11: Data process "tuning" of axial resolution by setting an intensity cut-off and its impact on particle throughput when interfaced to R-MHD microfluidics at 1.237 mm/s and using 20x magnification with a sensor binning of 5 µm x 5 µm. (a) An example of a bead image for a solution containing 455 particles/µL. (b) Axial sectioning ability of the e–LSCM using a mirror placed in the focal plane of the optical setup. (Same as in Figure S-9). Experimental details are provided in the main manuscript. (c)-(f) Binary masks–used to delineate the location of detectable beads- derived from pixel threshold values defined by axial resolution intensity cutoff ranging 4.5 µm – 36 µm using plot shown in (b). Preparation of the bead solution for studies involving R-MHD and imaging parameters are described in the *Experimental* section of the main manuscript.

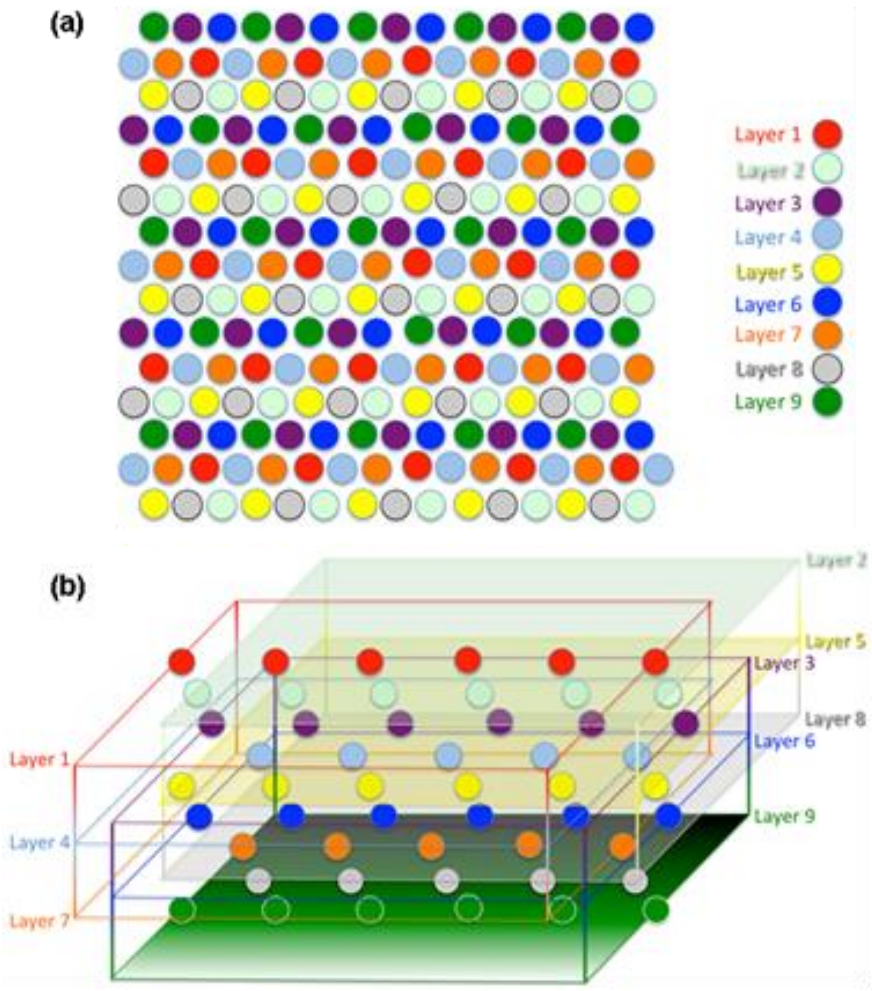

Figure S-12: Illustration of an arrangement of particles in a given volume where the two-dimensional projection provides a hexagonal pattern with the particles touching. In (a) is the top-down view. Each color represents particles from a different vertical layer as depicted in the (b) side-view perspective. In this example, particles are evenly spaced and up to nine layers of particles having this concentration and diameter can be fully imaged. Particles in layers greater than nine would be blocked by the particles above them.

5. 3D Velocity Profile Analysis of Redox-Magnetohydrodynamics (R-MHD) Induced Flow in a Microfluidic Chamber by Astigmatism Particle Tracking Velocimetry (APTV)

5.1 Introduction

Microfluidics deals with the study and manipulation of submillimeter length scale fluids. Microscale fluid manipulations on microchip has been very impactful for cell biology and medical research, drug discovery, kinetic study of protein folding, enzymatic assays, and analysis and detection of DNA. [1-5] The lab-on-a-Chip technology brings various opportunities to the scientific community where very small amount of sample is used (nano to pico-liter) and can be easily adapted with different analytical detection techniques that's allows high-selectivity and high-sensitivity.

Pumps are important component of lab-on-a-chip system to perform operations like transportation, mixing, separation, and filtration. Different types of pumping technology have been employed to control and manipulate fluid movement in microfluidic environment such as, pressure, electrostatic, thermo-pneumatic, electroosmotic, and magnetohydrodynamic (MHD) pump. Redox-MHD microfluidics governed by the right hand rule, $\mathbf{F_B = j \times B}$ (the magnetic part of the Lorentz force), where the body force ($\mathbf{F_B}$) pushes the fluid by perpendicular interaction of ionic current density ($\mathbf{j}$ (C/ s m^2)) and magnetic field ($\mathbf{B}$ (T)).[6] R-MHD microfluidics has design flexibility, capable of pump fluid in linear, loop, and bi-directional fashion, generates flat flow profile, valve and channel less, and operates at low voltages. [7-9] These flexibilities allowed R-MHD pumping approach to perform multiplex enzymatic assays and coupled with confocal microscope as a deep-chamber imaging cytometer. [10-11] Recently magnetic field gradient combined with R-MHD approach to manipulate fluid flow direction and paths.[12] The body force that pushes fluid scales with the ionic current density, **j**. The electronic current applied in

between the active electrodes either oxidize or reduces dissolved redox-species such as, $Fe[(CN)_6]^{-3}$ / $Fe[(CN)_6]^{-4}$ or electrode confined conducting polymer such as poly (3,4-ethylenedioxy thiophene) (PEDOT) to generate ionic current density in the presence of electrolyte solution.[6-7, 9, 11]

Unlike other pumping approaches, R-MHD is a body force driven flow and can be tuned by modifying the extent and direction of **j** and **B**. Fluid flow behavior in microfluidics can deviate considerably than macroscale, due to the low Reynolds number (often < 1), surface force, and enhanced heat transfer rates because of the large surface-to-volume ratio.[13] Therefore, a complete analysis of flow behavior of R-MHD system is of great interest. Previously fluorescence correlation spectroscopy (FCS) has been coupled with particle imaging and tracking velocimetry (PIV/ PTV) to analyze R- MHD induced flow profile in 3-dimensions where redox couple, $Fe[(CN)_6]^{-3}$ / $Fe[(CN)_6]^{-4}$ was dissolved in the pumping solution.[14] Due to the presence of solution redox species, this approach was affected by density gradient and imparted a considerable amount of vertical movement in the flow.[14-15] Therefore, to avoid analyte interference, density gradient, and harness high ionic current density, a conducting polymer such as poly (3,4-ethylenedioxythiophene) or PEDOT can be immobilized on the electrode surface.

Astigmatism particle tracking velocimetry (APTV) is a useful method where a single camera is used to determine all three velocity components in a 3D volume.[16-17] This technique uses astigmatic aberration to encode the out-of-plane position of a tracer particles in the measurement volume. In the standard microscopic system, a cylindrical lens can be placed in front of the CCD chip along with a convex lens which will produce astigmatic aberration in the yz plane, where as in xz it just acts as a mere flat widow due to being coaxial with x direction. Therefore, particles suspended in the focus plane would show prolate or oblate shape depending

upon their position close to xz or yz plane, respectively. A particle shape information can be evaluated to estimate its position in the out-of-plane direction. If the position of a particle can be known in x, y, and z direction and their corresponding change in time, then with the first order approximation particle velocity in all 3-directions can be evaluated with subpixel accuracy. This technology has certain advantages over the standard PIV system such as, evaluating fluid velocity in z-direction, avoiding biases because of the out-of-focus particles, and requirement of a single camera that has the adaptability with standard microscope.

In this work, a complete three-dimensional measurement of the fluid flow was performed and analyzed by changing different parameters related to R-MHD microfluidics, such as applied current, chamber height, and concentration of pumping electrolytes. Besides, the fluidic profiles assessed for different electrolyte concentration at constant applied current revealed a new insight for MHD microfluidics. Figure 1 shows the schematic of the R-MHD microfluidics and APTV coupled system, where the chip-gasket-magnet assembly flipped upside down over an epi-fluorescent microscope.

5.2 Experimental Section

5.2.1 Chemicals and Materials

3, 4-ethylenedioxythiophene (EDOT), propylene carbonate (anhydrous 99.7%), and tetrabutylammonium hexafluorophosphate were purchased from Sigma-Aldrich (St. Louis, MO). Sodium chloride was purchased from ORG Laboratory Chemistry GmbH (Bunde, Germany). Pre-cleaned micro cover glasses (24 mm × 30 mm) were purchased from VWR International, LLC (West Chester, PA). Polystyrene microbeads were purchased from Microparticles GmbH (Berlin, Germany). 0.37 T nickel coated NdFeB permanent magnet (3.5 cm diameter and 1.27

cm height, grade N40) was purchased from Amazing Magnets, Irvine, CA. Silicon wafer for chip fabrication purchased from Silicon Quest International (San Jose, CA). Edge connectors (solder contact, 20/40 position, and 0.05 in. pitch) were acquired from Sullins Electronics Corp. (San Marcos, CA). Sylgard184 silicon elastomer base, Sylgard 184 silicon elastomer curing agent, and OS-30 solvent for PDMS fabrication were purchased from Ellsworth Adhesives, Milwaukee, WI.

5.2.2 Chip Preparation and Electrode Modification

Each chip (1 in. × 2 in.) contains four gold band electrodes (650 μm width and 1.5 cm in length) which are individually addressable. The procedure to fabricate chip with patterned electrodes has already reported before [7]. Six chips were fabricated on a five-inch silicon wafer and individual chip was acquired by dicing. After dicing, each chip went through oxygen plasma cleaning (Harrick Plasma Cleaner PDC -32G, Ithaka, NY) for about 20 min at 60 mTorr pressure and 6.8 W of power applied to the RF coil) to remove any remaining organics. Figure S1 shows the picture of a fabricated chips where two outermost sets of electrodes and two inner electrodes are spaced by 0.32 and 0.47 cm, respectively.

Each electrode was pre-characterized in the mixture of 1mM $K_3Fe(CN)_6$ and 0.10 M KCl and in only 0.10 M NaCl. Cyclic voltammetry was performed in both characterizing solutions at 0 to 0.50 V potential window with 0.10 V/s scan rate. After rinsing with DI water and dried at room-temperature, chips were cleaned by oxygen plasma to remove any probable organics. EDOT was electropolymerized on the gold band electrodes by cycling the potential from -0.455 to 1.4 V at 5 mV/s, vs Ag/AgCl reference (in saturated KCl) electrode for 12 cycles. Monomer

solution contained 0.010 M EDOT and 0.100 M $TBAPF_6$ in propylene carbonate (PC). The details of the electro polymerization procedure have been reported before.[18]

5.2.3 Electrochemical Characterization of PEDOT Films

The resultant PEDOT films were characterized in 0.10 M NaCl by cyclic voltammetry (CV) and chronoamperometry (CA) method. CV was performed with -0.800 to +0.800 V widow at 0.05 V/ s scan rate. CA was performed by holding the potential at -0.800 V for 20 s (quiet time) to charge up the polymer, and then stepped to +0.800 V for the next 20 s. All electrochemical characterizations were performed in a three-electrode cell, vs Ag/AgCl reference and Pt foil counter electrode. The maximum current was measured at 0.001 s of the CA response and normalized with the nominal electrode area to evaluate the maximum current density. The total charge from the PEDOT film was evaluated by integrating the CA response and the charge density was achieved by normalizing with the electrode area.

5.2.4 Preparation of Solutions and PDMS Gaskets

For APTV studies, 5 um fluorescent polystyrene beads were added to the electrolyte solutions (about 500 uL) at 1:800 volume ratio. For µPIV studies, 2.5 um fluorescent polystyrene beads were added to electrolyte solutions (about 1 mL) at 1:20 volume ratio. The microbead/electrolyte mixture was then added into the gasket opening by using a micropipette, followed by sealing with a glass coverslip. Three PDMS gaskets of different thicknesses (nominally 0.50, 1.00, and 2.00 mm) were prepared. A rectangular opening was cut out from each with dimensions of 3 × 1.7 cm. These gaskets formed a chamber and contained the electrolyte solution with microbeads. The actual height of the microfluidics chamber was measured before the experiment when the chamber was freshly assembled.

5.2.5 Formation of the Microfluidics Chamber and APTV Microscope Setup

Figure 2 shows the photograph of the actual R-MHD / APTV coupled setup. An inverted epi fluorescent microscope (AxioObserver 7, Zeiss) (Figure 2 (a)) was used for the experiment. A gasket was positioned over the electrode chip so as the modified electrodes were exposed (Figure 2 (c)). The solution containing the electrolyte and microbeads was pipetted into the rectangular opening so that it was overflowing. A glass coverslip was placed over the PDMS gasket and gently squeezed together to make a sealed system. This chip-gasket-coverslip assembly was flipped upside down and placed onto a 3D-printed chip holder which has already pre-set on the microscope stage. The whole assembly was arranged in a way that, the coverslip over the gasket would face the microscope objective (LD Plan-Neofluar, 20x/0.4, Zeiss). A permanent NdFeB magnet (35 mm diameter) placed onto the backside of the chip and clipped into place (Figure 2 (d)). A 525 nm green, high-power LED light source (SOLIS-525C, Thorlabs) was used for the excitation purpose. The fluorescence emitted from the microbeads (excitation /emission: 540/607 nm) in the MHD pumping solution was observed with a microscope objective and captured by a monochrome camera (Imager sCMOS, LaVision GmbH) operating in single-frame mode.

Astigmatic particle images in the solution were obtained by placing a cylindrical lens (focal length of 200 mm) between the tube lens and the sCMOS camera. APTV interrogation of the fluid velocity was performed between the activated, PEDOT-modified parallel band electrodes by traversing through the measurement volume in y direction (at $x = 0$ and $z = 0$) to obtain velocity profiles in the horizontal plane and in the z direction (at $x = 0$ and $y = 0$) to obtain velocity profiles in the vertical plane. Data points were obtained by spatial increments of 250 and

5 um in y and z directions, respectively to get an overlap between measurement positions. The measurement volume of the APTV amounted to ($w_x \times w_y \times w_z$) = (680 × 1050 × 80) μm^3.

5.2.6 R-MHD Induced Fluid Flow by Changing Different Parameters

Redox-MHD flow was achieved by the modification of different parameters such as gasket height, applied current, and electrolyte concentration. In the first set of experiments, with a 0.50 mm thick nominal gasket and 0.10 M NaCl, three different current such as ± 100, ± 200, and ± 400 µA were applied in between active electrodes. The applied current held constant at ± 400 µA, whereas the gasket heights were varied (0.50, 1.0, and 2.0 mm nominal thickness) in the second set of experiments. The fluid flow achieved in the first two sets of experiments were analyzed by APTV technique.

In the third set of experiments, the concentrations of pumping electrolyte were varied from 0.10 to 1.30 M while applying four different currents (± 50, ± 400, ± 800, and ± 1000 µA) with a 2 mm thick gasket. The fluid flow achieved from this set of experiments was analyzed by µPIV technique.

5.2.7 Flow Analysis by APTV and µPIV Techniques

APTV detects position and velocity of individual particles that are randomly distributed within the measurement volume. All randomly distributed particle velocity vectors (for both biases (±) of electrical currents) were ensemble-averaged and interpolated onto a rectangular grid using Gaussian-weighted interpolation based on the vector distance from the grid nodes. The size of the bins was varied (such as, Δy x Δz = 500 x 10, 500 x 20 and 200 x 20 μm^2) and the overlap between neighboring bins yielded a velocity grid spacing in spanwise direction (y and z). Spatial

resolution in streamwise direction was given by the size of the measurement volume in x-direction (approximately 800 µm).

Microparticle image velocimetry (µPIV) evaluate the particle velocity by measuring the displacement of the tracer particle in a suspended volume. This displacement can be obtained from two subsequent particle images which are separated by known time interval. [19] Compared to the standard PIV system, in µPIV the entire flow region is illuminated. Therefore, the depth of measurement plane is limited by the depth of field of the microscope lens, rather than the thickness of the illuminating light sheet. For this work, to evaluate fluid flow at each measurement position (z), a multi-pass, multigrid approach was used with interrogation windows (IW) of 512 × 512 px in size and 50% overlap between neighboring IW. Assuming no velocity variation occurs at the measurement position, all vectors were ensemble-averaged (in time and space). Therefore, spatial resolution of the measurement in lateral direction is given by the FOV (approximately 810 µm in streamwise (x) and 680 µm in spanwise direction (y)), while the spatial resolution in z-direction is given by the effective step width of the traversing.

5.3 Result and Discussion

5.3.1 Electrochemical Characterization of Chip Electrode

Chip electrodes were characterized before and after the PEDOT film deposition in different electrolyte solutions. Bare electrodes in 1mM $K_3Fe(CN)_6$ and 0.10 M KCl (for a single electron transfer homogenous reaction) generated experimental anodic and cathodic peak currents (1.33×10^{-6} and 2.35×10^{-6} A), with peak potential difference of 0.190 V. The charging currents obtained by cyclic voltammetry in 0.10 M NaCl with a bare electrode were 1.20×10^{-7} and 5.75×10^{-7} A, respectively at 10 and 50 mV/s scan rate. Figure S-2 shows CV responses of a

single bare electrode in 1mM $K_3Fe(CN)_6$ and 0.10 M KCl (red) and in 0.10 M NaCl (black and blue). PEDOT electrodeposited from propylene carbonate by CV method at 5 mV/s scan rate for 12 cycles. The dark blue films electrodeposited on band electrodes were characterized in 0.10 M NaCl by CA and CV. Figure S-3 shows CV and CA responses of PEDOT coated electrode. Charging current obtained from PEDOT film was (6.15×10^{-4} A) 1068× higher than the bare electrode. The diagnostic CV shape (Figure S-3 (a)) shows a capacitive behavior and the 1068× increased in charging current of polymer coated electrode than the unmodified one. Figure S-3 (b) and (c) show CA and integrated CA responses of PEDOT film in 0.10 M NaCl solution. The area normalized maximum current and charge density obtained were 198 ± 1 mA/cm^2 and 192 ± 2 mC/cm^2. These electrochemical responses are in rationale with our previous work and studied at length before. [11, 18]

5.3.2 R-MHD Fluid Flow Under Controlled Current Condition

We applied currents in between active electrodes by using chronopotentiometry to pump fluid. CP allowed us to have better current control and the capability to monitor the change in potential. Also, the programmability in the CP technique allows us to apply a reverse current which will recharge the polymer film. Figure S-4 shows triangular CP responses of ± 50, ± 400, ± 800, and ± 1000 µA applied currents. At anode, PEDOT changed to its oxidized (+1 state) from neutralized state by the application of an oxidation current and this change in state associated with the migration of anions from the surrounding solution to compensate the charge imbalance. At the cathode, the opposite process happens. Through this oxidation-reduction of polymer films on working and counter-reference electrodes, a net ionic migration occurs. This ion movement give rise to the ionic current density (j) which interacts in perpendicular with the magnetic field (B) to produce a body force (F_B) that will push the fluid in between PEDOT

coated electrodes. The charge density of the PEDOT film limits the total flow duration whereas the maximum current density limits the achievable speed. Higher applied currents induce faster oxidation and reduction of the polymer film, thus generates faster speed but for shorter duration. On the other hand, low current generates slow fluid speed but for longer time. Therefore, in terms of duration and speed R-MHD flow is highly tunable. This flow duration and speed has linear dependency with applied current which has been reported before. [11] For this study, instead of switching the current bias at a certain potential, opposite bias (such as ± 400 µA) currents were applied for a specific time (Figure S-4). Therefore, the potential responses were different for varied applied currents.

5.3.3 The Dimensional, Three Component Velocity Profile Analysis by Varying Applied Current

In the first set of experiments, three different currents ±100, ±200, and ±400 µA were applied in between active electrodes to generate fluid flow in 0.10 M NaCl solution and then the APTV technique used to analyze the flow profile. The nominal dry gasket height for this setup was 0.50 mm but after making a sealed gasket with pumping solution, the measured chamber height became 433-450 µm. The fluid velocity in x-direction (V_x) has been measured (Figure 3 (a)) along chip surface up to the glass coverslip (along the vertical position (z)). Also, V_x values were measured (Figure 3 (b)) in between the pumping electrodes (along the horizontal position (y)). The flow profile in vertical position shows pressure driven flow characteristics or parabolic flow profile, where the maximum velocity ($V_{x,\,max}$) obtained in the middle of the chamber (~ half of the chamber height) and close to the chip surface and coverslip shows nearly zero velocity (no slip boundary condition). Polynomial fit equations for applied currents of 100, 200, and 400 uA are: $y = - 0.0009 (\pm 5.42 \times 10^{-6}) x^2 + 0.409 (\pm 0.002)x + 0.68 (\pm 0.24)$, $R^2 = 0.9974$; $y = - 0.002$

($\pm$ 9.62 × 10^{-6}) x^2 +0.783 ($\pm$ 0.004)x - 1.51 ($\pm$ 0.34) , R^2 = 0.9982; and y = - 0.004 ($\pm$ 1.38 × 10^{-5}) x^2 +1.590 ($\pm$ 0.006)x - 4.64 ($\pm$ 0.62) , R^2 = 0.9989, respectively. The slopes were increased by 2.22× and 4.44× with the 2× and 4× current increment from 100 µA applied current. This linear dependency of the fluid speed with applied current has already reported before with our previous work. [9, 11] On the other hand, the flow velocity (V_x) along the horizontal direction (y) has proven to be flat in between working and counter / reference electrodes. This horizontal uniform flow behavior is important for applications like separation on a lab-on-a-chip device and already reported earlier. [7]

Figure S-5 shows the velocity profile of three components (V_x, V_y, and V_z) along the vertical position (z). Though V_x shows parabolic flow profile (Figure S-5 (a)), there are no significant velocity component in y and z direction (Figure S-5 b and c)). Such flow profiles mimic the pressure-driven flow characteristics of rectangular microchannels consisting high aspect ratio.

5.3.4 Varied Gasket Thickness with the Same Applied Current

In the second set of experiments, ±400 µA current applied to generate fluid flow with 0.50 (Gasket 1), 1.0 (Gasket 2), and 2.0 mm (Gasket 3) thick gaskets. After sealing off the fluid chamber with 0.10 M NaCl solution, the final measured experimental chamber heights were 429, 856, and 1680 µm. The increase in gasket heights (fluid chamber height) resulted in increased fluid velocity due to the drop in the fluid flow resistance (Figure 4 (a)). The flow profiles obtained in three different gasket heights shows parabolic characteristics with these following fit-line equations Gasket 3, y = -0.004 ($\pm$ 1.61×10^{-5}) x^2 + 1.600 ($\pm$ 0.007)x – 3.020 ($\pm$ 0.672) , R^2 = 0.9994; Gasket 2, y = -0.002 ($\pm$ 4.08×10^{-6}) x^2 + 1.590 ($\pm$ 0.003)x -3.064 ($\pm$ 0.632) , R^2 = 0.9996;

and Gasket 1, $y = - 0.0009 (\pm 3.0 \times 10^{-6}) x^2 + 1.445 (\pm 0.005)x - 4.643 (\pm 1.815)$, $R^2 = 0.9983$. The slopes were increased by 2.22× and 4.44× with the 2× and 4× increment of gasket chamber heights. This is also linear increment of flow speed with increasing chamber heights at a constant applied current. The normalized representation in Figure 4 (a) ($V_x/V_{x,max}$ vs z/H) shows very similar flow profiles for all three gaskets, whereas the maxima for the gasket 1, 2, and 3 fit-lines are $0.5004 \pm 3.10 \times 10^{-3}$, $0.5009 \pm 1.55 \times 10^{-3}$, and $0.4997 \pm 2.42 \times 10^{-3}$. All these maxima values are within each other error. The ratio of the chamber heights to electrode gap were 0.14, 0.28, and 0.56 for 0.50, 1.0, and 2.0 mm gaskets, respectively. It is evident from the result that, up to 0.56 chamber height / electrode gap ratio the flow profiles remain unchanged.

5.3.5 Varied Electrolyte Concentration

Three different concentrations such as 0.10, 0.50 and 1.30 M NaCl were used as pumping solution in the R-MHD fluid chamber. For each pumping solution four currents (± 50, ± 400, ± 800, and ± 1000 µA) were applied to generate fluid flow. The nominal dry gasket and measured chamber heights were 2.0 mm and 1690 µm, respectively. The reason behind applying high current and high salt concentration was to see any probable flow profile deviation from the usual parabolic characteristics. Higher ionic presence with high applied electronic currents in between the electrodes should concentrate ionic current field lines close to the chip (electrodes) surface. Assuming magnetic field (B) is homogeneous throughout the chamber height, this phenomenon should move the maxima of the flow profiles close to the chip rather than the middle of the chamber. Figure 5 (a), (c), and (e) show fluid velocity profile (V_x) along the vertical position (z) of the fluid chamber, whereas (b), (d), and (f) show their normalized flow profiles. As expected, for a specific electrolyte concentration, flow velocity (V_x) increases with increased applied currents (Figure 5 (a), (c), and (e)). The fit-line equations for all the flow profiles and maxima for

normalized flow profiles are included in the Supporting Information. Across three different electrolyte concentration, all the maxima values stay in each other errors. This evident suggest the fluidic profile directs by the viscous force even with the application of high salt concentration and applied current, at least for this specific chamber height and electrode gap ratio (0.56).

On the other hand, the maximum R-MHD flow velocity ($V_{x, max}$) dependency with applied currents across the electrolyte concentration revealed an interesting phenomenon. The slopes of the linear trend have increased by 1.37× and 1.65×, when the concentration increased by 5× and 13× from 0.10 M. At a constant applied current in between active electrodes, higher ionic current density (j) generates due to the presence of higher number of ions. The abundancy of electrolyte ions in the fluidic chamber give rise to high number of ion flux per area that induced by a constant applied current. The rise is the viscosity with the electrolyte concentration resulted in the smaller slope hikes in maximum velocity ($V_{x, max}$) trend (1.37× and 1.65×) compared to the concentration increment (5× and 10×). The linearity deviates by 0.40 % and 1.2 % from 1.000, when electrolyte concentration increased by 5× and 10× from 0.10 M NaCl. The probable cause for this deviation is viscosity and high ionic strength of electrolyte solution.

5.4 Conclusions

This is the very first approach to combine APTV with R-MHD microfluidic pumping system. APTV allowed us to analyze flow profile with high resolution in three dimensions. The result from this work supported the tunability of R-MHD pumping system. Not only the flow speed has a linear dependency on the applied current, speed can also be tuned with the modification of gasket height (fluidic resistance) and pumping solution (electrolyte concentration). It was evident form this study that, flow in stream-wise direction scales with the

Lorentz-force and no significant velocity vectors observed in y and z direction. As per the flow profile goes, the parabolic characteristics remain unchanged for all the experimental variations and up to 0.56 chamber height to electrode gap ratio. This is the indication of dominant viscous force ($Re \leq 1$). Further study with the larger ratio of chamber height to the electrode gap is required to have a better understanding of the correlation between Lorentz force and R-MHD flow profile.

5.5 Supporting Information

Supporting information contains fit-line equations of flow profiles while the concentrations of pumping solution were varied, maxima values for normalized flow profiles, design schematic of the chip, CV of bare electrode, CA and CV characterization of PEDOT film in 0.10 M NaCl, CP responses at different applied current during MHD pumping, and velocity profiles of three components along the chamber height (z) that was achieved with constant chamber height but with varied applied currents.

5.6 Acknowledgements

The author gratefully thanks Dr Jörg König, Professor Dr. Christian Cierpka, Wiebke Rösing, and Gerd Mutschke for their help. The author also gratefully acknowledges financial supports from Deutsche Forschungsgemeinschaft (DFG) within the re-search training group 1567 “Lorentz Force Velocimetry and Lorentz Force Eddy Current Testing”, grant number CI 185/, and National Science Foundation grants (CBET-1336853 and CHE-1808286).

5.7 References

(1) Sackmann, E. K.; Fulton, A. L.; Beebe, D. J. The present and future role of microfluidics in biomedical research. *Nature* **2014,** *507*, 181, DOI: 10.1038/nature13118.

(2) Tegenfeldt, J. O.; Prinz, C.; Cao, H.; Huang, R. L.; Austin, R. H.; Chou, S. Y.; Cox, E. C.; Sturm, J. C. Micro- and nanofluidics for DNA analysis. *Analytical and Bioanalytical Chemistry* **2004,** *378* (7), 1678-1692, DOI: 10.1007/s00216-004-2526-0.

(3) Dittrich, P. S.; Manz, A. Lab-on-a-chip: microfluidics in drug discovery. *Nature Reviews Drug Discovery* **2006,** *5* (3), 210-218, DOI: 10.1038/nrd1985.

(4) Rondelez, Y.; Tresset, G.; Tabata, K. V.; Arata, H.; Fujita, H.; Takeuchi, S.; Noji, H. Microfabricated arrays of femtoliter chambers allow single molecule enzymology. *Nature Biotechnology* **2005,** *23* (3), 361-365, DOI: 10.1038/nbt1072.

(5) Lipman, E. A.; Schuler, B.; Bakajin, O.; Eaton, W. A. Single-Molecule Measurement of Protein Folding Kinetics. *Science* **2003,** *301* (5637), 1233, DOI: 10.1126/science.1085399.

(6) Weston, M. C.; Gerner, M. D.; Fritsch, I. Magnetic Fields for Fluid Motion. *Analytical Chemistry* **2010,** *82* (9), 3411-3418, DOI: 10.1021/ac901783n.

(7) Sahore, V.; Fritsch, I. Flat Flow Profiles Achieved with Microfluidics Generated by Redox-Magnetohydrodynamics. *Analytical Chemistry* **2013,** *85* (24), 11809-11816, DOI: 10.1021/ac402476v.

(8) Sahore, V.; Fritsch, I. Microfluidic rotational flow generated by redox-magnetohydrodynamics (MHD) under laminar conditions using concentric disk and ring microelectrodes. *Microfluidics and Nanofluidics* **2015,** *18* (2), 159-166, DOI: 10.1007/s10404-014-1427-6.

(9) Nash, C. K.; Fritsch, I. Poly(3,4-ethylenedioxythiophene)-Modified Electrodes for Microfluidics Pumping with Redox-Magnetohydrodynamics: Improving Compatibility for Broader Applications by Eliminating Addition of Redox Species to Solution. *Analytical Chemistry* **2016,** *88* (3), 1601-1609, DOI: 10.1021/acs.analchem.5b03182.

(10) Sahore, V.; Fritsch, I. Redox-Magnetohydrodynamics, Flat Flow Profile-Guided Enzyme Assay Detection: Toward Multiple, Parallel Analyses. *Analytical Chemistry* **2014,** *86* (19), 9405-9411, DOI: 10.1021/ac502014t.

(11) Khan, F. Z.; Hutcheson, J. A.; Hunter, C. J.; Powless, A. J.; Benson, D.; Fritsch, I.; Muldoon, T. J. Redox-Magnetohydrodynamically Controlled Fluid Flow with Poly(3,4-ethylenedioxythiophene) Coupled to an Epitaxial Light Sheet Confocal Microscope for Image Cytometry Applications. *Analytical Chemistry* **2018,** *90* (13), 7862-7870, DOI: 10.1021/acs.analchem.7b05312.

(12) Haehnel, V.; Khan, F. Z.; Mutschke, G.; Cierpka, C.; Uhlemann, M.; Fritsch, I. Combining magnetic forces for contactless manipulation of fluids in microelectrode-microfluidic systems. *Scientific Reports* **2019,** *9* (1), 5103, DOI: 10.1038/s41598-019-41284-0.

(13) Bayraktar, T.; Pidugu, S. B. Characterization of liquid flows in microfluidic systems. *International Journal of Heat and Mass Transfer* **2006,** *49* (5), 815-824, DOI: https://doi.org/10.1016/j.ijheatmasstransfer.2005.11.007.

(14) Gao, F.; Kreidermacher, A.; Fritsch, I.; Heyes, C. D. 3D Imaging of Flow Patterns in an Internally-Pumped Microfluidic Device: Redox Magnetohydrodynamics and Electrochemically-Generated Density Gradients. *Analytical Chemistry* **2013,** *85* (9), 4414-4422, DOI: 10.1021/ac3036926.

(15) Sahore, V.; Kreidermacher, A.; Khan, F. Z.; Fritsch, I. Visualization and Measurement of Natural Convection from Electrochemically-Generated Density Gradients at Concentric Microdisk and Ring Electrodes in a Microfluidic System. *Journal of The Electrochemical Society* **2016,** *163* (4), H3135-H3144.

(16) Cierpka, C.; Rossi, M.; Segura, R.; Kähler, C. J. On the calibration of astigmatism particle tracking velocimetry for microflows. *Measurement Science and Technology* **2010,** *22* (1), 015401, DOI: 10.1088/0957-0233/22/1/015401.

(17) Cierpka, C.; Segura, R.; Hain, R.; Kähler, C. J. A simple single camera 3C3D velocity measurement technique without errors due to depth of correlation and spatial averaging for microfluidics. *Measurement Science and Technology* **2010,** *21* (4), 045401, DOI: 10.1088/0957-0233/21/4/045401.

(18) Khan, F. Z.; Fritsch, I. Chip-Scale Electrodeposition and Analysis of Poly(3,4-ethylenedioxythiophene) (PEDOT) Films for Enhanced and Sustained Microfluidics Using DC-Redox-Magnetohydrodynamics. *Journal of The Electrochemical Society* **2019**, (in revision).

(19) Rossi, M.; Segura, R.; Cierpka, C.; Kähler, C. J. On the effect of particle image intensity and image preprocessing on the depth of correlation in micro-PIV. *Experiments in Fluids* **2012,** *52* (4), 1063-1075, DOI: 10.1007/s00348-011-1194-z.

5.8 Figures

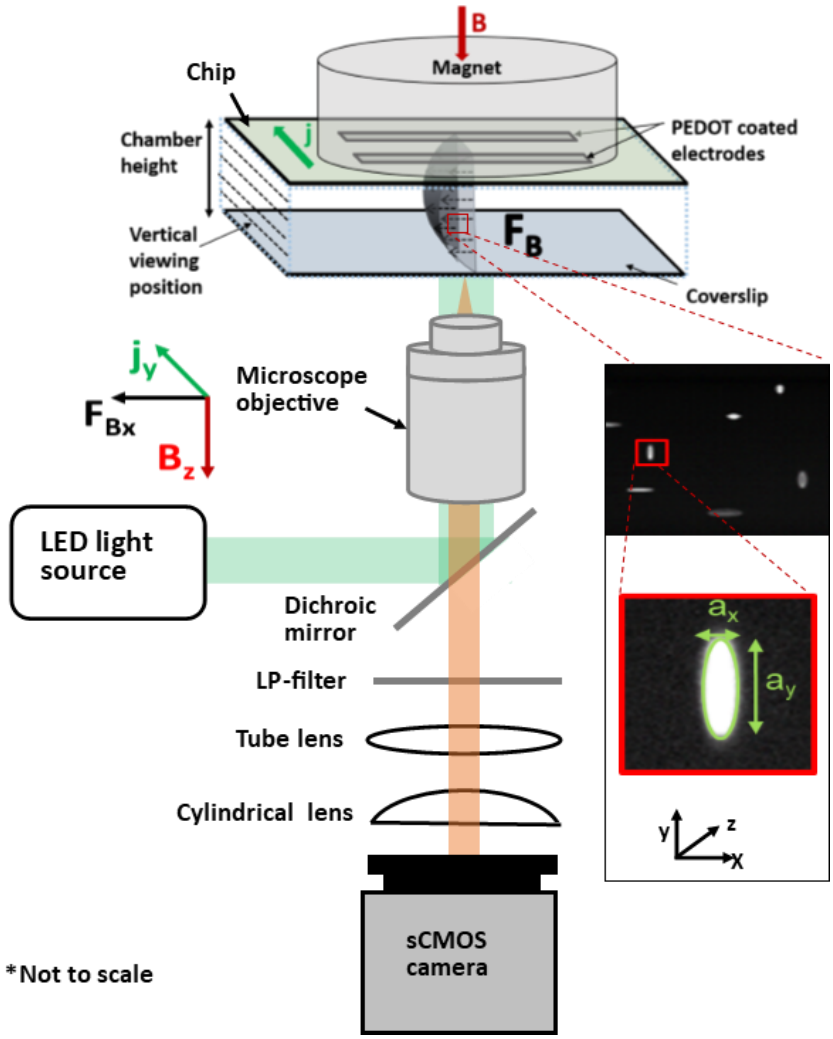

Figure 1: R-MHD / APTV coupled setup where the fluidic chamber placed upside down on a stage over the epi-fluorescent microscope. Green LED light excites the fluorescent labeled particles in the flow chamber through the objective. A thin coverslip placed over the gasket acted as lid and allowed optical access to the flow region. A cylindrical lens (200 mm focal length) along with a convex lens placed in front of the CMOS camera. The inset images show suspended prolate and oblate shaped beads in the flow chamber.

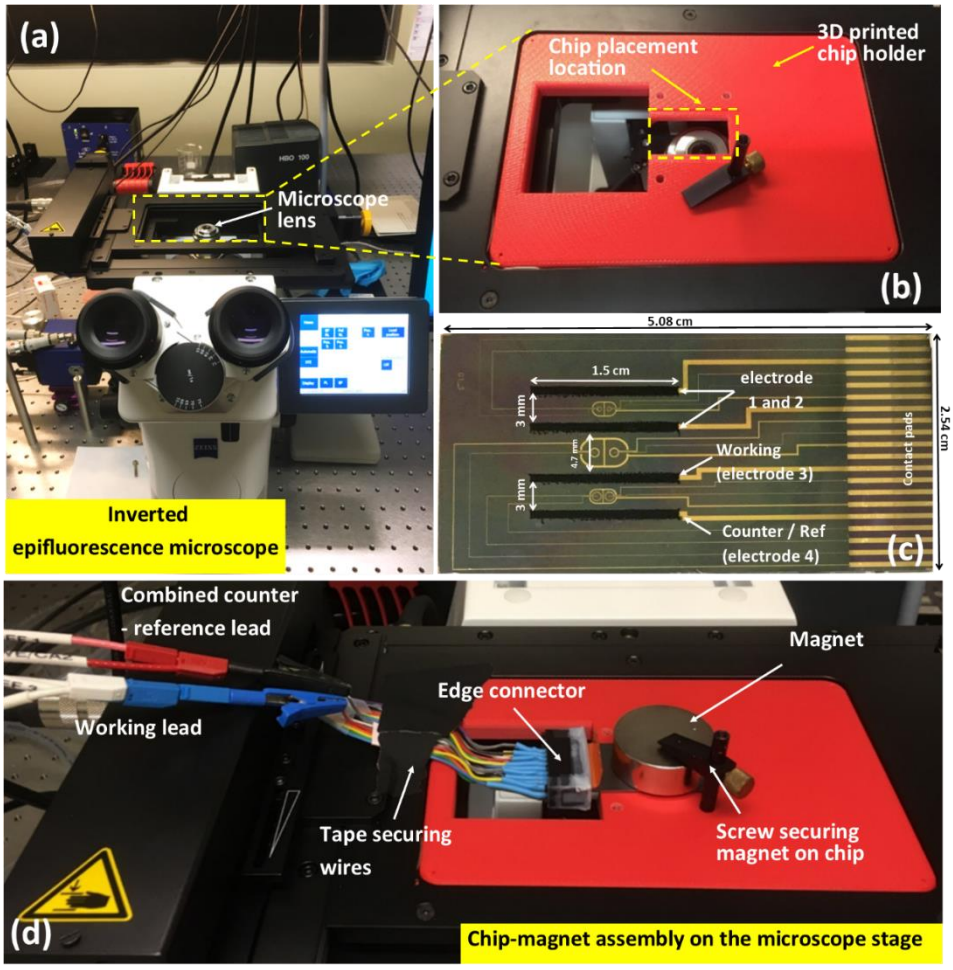

Figure 2: (a) An inverted epifluorescence microscope consisting microscope stage over the microscope lens. (b) a 3D printed chip holder consisting the "chip placement location" that is grooved with the same size of the chip. (c) a chip electrodeposited with PEDOT films on four band electrodes whereas electrode 3 and 4 served as working and counter / ref electrode.
(d) The "chip-gasket-coverslip" assembly placed upside down on the "chip placement location" and a permanent magnet placed on the backside of the chip and secured with a screw. Working and counter-reference lead from the galvanostat were attached with the edge connector wires and the wires were taped on the stage to ensure minimum movement.

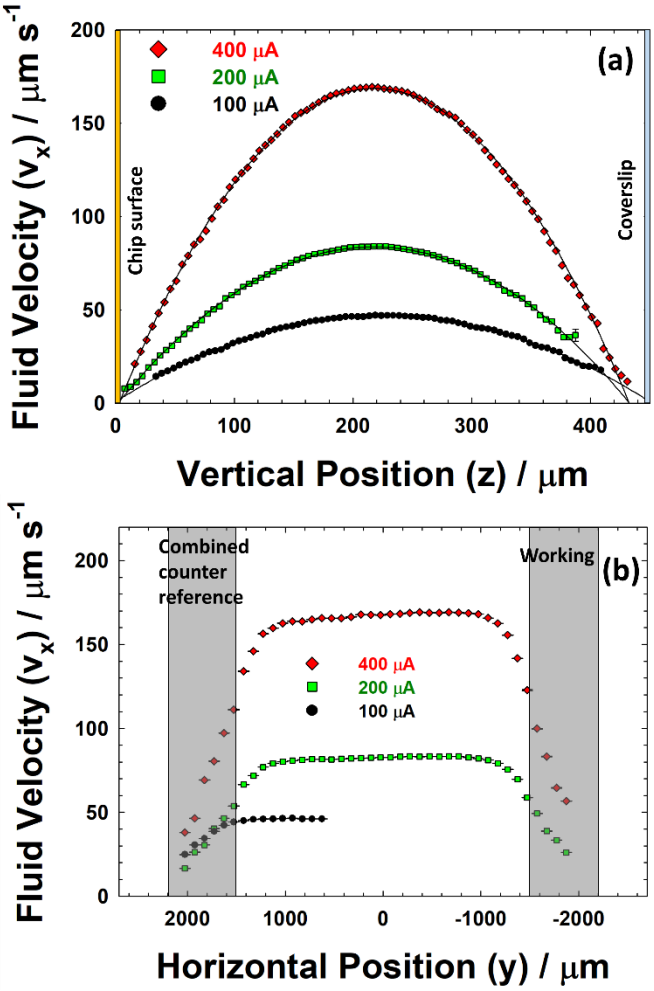

Figure 3: Fluid velocity profiles of V_x in the (a) vertical (at x = 0, y = 0) and (b) horizontal (x = 0, z = 0) planes obtained by APTV at different currents between PEDOT-modified electrodes in 0.10 M NaCl using a fixed gasket thickness (chamber height = 433 to 450 μm). Equations with the least squares polynomial fit to the data for applied currents of 100, 200, and 400 uA are: $y = - 0.0009 (\pm 5.42 \times 10^{-6}) x^2 + 0.409 (\pm 0.002)x + 0.68 (\pm 0.24)$, $R^2 = 0.9974$; $y = - 0.002 (\pm 9.62 \times 10^{-6}) x^2 + 0.783 (\pm 0.004)x - 1.51 (\pm 0.34)$, $R^2 = 0.9982$; and $y = - 0.004 (\pm 1.38 \times 10^{-5}) x^2 + 1.590 (\pm 0.006)x - 4.64 (\pm 0.62)$, $R^2 = 0.9989$, respectively.

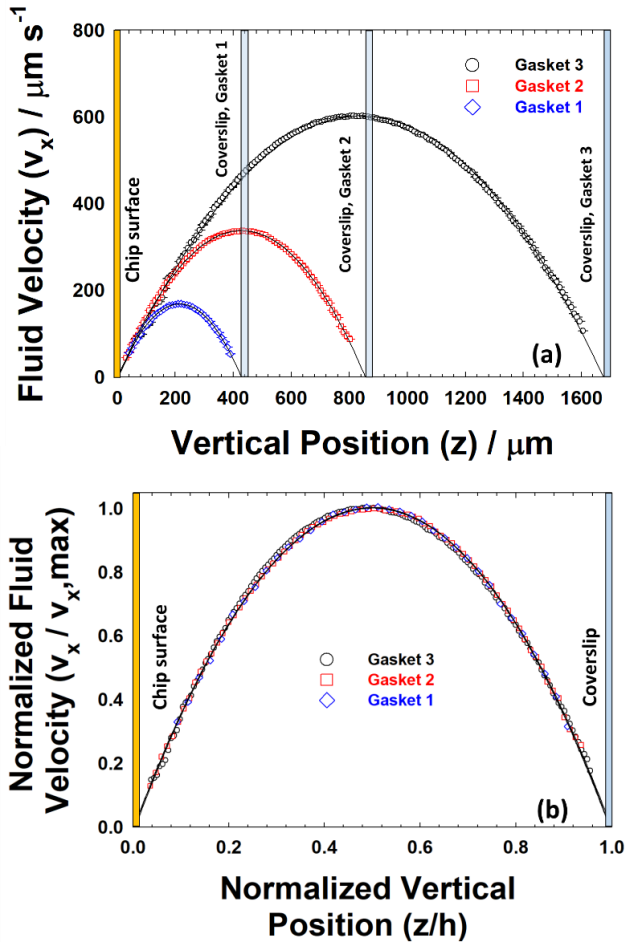

Figure 4: (a) Non-normalized (v_x, at x = 0, y = 0) and (b) normalized ($v_x/v_{x,max}$ at x = 0, y = 0) fluid velocity profiles in the vertical plane obtained by APTV for different chamber heights (Gasket 1 (429 μm) , Gasket 2(856 μm) , and Gasket 3 (1680 μm)) for a fixed applied current (400 μA) between PEDOT-modified electrodes in 0.10 M NaCl. Profiles shown across the vertical dimension, z, in (a) have least squares polynomial fits for the three chamber heights as follows: Gasket 3, $y = -0.004 (\pm 1.61 \times 10^{-5}) x^2 + 1.600 (\pm 0.007)x - 3.020 (\pm 0.672)$, $R^2 = 0.9994$; Gasket 2, $y = -0.002 (\pm 4.08 \times 10^{-6}) x^2 + 1.590 (\pm 0.003)x - 3.064 (\pm 0.632)$, $R^2 = 0.9996$; and Gasket 1, $y = -0.0009 (\pm 2.99 \times 10^{-6}) x^2 + 1.445 (\pm 0.005)x - 4.643 (\pm 1.815)$, $R^2 = 0.9983$. Profiles shown across the vertical dimension that is normalized to the z-position where the maximum velocity was observed, $v_{x,max}$, in (b) have least squares polynomial fits for the three chamber heights as follows: Gasket 1, $y = -4.079 (\pm 0.018) x^2 + 4.082 (\pm 0.018)x - 0.018 (\pm 0.004)$, Gasket 2, $R^2 = 0.9994$; $y = -4.026 (\pm 0.009) x^2 + 4.034 (\pm 0.009)x - 0.009 (\pm 0.002)$, $R^2 = 0.9996$; and Gasket 3, $y = -4.044 (\pm 0.014) x^2 + 4.042 (\pm 0.014)x - 0.008 (\pm 0.003)$, $R^2 = 0.9983$. The maxima in (b) appear at 0.5004 (Gasket 1), 0.5009 (Gasket 2), and 0.4996 (Gasket 3).

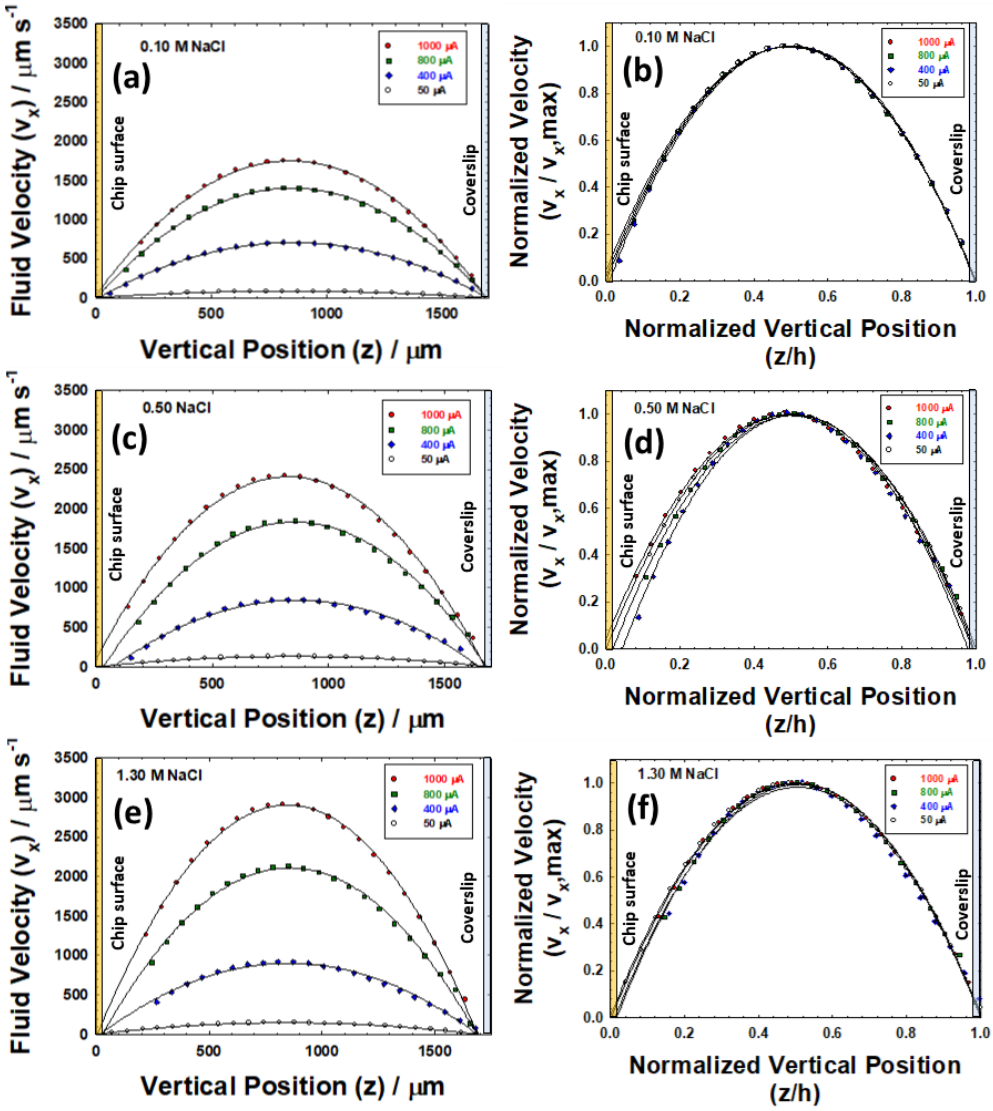

Figure 5: (a), (c), and (e) are non-normalized (v_x at x = 0, y = 0) and (b), (d), and (f) normalized ($v_x/v_{x,max}$ at x = 0, y = 0) fluid velocity profiles in the vertical plane obtained by µPIV for a series of different applied currents (50, 400, 800, and 1000 µA) between PEDOT-modified electrodes at three different electrolyte concentrations (a) 0.10, (b) 0.50, and 1.30 M NaCl), and for a single gasket (chamber height = ~ 1690 µm). The least squares best polynomial fits for (a) – (f) are included in the Supporting Information.

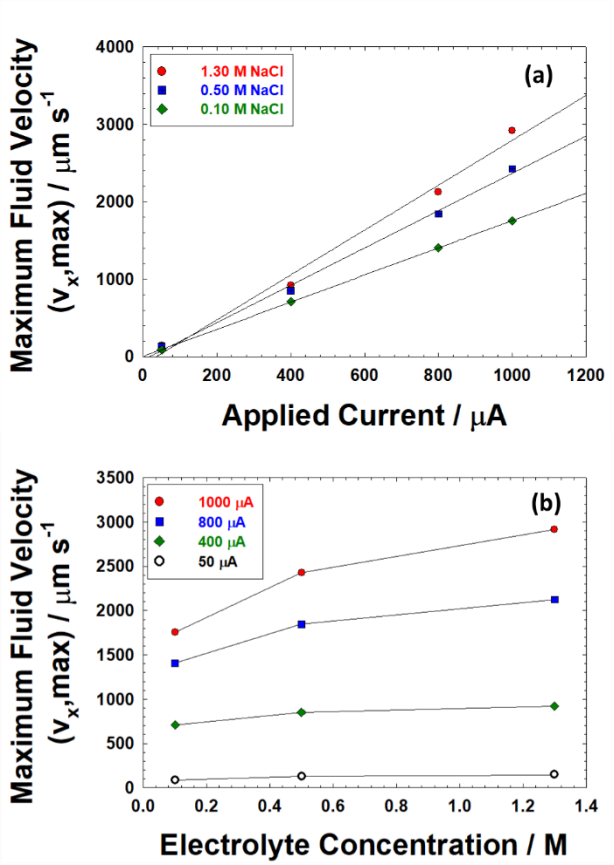

Figure 6: Comparison of maximum fluid velocities in the vertical plane ($V_{x,max}$ at x = 0, y = 0) obtained by μPIV at four different applied currents (50, 400, 800, and 1000 uA) between PEDOT-modified electrodes and at three electrolyte concentrations (0.10, 0.50, and 1.30 M NaCl) for a fixed gasket thickness (chamber height ~ 1690 um). In (a), maximum velocities are shown as a function of applied current for a given concentration, with with following least squares polynomial fits: at 1.30 M NaCl, y = 2.90 (±0.22) x – 103.45 (± 148.81), R^2= 0.9884; at 0.50 M NaCl, y = 2.41 (±0.11) x – 42.36 (± 73.39), R^2= 0.9959; and at 0.10 M NaCl, y = 1.754 (±0.003) x + 1.94 (± 2.24), R^2= 1.000. In (b), maximum velocities are shown as a function of electrolyte concentration for a given current.

5.S Supporting Information: 3D Velocity Profile Analysis of Redox-Magnetohydrodynamics (R-MHD) Induced Flow in a Microfluidic Chamber by Astigmatism Particle Tracking Velocimetry (APTV)

Supporting information contains fit-line equations of flow profiles while the concentrations of pumping solution were varied, maxima values for normalized flow profiles, design schematic of the chip, CV of bare electrode, CA and CV characterization of PEDOT film in 0.10 M NaCl, CP responses at different applied current during MHD pumping, and velocity profiles of three components along the chamber height (z) that was achieved with constant chamber height but with varied applied currents.

5.S1 Fit-Line Equations of Flow Profiles While the Concentrations of Pumping Solution Were Varied.

For each concentration of electrolyte solution (0.10, 0.50, and 1.30 M), four different current were applied in between active electrodes (50, 400, 800, and 1000 µA) to generate R-MHD induced fluid flow. Each flow was analyzed by APTV technique and the equations for the fit-lines are given below.

For 0.10 M NaCl, equations of fit lines for 1000, 800, 400, and 50 µA applied currents are, $y = -0.0024 (\pm 2.25\times10^{-5}) x^2 + 4.0905 (\pm 0.0421) x + 25.7724 (\pm 17.0655)$, $R^2 = 0.9986$; $y = -0.0020 (\pm 1.95\times10^{-5}) x^2 + 3.3236 (\pm 0.0353)x - 7.3336 (\pm 13.6307)$, $R^2 = 0.9981$; $y = -0.0010 (\pm 9.08\times10^{-6}) x^2 + 1.7111 (\pm 0.0158)x - 23.5384 (\pm 5.8075)$, $R^2 = 0.9983$; and $y = -0.0001 (\pm 1.06\times10^{-6}) x^2 + 0.1998 (\pm 0.0021)x + 3.7014 (\pm 0.9379)$, $R^2 = 0.9992$.

For 0.50 M NaCl, equations of fit lines for 1000, 800, 400, and 50 µA applied currents are, $y = -0.0034 (\pm 4.01\times10^{-5}) x^2 + 5.5727 (\pm 0.0725) x + 98.7785 (\pm 28.0089)$, $R^2 = 0.9973$; $y = -0.0027 (\pm 4.60\times10^{-5}) x^2 + 4.6118 (\pm 0.0840)x - 141.5214 (\pm 33.1360)$, $R^2 = 0.9947$, $y = -0.0014 (\pm 3.29\times10^{-5}) x^2 + 2.3392 (\pm 0.0579)x - 167.3275 (\pm 21.8433)$, $R^2 = 0.9889$; and $y = -0.0002 (\pm 1.02\times10^{-6}) x^2 + 0.3109 (\pm 0.002)x - 0.3718 (\pm 0.7658)$.

For 1.30 M NaCl, equations of fit lines for 1000, 800, 400, and 50 µA applied currents are, $y = -0.0041 (\pm 3.96\times10^{-5}) x^2 + 6.9241 (\pm 0.0751) x - 30.3027 (\pm 31.0747)$, $R^2 = 0.9985$; $y = -0.0031 (\pm 5.06\times10^{-5}) x^2 + 5.2536 (\pm 0.0374)x - 145.4296 (\pm 41.4322)$, $R^2 = 0.9959$; $y = -0.0013 (\pm 3.60\times10^{-5}) x^2 + 2.2090 (\pm 0.0715)x - 43.7165 (\pm 31.2162)$, $R^2 = 0.9896$; and $y = -0.0002 (\pm 1.35\times10^{-6}) x^2 + 0.3452 (\pm 0.0024)x + 0.9180 (\pm 0.9336)$, $R^2 = 0.9991$.

5.S2 Supporting Information Tables

Table S 1: Maxima or apex values of normalized fit lines while concentrations of the pumping solution were varied

Applied Current	0.10 M NaCl	0.50 M NaCl	1.30 M NaCl
50	0.4943 ± 0.0070	0.5009 ± 0.0041	0.5012 ± 0.0048
400	0.5031 ± 0.0065	0.5113 ± 0.0177	0.5065 ± 0.0216
800	0.4996 ± 0.0072	0.5069 ± 0.0126	0.5087 ± 0.0126
1000	0.4966 ± 0.0070	0.4906 ± 0.0092	0.5026 ± 0.0073

5.S3 Supporting Information Figures

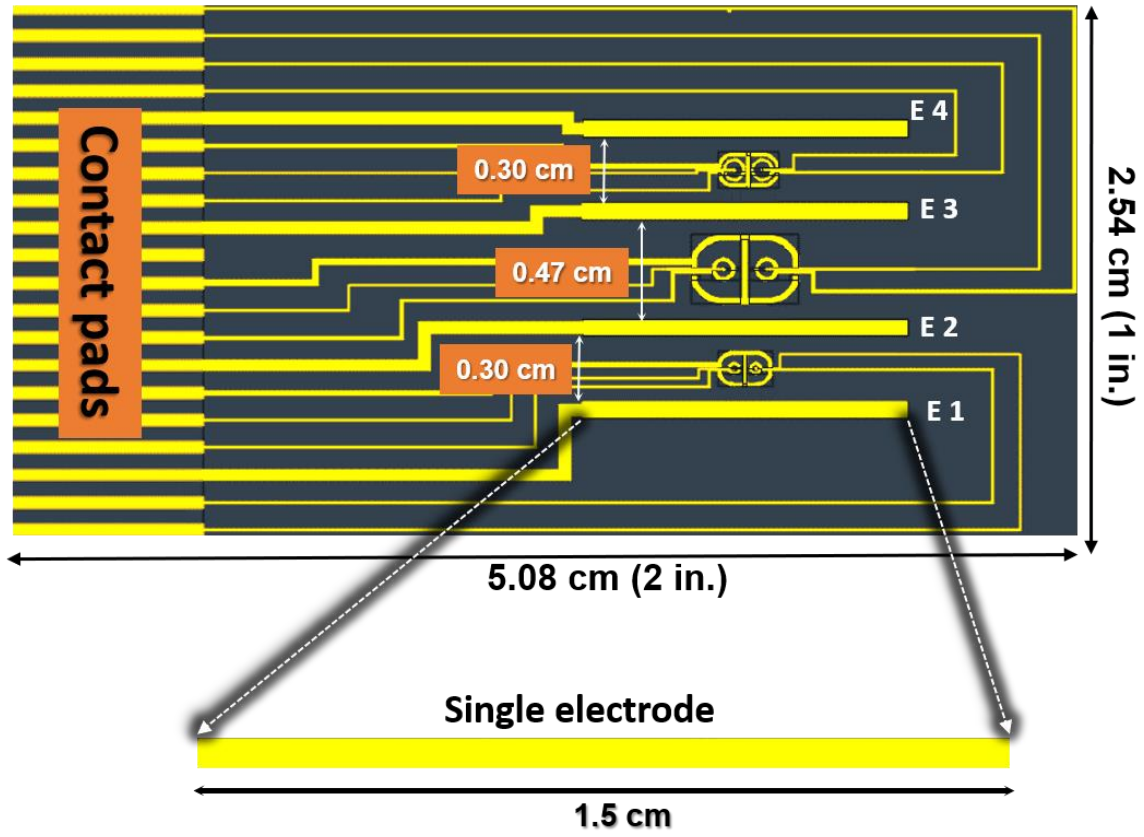

Figure S-1: The schematic of the chip with a dimension of 2 in. × 1 in. Each chip contains four band electrodes where each of them are in 1.5 cm in length and 650 µm in width. The outer most two electrode pairs are 0.30 cm apart whereas the inner most two electrodes have 0.47 cm gap between them. Each band electrode can be individually addressed through the contact pads.

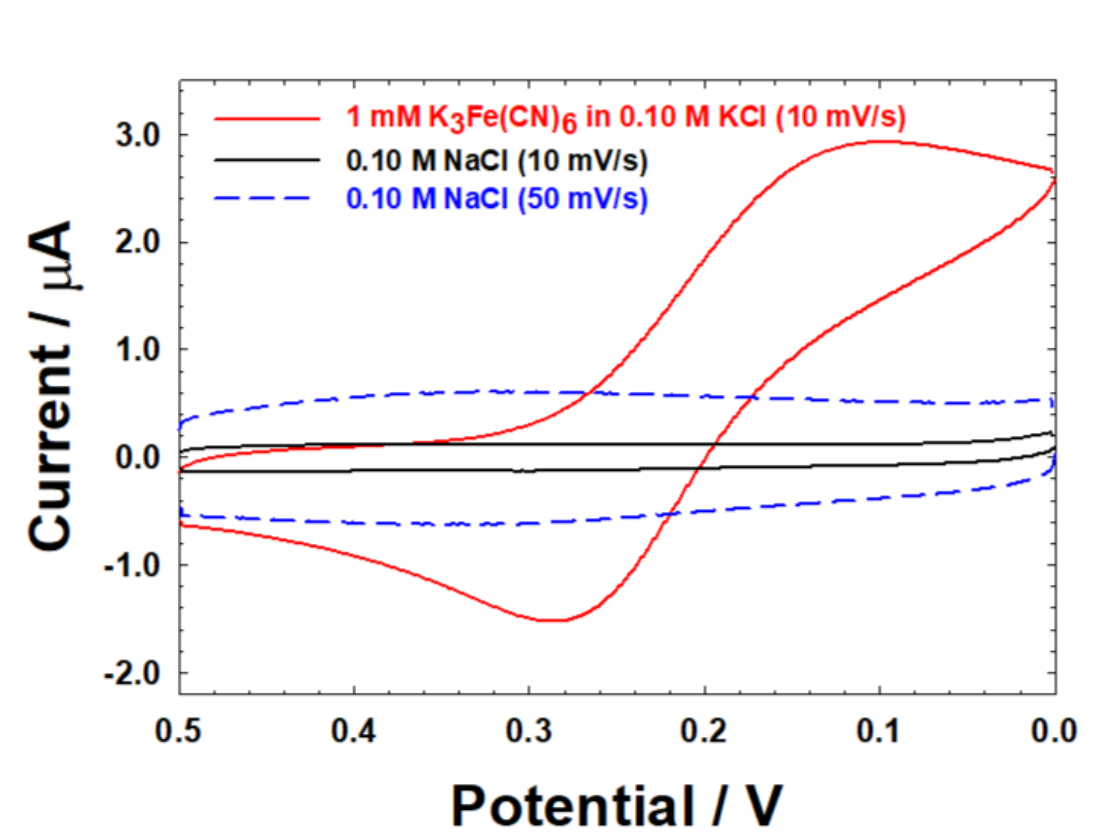

Figure S-2: The cyclic voltammetry responses of bare gold electrode in 1 mM $K_3Fe(CN)_6$ / 0.10 M KCl solution (red) and in 0.10 M NaCl (black and blue). The experiments were performed in a three-electrode setup where Ag/AgCl (saturated KCl) used as reference and Pt flag used as counter electrode. CV experiments were performed at 0 to 0.5 V potential window and 10 to 50 mV/s scan rates.

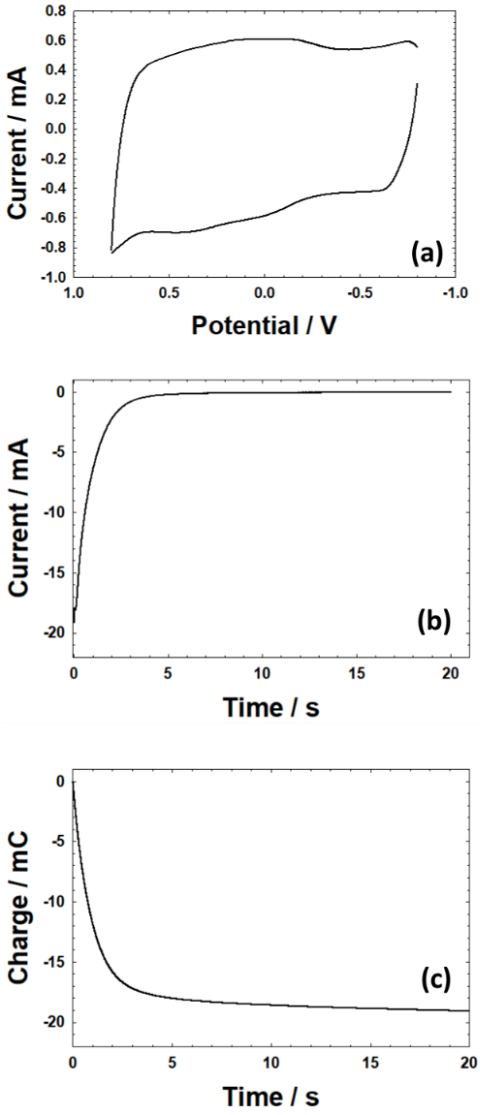

Figure S-3: (a), (b), and (c) show CV, CA, and integrated CA responses of PEDOT-coated electrode in 0.10 M NaCl solution. The experiments were performed in a three-electrode setup where Ag/AgCl (saturated KCl) used as reference and Pt flag used as counter electrode. CV experiments were performed at -0.800 to +0.800 V potential window at 50 mV/s scan rate. CA was done by holding the potential at -0.800 V for 20 sec and then stepped to +0.800 V for the

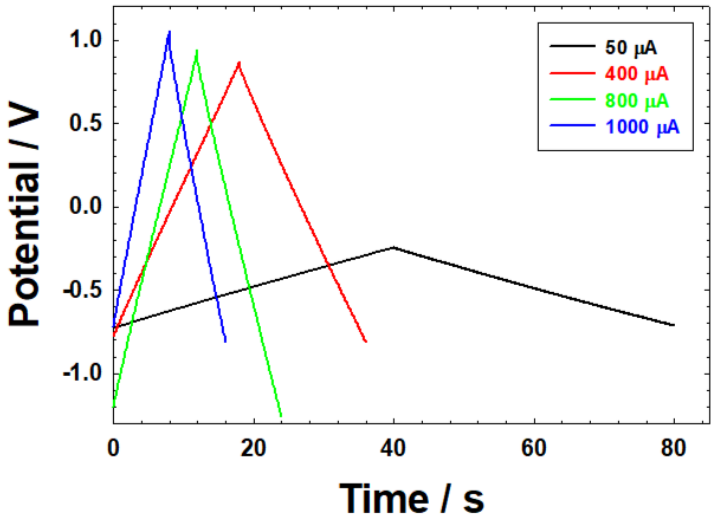

Figure S-4: CP responses of ± 50, ± 400, ± 800 and ± 1000 µA currents that involves in characterizing R-MHD fluid flow in a microfluidic device containing 0.10 M NaCl solution. Two co-planner and adjacent PEDOT coated electrodes were served as working and quasi counter/reference electrode to perform the MHD experiments. Cut-off voltages of -1.4 to +1.4 V used to avoid overoxidation of PEDOT film.

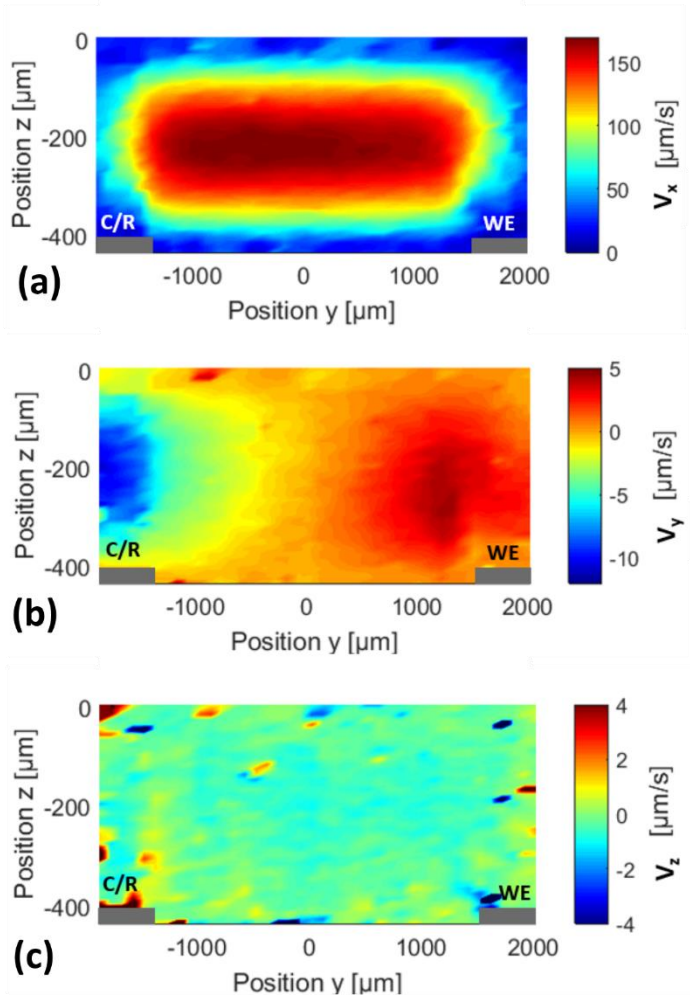

Figure S-5: (a), (b), and (c) depict the velocity profile in x,y and z direction along the height (z) of the fluid chamber. The fluid flow was achieved in a microfluidic chamber where ± 400 µA current was applied in between two adjacent PEDOT coated electrodes, which were selected as working and counter / reference. 0.10 M NaCl poured as pumping solution within a well that formed by a 0.50 mm nominal dry gasket.

6. Sustained Microfluidics Pumping with Conducting Polymer-Modified, DC-Redox-Magnetohydrodynamics (R-MHD) Achieved by Switching Permanent Magnets

6.1 Introduction

The ability to maneuver small amounts of fluids on a chip at low cost makes microfluidics promising for chemical synthesis, mixing, separations and chemical analysis applications. Microfluidics offers high specificity and allow short analysis time. [1-2] Lab-on-a-chip microfluidics has been a subject of interest in recent years as a diagnostic tool for biomedical applications. According to the World Health Organization, deployable diagnostic devices in developing countries should be sensitive, affordable, rapid and robust, specific, and equipment free.[3] The small and deployable system must have a way to introduce, mix, and transport samples through them. Different approaches to moving fluids, such as centrifugal force, electroosmotic processes, diffuser, and optically driven have been used in a microfluidic setups.[4-7] Paper based microfluidics offer easily modifiable and pumpless cheaper alternative to conventional laboratory testing methods but suffer from uncontrolled sample transport. [8-10]. Therefore, there are still gaps that still need to be filled with other microfluidics approaches, such as Redox- magnetohydrodynamics (R-MHD). It is a unique addition to microfluidic approaches that can produce a flat horizontal flow profiles over large distances (>5 mm) with flexibility in device size and design. This approach has been shown to tune speed and flow duration, pump in a loop, and start, stop, and reverse directions of fluid flow over a chip containing co-planar microelectrodes.,[11-14] It does not require valves, channels, nor high voltages (> 2 V) compared to other pumping methods. R-MHD is governed by the right-hand rule, $\mathbf{F_B = j \times B}$ (the magnetic portion of the Lorentz force) where the perpendicular interaction between an ionic current (**j**, C/s m^2) and magnetic field (**B**, T) generates a body force ($\mathbf{F_B}$), in a direction perpendicular to both **j**

and **B**.[11] Solution-dissolved or electrode-confined redox species convert electronic current into ionic current at the electrode-solution interface, thereby avoiding bubble formation, electrode corrosion, and joule heating due to application of high applied voltages (> 10V).[15]

Different shapes of electrode with individual addressability can be patterned on the silicon substrate as chip by using photolithography approach. Redox species that can be immobilized on these electrode surface, such as a layer of conducting polymer (CP) poly(3,4-ethylenedioxythiophene) (PEDOT), offer higher initial current density, minimal analyte interference, and compatibility with biological samples compared to adding redox species to solution. [12-13] When current or potential applied in between these modified electrodes, ionic current density (j) generate in the electrolyte solution through the redox reaction of CP.

The charge capacity of the polymer film, however, ultimately limits the duration of pumping. A maximum fluid speed requires the highest current, and therefore fastest consumption of charge in the polymer film, thus producing a short pumping time. [12-14] To recharge the polymer, an oppositely biased current must be applied. However, if the direction of the magnetic field from a magnet placed under the chip is left unchanged, then reversing the current will change the direction of flow. This periodically reversed fluid flow can be useful in some applications like in image cytometry as we have recently described.[14, 16] Nonetheless, for many other applications, it is desirable to further increase pumping duration in a single direction. To do so, electrodeposition of PEDOT has been optimized by varying electrolytes, solvents, and electrodeposition techniques. Derivatives of PEDOT have also been investigated through selection of other monomers.[14, 17-18]

The need to pump in a single direction indefinitely remains to be addressed. Continuous redox-magnetohydrodynamics pumping, for example, would offer higher throughput and flexibility in applications such as on-chip separations, imaging cytometry, and biological cell sorting.

Continuous, PEDOT R-MHD pumping can be established when both the current bias and magnetic field direction are simultaneously changed. One approach used previously is AC magnetohydrodynamics, where a sinusoidal perturbation of current at electrodes and the field of electromagnets are synchronized.[19-21] In the more traditional etched narrow channel on a silicon substrate, [19-20] the AC-MHD produces a parabolic-like horizontal velocity profile between electrodes, more typical of pressure-driven flow. Those studies also required high frequencies (such as 1 KHz) and suffered from inductive heating. Also, a consequence of an AC electromagnet is that it generates lower magnetic field strengths than DC electromagnets. [19, 21] Unless offset by an equivalent increase in electronic current, lower fluid velocities are obtained.

Here, it is shown that by flipping a permanent magnet or using a sequence of permanent magnets with their magnetic fields oriented in opposing directions, it is possible to avoid the disadvantage of the AC-electromagnet-driven MHD. Permanent magnets are simpler than electromagnets and devices that use them can be more easily miniaturized, because they do not require an electronic current supply and synchronizing electronics. We demonstrate a proof-of-concept with an automatic magnet switching device, instead, consisting of two magnets mounted with opposite field directions and sequentially positioned under an MHD chamber. The switching of magnet position is synchronized with reversal of the electrode current bias (using a step function, instead of a sinusoidal one), that propels fluid in the chamber indefinitely in the same direction. The effects of the spatially inhomogeneous magnetic fields of the permanent

magnets on the MHD fluid flow is also addressed to establish a suitable magnet-switching procedure.

Figure 1 shows a representative depiction of magnet switching principal. A negative current was applied for the first 1/3rd of the experimental duration and the chip was over the magnet B (M_B). R-MHD phenomenon pushes the fluid in forward direction at this time. Then for the next 1/3rd duration, zero current was maintained between active electrodes. In this period, magnet A (M_A), which was at the opposite bias than magnet B, switched under the chip by the movement of translational stage. Because of the absence of any current, no fluid flow occurs at this time. A positive current applied for the last 1/3rd duration and the synchronized change in magnetic and current bias sustains the flow direction (to satisfy the right-hand rule ($F_B = j \times B$)).

6.2 Experimental Section

6.2.1 Chemicals and Materials

All aqueous solutions were made with reagent grade deionized water from Ricca Chemical company (Arlington, TX). Propylene carbonate (anhydrous 99.7%), tetrabutylammonium hexafluorophosphate, 3, 4-ethylenedioxythiophene (EDOT), and phosphate buffered saline tablets were purchased from Sigma-Aldrich (St. Louis, MO). Sodium chloride, potassium chloride (99%) and pre-cleaned micro cover glass (24 mm × 30 mm) were obtained from VWR International, LLC (West Chester, PA). Two 0.14 T nickel coated NdFeB permanent magnets (3.5 cm diameter and 1.27 cm height, grade N40) were acquired from Amazing Magnets, Irvine, CA. A DC magnetometer from Alpha lab Incorporation has been used to measure the DC field at 0.01 gauss resolution. Edge connectors (solder contact, 20/40 position, and 0.05 in. pitch) were acquired from Sullins Electronics Corp. (San Marcos, CA). The

fabrication of poly(dimethylsiloxane), PDMS, involved Sylgard184 silicon elastomer base, Sylgard 184 silicon elastomer curing agent, and OS-30 solvent, which were purchased from Ellsworth Adhesives, Milwaukee, WI.

6.2.2 Electrode Chip Design

A 2 in. × 1 in. (50.8 mm × 25.4 mm) silicon-based chip was used as the substrate for electrodes in the MHD experiments (Figure S-1). There were four, coplanar, individually addressable, parallel band electrodes, 1.5 cm long, 650 µm wide and ~250 nm thick. Two outermost and two innermost pairs of electrodes are separated by 0.30 and 0.47 cm, respectively. Further details on electrode fabrication and dimensions are included in the Supporting Information.

6.2.3 PEDOT Electrode Deposition and Characterization

All deposition and characterization studies were performed using a CH Instruments 760B potentiostat / galvanostat (Austin, Texas). (The current convention used throughout this paper assigns anodic current as positive.) Prior to electrodeposition, the electrode chips were plasma cleaned in a Harrick plasma cleaner (PDC -32G, Ithaka, NY) for 20 min at 60 mTorr pressure with 6.8 W of power to remove organics from the electrode surface. PEDOT films were deposited on the electrodes by using cyclic voltammetry (CV) from a solution consisting of 0.010 M EDOT monomer and 0.100 M $TBAPF_6$ electrolyte in propylene carbonate (PC). The potential was cycled at 0.005 V/s from -0.455 to 1.4 V vs Ag/AgCl (saturated KCl) reference electrode and using a Pt foil counter electrode. After 12 deposition cycles, a dark blue film can be observed that has overgrown the electrode edges to form fingerlike projections (Figure S-1). See Figure S-2 (a) in Supporting Information for an example of 12 sequential deposition cycles.

The films were then cycled at least five times in monomer-free solution (propylene carbonate and electrolyte only) to stabilize them. After thoroughly rinsing with propylene carbonate and water, the PEDOT-coated chips were stored in water only.

Before performing the MHD studies, the PEDOT-deposited electrodes were characterized in PBS: glycerol electrolyte (v/v, 70% 0.01 M PBS (phosphate buffer saline) with 30% proteome grade glycerol) with a three-electrode system (same as for electrodeposition). The polymer-deposited chips were presoaked in PBS: glycerol for 30 min. and then characterized by CV, chronoamperometry (CA), and chronopotentiometry (CP). Examples of the corresponding electrochemical responses are shown in Figure S-2 (b)-(d) of the Supporting Information, respectively. CV was performed over a potential window of -0.80 to +0.80 V at 0.05 V/s In CA, the potential was held at -0.80 V for 10 s and then stepped to +0.80 V for 10 s. For CP, the applied current was +50 µA and the potential limits were -0.20 and 0.60 V. After characterization, the chips were stored in DI water once again.

6.2.4 Preparation of the R-MHD Microfluidic Chamber

The R-MHD microfluidic chamber was prepared by inserting the PEDOT modified chip in a 20-pin edge connector (Sullins connector solutions, California) by ensuring proper alignment of the chip's pads with edge connector contacts. This ensures the individual addressability of polymer electrodes on the chip. A PDMS gasket of ~762 µm thickness (measured dry), 3 × 2.5 cm in outer dimension, and with a cut-out opening of 2 × 1.8 cm, was placed on the chip to define the microfluidic chamber dimensions. An aliquot of 400 µL PBS: glycerol electrolyte, and 12 µL of 10 µm polystyrene beads (Alfa Aesar, Massachusetts, USA) were added to the chamber and a glass coverslip (2.4 × 3.0 cm and 0.16 mm thickness) was

placed on top to serve as a lid. This solution composition will be denoted as the “buffer / glycerol / bead” solution throughout this paper. Two adjacent polymer modified electrodes (Figure 2 (a) and (b)) were selected as working (electrode 1) and quasi counter / reference electrode (electrode 2). Leads from the galvanostat (PalmSens 4, Houten, The Netherlands) were clipped to the wires coming from the edge connector to individually control the two selected electrodes.

6.2.5 Preparation of “Magnet Switching Assembly” for Automatic Switching Study

The servo-driven magnet switching assembly was machined from phenolic sheet with a nominal thickness of 12.7mm. Two identical sections were machined to approximately 38 × 300 mm and serve as the outer, stationary portion of the mechanism (Figure S-3). These stationary sections have 3 × 12.7 mm nylon splines recessed into stopped dadoes in their inward-facing surfaces. These dadoes were machined using standard high-speed steel tooling on a vertical mill. The nylon splines serve as rails on which the 50 × 300 mm center section, which has corresponding full-length dadoes, moves. Two magnets, approximately 12.7 mm thick and 35 mm in diameter, were press fit into slightly undersized holes bored through the center section and are spaced approximately 85 mm center to center. These bores were made with a small adjustable boring head on the same vertical milling machine use for the stopped and full-length dadoes on the other pieces. The entire assembly was mounted on an aluminum sheet to facilitate installation and removal from the associated microscope stage. The rectilinear motion of the center section housing the magnets is accomplished by two servos acting on two rigid vertical pins sliding in 35 mm slots machined into identical aluminum arms approximately 115 mm long. The aluminum servo arms were machined on the vertical mill with high-speed steel tubing.

6.2.6 Coupling Current Controller with "Magnet Switching Assembly" for Automatic Switching Study

Coupling of the current controller with the magnet switching assembly was accomplished by attaching a servo trigger board's input to a digital output line of the controller. The servo trigger board is a simple pulse width modulation device that moves a servo between two positions when there is a state change on the input. There is a pull-up resistor on the input which allows the signal from the digital line from the current controller to be treated as a normally open switch. The default bi-stable settings of the microcontroller on the board were used. The configuration trimmers for initial position (when the input is open) and second position (when the input is closed) were adjusted to center the magnets under the stationary chip. The rate of movement between the two positions is adjusted by the remaining trimmer to minimize unwanted movement in the assembly. The output from the board that drives the servos is electrically parallel and the servos act in a mechanical push-pull arrangement.

6.2.7 Manual Magnet Switching for the Proof-of-Concept Fluid Flow

Before performing magnet switching in an automatic process, magnet switching was performed in manual process for the proof of concept and to assess the effect of different magnet positions on R-MHD. Figure S-4 (a) shows a chip-magnet holder assembly made of stainless-steel block as a base (8.4 × 6.3 × 0.15 cm) and two sets of glass slides (7.5 × 2.5 × 0.20 cm) taped on the top and bottom portion of the stainless-steel block. These sets of glass slides produced a 3.5 cm wide channel to translate a wooden ruler (having a width of 3.3 cm) lengthwise and onto which two magnets (~ 0.14 T, 2.5 cm in diameter, and 0.63 mm thick) were secured with tape, 2.5 cm apart (edge-to-edge) and with magnetic fields in opposite orientation

(bias) (Figure S-4 (b). The ruler was thinner than the height of the sets of glass slides by 0.20 cm. This determined the clearance between the chip and the magnets so that the magnets could be moved freely beneath the chip. A second edge connector was taped on the top of one set of glass slides into which the edge of the chip opposite to the contact pads was inserted to hold the chip perfectly flat. Figure S-4 (c) and (d) shows the chip with PEDOT coated on four individual electrodes and the complete assembly on the microscope stage, respectively. The current function used for pumping consisted of applying a current of +50 µA between the active PEDOT-modified electrodes for 10 s, followed by 5 s of "open circuit" (zero current). Then a current of opposite bias of -50 µA was applied for 10 s, followed by another 5 s of open circuit. Upon completion of a singular bias current and at the start of the 5 s open circuit period, the magnets A and B, having opposite field direction, were interchanged manually (see Figure S-4 (d) in Supporting Information) by pushing or pulling the wooden ruler under the activated chip/microfluidic chamber. This procedure was repeated six times.

6.2.8 Evaluation of Horizontal Fluid Flow at Different Magnet Positions Using the Manual Magnet Switching Apparatus

Horizontal fluid velocities were analyzed for seven different positions on and off of Magnets A and B under the activated PEDOT-modified electrodes in the microfluidic chamber (see Figure 5). A constant current of + 50 and then – 50 µA were applied for 20 s at a given position, but the fluid flow only recorded for + 50 µA current. Opposite biases of currents were necessary to recharge the already charge exhausted polymer film, in order to sustain the fluid flow Then, this procedure was repeated for each subsequent position. The measurement window between the active electrodes in the chamber was made at a ~ 3 mm offset from a line connecting the centers of the magnets. For each magnet, the center measurement position (position b for

Magnet A and position f for Magnet B) was aligned with its central axis (but with the 3 mm offset as described above). Two other positions were at the magnet edges (positions a and c for Magnet A and positions e and g for Magnet B), spaced out by ~ 1 cm from each magnet's center position. Position d was between and equidistant from the two magnets (Figure S-5).

6.2.9 Sustained R-MHD Pumping with the Automated-Switching Assembly and Galvanostat-Triggering

Both the current for the fluid pumping and the triggering of the magnet switching were controlled by a PalmSens4 in galvanostat mode, using the following procedure. The R-MHD microfluidic chamber or "chip-gasket assembly" was placed on Magnet B (M_B) (Figure 3**)** and pumping electrodes were connected with the PS4 sensor leads. Fluid pumping involved applying ± 50, ± 100, and ± 200 µA current between the PEDOT-modified pumping electrodes with a cut-off potential range of -1.0 to +1.10 V. These potential values were set to avoid excursions into the low capacity region of the PEDOT and accidental over-oxidation, respectively. Electrode 1 and 2 ((Figure 2(b)) of the chip were used as working and combined counter/ quasi-reference electrodes, respectively. The two servos on the stationary rail of the automated magnet switching assembly were triggered by the galvanostat's digital signal commands through the aid of the servo trigger board.

Using scripting functionality in the PS4, a sequence of six commands were performed automatically. The first command applied a positive (anodic) current (e.g. +50 µA) for 10 s using the CP technique while the chip-gasket assembly stayed over Magnet B. The second command was a "wait" time for 1 s, effectively an open circuit. The third command sent a digital signal (signal 1) to a connected device, which was the servo trigger to move the magnets and place

Magnet A (M_A) under the chip. The fourth command applied a negative bias current through CP with the same amplitude (e.g. -50 µA) for 10 s while the chip stayed on Magnet A. The fifth and sixth commands were the "wait" time for 1 s and a digital signal (signal 2) to trigger the servo to bring back Magnet B (M_B) under the chip, respectively. This sequence of six commands was repeated five times for each of the applied current values (± 50, ± 100, and ± 200 µA). Data reported here were obtained from these experiments performed in triplicate.

6.2.10 Flow Speed and Profile Evaluation

Fluid velocities were obtained by recording the movement of microbeads that were added to the microfluidic chamber and processing their motion in two different ways. A Sony Handycam digital camera (model: HDR-XR 500V, 30 fps) was interfaced with the microscope to visualize and record the fluid movement

Particle image velocimetry (PIV) software (Dynamic Studio, v. 3.00, Dantec Dynamics, Copenhagen, Denmark) was used for analyzing the fluid flow at the different positions of the magnets under the R-MHD chamber. The PIV analysis is based on image extraction from the video recording by maintaining original resolution and aspect ratio. Every 10th frame of all images acquired from video was loaded into the software, and the bead movement in that sequence was analyzed. Image preprocessing includes the subtraction of mean intensity, maintaining proper image contrast, and interpolating the group into (N-1) double frames. Finally, the 2D2C vector field was evaluated by using averaging in the correlation plane of these double frames, which is known to give reliable data especially in microfluidics.

Flow speed and duration for all other studies were analyzed by particle tracking software. This was accomplished with Tracker® software (https://physlets.org/tracker/). The videos were

directly loaded into the software first. The video pre-processing steps include selecting initial and end frame, setting up true video frame rate, image calibration, and setting the reference frame. After that, a focused bead was selected and tracked automatically by using the autotracker option. At least 3 beads were tracked for each applied current

6.3 Results and Discussion

6.3.1 PEDOT Electrodeposition and Characterization

Thick PEDOT films were electrodeposited on each of the band electrodes to achieve a high charge capacity to maximize the pumping time before reversing the current and switching the magnetic field direction. PEDOT electrodeposited on all the four band electrodes altogether for a total of 572 mC charge and on average on a single electrode electrodeposited for 143 mC. The amount of charge deposited in the film is based on the sum of the integration of each CV cycle during electrodeposition. The total time of deposition was 2748 sec. The electrodeposited PEDOT film went under electrochemical characterization in PBS: glycerol (70% 0.01 M PBS with 30% proteome grade glycerol) solution. The CV response at -0.80 to +0.80 V potential window at 0.05 V/s (Figure S-2 (b)) shows capacitor like behavior with 4.14 ± 0.01 mA/cm^2 charging current density which is ~ 608× higher than the bare gold electrode. The capacitance obtained from the CV response is 82.84 ± 0.28 mF/cm^2. The maximum current responses from the CA data generates 130 ± 2 mA/cm^2 current density. This maximum current density defines how fast the fluid will flow under redox-MHD.

6.3.2 Effect of Magnet Position on Horizontal Flow Velocities

The R-MHD induced flow was evaluated by placing different positions of the magnets under the measurement region of the chip. An understanding of the velocities across the magnet configuration assists in determining restrictions of current-magnet relationships when setting up a magnet-switching protocol. Figure 4 depicts the PIV-analyzed flow profiles across a ~ 2400 µm region between the activated PEDOT-modified band electrodes in two positions (position a, and b) over the magnets. The measurement region of fluid flow covers only the 3/4th of the gap between the active electrodes. Also shown in Figure 4 (c) is the magnetic flux density as predicted by COMSOL simulation. The magnetic flux density measured by gaussmeter (~ 0.14 T) in the middle of the magnet was 0.02 T less than the simulated value (nearly 0.12 T, Figure 4 (c)). Figure 4 (b) shows the chip placement on "position b" which is along the mid-axis of Magnet A. The simulation shows that the largest component of the magnetic flux density there is ~0.11 T, perpendicular to the magnet surface (z-component) and relatively uniform across the 2400 µm observation window, which covers only $12/175^{th}$ of the diameter of a magnet. The experimental velocity vectors in the chamber at "position b" are parallel to each other and to the surface of the chip in the x-direction. This is consistent with parallel ionic current paths in the y-direction that are expected in the center of the chamber and in the middle of the gap between electrodes. In Figure S-6(d) of the Supporting Information, where the microfluidic chamber is at "position f", over the mid-axis of Magnet B, the fluid velocity vectors are oriented in the opposite direction and on average 15 µm/s, which is slightly higher (1.07 times) than that over Magnet A, which averages to 14 µm/s. This is to be expected, however, because the magnetic field is also expected to be slightly higher at the center of Magnet B and 1.09 times that for Magnet A. It is noteworthy to explain the decreasing speed of the fluid going toward the edge of

the magnet where the magnetic flux density is higher. Because mass and momentum must be conserved, there must be a v_z component. This may be a result of tilt in the chamber or a vertically varying z-component of the magnetic field across the x-y plane.

Figure S-6 (a) shows the chip placement over "position c" which is on the right most edge of Magnet A. Upon application of +50 μA current in between active electrodes, fluid flows mostly in the x-direction, but with a small y-component. This could be due to a cross product of j_z and B_x that might dominate the flow at the magnet edge where the magnetic flux density is high, and the ionic current path is curved. Tilt could also affect the uniformity of the speed along the x-y plane of the image. A similar PIV image is obtained in position g shown in Figure S-6(e) of the Supporting Information, except the fluid flows in the opposite direction because of the flipped magnetic field of Magnet B. Likewise mirror images of the PIV images at position c on Magnet A and position g on Magnet B are observed at positions a and e, respectively (Figure 4 (a) and S-6 (c) of the Supporting information). This can be explained by the reversed distribution of the magnetic flux density on the opposite side of each of the magnets.

In the region of position d, where the magnetic flux density between the magnets is very low, one might expect an MHD force of zero. The measured fluid flow in this region and is shown in Figure S-6(b) is extremely slow, but in a direction parallel to the ionic current. The direction of the flow can be explained through natural convection from heating due to illumination by the microscope's lamp.

These studies reveal important considerations for unidirectional R-MHD pumping that maintains a relatively constant speed with minimal perturbation and were implemented in designing the magnet-switching protocol. First, the pumping region of the chip, when current is

applied, should be flat when the activated electrodes are centered on the magnet. In addition, when the magnets are switched beneath the chip, there should be no current between the active electrodes.

6.3.3 Unidirectional Fluid Flow by Manually Switching Magnets Under the Chip

Magnets of opposite field directions (Magnet A and B) were moved under the chip within an "open circuit" time of 5 s between application of currents of opposite biases. The value of the "open circuit" time was set to accommodate the imprecise manual switching of the magnets. Switching was achieved by manually pushing or pulling the ruler to which the magnets were affixed under the chip assembly at the appropriate time while monitoring the chronopotentiometric response , Therefore, the actual time the magnets were switched and the time it took to move the magnets from position b to position f and back were slightly different for each cycle. The first 40 sec of total 180 s experiment was chosen for the analysis purpose.

Figure 5 (a) shows the current vs time graph where both parameters were set in the galvanostat software. Figure 5 (b) and (c) shows the flow distance and fluid velocity responses over 40 sec experiment period. The experiment was divided into two major regions; Flow regions where flow distance increases linearly with time (Reg A, C and E) and "open circuit" regions where fluid do not flow (constant flow distance) due to the absence of current (Reg B and D). Though from the galvanostat software flow and open circuit time were set for 10 and 5 s, experimentally those times deviated a bit. Such as flow duration for "Reg A" and "Reg D" were 9.2 and 10 sec respectively, whereas the open circuit 'Reg B" and "Reg D" both were 6 s. This small mismatch of set and experimental time was due to manually moving the magnets under the chip. The translational object / wooden ruler was moved by hand slowly to minimize the

vibration of the chip assembly but still there are some spikes in the velocity (Figure 5 (c)) were observed. The average velocities for three flow regions were 18.0 ± 0.7, 18.3 ± 0.3, and 18.2 ± 0.5 μm/s. The change in magnetic bias with the applied current keeps the body force (F_B) direction unchanged and the fluid keeps flowing in a single direction.

6.3.4 Unidirectional Fluid Flow Achieved by Automated Switching of Magnets Under the Chip

Three different currents; ± 50, ± 100, and ± 200 μA applied in between the polymer modified electrodes to pump fluid. Figure 6 (a), (b), and (c) shows the fluid velocity, change in applied current, and displacement with time for the first 25 sec of video which consist a little over 1 s of no flow, 10 s of fluid movement (for -50 μA current), total of 2 s of wait time (in addition of triggering time), and another 10 s of fluid movement (due to +50 μA current). All figures are on the same time scale and its evident that right after the flow time fluid flows at a homogeneous speed for 10s. The fluid velocity increases proportionally with the applied current. After the first 10s of flow time, an open circuit and digital trigger signal applied so that the magnets can be interchanged their positions upon triggering under the chip in the presence of "no current". Though the "open circuit" time was set to 1 sec in the galvanostat software, in the experimental velocity (a) and fluid displacement (b) figures the total time was ~2s. So, it took nearly a sec while the galvanostat was triggering the switching device. Then with the application of opposite bias current (+ 50 μA) and magnet, fluid started to flow in the same direction with similar velocity for another 10s. This process of repeated 5 times to pump fluid unidirectionally with a ~2s stop time in between flow. SI Video 1 shows a side-by-side video of the fluid flow at the measurement region and the corresponding magnet switching. This video confirms the synchronizations of current and magnet bias change which results in unidirectional fluid flow.

This automatic galvanostat triggered magnet switching process is an improvement in terms of wait time / Open circuit between flow times compared to the manual switching process (5 s wait time) and minimizing vibration of the pumping setup. Also, the automatic switching method needs minimal manual observation and has good reproducibility.

6.4 Conclusions

The automatic galvanostat triggered magnet switching device is very useful to generate unidirectional, unlimited, and semi-continuous pumping. Previously sustaining high speed flow was a problem in R-MHD microfluidic pumping as it depended upon the overall charge capacity of the deposited PEDOT film. Electrodeposition of very thick film over small electrode creates delamination issue through multiple pumping usage or during assembling / dissembling of the chip-gasket-coverslip setup. Therefore, with the advent of automatic permanent magnet switching under the chip, high speed flow can be sustained indefinitely. Repetitive opposite bias current application ensures regeneration of polymers and synchronized magnet switching with applied current make use of the Lorentz force to push fluid in the same direction, indefinitely. Future modifications of the translational stage could reduce the stop time between MHD flow conditions. One possibility is to synchronize a programmed ionic current with the varying magnetic field while the microfluidic chamber travels across each magnet. This approach would utilize the entire path across the permanent magnets while sustaining a constant MHD force during a deceleration and acceleration period when reversing direction, presumably allowing for a more continuous motion of the magnets. A simpler scenario that would avoid vibrations associated with reversal of direction altogether and improve switching time is to house multiple magnets of alternating fields on a circular base that rotates continuously in a single direction beneath the microfluidic chamber.[22]

6.5 Supporting Information

Supporting information includes chip pictures with before and after PEDOT deposition on the electrodes, CV responses during deposition and during characterization in electrolyte solution of PEDOT films; CP and CA responses of PEDOT films in electrolyte solution; picture and schematic of automatic magnet switching device; pictures of manual magnet switching setup, and PIV flow profile and simulated magnetic field lines at various positions on the magnet.

6.6 Acknowledgements

We are grateful for financial support from the National Science Foundation (CBET-1336853 and CMI-1808286), the Women's Giving Circle, and the Arkansas Bioscience Institute, the major research component of the Arkansas Tobacco Settlement Proceeds Act of 2000. We are grateful to Mr. Mathew Gerner for the initial chip design and Mr. Benjamin J. Jones for design modification.

6.7 References

(1) Whitesides, G. M. The origins and the future of microfluidics. *Nature* **2006,** *442,* 368, DOI: 10.1038/nature05058.

(2) Manz, A.; Harrison, D. J.; Verpoorte, E. M. J.; Fettinger, J. C.; Paulus, A.; Lüdi, H.; Widmer, H. M. Planar chips technology for miniaturization and integration of separation techniques into monitoring systems: Capillary electrophoresis on a chip. *Journal of Chromatography A* **1992,** *593* (1), 253-258, DOI: https://doi.org/10.1016/0021-9673(92)80293-4.

(3) Peeling, R. W.; Holmes, K. K.; Mabey, D.; Ronald, A. Rapid tests for sexually transmitted infections (STIs): the way forward. *Sexually Transmitted Infections* **2006,** *82* (suppl 5), v1, DOI: 10.1136/sti.2006.024265.

(4) Duffy, D. C.; Gillis, H. L.; Lin, J.; Sheppard, N. F.; Kellogg, G. J. Microfabricated Centrifugal Microfluidic Systems: Characterization and Multiple Enzymatic Assays. *Analytical Chemistry* **1999,** *71* (20), 4669-4678, DOI: 10.1021/ac990682c.

(5) Andersson, H.; van der Wijngaart, W.; Nilsson, P.; Enoksson, P.; Stemme, G. A valve-less diffuser micropump for microfluidic analytical systems. *Sensors and Actuators B: Chemical* **2001,** *72* (3), 259-265, DOI: https://doi.org/10.1016/S0925-4005(00)00644-4.

(6) Lazar, I. M.; Karger, B. L. Multiple Open-Channel Electroosmotic Pumping System for Microfluidic Sample Handling. *Analytical Chemistry* **2002,** *74* (24), 6259-6268, DOI: 10.1021/ac0203950.

(7) Leach, J.; Mushfique, H.; di Leonardo, R.; Padgett, M.; Cooper, J. An optically driven pump for microfluidics. *Lab on a Chip* **2006,** *6* (6), 735-739, DOI: 10.1039/B601886F.

(8) Gong, M. M.; Sinton, D. Turning the Page: Advancing Paper-Based Microfluidics for Broad Diagnostic Application. *Chemical Reviews* **2017,** *117* (12), 8447-8480, DOI: 10.1021/acs.chemrev.7b00024.

(9) Dungchai, W.; Chailapakul, O.; Henry, C. S. Electrochemical Detection for Paper-Based Microfluidics. *Analytical Chemistry* **2009,** *81* (14), 5821-5826, DOI: 10.1021/ac9007573.

(10) Cate, D. M.; Adkins, J. A.; Mettakoonpitak, J.; Henry, C. S. Recent Developments in Paper-Based Microfluidic Devices. *Analytical Chemistry* **2015,** *87* (1), 19-41, DOI: 10.1021/ac503968p.

(11) Weston, M. C.; Gerner, M. D.; Fritsch, I. Magnetic Fields for Fluid Motion. *Analytical Chemistry* **2010,** *82* (9), 3411-3418, DOI: 10.1021/ac901783n.

(12) Sahore, V.; Fritsch, I. Flat Flow Profiles Achieved with Microfluidics Generated by Redox-Magnetohydrodynamics. *Analytical Chemistry* **2013,** *85* (24), 11809-11816, DOI: 10.1021/ac402476v.

(13) Nash, C. K.; Fritsch, I. Poly(3,4-ethylenedioxythiophene)-Modified Electrodes for Microfluidics Pumping with Redox-Magnetohydrodynamics: Improving Compatibility for Broader Applications by Eliminating Addition of Redox Species to Solution. *Analytical Chemistry* **2016,** *88* (3), 1601-1609, DOI: 10.1021/acs.analchem.5b03182.

(14) Khan, F. Z.; Hutcheson, J. A.; Hunter, C. J.; Powless, A. J.; Benson, D.; Fritsch, I.; Muldoon, T. J. Redox-Magnetohydrodynamically Controlled Fluid Flow with Poly(3,4-ethylenedioxythiophene) Coupled to an Epitaxial Light Sheet Confocal Microscope for Image Cytometry Applications. *Analytical Chemistry* **2018,** *90* (13), 7862-7870, DOI: 10.1021/acs.analchem.7b05312.

(15) Homsy, A.; Koster, S.; Eijkel, J. C. T.; van den Berg, A.; Lucklum, F.; Verpoorte, E.; de Rooij, N. F. A high current density DC magnetohydrodynamic (MHD) micropump. *Lab on a Chip* **2005,** *5* (4), 466-471, DOI: 10.1039/B417892K.

(16) Hutcheson, J. A.; Khan, F. Z.; Powless, A. J.; Benson, D.; Hunter, C.; Fritsch, I.; Muldoon, T. J. A light sheet confocal microscope for image cytometry with a variable linear slit detector, *Proc. SPIE.* **2016**, 9720, 97200U, DOI: https://doi.org/10.1117/12.2211164.

(17) Khan, F. Z.; Fritsch, I. Materials Study for Optimization of Redox-Magnetohydrodynamics (R-MHD) for Pumping in Microfluidics Systems. *Meeting Abstracts* **2016,** *MA2016-01* (41), 2064-2064.

(18) Khan, F. Z.; Fritsch, I. Performance of Conducting Polymers Electropolymerized Under Various Conditions for Redox–Magnetohydrodynamics (R-MHD) Pumping. *Meeting Abstracts* **2017,** *MA2017-01* (43), 2017-2017.

(19) Lemoff, A. V.; Lee, A. P. An AC magnetohydrodynamic micropump. *Sensors and Actuators B: Chemical* **2000,** *63* (3), 178-185, DOI: https://doi.org/10.1016/S0925-4005(00)00355-5.

(20) Eijkel, J. C. T.; Dalton, C.; Hayden, C. J.; Burt, J. P. H.; Manz, A. A circular ac magnetohydrodynamic micropump for chromatographic applications. *Sensors and Actuators B: Chemical* **2003,** *92* (1), 215-221, DOI: https://doi.org/10.1016/S0925-4005(03)00267-3.

(21) Nash, C. K. The 2014 Colin G. Fink Summer Research Fellowship — Summary Report: Advanced Microfluidic Pumping at Poly(3,4-ethylenedioxythiophene)-Modified Electrodes via AC-Magnetohydrodynamics. *The Electrochemical Society Interface* **2014,** *23* (4), 79-80.

(22) Fritsch, I., Nash, C., Kumar, S., Muldoon, T., Balachandran, K., Claycomb, A., Gerner, M.D., Hutcheson, J., Khan, F.Z., Powless, A. and Prieto, S., 2018. Magnetohydrodynamic Microfluidic Systems Including Modified Electrodes and Methods of Using the Same. U.S. Patent Application 15/957,832.

6.8 Figures

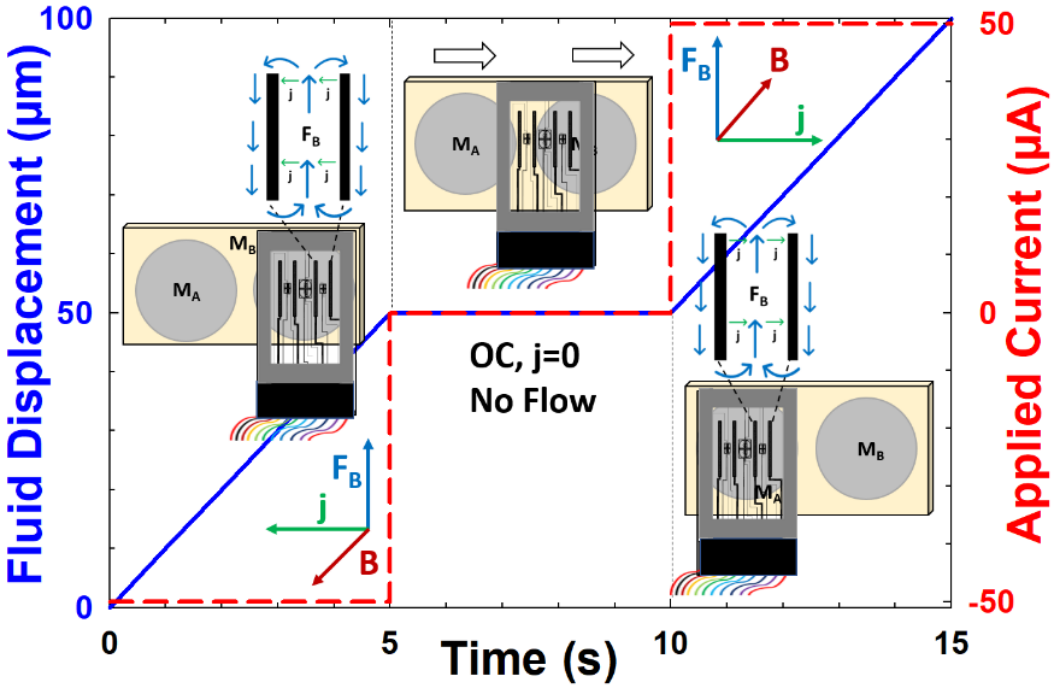

Figure 1: The concept of magnet switching. It provides indefinitely sustained MHD microfluidics. Shown is a representative plot of fluid displacement and applied current as a function of time during a switching experiment. Top-down schematics are depicted of the relative positions of the chip and the two magnets with fields in opposite directions during the experiment at each time interval, with the resulting direction of fluid movement. A current of -50 µA (anodic) is applied from 0-5 s while Magnet A (M_A) is under the chip, zero current is maintained from 6 -10 s when Magnet B is moved under the chip, and a current of +50 µA (cathodic) is applied from 11 -15 s while Magnet B (M_B) is under the chip. Coordinates indicate relative orientation of current, **j**, magnetic field, **B**, and resulting MHD force, $\mathbf{F_B}$, at each experiment interval. The magnetic field of Magnet A is oriented out of page and that of Magnet B is oriented into the page.

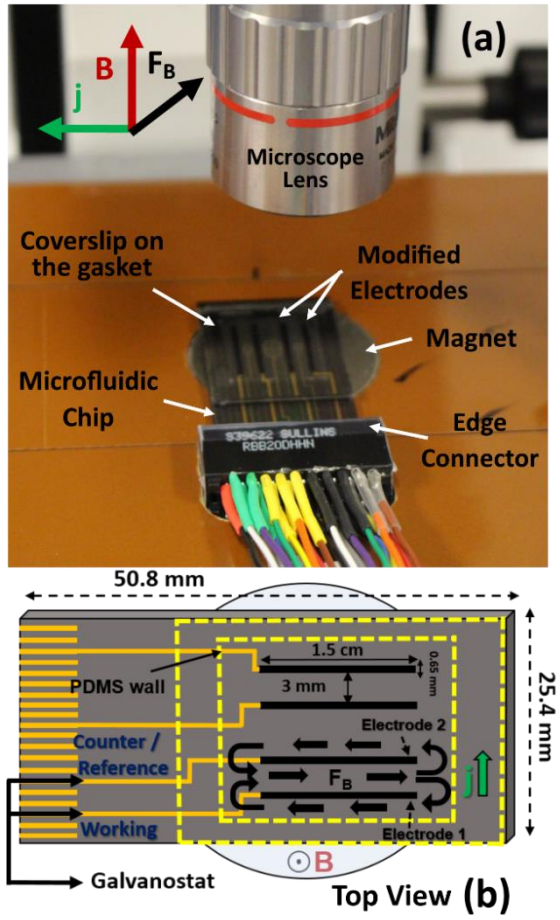

Figure 2: Experimental setup. In (a), the chip-gasket assembly is placed on the permanent magnet (NdFeB, 0.37 T) that is housed on a translational stage. The whole chip-gasket-magnet assembly is located on the microscope stage. A glass coverslip is placed over the gasket which contains the "buffer / glycerol / beads" solution. The pair of electrodes labeled as "Modified Electrodes" are the ones that were activated for pumping fluid. The edge connector maintains individual electrical connection between electrode and current controller. The schematic in (b) depicts a chip and solution region defined by the opening in the PDMS gasket (outlined by yellow dashed lines) over a magnet with the direction of fluid flow (black arrows) between and around the activated electrodes. For this study electrodes 1 and 2 served as the working and combined counter/reference electrodes, respectively.

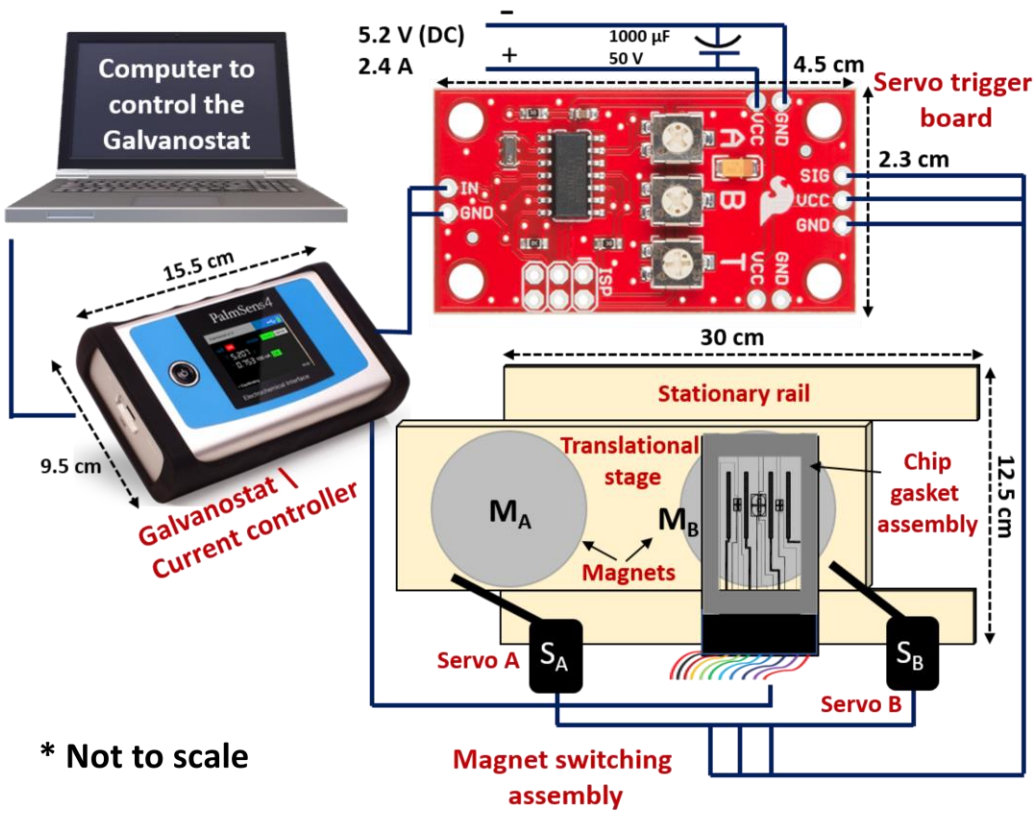

Figure 3: The automated magnet switching system has four distinctive parts: the computer to run galvanostat software, galvanostat (current controller), servo trigger board and translational stage with magnets having opposing field directions, and chip-gasket assembly. The galvanostat is connected with the computer through USB C cable. The servo trigger board's input is connected to a digital output line of the current controller through a 15-pin D-sub auxiliary connector. The servo trigger board output lines connect with the servos S_A and S_B that attach to the stationary rail of the translational stage. The translational stage has one moving section (5 × 30 cm) that attaches through nylon splines to two identical stationary sections (3.8 × 30 cm), so that the translational section can move freely. Two NdFeB permanent magnets, oriented with opposite field directions, and 50 mm apart from magnet edge to edge, are press-fit into holes bored through the center section.

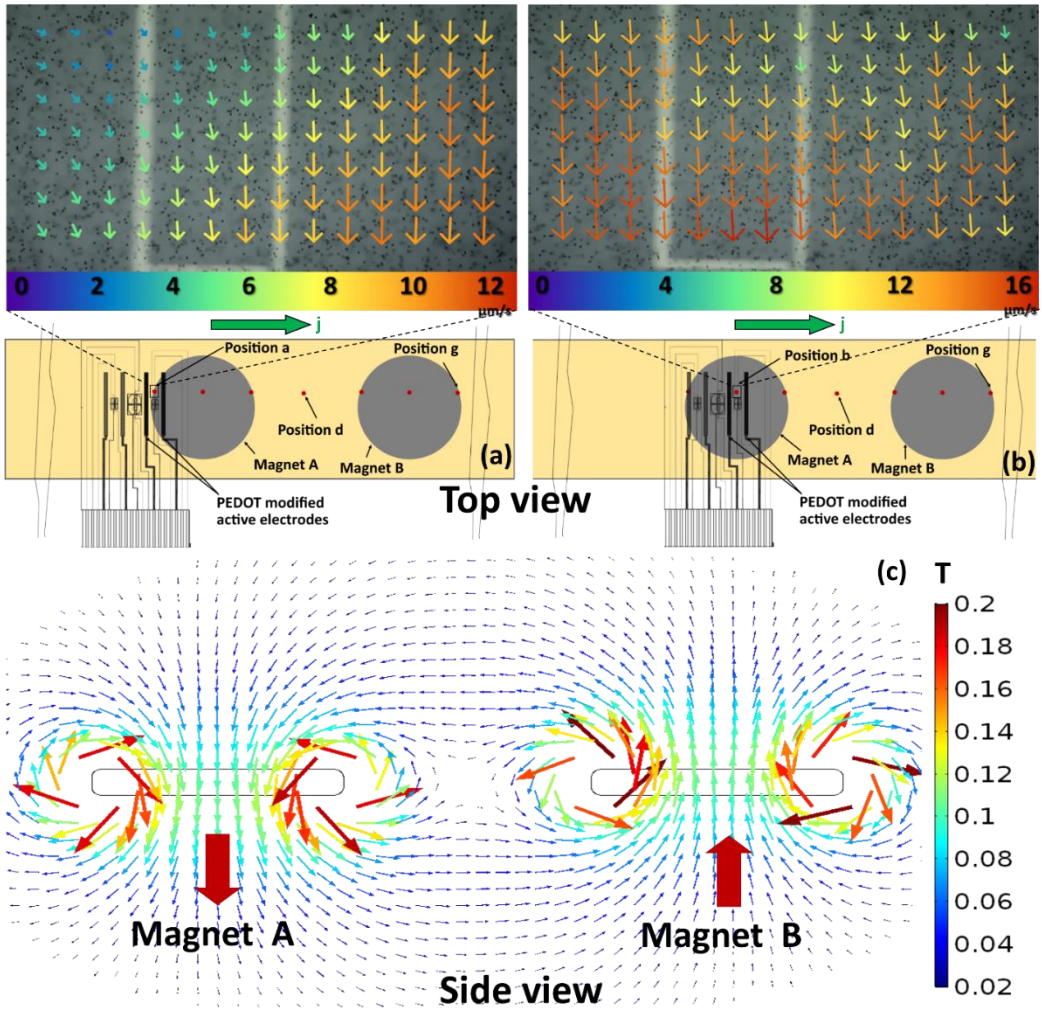

Figure 4: (a) and (b) are the top view of the chip placement over the magnets on a translational stage schematic. In (a), the measurement region of the chip was placed over "position a" (at the edge of magnet A) and the expanded PIV flow profile shows the flow characteristics and experimental fluid velocity. (b) shows a similar figure as (a) when the chip placed over "position b" on Magnet A. (c) shows the simulated magnetic field lines for two magnet system attained by COMSOL simulation.

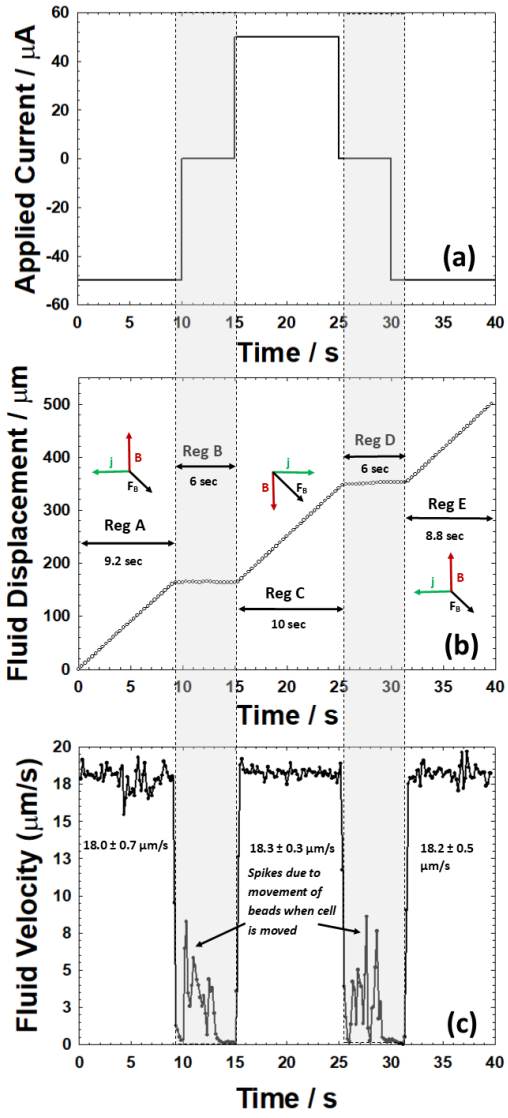

Figure 5: Data were collected from the manual magnet switching experiment. In (a) the function of applied current with time is shown, where both the current value and time were set in the galvanostat's software. In (b) and (c) the resulting displacement of fluid and corresponding velocity are plotted, respectively. Horizontal speed at 640 μm vertical position in a chamber of 760 μm height are shown, where ± represents one standard deviation of the averages of the velocities for every flow region (Reg A, C, and E).

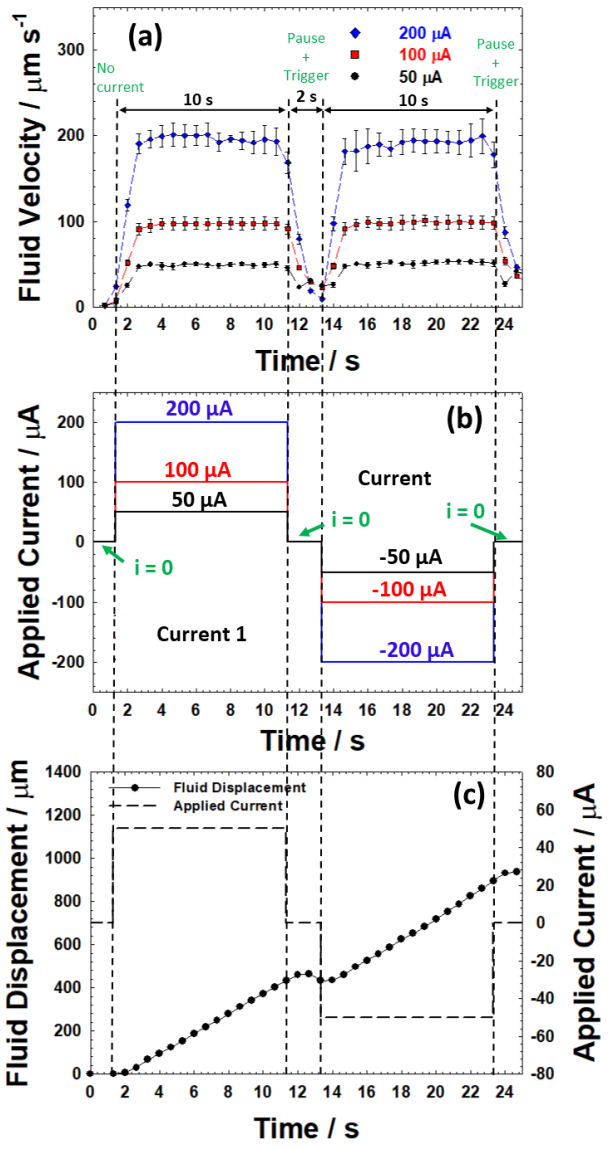

Figure 6: (a), (b) and (c) show the fluid velocity, change in applied current, and fluid displacement relationships with the time. Instantaneous fluid velocity at each time of the experiment (a) was obtained using the displacement data in (c) for a given time interval (<give time, s>) and dividing by that time interval. All data acquired from the first 25 second videos that obtained during automatic magnet switching experiments for 50,100, and 200 uA applied currents when chip is over a given magnet. Fluid velocity and displacement data acquired by tracking polystyrene beads in MHD chamber using Tracker software.

6.S Supporting Information: Sustained Microfluidics Pumping with Conducting Polymer Modified, DC-Redox-Magnetohydrodynamics (R-MHD) Achieved by Switching Permanent Magnets

Supporting information includes Chip pictures with before and after PEDOT deposition on the electrodes, CV responses during deposition and during characterization in electrolyte solution of PEDOT films; CP and CA responses of PEDOT films in in electrolyte solution; picture and schematic of automatic magnet switching device; pictures of manual magnet switching setup, and PIV flow profile and simulated magnetic field lines at various positions on the magnet.

6.S1 Supporting Information Figures

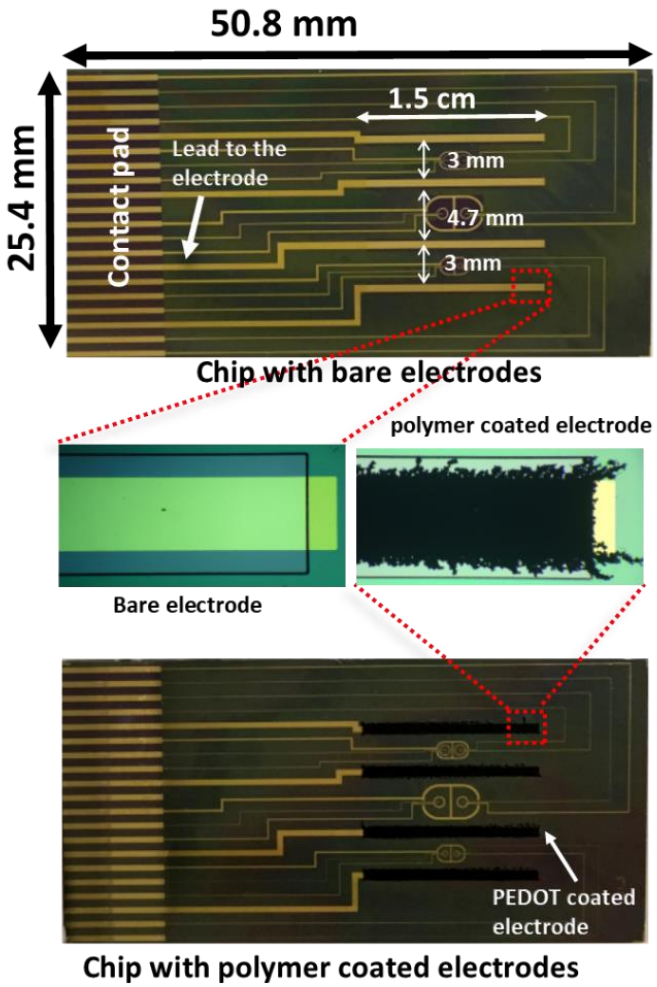

Figure S-1: (Top figure) Electrode chip picture before electrodeposition of PEDOT films. Each chip is 50.8 × 25.4 mm (1 in. × 2 in.) in dimension and has four individually addressable electrodes. Each electrode is 1.5 cm in length and 650 µm width. The outer most electrode pairs are spaced out by 3 mm whereas the middle two electrodes have 4.7 mm gap. Each electrode electronically connected with current controller through contact pads and edge connector (not shown here). (bottom figure) is the chip picture after electrodeposition of PEDOT on all the four electrodes. The expanded pictures show the bare and polymer coated electrode.

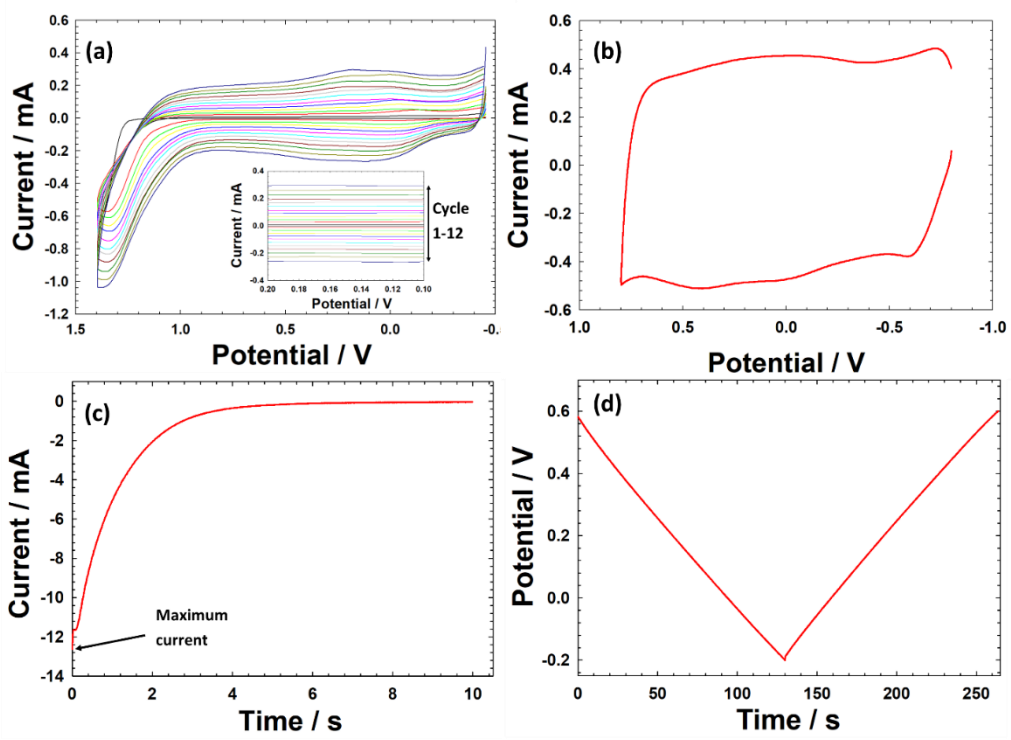

Figure S-2: (a) CV responses during electropolymerization in propylene carbonate solutions containing 0.010 M EDOT in 0.100 M TBAPF6 in a potential window of -0.455 to 1.40 V for 12 cycles. (b) CV characterization at 50 mV/s in 0.100 M NaCl aqueous solution of PEDOT modified electrode. PEDOT films were deposited for 12 cycles at 5 mV/s. (c) A representative chronoamperometry response acquired by holding the potential at -0.80 V for 10 sec and then stepped to +0.80 V for 10 sec. (d) A representative chronopotentiometry response acquired by applying +50 µA current with -0.20 to 0.60 V potential window. For all experiments here a three-electrode cell was used with a Ag/AgCl (saturated KCl) reference and Pt flag counter electrodes with 20 mL of monomer / characterizing solution in a 20 mL glass beaker.

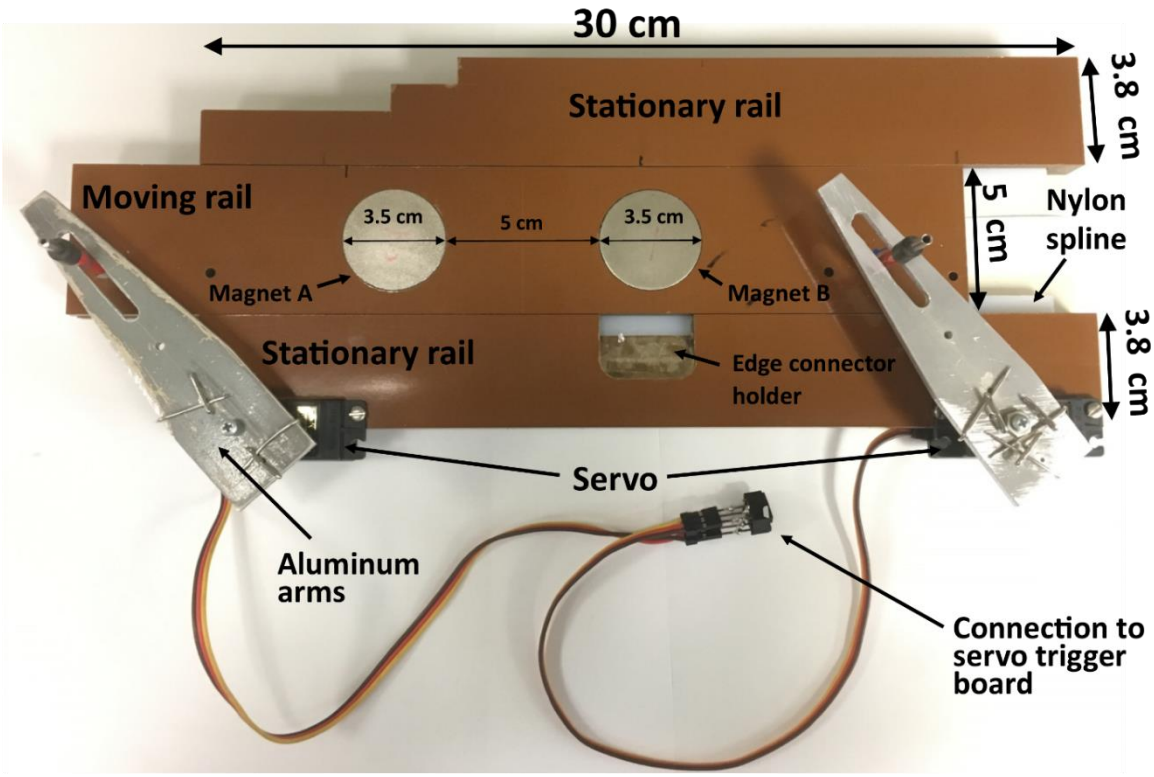

Figure S-3: The top view of servo-driven magnet switching assembly. The moving rail can move between two stationary rails. Two opposite biases magnets were press fit into the bored holes on the moving rail. Two standard servos were attached on two ends of the bottom stationary rail and each one is attached with a machine milled aluminum arms which moves the moving rail.

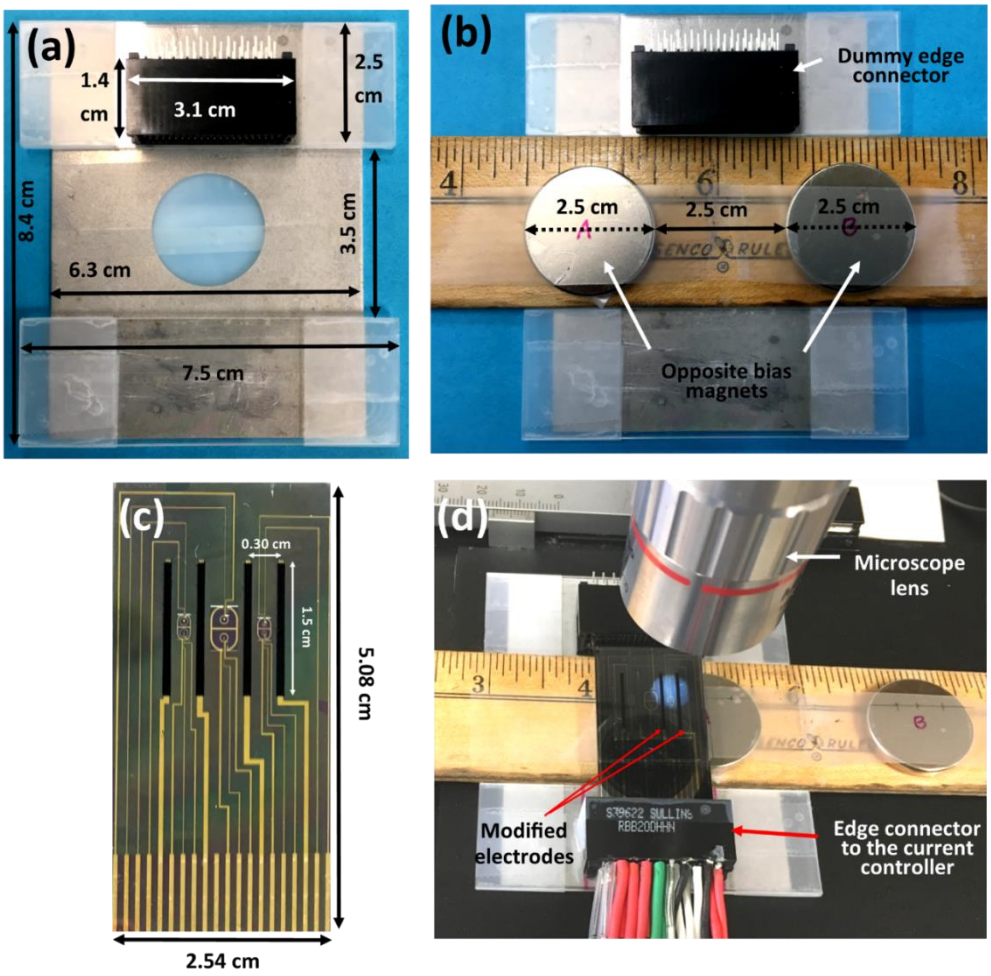

Figure S-4: (a) shows the chip-magnet holder assembly where the base is made of stainless-steel block (8.4 × 6.3 × 0.15 cm) and two sets of glass slides (7.5 × 2.5 × 0.20 cm) taped on the top and bottom portion of the stainless-steel block. A dummy edge connector is taped on the top slides set to hold the chip still. (b) Two opposite bias magnets (~ 0.14 T) were taped on a wooden ruler (3.3 cm width) which was placed within the gap between glass slide sets. (c) a picture of chip with PEDOT coated electrodes. (d) the complete assembly on the microscope stage where the chip (with PEDOT coated) with gasket and glass slides placed on top fit perfectly flat on the stage and wooden ruler with magnets moves freely beneath it.

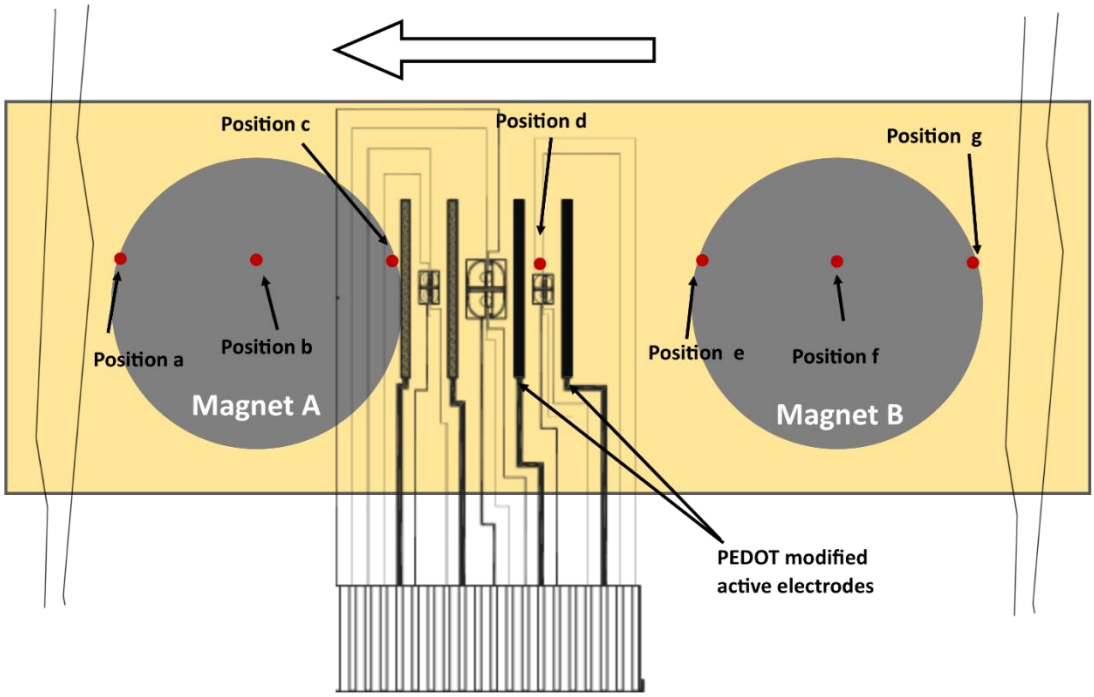

Figure S-5: The schematic shows the chip placement on different positions of two opposite biases magnets that fit on a translational stage (wooden ruler). Two magnets were separated by 2.5 cm from edge to edge. Each magnet has 3 coaxial positions on which the measurement region of the chip will be placed over to analyze fluid flow; two at two edges of the magnet and one at the mid axis. Besides, fluid flow will also be analyzed at the middle of the gap between the magnets (position d).

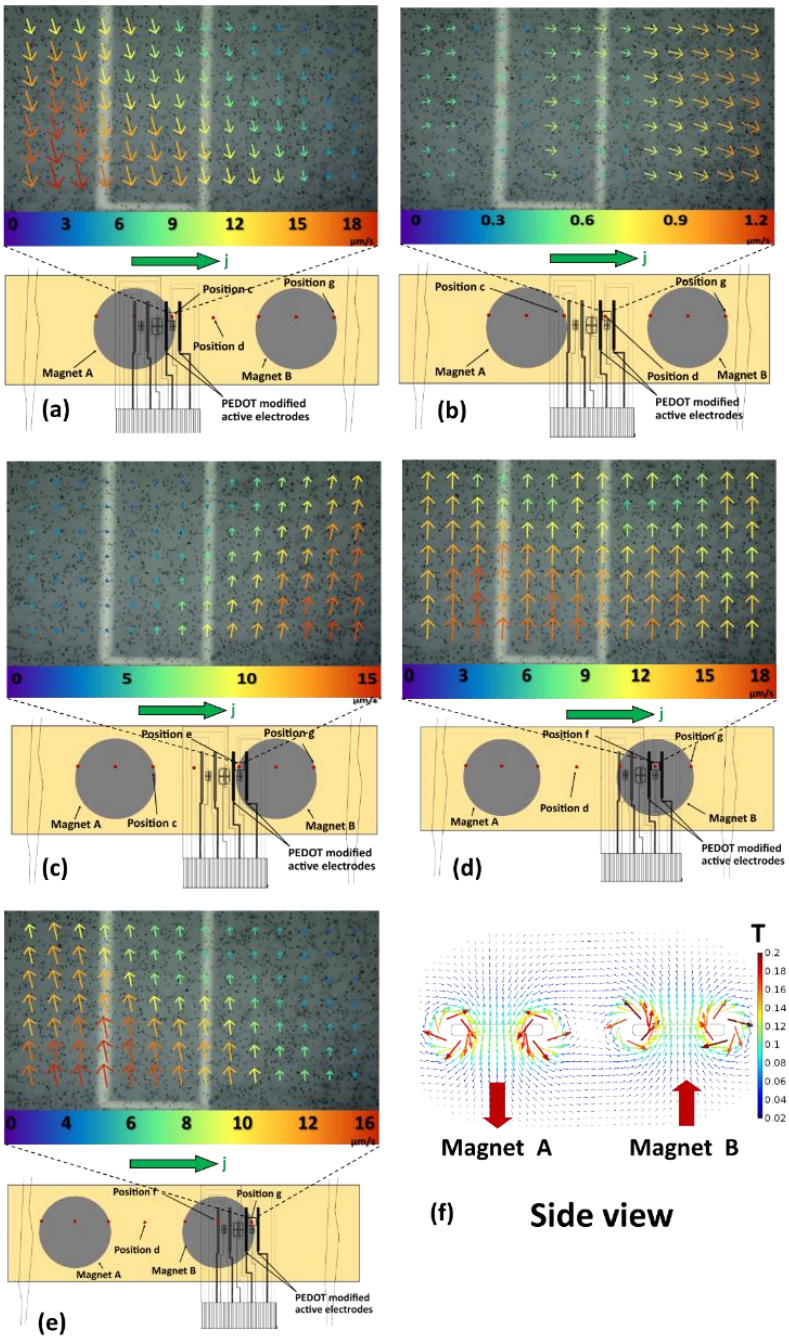

Figure S-6: (a), (b), (c), (d), and (e) are the top views of the chip placement over two magnets at the position c, d, e, f, and g. The expanded views of (a)-(e) show the PIV flow profile that depicts the flow characteristics and experimental fluid velocity at those positions on the magnets. (f) shows the simulated magnetic field lines for two magnet system attained by COMSOL simulation.

7. Conclusions and Future Work

7.1 Conclusions

This dissertation includes a series of research work that demonstrate the improvement of electrodeposited conducting polymer film properties for enhanced R-MHD flow performance, employment of a unique method, APTV to analyze the flow profile in three-dimensions, and a successful merging of R-MHD and light sheet confocal microscopy (e-LSCM) as imaging cytometer. Also, this dissertation includes a device modification approach which aided to sustain high speed R-MHD fluid flow unidirectional, for unlimited time.

Ionic current density (j) generates from the conversion of electronic current through the oxidation-reduction of conducting polymers. The fluidic speed scales with this j, but the flow duration depends on the total charge (Q). In the first two chapters of this dissertation, PEDOT electropolymerization has been optimized for maximum current and charge density. PEDOT from propylene carbonate solvent with $TBAPF_6$ electrolyte demonstrated 108 % faster and 244 % longer R-MHD induced flow than previous aqueous deposition approach. EDOT monomer showed better electrochemical performance than ProDOT and polymers from propylene carbonate demonstrated better mechanical stability than acetonitrile.

R-MHD velocity profile characterization in three-dimensions inside the microfluidic chamber was another important aspect of this research work. R-MHD pumping parameters such as electrolyte concentration, chamber height, and applied current were varied and the resulted flow profiles were analyzed by astigmatism particle tracking velocimetry (APTV) method. This high-resolution velocimetry method revealed that, the flow in stream-wise direction scales with Lorentz-force and no significant velocity vectors observed in y and z direction.

As an application, the improved polymer-modified R-MHD pumping system merged with a light sheet confocal microscope to simultaneously image and count leukocytes cells in a deep microfluidic chamber. This research work has resulted with ~ 5000 particles / sec theoretical throughput and 0.6 μm lateral image resolution.

Some microfluidic applications, such as on-chip separation requires even longer pumping duration, at a high speed, and in a single direction. To address this limitation, a device was built which synchronized opposite bias currents and magnetic fields that sustained unidirectional high-speed pumping, for indefinite time.

7.2 Future Work

This dissertation contains a series of research projects that collectively achieved an automated, high-speed and unidirectional fluid pumping system. Materials optimization (polymer and electrolyte) alone has enhanced the fluidic speed but the flow duration was still dependent upon the total charge. Therefore, the polymer recharging was necessary and fluid flow was only continuous by pushing them back and forth. This version of R-MHD system was merged with a confocal microscope to use as an imaging cytometer. But after the device optimization with switching magnets, R-MHD pumping became independent of the polymer's charge capacity. Therefore, the system became ready to be used in applications where unidirectional and unlimited flow is necessary.

The Enumeration and classification of phytoplankton species in freshwater might predict harmful algal blooms and damaging ecological events. The continuous R-MHD system can be combined with wide-field fluorescence microscopy to form a phytoplankton-specific imaging prototype. Samples from lakes or rivers which are naturally abundant with phytoplankton can be

transported through the R-MHD pumping system continuously in a single direction with the capability to stop the flow, take images and then flow in opposite direction if necessary. This technique will allow precise control of phytoplankton containing suspensions and has the capability to be a field portable pumping-imaging device. Figure 1 shows the schematic of R-MHD / widefield fluorescence imaging couple (a) where a programmable Raspberry Pi microcontroller and self-contained battery pack, will configure the system to transport small volumes of suspended cells through the imaging region. Fig (b) shows a mixture of two model species (*Anabaena* and *Microcystis*) imaged under the widefield fluorescence microscope. These digital autofluorescence images contain information about cellular morphology, size, and colorimetric features of chlorophyll that can be used in MATLAB post-processing for differentiating various phytoplankton.

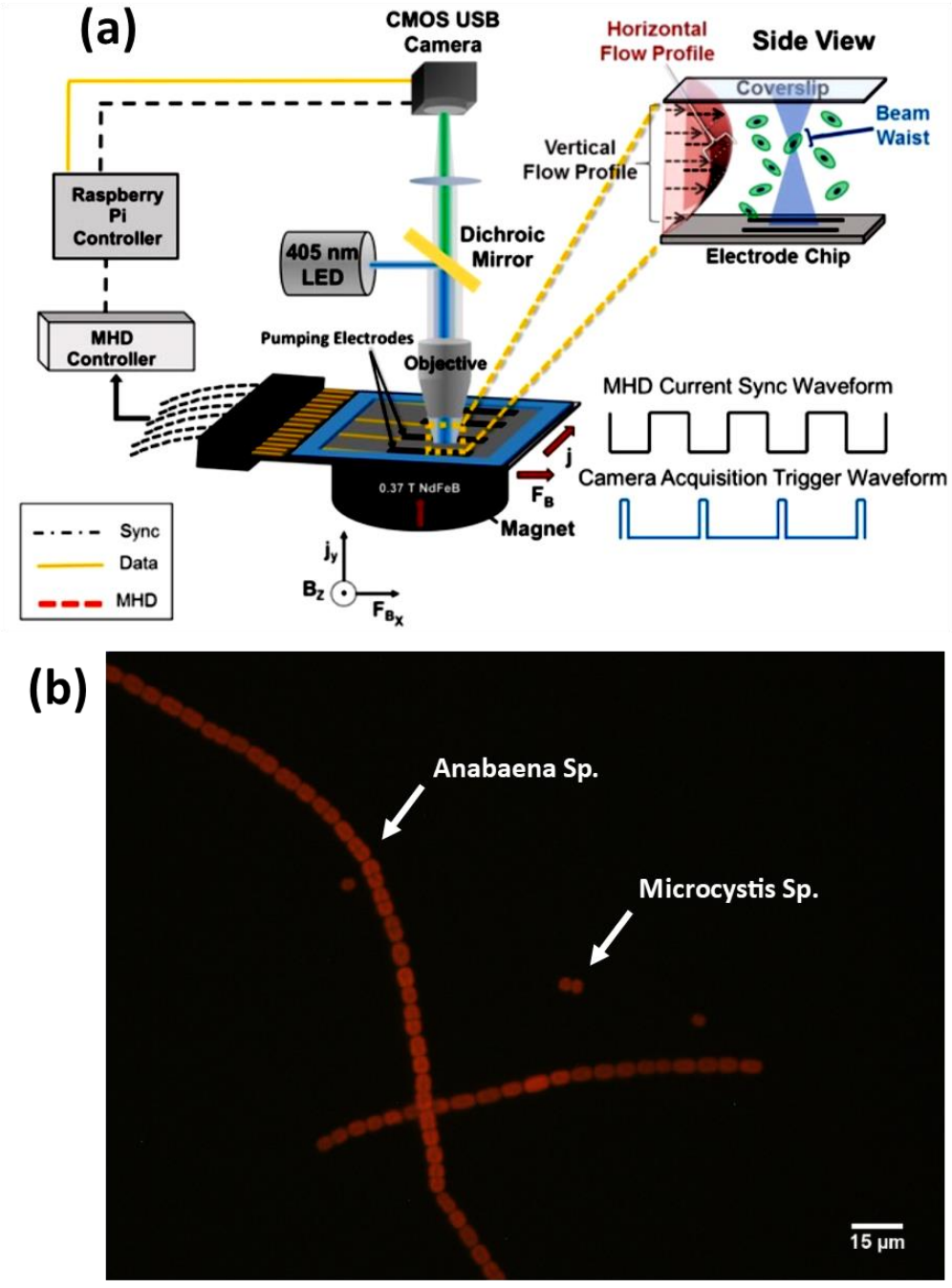

Figure 1: (a) schematic of a portable R-MHD / widefield fluorescence microscope couple to enumerate and classify important phytoplankton from freshwater. (b) autofluorescence image of a mixture of *Anabaena* and *Microcystis* species.